Markus Zimmermann

Multi-particle Correlation Studies in Heavy-Ion Collisions at the LHC

- 2016 -

Experimentelle Physik

Multi-particle Correlation Studies in Heavy-Ion Collisions at the LHC

Inaugural-Dissertation
zur Erlangung des Doktorgrades
der Naturwissenschaften im Fachbereich Physik
der Mathematisch-Naturwissenschaftlichen Fakultät
der Westfälische Wilhelms-Universität Münster

vorgelegt von
Markus Zimmermann
aus Warendorf

- 2016 -

Dekan:	Prof. Dr. Christian Weinheimer
Erster Gutachter:	Prof. Dr. Johannes P. Wessels
Zweiter Gutachter:	Dr. Andreas Morsch

Tag der Disputation:
Tag der Promotion:

Contents

1. Introduction **1**

2. Theoretical Background **3**
2.1. The Standard Model . . . 3
2.2. Quark-Gluon Plasma . . . 6
2.3. Jet Quenching . . . 9
2.4. Flow . . . 13
2.5. HIJING . . . 14
2.6. The Nuclear Suppression Factor R_{AA} . . . 15
2.7. Two Particle Correlations in Pb–Pb and pp Events . . . 18
2.8. Two Plus One Particle Correlations at STAR . . . 20

3. The LHC and the ALICE Detector **25**
3.1. The Large Hadron Collider . . . 25
3.1.1. Design Performance of the LHC . . . 27
3.1.2. The Experiments . . . 28
3.2. ALICE . . . 29
3.2.1. Central Barrel . . . 29
3.2.2. Forward Detectors . . . 35
3.2.3. The ALICE Trigger System . . . 36
3.2.4. Computing Tools . . . 38

4. Event and Track Selection **41**
4.1. Beam-Gas-Interactions . . . 41
4.2. Centrality . . . 42
4.3. Vertex Selection . . . 46
4.4. Event Selection . . . 46
4.5. Track Selection . . . 47

5. Two Particle Correlations **51**
5.1. Toy Event Generator . . . 51
5.2. Correlations within the Same Event . . . 53
5.3. Correlations within the Mixed Event . . . 57
5.4. Single Particle Efficiency Correction . . . 59
5.5. Background . . . 61
5.6. Peak Yield Extraction using a Fit . . . 63
5.7. Peak Yield Extraction using direct Bin Counting . . . 63

6. Two Plus One Particle Angular Correlations 65
6.1. Correlations within the Same Event . . . 65
6.2. Correlations within the Mixed Event . . . 67
6.3. Efficiency Correction . . . 70
6.4. Background from Uncorrelated Trigger Combinations . . . 71
6.4.1. Mixed Combinatorics Method . . . 72
6.4.2. Background Same Method . . . 75
6.4.3. Background Components . . . 75
6.4.4. Scaled 1+1 Events . . . 84
6.5. Uncertainty as a Function of Jets per Event . . . 86
6.6. Yield Extraction in the 2+1 Analysis . . . 86
6.7. Observables of the 2+1 Correlation Measurements . . . 87
6.7.1. Ratio of the Yield from PbPb and pp Events . . . 88
6.7.2. Ratio of the Trigger 1 and Trigger 2 Peak Yield R_{T1T2} . . . 89

7. Two plus One Particle Correlations in HIJING Events 91
7.1. Trigger Combinations . . . 91
7.2. Signal Extraction . . . 92
7.3. The Integrated Correlation Peaks in HIJING . . . 96
7.4. Centrality Dependence of the Particle Yield . . . 98
7.5. Trigger Dependence of the Particle Yield . . . 98
7.6. Summary . . . 101

8. Systematic Uncertainties 103
8.1. Check of the Barlow Criteria . . . 103
8.2. Sources of Systematic Uncertainties . . . 107
8.3. Systematic Uncertainty from the Bin Positions . . . 113
8.4. Summary . . . 114

9. Two Plus One Particle Correlations in Pb–Pb Collisions 119
9.1. Signal Extraction . . . 119
9.2. Trigger Combinations . . . 123
9.3. Comparison of the per Trigger Yield . . . 124
9.4. Integration of the Correlated Yield . . . 127
9.5. Centrality Dependence of the Particle Yield . . . 130
9.6. Comparison of the Pb–Pb and pp Peak Yield . . . 133
9.7. Trigger Dependence of the Particle Yield . . . 137
9.8. Comparison of the ALICE and STAR I_{AA} . . . 139
9.9. Summary . . . 140

Summary 143

Zusammenfassung 145

A. The LEGO Train System **147**
A.1. Workflow . . . 148
A.1.1. Starting a Train Run . . . 149
A.2. Train Runs . . . 150
A.2.1. The Web Page . . . 150
A.2.2. Testing a Train . . . 152
A.2.3. Splitting of the Train Jobs . . . 154
A.2.4. Merging the Jobs . . . 154
A.2.5. Killing and Resubmitting Jobs . . . 155
A.3. Interface . . . 156
A.3.1. Activating Wagons . . . 156
A.3.2. Subwagons . . . 157
A.4. System Improvements . . . 158
A.4.1. Input Files per Train Run . . . 158
A.4.2. Basket Distribution . . . 159
A.4.3. Basket Clean Up . . . 160
A.4.4. Skip Processing per Run Number . . . 161
A.4.5. Turn Around Time . . . 161
A.4.6. Running Time Optimization . . . 163
A.4.7. Usage of the Train System . . . 163
A.5. Summary . . . 164

B. Acronyms **167**

1. Introduction

In the Large Hadron Collider (LHC) protons and Pb-ions collide at collision energies which have never been reached before in a collider experiment. It is located at the European Organization for Nuclear Research (CERN[1]). The particle collisions are measured by seven experiments at four interaction regions of the LHC. These experiments study the properties of the collision products. Different research topics are addressed from the analysis of the fundamental forces over particle decays to the properties of the early universe.
One of the experiments is ALICE (A Large Ion Collider Experiment) which is optimized for the study of Pb–Pb collisions. The main goal is to study the properties of the Quark-Gluon Plasma (QGP). It is a new state of matter in which quarks and gluons do not belong to a certain baryon or meson anymore.
In heavy-ion collisions signatures of the QGP were observed. The single particle yield as a function of transverse momentum is suppressed at high transverse momenta in Pb–Pb collisions compared to the expectations from pp collisions. Several other observables measure the energy loss of partons which interact with the new medium. Before these partons reach the detector, they hadronize. In this process a collimated shower of particles is created at a small angular distribution. The particles are identified as jets with dedicated jet finder algorithms which is a non-trivial process in heavy-ion collisions, because all other hadronized particles from the QGP form the underlying event.
One example for a QGP signature can be found in di-jet measurements. A di-jet is the combination of two jets back-to-back in azimuth which are created by the same hard collision. If a parton with a large transverse momentum is created, due to momentum conservation a second parton needs to have the same transverse momentum in the opposite direction. The hadronization of these partons forms a di-jet.
In some di-jets the jets have a different jet transverse momentum. One interpretation of this difference is that one parton, before it hadronized into a jet, interacted more with the QGP than the recoiling parton. This way the first parton could transfer more momentum to the QGP than the second one. In events with such a di-jet the transverse momentum difference between the jets has been found as additional transverse momentum contained in the underlying event in direction of the lower transverse momentum jet. Jets which transfered some momentum to the underlying event are called quenched.
Due to fluctuations in the underlying event the jet momentum analysis is only possible for high momentum jets. For low momentum jets the jet finders may misidentify a

[1]The acronym CERN originally stood for Conseil Européen pour la Recherche Nucléaire.

fluctuation in the underlying event as jet. Additionally the measured jet momentum has large uncertainties. But other measurements are possible which do not require jet finders. One example is two particle angular correlations.
Instead of reconstructing a jet, a single particle of a certain transverse momentum is taken as proxy for a jet and the surrounding particles in the same event are analyzed. The proxy particle is called a trigger and the other particles in the event are called associated particles. In the hadronization of a parton multiple particles are created. Due to the high initial momentum of the parton, the new particles are measured at a small angular difference compared to the original parton direction. Particles which were created in the same fragmentation process are obviously correlated with each other. These particles form the associated particle yield and they are analyzed for different trigger momenta.
In the next step the associated yield of jets in Pb–Pb and pp collisions can be compared. In Pb–Pb events more particles with a low associated transverse momentum have been found than in pp events. In a single event the associated particles from the trigger cannot be compared with the associated particles of the recoil jet because this recoil jet cannot be identified. It can only be analyzed averaged over many events. There the averaged recoil jet yield is smaller in Pb–Pb events than in pp events.
In this thesis a further development of the two particle correlation method is presented. The two plus one particle angular correlations analyze the associated particles around two trigger particles, which are back-to-back in azimuth. This method allows the comparison of the associated particle yield from Pb–Pb events with the yield from pp events and the associated particle yield from one trigger with the associated particle yield from the recoiling trigger.
This thesis is structured as follows. Chapter 2 introduces the basic theoretical concepts. Several theoretical models are explained together with experimental observations. Part of these measurements are the above described measurements.
Chapter 3 briefly describes the LHC and ALICE. The event and track selection which are used for the analysis in this thesis are specified in Chapter 4.
In Chapter 5 the concept of two particle angular correlations is explained. The practical measurements are described and illustrated together with a theoretical description of the observables. This concept is extended into two plus one particle angular correlations in Chapter 6.
The two plus one correlations have been measured in HIJING simulations which is presented in Chapter 7. HIJING is a MC generator and this analysis is used to cross-check the new correlation method.
The systematic uncertainties of the data analysis are discussed and evaluated in Chapter 8. In Chapter 9 the results of two plus one correlations are presented and discussed. The associated particle yield and the derived observables are calculated. They are compared with earlier measurements from STAR.
Part of this thesis was the technical work on the LEGO train system which is described in appendix A. Several monitoring tools have been developed to identify bottlenecks of the system. Subsequently the efficiency and the handling of the system were improved.

2. Theoretical Background

This chapter gives a short overview of the basic theoretical concepts and measurements which are relevant for the analysis in this thesis. The standard model of particle physics is described in Section 2.1. Afterwards the Quark-Gluon Plasma (QGP) is introduced in Section 2.2. The properties of this medium are the main analysis focus of this thesis. In Section 2.3 the effect of the QGP on jet probes is described. This is measured with high energetic di-jets in heavy-ion collisions. In these systems the energy transfer from a jet to the medium can be observed.
Apart from the energy loss, in heavy-ion collisions a collective effect exists which is called particle flow. This effect is part of the background for the correlation analysis in this thesis. It is briefly described in Section 2.4.
In this thesis events from Monte Carlo (MC) simulations are used to validate a new particle correlation method. The events are simulated with the HIJING event generator, which is described in Section 2.5.
In the comparison of pp and Pb–Pb events a signature of the QGP has been identified. An observable to quantify the medium effects in heavy-ion collisions is introduced in Section 2.6 and results from measurements in ALICE are presented.
In Section 2.7 the particle correlation analysis is introduced which determines the jet yield at lower energies. Dedicated observables are explained and results from ALICE are shown.
The further development of the particle correlation method is the two plus one particle correlation method. The method has been used by the STAR experiment and their results are presented in Section 2.8. This analysis method is the main topic of this thesis. It is further developed and applied on ALICE data in the later chapters of this thesis.

2.1. The Standard Model

The standard model (SM) of particle physics is a theory which describes the fundamental particles and forces. They interact via the strong, the weak and the electromagnetic force. In this chapter a rough overview of the standard model is given. A more detailed description can be found in a text book like [Per00].
The fundamental forces, their mediators and the particles which are affected by the force are shown in Table 2.1. Additionally to the already mentioned forces, gravity is a fundamental force as well, but it cannot be explained by the standard model. Due to the low relative strength it has practically no impact on particles with the dimensions of fundamental particles. If these particles get very close to each other, gravity has

Interaction	Mediator	Applies to	Relative Strength
strong	gluon, G	quarks, gluons	1
electromagnetic	photon, γ	charged particles	$\approx 10^{-2}$
weak	$W^{\pm}, Z^0$	quarks, leptons	$\approx 10^{-7}$
gravity	graviton, g	all massive particles	$\approx 10^{-39}$

Table 2.1.: The fundamental forces of the standard model. The strong, electromagnetic and weak force are described by the standard model. The mediator of gravity, the graviton, is postulated but not yet discovered. Values taken from [Per00].

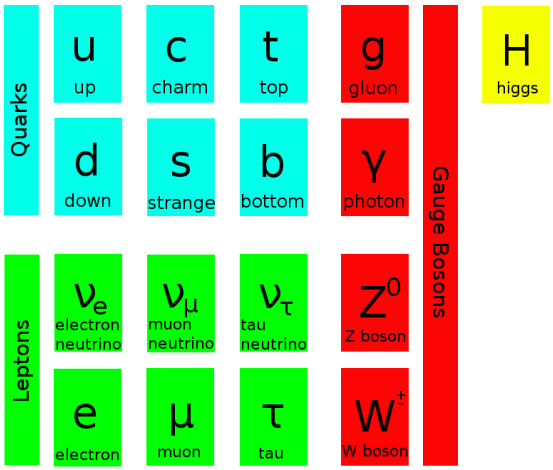

Figure 2.1.: The standard model of particle physics.

a non-negligible effect, but the necessary energies are not reached at current particle accelerators. Gravity is important for macroscopic objects.
In the SM all forces are mediated by gauge bosons which have a spin of 1. The mediators couple to different charges. Only particles which carry a charge are affected by the corresponding fundamental force. In the strong interaction the mediators are 8 different gluons (G) which couple with the color charge. The gluons carry a color charge themselves which allows them to couple to themselves additionally to the coupling to quarks.
In the electromagnetic interaction the gauge boson is the photon (γ). It is massless and couples to charged particles. The weak interaction is mediated by the charged weak current $W^{\pm}$ and the charged neutral current Z^0. These gauge bosons are massive particles with a mass of $M_W = 80.385 \pm 0.015\,\mathrm{GeV}/c^2$ and $M_Z = 91.1876 \pm 0.0021\,\mathrm{GeV}/c^2$. They couple to all weakly charged particles [Par14].
The gauge bosons and the affected particles of the interactions are shown in the overview of all particles in the SM in Figure 2.1. The quarks and leptons exist both in six flavors organized in three generations. They all have a spin of $\frac{1}{2}$ and belong to the group of fermions. The first generation of the particles are the most stable ones.

The different quark flavors are up (u), down (d), strange (s), charm (c), bottom (b) and top (t). This order lists the quarks with increasing mass. They can only decay via the weak interaction.
The heavier leptons muon (μ) and tau (τ) decay to electrons (e) and neutrinos (ν_e, ν_μ, ν_τ). In case of the tau, a decay into a muon, an anti muon neutrino and a tau neutrino is possible as well. This combination of two leptons and one anti-lepton (for example: $\mu \rightarrow e + \nu_\mu + \bar{\nu_e}$) is required because the lepton number is preserved in the decay. The electron is stable. The neutrinos have no charge and interact only via the weak interaction. The mass of the neutrinos is very small and at the time of writing this thesis not determined on an absolute scale. The square mass difference between the different flavors has been measured and proves that not all neutrinos can have a mass of zero [Par14].
The mass of the particles in the SM is generated by the particles coupling to the Higgs field. This so-called Higgs mechanism requires the existence of another particle, the Higgs particle. It was first predicted in 1964 [EB64, Hig64, GHK64]. In 2012 it was discovered by ATLAS and CMS [ATL12, CMS12c].
Not all particles of the SM can be directly observed. One example are quarks which are always bound in hadrons. Hadrons are particles which are affected by the strong interaction. Each quark carries one of the color charges red (r), green (g) or blue (b). The antiquarks carry the correspondent anti-colors anti-red, anti-green or anti-blue ($\bar{r}$, $\bar{g}$, $\bar{b}$). Because of color confinement only particles can be formed which have a neutral net color charge. This can be achieved with baryons, which consist out of three constituent quarks (rgb) or antiquarks ($\bar{r}\bar{g}\bar{b}$). An alternative are mesons which consist out of one quark and one antiquark. In 2015 measurements from LHCb have shown that there might be particles consisting out of five quarks [LHC15].
The only stable hadronic particle which is known at the time of writing this thesis is the proton. The neutron is only stable if it is bound in a nucleus. Both particles are baryons. The proton consists out of two up and one down quark, the neutron out of two down and one up quark.
The mass of particles which are compound out of particles from the SM is mainly created out of the binding energy of the constituents and not from the Higgs mechanism. Because of the gluon self coupling the strong interaction has a special behavior dependent on the 4-momentum transfer Q between two interacting particles. The coupling constant α_s is dependent on Q. Large momentum transfers mean that the distance between the particles is small. Low momentum transfers correspond to large distances between the involved particles. For very large momentum transfers (small distances) α_s asymptotically falls to zero. This means the quarks can move practically freely. This is called asymptotic freedom. As soon as the particles move further away from each other the coupling constant increases and the particles hold together. The behavior of α_s as a function of Q can be predicted with Quantum-Chromo-Dynamics (QCD) calculations. The result of these calculations together with a summary of measurements is shown in Figure 2.2.

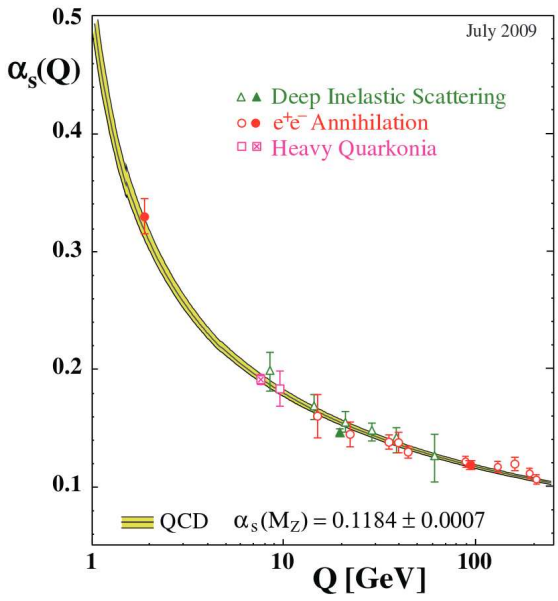

Figure 2.2.: Summary of the measurements of α_s dependent on the 4-momentum transfer Q. The curve is from QCD predictions. Figure taken from [Bet09].

2.2. Quark-Gluon Plasma

The strong interaction binds the color charged quarks together into color-neutral hadrons. This effect is called color confinement (see Section 2.1). The potential energy of the strong interaction between two quarks rises with the distance between them. If they are forced away from each other the potential energy rises until this energy is sufficient to create a new quark-antiquark pair.
For very high temperatures and/or high baryon densities a phase transition exists from a matter state with bound quarks and gluons into a new state in which the quarks and gluons do not belong to a certain baryon or meson anymore. This new state of matter is called the Quark-Gluon Plasma (QGP). In the QGP particles with a color charge can move independent of each other. The particles do still interact via the strong interaction but they are not bound in hadrons.
The order of the phase transition between this kind of matter and hadronic matter has not been measured. In Figure 2.3 a sketch of the QCD phase diagram is shown which is based on the color confinement and in some parts on lattice QCD calculations. Normal nuclear matter exists at low temperatures and at a baryo-chemical potential $\mu_{b,0}$. This state is inside the hadronic phase. The hadronic phase can be divided into multiple different states of hadronic matter. At low energies protons and neutrons can exist and bind to nuclei. For high energies close to the phase transition to the QGP the hadronic matter consists out of a hadron gas. This phase transition is supposed to be a cross-over for low μ_b and a first order phase transition for high μ_b. In between there is a critical point. The existence of the critical point has not been experimentally proven.

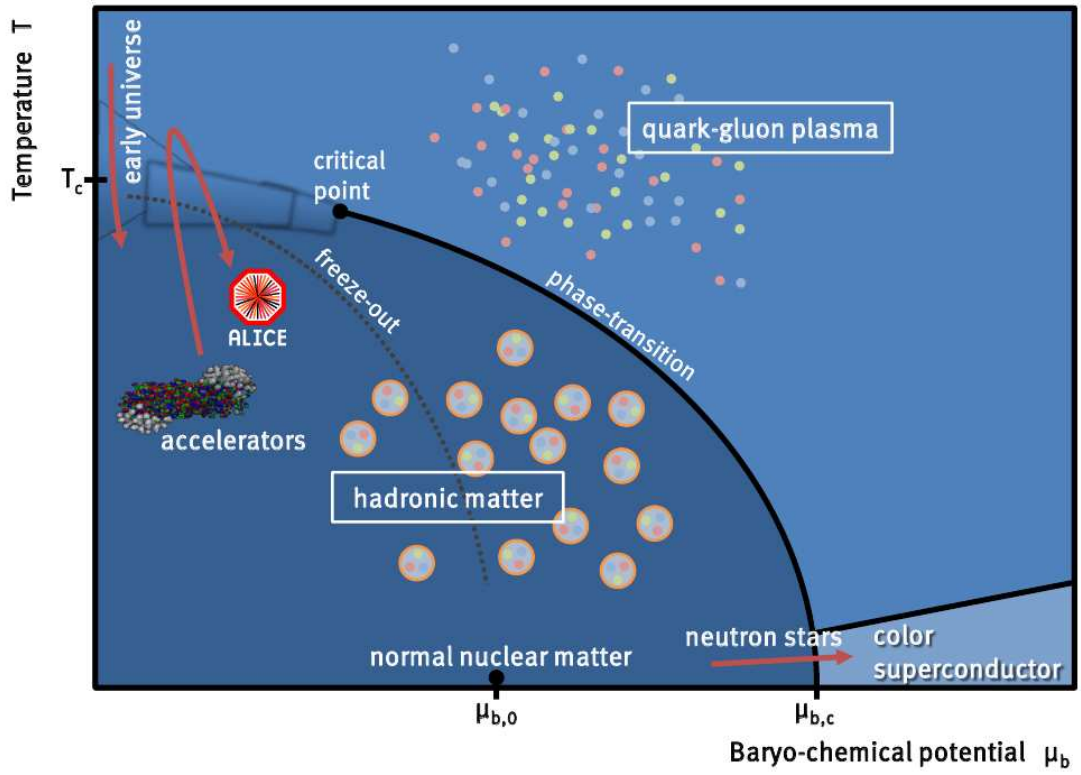

Figure 2.3.: Sketch of the QCD phase diagram. The diagram shows the phase transition between hadronic matter and the QGP. The phase transitions are shown as a function of the baryo-chemical potential μ_b and the temperature T. At high μ_b it is supposed to be a first order phase transition while at low μ_b a cross-over phase transition. In between there is a critical point. The evolution of μ_b and T with time in the LHC collisions and in the early universe are illustrated with red lines. The Figure is taken from [Bat12].

At $\mu_b \approx 0$ different lattice QCD calculations exist which predict the phase transition between the hadronic phase and the QGP at a temperature $T_C \approx 155\,\text{MeV}$ [Bor10, Baz12, Bha14][1].
At this temperature the QGP in the early universe changed into the hadron gas phase. The QGP is supposed to have existed in the early universe up to $100\,\mu\text{s}$ after the Big Bang [YHM05]. The baryo-chemical potential was small compared to normal nuclear matter. The path trough the phase diagram is shown in Figure 2.3. Additionally the path for the medium which is created in heavy-ion collisions (at mid-rapidity) is shown. Both curves illustrate the qualitative trend and not a quantitative statement. At low temperatures and high baryon densities another state of matter is predicted, called the color superconductor. In this state of matter color Cooper pairs are supposed

[1] The more recent calculations determined $T_C = 154 \pm 9\,\text{MeV}$ [Baz12] and $T_C = 155 \pm 8\,\text{MeV}$ [Bha14].

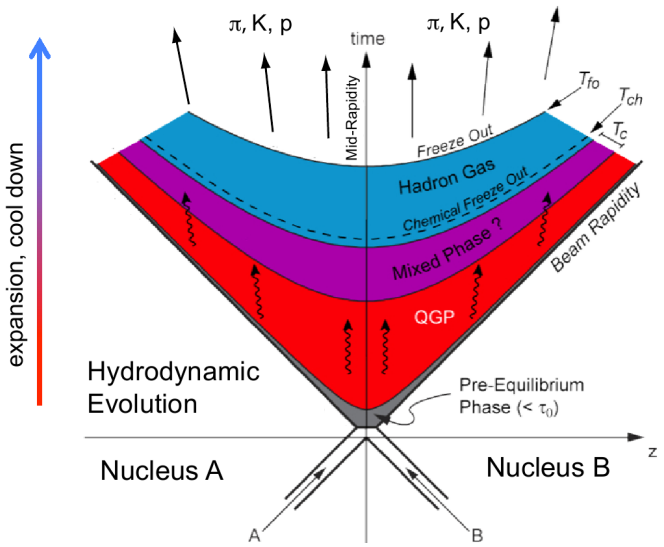

Figure 2.4.: Evolution of the QGP in a particle collision. The kind of matter is presented at a given position in direction of the beam pipe (z) and a certain time in the evolution of the fireball. Figure taken from [AK11].

to be formed out of quarks and gluons. This would lead to superconducting effects for the color charge. These conditions may exists in the core of neutron stars [BW09].
In Figure 2.4 the evolution of the QGP produced in ultra-relativistic heavy-ion collisions is shown in a light-cone diagram. At the beginning the Pb ions fly to the collision point. In the collision the so-called fireball is created which evolves through several evolution steps. The first stage is a pre-equilibrium phase which is not in thermal equilibrium. It expands quickly in all directions. In the figure this is indicated by the bigger covered area in z. After the thermal equilibrium is established the medium is in the QGP phase. In the expansion process it cools further down. At some point the QGP reaches a low enough temperature that quarks can bind again to other quarks. During this process the matter is in a mixed phase containing free and bound quarks. The medium continues to cool down and at some point no free quarks and gluons are left over and the medium goes from the mixed phase into a hadron gas state. Shortly after this the chemical freeze-out takes place which means that the particles cannot interact inelastically anymore. At this time the kind of the particles is fixed.
The expansion and cool down process continues in the hadron gas. In this phase the particles collide only elastically with each other so that the kinetic energy can change but not the kind of the particles. Of course instable particles can decay which allows some changes in the particle kind. After the kinetic freeze-out the particles continue to fly to the detector without interacting with each other [AK11].

2.3. Jet Quenching

High momentum quarks and gluons (partons) are created by hard scatterings in the early stage of the QGP. Collisional and radiative energy loss mechanisms cause such a parton to lose energy while traversing the QGP. This can be compared with the energy loss of ionizing radiation in baryonic matter. Unlike the Bethe-Bloch energy loss for ionizing radiation, the energy loss in the QGP is not fully described, yet.
A traversing parton interacts via elastic parton-parton scatterings with the partons of the QGP. In these interactions the parton transfers some energy to other already existing quarks or gluons in the QGP. Alternatively the energy loss can be due to radiation effects like gluon bremsstrahlung. In this parton interaction with the medium new gluons are created. For quarks the gluon radiation is suppressed at angles smaller than the ratio of the quark mass to its energy. This is the so-called dead-cone effect [DK01]. Because of the strong dependence on the quark mass it is mostly observed for heavy quarks.
The collisional and radiative energy loss has been compared for heavy quarks in Ref. [AGG13] with multiple models. The radiative energy loss has been found to dominate the energy loss for particle energies of a few GeV or higher. The two energy loss mechanisms depend differently on the temperature of the medium and the mass of the quark. At larger temperatures and lower quark masses the energy loss from radiative sources dominates already at smaller particle energies.
The energy loss cannot directly be measured because the parton fragments into many particles. First each parton creates a shower of quarks and gluons which hadronize afterwards. In the detector the resulting hadrons are measured at small angular differences to each other. Such an accumulation of hadrons in the detector is called a jet. The jet momentum represents the momentum of the parton which fragmented into this jet. In the measurement jets are identified with dedicated jet finder algorithms. They combine single particles into jets [CSS12]. The transverse momentum of potential jets is compared with the average momentum of the underlying event. If the jet momentum is significantly higher than the expected background, the jet is identified.
One possibility to identify the energy loss in the QGP is to measure two jets back-to-back and to analyze the energy difference. In case of an energy loss in such a di-jet system, the jets are expected to have different energies. The effect of lost energy in a jet due to the QGP is called 'jet quenching'. This is reported for high energy di-jets in Ref. [CMS11].
Within the CMS collaboration a measurement has been performed to measure the energy distribution in events with two high energetic jets. The di-jets have to be back-to-back in φ. They are required to have a transverse momentum of $p_{\mathrm{T},1} > 120\,\mathrm{GeV}/c$ for one jet and $p_{\mathrm{T},2} > 50\,\mathrm{GeV}/c$ for the other jet. The back-to-back requirement in azimuth was put on the restriction $|\Delta\phi - \pi| < \pi/6$. At these high energies it is clear that the jets have been produced in the same hard collision of two partons. So no combinatoric background due to non-correlated jets is considered. Due to momentum conservation both jets are expected to have the same transverse momentum. Small imbalances can be explained by higher order processes, initial state radiations or lim-

ited cone-sizes. Larger differences $p_{\mathrm{T},1} - p_{\mathrm{T},2}$ could be explained by the presence of the QGP. In this case the higher energetic jet fragmented directly into the vacuum and the other one traversed the QGP. But it is possible as well that the energy difference is created by a fluctuation of the underlying event.
For the found jets the following jet asymmetry is defined with respect to the sum of the transverse momenta of both jets [CMS11, CMS12a].

$$A_J = \frac{p_{\mathrm{T},1} - p_{\mathrm{T},2}}{p_{\mathrm{T},1} + p_{\mathrm{T},2}} \tag{2.1}$$

The asymmetry variable A_J describes the relative energy difference of the two jets. The relative energy difference for all jet pairs in an A_J bin is the same, but both jets in a single jet pair may have lost some energy first. In the following A_J is used to categorize the events into different classes of energy losses.
More information about the transverse momentum balance in the di-jet events can be obtained by using the projection of the jet transverse momentum on the di-jet axis in the azimuthal plane φ_{Dijet}. The direction of each jet is determined with a p_{T} weighted sum of the single particle directions. Afterwards the di-jet axis is midway between the axis of the leading jet and the opposite direction of the subleading jet. Because the axis of these two jets are required to be approximately back-to-back the di-jet axis is laying closely to the axis from the leading jet. All particles in an event are included in the calculation of the overall transverse momentum balance.

$$\not{p}_T^{||} = \sum_i -p_{\mathrm{T}}^i \cos\left(\varphi_i - \varphi_{Dijet}\right) \tag{2.2}$$

The observable $\not{p}_T^{||}$ is negative if more transverse momentum from the event is oriented in direction of the leading jet than in the direction of the subleading jet. The results of this calculation are averaged over all events for each A_J bin to get the average transverse momentum balance $\langle \not{p}_T^{||} \rangle$.
In Figure 2.5 $\langle \not{p}_T^{||} \rangle$ is shown for pp and Pb–Pb collisions. In case of Pb–Pb collisions this is divided into four centrality classes. For events with an asymmetry $A_J > 0.11$ the side of the leading jet has more energy from particles with $p_{\mathrm{T}} > 8\,\mathrm{GeV}$, the side of the subleading jet has more energy from particles with $p_{\mathrm{T}} < 8\,\mathrm{GeV}/c$. The energy excess in the different p_{T} ranges balance each other within the uncertainties. This is shown by the sum over all particles which is plotted with the big symbols. The small negative trend with increasing A_J is a consequence of the p_{T} threshold and the CMS tracker acceptance. If particles with less than $0.5\,\mathrm{GeV}/c$ could be included as well this might balance out better.
In the lower plots of Figure 2.5 the difference between the Pb–Pb and pp yield is shown. The overall sum of $\langle \not{p}_T^{||} \rangle$ for all particles with $p_{\mathrm{T}} > 0.5$ is close to zero. So no energy is lost in Pb–Pb collisions. But these plots do still contain an energy imbalance. For peripheral collisions the contributions to the imbalance is mainly from higher energetic particles. Towards more central Pb–Pb events the imbalance of the jet energy increases and lower energetic particles have a significantly higher contribution. In the presence of the QGP more hard scattering processes create more particles

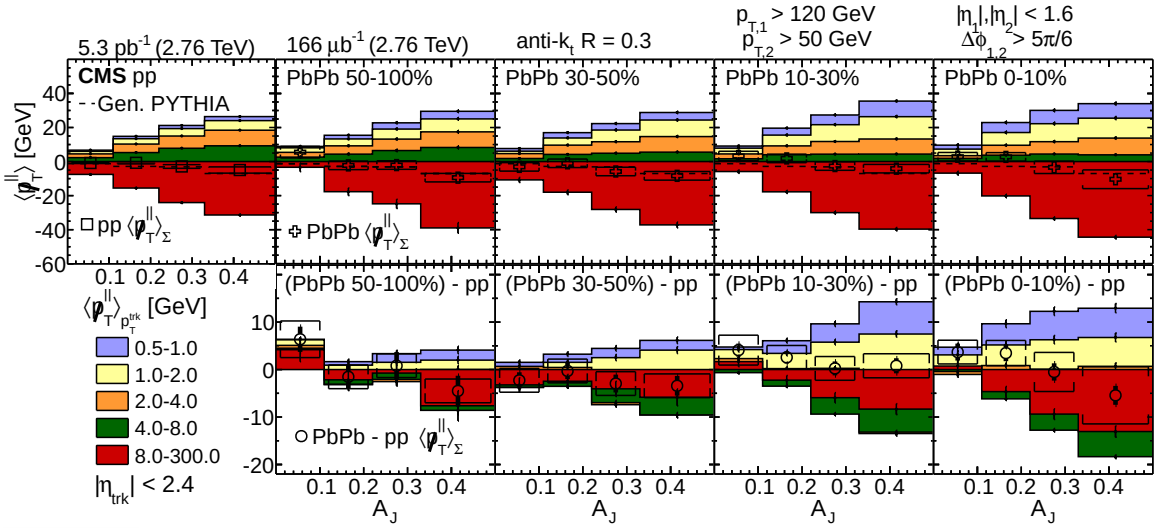

Figure 2.5.: In the top row the average transverse momentum balance $\langle \not{p}_T^{\parallel} \rangle$ is shown for pp (left) and four different Pb–Pb centralities. The jets are identified with the $anti - k_T$ algorithm and a jet radius of $R = 0.3$. The average transverse momentum balance is calculated from the whole event (shown with the black symbols). Further the particles of the event are split into five momentum ranges (shown with the different colors). The subleading jets contain more particles with $p_{\mathrm{T}} < 8\,\mathrm{GeV}/c$ ($\langle \not{p}_T^{\parallel} \rangle$ is positive) and the leading jets contain more particles with $p_{\mathrm{T}} > 8\,\mathrm{GeV}/c$ ($\langle \not{p}_T^{\parallel} \rangle$ is negative). In the lower row the difference of $\langle \not{p}_T^{\parallel} \rangle$ from Pb–Pb events and pp events is shown. Error bars and brackets represent statistical and systematic errors respectively. Figure taken from [CMS16].

with low p_{T} in Pb–Pb events compared to pp events. This is a jet quenching effect in the QGP [CMS16].
The distribution of the energy relative to the di-jet axis was analyzed in a second analysis which is shown in Figure 2.6. In the plots on the left side particles within a radius of $R < 0.8$ around the leading and subleading jet axis were considered. This is called in-cone. For the plots on the right side all the other particles in the event (with $R > 0.8$ around the jet axes) were considered which is called out-of-cone. In the top row simulations with PYTHIA and HYDJET are shown while the lower row shows CMS data analysis. In all plots the momentum loss is shown for five different p_{T} ranges. The sum of all particles is shown with the solid points.
In the in-cone analysis one can see that the simulations can describe well the momentum imbalance of all particles as well as the imbalance of the sub p_{T} ranges. The sum of all particles for $A_J > 0.33$ is $\langle \not{p}_T^{\parallel} \rangle \approx -20\,\mathrm{GeV}/c$. This is canceled by an out-of-cone imbalance of $\langle \not{p}_T^{\parallel} \rangle \approx 20\,\mathrm{GeV}$. For the other asymmetries A_J these values cancel as well. However, the positive asymmetry in the out-of-cone simulations is mostly created by particles with $p_{\mathrm{T}} > 4\,\mathrm{GeV}/c$. Contrary to that the imbalance for the out-of-cone data

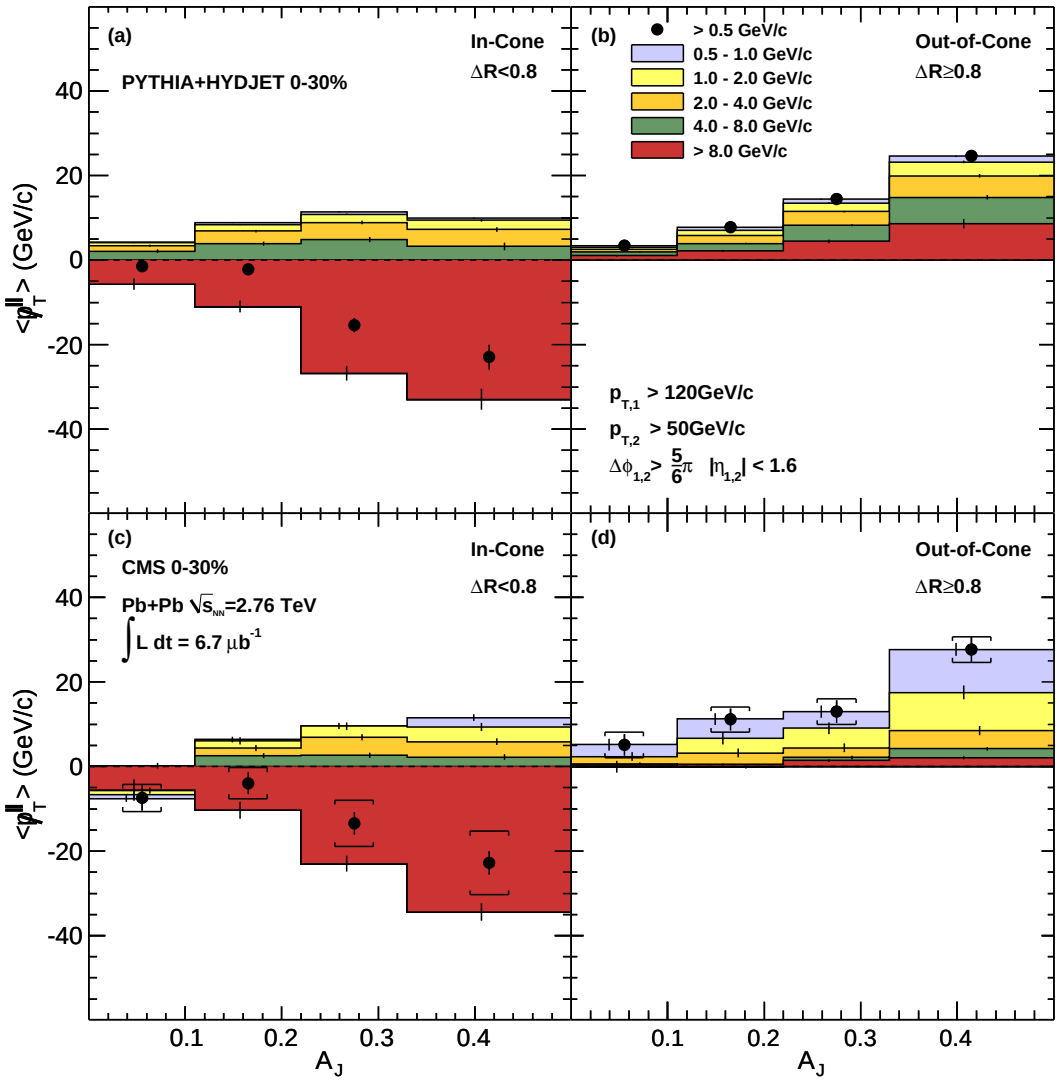

Figure 2.6.: CMS analysis of the average missing transverse momentum $\langle \not{p}_T^{||} \rangle$ of the subleading jet compared with the leading jet. The missing momentum is shown dependent on the di-jet asymmetry A_J. The results are shown for the 30% most central events. On the left side the results are shown for particles inside a jet radius $R < 0.8$, on the right side for particles outside this radius. In the top row the results are obtained from PYTHIA and HYDJET simulations, in the lower row from data. The missing momentum is shown for several color coded p_{T} ranges. The sum of the missing energy is shown with solid points. The statistical and systematic uncertainties are shown with vertical bars and brackets, respectively. A further description of the plots is given in the text. Figure taken from [CMS11].

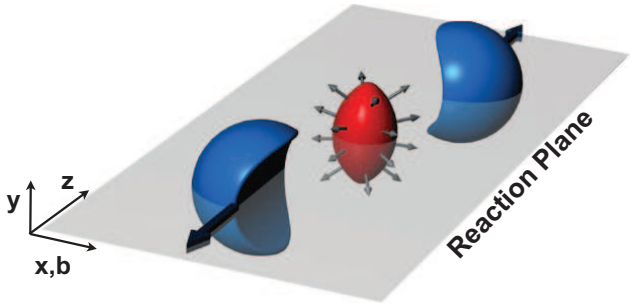

Figure 2.7.: Non-central collision of two ions (blue). The almond shaped interaction area (red) is shown in the middle. The left over parts of the ions continue to fly in the original flight direction. The reaction plane is indicated as the xz plane. The momentum anisotropy (flow) of the particles in the interaction area is indicated by the arrows. Figure taken from [Sne11].

analysis is build up out of particles with $p_T < 4\,\mathrm{GeV}/c$.
Like the analysis in Figure 2.5 the data analysis in Figure 2.6 clearly shows that the higher energy of the leading jet compared to the subleading jet is created by particles with $p_T > 8\,\mathrm{GeV}/c$ (in-cone). This higher energy in the leading jet can be balanced by particles with $p_T < 8\,\mathrm{GeV}/c$ (in-cone and out-of-cone) from the subleading jet. Many of the low energetic particles which create this balance are found at large angles with respect to the jet axis on the side of the subleading jet. Due to this large angles the particles are not included in the jet reconstruction of the jet finder [CMS14].

2.4. Flow

In heavy-ion collisions a collective effect is observed which is called particle flow. It is a sign for multiple interactions between the constituents of the medium which was created in the collision. The interactions of the constituents thermalize the medium. Therefore, a strong flow signal is a good probe for the thermalization. The tools for the theoretical description of the flow are hydrodynamics or microscopic transport models [Sne11].
The anisotropic flow is created by the non-spherical distribution of the colliding particles. In Figure 2.7 a non-central collision of two ions is shown. From the incoming two ions only some of the nucleons actually collide with some nucleons of the other ion. The other nucleons continue to fly straight. The colliding nucleons create an almond shaped interaction volume. In the figure the x-z direction is the reaction plane of this collision. The reaction plane is defined by the direction of the impact parameter (x) and the beam direction (z). In the azimuthal direction the reaction plane is described by the angle ψ relative to the coordinate system. The interaction volume of the collision is larger transversal to the reaction plane than in direction of it.
The QGP is created in the interaction volume. Due to the stronger pressure gradient the medium expands quicker in the direction of the reaction plane than transversal to

it. At the same time the momentum distribution changes in the opposite direction. It starts symmetrical in azimuth (=spherical) and changes into the preferred direction of the reaction plane. The azimuthal distribution of the particles with respect to the reaction plane can be described with Fourier coefficients.

$$v_n = \langle \cos[n(\varphi - \psi_n)] \rangle \tag{2.3}$$

φ represents the azimuthal angle of the particle and ψ_n the angle of the reaction plane of the n-th harmonic order. The first order flow v_1 is the directed flow. It has been observed [ALI13a] but it is small. The almond shape of two overlapping perfect spheres creates the elliptic flow v_2. This is the dominant flow contribution in heavy-ion collisions [ALI10]. Due to fluctuations of the initial energy density distribution in the transverse plane higher order flow coefficients v_n are not zero [ALI11a].
For the analysis of the associated particle yield in the 2+1 and 1+1 particle correlations in this thesis, the flow is part of the background distributions. The background subtraction method is explained in Section 5.5.

2.5. HIJING

For simulations of Pb–Pb collisions, Monte Carlo generators are used. In these generators the collision is simulated including different physics effects. The physical processes in particle collisions can be investigated by comparing measured particles from real collisions with particles from MC generators. If the results agree with each other, a description of the collision may be found. Disagreements between the Monte Carlo particles and the measured particles show that the simulation is incomplete.
In this thesis one generator called HIJING (Heavy Ion Jet INteraction Generator) has been used [WG91, GW94]. It generates heavy-ion events by overlapping many parton-parton collisions which can be described by perturbative QCD (pQCD). This overlapping procedure describes the heavy-ion collision without the QGP medium properties.
HIJING assumes that events can be generated from independent minijets. It uses pQCD calculations to determine the number of hard collisions for a nucleon-nucleon collision. For each collision PYTHIA subroutines [BS87] are used to generate the partons and their momenta.
Besides hard interactions, the interacting particles can have soft interactions. These are modeled with a phenomenological model. It contains gluon production and soft radiation. The radiated gluons are restricted to low momentum because at high energies they are contained in the minijets which are calculated with pQCD. Finally the produced particles are hadronized with subroutines from JETSET [SB87].
With this generation procedure for parton-parton events, HIJING creates heavy-ion events. It is assumed that nucleon-nucleon collisions are build up out of a superposition of binary parton-parton collisions. This is called the binary approximation. Each parton can only scatter once [GW94].
Dependent on the impact parameter of the collision the amount of superpositioned

binary parton-parton collision varies. It is possible to restrict the impact parameter of the collision. A smaller impact parameter corresponds to an enhanced number of binary collisions which leads to more minijets in the event.
In bound nucleons the effective number of quarks and antiquarks carrying a small fraction of the particle momentum (= low Bjorken x) is reduced compared to free nucleons. This effect has been observed in deep inelastic muon scattering [Eur88] and it is called the nuclear shadowing effect. Although it was not observed for gluons it is assumed that the effect is identical for them. In HIJING the effect is parametrized as a function of the impact parameter b.
Due to the binary approximation the simulated events cannot contain any effects from the QGP. Each new created particle is not affected by the other particles. HIJING has an option to simulate the energy loss of particles which would interact with the QGP. If hard scattered partons traverse the dense matter, some energy from the partons is transfered to other particles in the traversed matter [GW94]. This energy loss option of HIJING is not used in this thesis because the simulations are used to investigate the 2+1 correlations method in the absense of QGP effects.
In this thesis the simulated centrality is adjusted to the measured centrality in the data. The HIJING events are created at two centralities. One centrality is 30–50%. For more central events at 0–7.5% centrality small differences in the yield of a single jet compared to the 30–50% most central events have been measured which are partly created by the nuclear shadowing effect. To study if the analysis has a multiplicity dependence, a super-position of three events with the centrality 30–50% are used for the simulation of central events. In this configuration HIJING uses the same single jet yield at both centralities.

2.6. The Nuclear Suppression Factor R_{AA}

The medium effects of the QGP can be analyzed by comparing the created particles in Pb–Pb collisions and pp collisions. To quantify these medium effects the nuclear modification factor R_{AA} is used. It is defined as the ratio of the yield in Pb–Pb and pp collisions scaled by the average number of binary collisions $\langle N_{coll}\rangle$.

$$R_{\mathrm{AA}} = \frac{(1/N_{evt}^{AA})d^2N_{ch}^{AA}/d\eta dp_{\mathrm{T}}}{\langle N_{coll}\rangle(1/N_{evt}^{pp})d^2N_{ch}^{pp}/d\eta dp_{\mathrm{T}}} \tag{2.4}$$

The average number of binary collisions $\langle N_{coll}\rangle$ is calculated following the Glauber model [GM70] by colliding nucleons which are bound in Pb ions. The ions are displaced by the impact parameter b. Each nucleon of the first ion is moved on a straight track through the second ion. With the inelastic nucleon-nucleon cross section the amount of collisions with nucleons in the second ion are counted by neglecting any change of the flight direction of the involved nucleons. This process is repeated for all nucleons of the first ion. Dependent on the impact parameter a different amount of nucleons collides with nucleons from the other ion. The sum of all collisions is N_{coll}. $\langle N_{coll}\rangle$ is calculated by repeating this simulation several times and taking the

average [Mil07].
The charged particle yields N_{ch}^{AA} and N_{ch}^{pp} are measured with events from pp and Pb–Pb collisions. They are normalized with the correspondent number of events N_{evt}^{AA} and N_{evt}^{pp}.
The R_{AA} indicates how many less particles are measured in the heavy-ion collisions than would be expected from pp collisions. This estimation works only for particles which have a momentum of a few GeV/c because at lower momenta the created particles in heavy-ion collisions do not scale with N_{coll} anymore. Thus R_{AA} has additional effects at low momenta.
If Pb–Pb collisions are an incoherent superposition of pp collisions, the R_{AA} is expected to be 1. Deviations from 1 indicate medium effects. For particles which lose energy in the QGP this means that the p_{T} dependent R_{AA} falls below 1 with increasing p_{T}. This can be explained by looking at one single p_{T} bin in the spectrum. This bin is called p_{T0}. In the Pb–Pb collisions some particles which are created with p_{T0} lose some of their energy and they are measured with a lower p_{T}. The same happens for particles which have a higher energy than p_{T0}. They lose some energy in the QGP and then they are measured with p_{T0}. Because the p_{T} spectrum is a strongly falling spectrum more particles are lost from p_{T0} than they are added from higher p_{T}. Compared to the measurements from pp collisions where no particle loses energy there are less particles with p_{T0} in Pb–Pb collisions than expected.
With the increasing collision energy $\sqrt{s_{NN}}$ at the LHC compared to other accelerators the QGP has been observed to be hotter, larger and longer-lived [ALI11b]. Because of this, larger medium effects are expected in the R_{AA}. But this effect is partly countered from the p_{T} spectrum which gets flatter at higher collision energies. Other effects like gluon shadowing and saturation effects may influence the R_{AA} as well [ALI11d].
To test this method, probes can be used which do not interact via the strong interaction. One possible probe are photons which interact only electromagnetically. Because of this no effect from the QGP is expected and the R_{AA} should be unity. CMS has measured this and within the uncertainties the result is $R_{\mathrm{AA}} = 1$ [CMS12b].
In more central events the QGP is expected to be larger and longer-lived. In these events the R_{AA} signal from the QGP is expected to be stronger as well. So different centralities are analyzed and compared with each other. For peripheral collisions the nuclear modification factor is expected to be close to unity.
In Figure 2.8 the R_{AA} for 9 different centrality bins is shown. For all centrality bins the R_{AA} is below 1 which shows that there is a medium effect in Pb–Pb collisions and not just a super position of proton-proton collisions. For peripheral events it can be seen that the R_{AA} is close to unity and constant. It does not reach unity because the events contain more than one hard collision. Additionally cold nuclear matter effects[2] can have an effect. At more central collisions a minimum is developed at $p_{\mathrm{T}} = 6-7\,\mathrm{GeV}/c$. For higher p_{T} there is a rise in the spectrum which becomes less steep with rising p_{T}. At lower momenta than the minimum no further conclusions can be drawn because

[2]Cold nuclear matter effects describe the difference between nucleon-nucleon collisions and pp collisions because the nucleons are bound in nuclei.

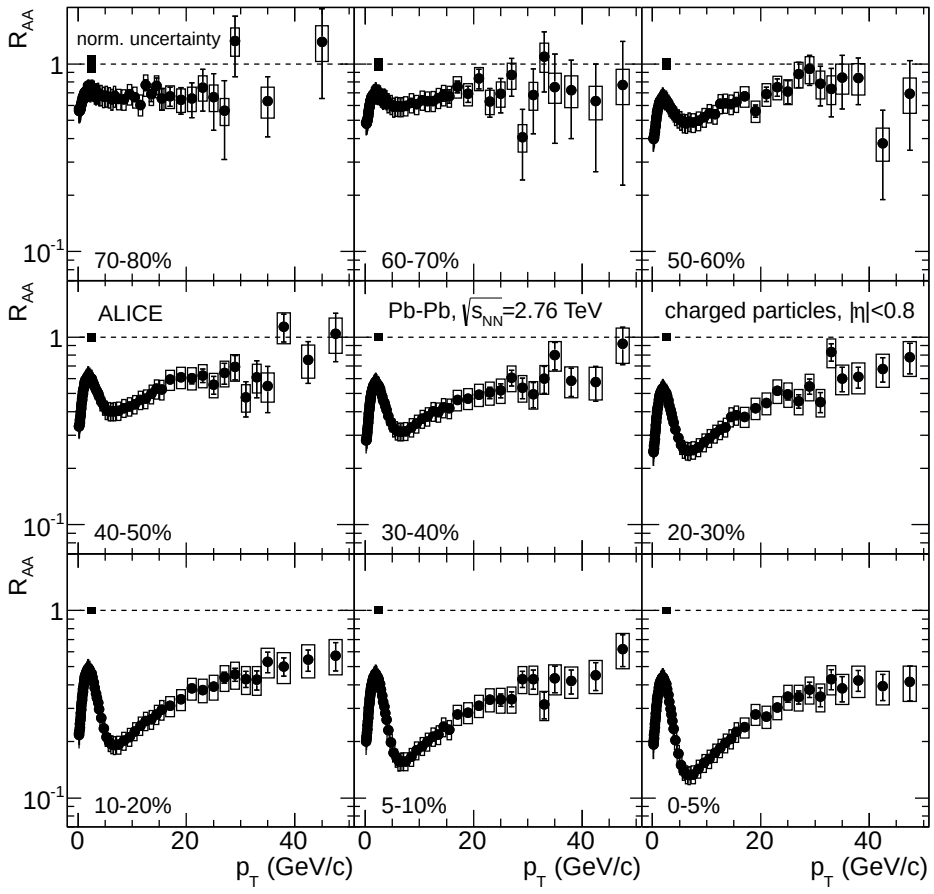

Figure 2.8.: The nuclear modification factor R_{AA} for 9 different centrality bins at $\sqrt{s_{NN}} = 2.76\,\mathrm{TeV}$. The error bars show the statistical uncertainties while the boxes show systematic uncertainties dependent on the p_{T}. The systematic uncertainty related to the normalization of the pp data and $\langle N_{coll} \rangle$ is shown as box at $R_{\mathrm{AA}} = 1$. Figure taken from [ALI13b].

the scaling with N_{coll} in the R_{AA} is not valid anymore.
The biggest suppression can be observed for the most central events (0–5%). The minimum is $R_{\mathrm{AA}} \approx 0.13$ and it reaches $R_{\mathrm{AA}} \approx 0.4$ for $p_{\mathrm{T}} > 30\,\mathrm{GeV}/c$ without any further significant rise [ALI13b].
The R_{AA} provides a strong signature of the QGP. In this analysis all particles in all collisions are considered. Other analysis techniques can be used to focus on probes which may have interacted with the QGP. One example are the jet measurements which have been introduced in Section 2.3. That analysis selects events with high energetic di-jets.

2.7. Two Particle Correlations in Pb–Pb and pp Events

At low energies the energy loss of jets cannot be measured with reconstructed jets because of the large fluctuations from the underlying event compared to the jet energy. For identified jets the average transverse momentum of the underlying event in the phase space of the jets is a background which has to be subtracted. At small jet transverse momenta this results into a large jet transverse momentum uncertainty. So the momentum difference between two jets has an even bigger uncertainty. Some jets are not measured because they vanish in a downward fluctuation of the background. Contrary to this, an upward fluctuation of the background can fake a jet. An alternative measurement is possible with particle correlations. In the following the two particle angular correlation measurement is briefly explained. A more detailed explanation of the methods with the mathematical equations describing the yield is given in Chapter 5.

Instead of using a jet finder to identify a jet, a single particle within a certain transverse momentum range is taken as proxy for the jet. Every particle which fulfills the transverse momentum requirement is called a trigger particle. The angular difference $\Delta\varphi$ and $\Delta\eta$ is calculated between the trigger and all other particles in the event and it is is filled into a histogram. This is done for each trigger and associated transverse momentum bin $p_{\mathrm{T,trig}}$ and $p_{\mathrm{T,assoc}}$ separately. In this thesis the two particle angular correlations are denoted as 1+1 correlations. This represents the trigger particle plus the associated particle.

An example for the resulting angular correlations in one trigger and associated transverse momentum bin is shown in Figure 2.9. A jet peak can be found at $\Delta\varphi = \Delta\eta = 0$. The away side jet is visible at $\Delta\varphi \approx \pi$ as a ridge. At low jet momenta $p_{\mathrm{T,jet}}$ compared to the collision energy $\sqrt{s_{NN}}$ the away side jet is not focused in $\Delta\eta$. In the center of mass system of the hard collision which created the two jets, the jets are correlated back-to-back in η. But in the lab system this interaction is boosted dependent on the net momentum of the interacting partons. For every collision the strength of the boost is different. As a consequence jets are not correlated in the $\Delta\eta$ measurement.

The measured yield contains multiple kind of background correlations. Some associated particles in the event are not correlated at all with the trigger particle. In the correlation plot these particles appear as flat background. Other associated particles can be correlated with the trigger due to flow (see Section 2.4). There are several methods how this content can be subtracted. In all methods the background is sampled at angular positions far away from the peak.

After the background subtraction, the jet yield is integrated. On the near side the integration is done within a small range of $\Delta\varphi$ and $\Delta\eta$. On the away side the jet ridge is integrated for all $\Delta\eta$. This measurement returns the integrated associated jet yield for a certain trigger particle. To learn if the jet yield is affected by the QGP it has to be compared to a baseline. So the same measurement has to be done in a system which does not contain effects from the QGP.

One possible baseline for the measurement can be obtained from pp collisions. The observable I_{AA} is defined as the ratio of the yield in Pb–Pb collisions over the yield

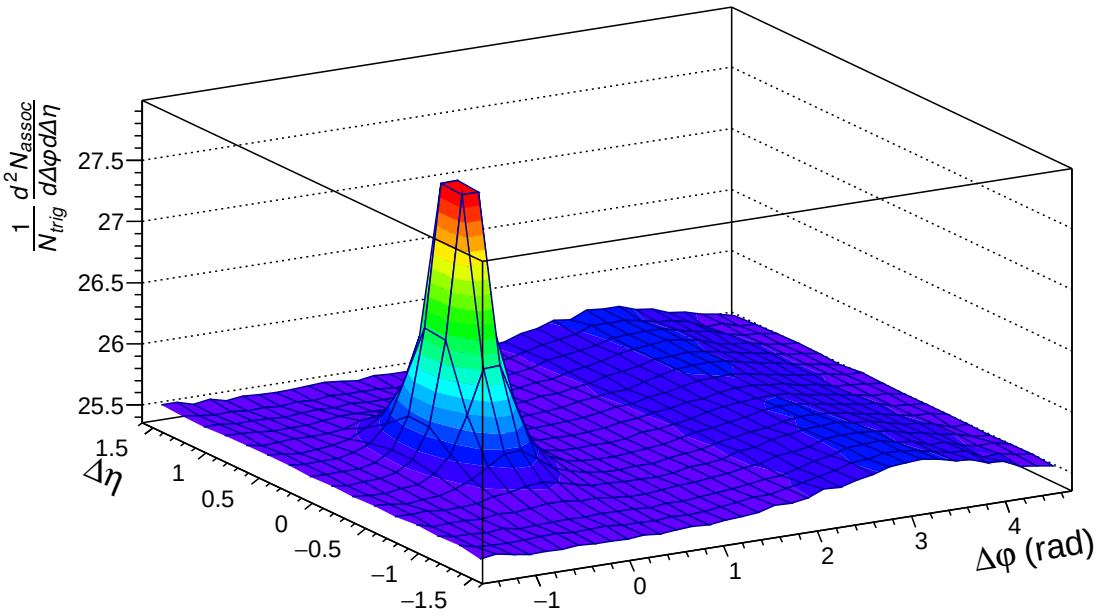

Figure 2.9.: Example for the 1+1 angular correlations. The near side jet peak can be observed at $\Delta\varphi = \Delta\eta = 0$ and the away side jet ridge at $\Delta\varphi \approx \pi$.

from pp collisions. Alternatively the yield from peripheral Pb–Pb collisions can be used which are expected to contain a much smaller QGP than the more central Pb–Pb collisions. The advantage of these peripheral collisions is that they were created by the same kind of colliding particles. The ratio of the yield from central and peripheral Pb–Pb collisions is called I_{CP} [ALI12].

$$I_{\mathrm{AA}} = \frac{\text{Pb–Pb(0–5\%)}}{\text{pp}} \tag{2.5}$$

$$I_{\mathrm{CP}} = \frac{\text{Pb–Pb(0–5\%)}}{\text{Pb–Pb(60-90\%)}} \tag{2.6}$$

The I_{AA} (I_{CP}) describes the relative amount of associated particles in (central) Pb–Pb events compared to pp (peripheral Pb–Pb) events.
In Figure 2.10 the I_{AA} measurement from ALICE is shown. On the near side the Pb–Pb yield is larger than the pp yield. Dependent on the used background method and the $p_{\mathrm{T,assoc}}$ bin, the enhancement over unity varies between 10% and 40%. It decreases with increasing $p_{\mathrm{T,assoc}}$. Only the last bin, which describes an associated momentum equal to the trigger momentum, shows an increasing trend. The I_{AA} measurement indicates that more low energetic jet particles are produced in central Pb–Pb collisions. The deviation from unity shows that the jets are affected by the medium effects in these collisions.
On the away side the I_{AA} shows a suppression of the yield in Pb–Pb events ($I_{\mathrm{AA}} \approx 0.6$).

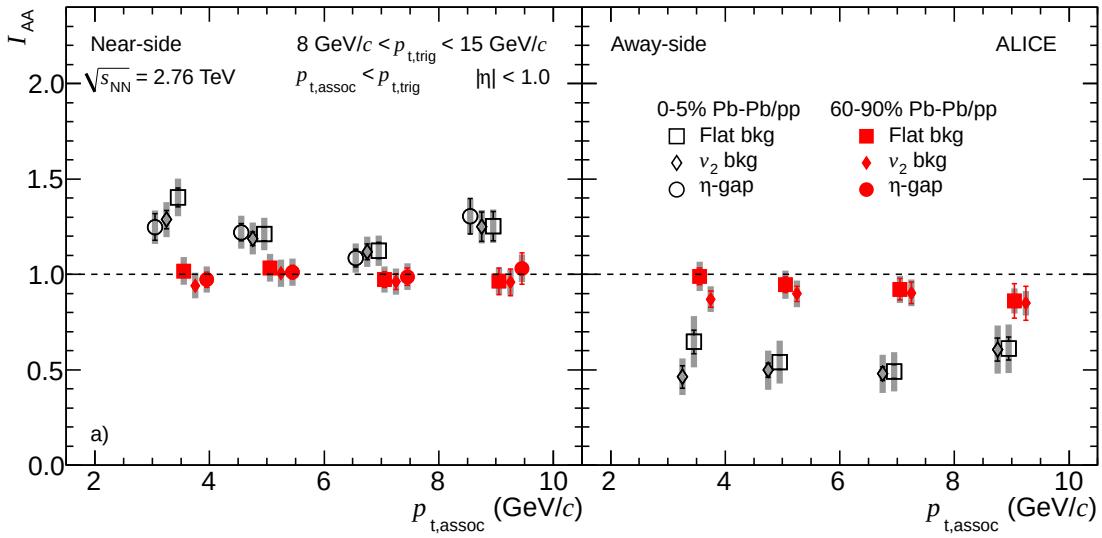

Figure 2.10.: The I_{AA} is measured with 3 different background subtraction techniques for $8 < p_{\mathrm{T,trig}} < 15\,\mathrm{GeV}/c$ and multiple $p_{\mathrm{T,assoc}}$ bins. On the left side the measurements from the near side ($\Delta\varphi \approx 0$) are presented and on the right side the measurements from the away side ($\Delta\varphi \approx \pi$). The full symbols (red) represent the I_{AA} obtained with measurements from peripheral Pb–Pb events and the open symbols measurements from central Pb–Pb events. Figure taken from [ALI12].

This suppression is constant over the full momentum range. It is evidence for energy loss in the QGP.
In the same plot the I_{AA} is presented for peripheral (60–90%) events instead of the 0–5% most central events. The near and away side measurements both agree within the uncertainties with unity. On the away side the I_{AA} is for all $p_{\mathrm{T,assoc}}$ slightly below unity which indicates the energy loss which has been observed in more central events. The convergence to unity for more peripheral events is expected because the medium effects are smaller in more peripheral Pb–Pb collisions.
The I_{CP} has been measured as well. It is very similar to the I_{AA} with the 0–5% most central Pb–Pb events [ALI12].

2.8. Two Plus One Particle Correlations at STAR

The STAR (Solenoidal Tracker At RHIC) experiment studied jet medium interactions in Au–Au and d–Au collisions at a collision energy of $\sqrt{s_{NN}} = 200\,\mathrm{GeV}$. The experiment is located at RHIC (Relativistic Heavy Ion Collider) at the Brookhaven National Laboratory (BNL) near New York in the USA.
STAR uses two plus one particle angular correlation for the analysis of di-jets in Au–Au and d–Au collisions. This method is explained in detail in Chapter 6. In this thesis

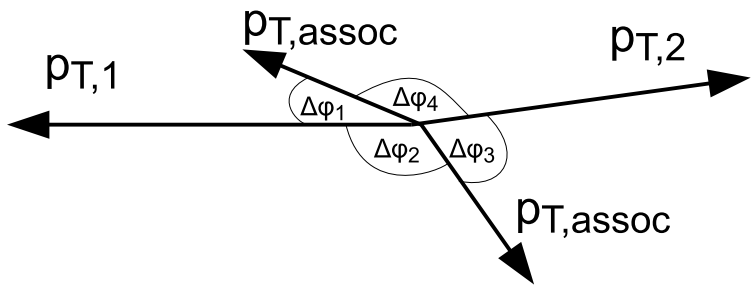

Figure 2.11.: Sketch of the 2+1 analysis in azimuthal direction. The trigger 1 particle with $p_{\mathrm{T1,trig}}$ is back-to-back with trigger 2 which has $p_{\mathrm{T2,trig}}$.

the two plus one angular particle correlations are denoted as 2+1 correlations. A brief description of the method is given in the following.
The 2+1 correlations method describes the associated particle yield of di-jets which were produced in heavy-ion collisions. Instead of taking one trigger particle as a proxy for a jet, two trigger particles are taken back-to-back. This trigger configuration is a proxy for a di-jet. The momentum ranges in which the two trigger particles are searched for can be separated, overlapping or identical. But the trigger momentum of trigger 2 has to be smaller than the momentum of trigger 1. The second trigger particle has to be within a cone of α around the back-to-back position of the first trigger $|\Delta\varphi| - \pi < \alpha$. In STAR $\alpha = 0.2$ is used. Afterwards the angular correlations of all other particles in the event are measured relative to both trigger particles separately. One plot for the correlation with each trigger particle is filled. The plot with the angular differences relative to trigger 1 is called the trigger 1 associated yield, and the plot with the angular differences relative to trigger 2 is called the trigger 2 associated yield.
This procedure is sketched in Figure 2.11. The length of the arrows indicate the momentum of the particles. A longer arrow corresponds to a larger momentum. In this example the particles T1 and T2 fulfill the trigger requirements. The angular differences $\Delta\varphi_1$ and $\Delta\varphi_2$ are measured relative to trigger 1. They are filled into the same histogram. Respectively $\Delta\varphi_3$ and $\Delta\varphi_4$ are filled into another one. These histograms describe the associated yield of trigger 1 and trigger 2. Qualitatively both look like the 1+1 correlations in Figure 2.9 with a near and an away side. In both histograms only the near side is analyzed. Instead of analyzing the away side of a trigger particle, the near side of the other trigger particle is analyzed.
In this measurement the jet yield on the near and away side can both be extracted from a peak. This improves the background correction at low $p_{\mathrm{T,assoc}}$ because these yields have a high flow contribution.
The trigger combinations that were found are not necessarily correlated with each other. It is possible that the trigger particles were created independently of each other. The associated particles of these trigger particles should not be included in the analysis. The background estimation from these uncorrelated trigger particles in the STAR analysis is similar to the scaled 1+1 event method which is described in Section

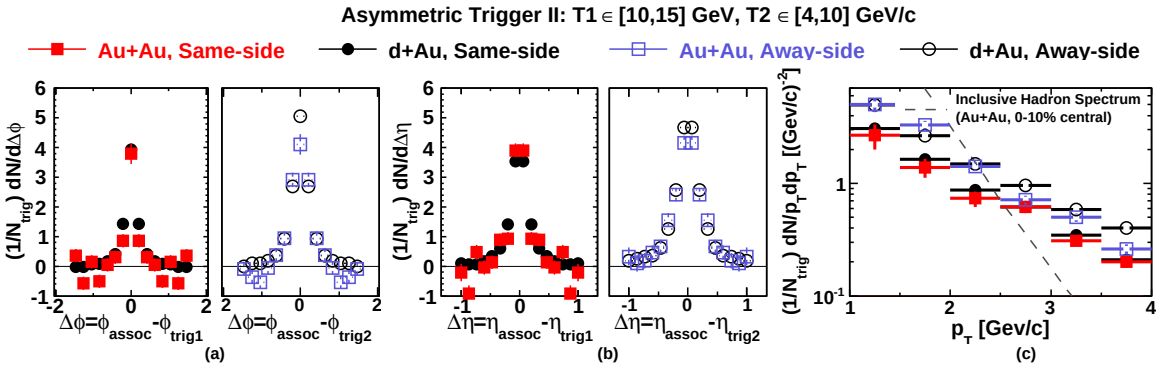

Figure 2.12.: Measurement of the 2+1 correlations for the trigger conditions $10 < p_{\mathrm{T1,trig}} < 15\,\mathrm{GeV}/c$, $4 < p_{\mathrm{T2,trig}} < 10\,\mathrm{GeV}/c$ and $1 < p_{\mathrm{T,assoc}} < 10\,\mathrm{GeV}/c$. The associated particle yield is measured for both trigger particles separately in the 0–20% most central Au–Au and in d–Au events. The projections of the 2D correlation functions are shown for $\Delta\varphi$ (a) and $\Delta\eta$ (b). In c) the transverse momentum around the trigger particles is integrated ($|\Delta\varphi| < 0.5$, $|\Delta\eta| < 0.5$). For comparison the inclusive hadron spectrum for central Au–Au events (0–10%) is shown. Figure taken from [STA13].

6.4.4. To calculate the 2+1 trigger 1 associated yield, first the 1+1 correlation of the 2+1 trigger 1 and the 2+1 associated particles is calculated. The resulting yield is scaled to the correct background level and then it is subtracted from the 2+1 yield. This is done in the 2+1 measurement of this thesis as well. STAR additionally subtracts a second 1+1 correlation measurement. In this 1+1 correlations the 2+1 trigger 2 is used as trigger particle and the 2+1 associated particles are used as associated particles. In the subtraction the away side of the 1+1 correlations is subtracted from the 2+1 near side. This subtraction removes part of the background ridge around $\Delta\varphi \approx 0$. For the 2+1 trigger 2 associated yield, the same subtraction is done with the away side of the trigger 1 associated particles. The remaining ridge contains flow effects. It is subtracted with a model curve which has been determined in independent STAR measurements. After this background subtraction the remaining di-jet yield is analyzed by integrating the bin content within $|\Delta\varphi| < 0.5$ and $|\Delta\eta| < 0.5$ [STA11, STA13].
In Figure 2.12 the results from STAR for one trigger configuration after the background subtraction are shown. The associated particle yields are plotted for the trigger 1 associated particles (near side) and the trigger 2 associated particles (away side) separately. The momentum range in which STAR measures the second trigger particle and the associated particles is very large. The momentum range of trigger 1 and trigger 2 does not overlap. This creates an asymmetry between the two trigger particles. The idea of the measurement is that the parton which fragmented into trigger 2 had a longer path length in the QGP than the parton which fragmented into trigger 1. Due to this longer path length, trigger 2 suffered a bigger energy loss which results in the smaller trigger 2 momentum compared to trigger 1. But it is possible that both jets were

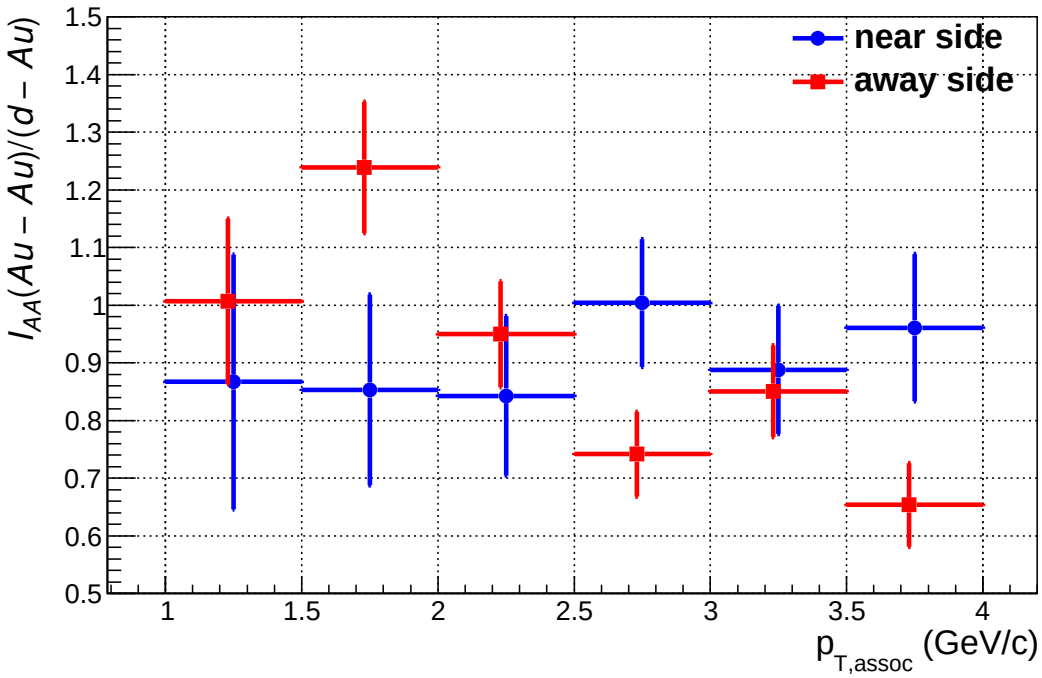

Figure 2.13.: Ratio between the Au–Au and d–Au yield from Figure 2.12. The trigger conditions are $10 < p_{\mathrm{T1,trig}} < 15\,\mathrm{GeV}/c$, $4 < p_{\mathrm{T2,trig}} < 10\,\mathrm{GeV}/c$. The shown uncertainties are purely statistical. A systematic uncertainty is not provided. The data is taken from [STA13].

affected by the same energy loss and the energy difference of the triggers was created randomly in the hadronization.
For both trigger particles the associated particle yields from Au–Au and d–Au collisions in the $\Delta\varphi$ and $\Delta\eta$ projections are in a good agreement with each other. In Figure 2.12 c) the integrated yield for different $p_{\mathrm{T,assoc}}$ shows a slightly higher particle yield from the away side analysis compared to the near side analysis. The relative difference is independent of $p_{\mathrm{T,assoc}}$ [STA13].
The ratio of the Au–Au and d–Au yield is not part of the original paper presented by STAR. For a detailed comparison of the Au–Au data points with the respective d–Au points, the data points are taken from c). The ratio between the Au–Au and d–Au yield was calculated and the result is shown in Figure 2.13. This ratio is denoted I_{AA} because it contains the ratio of the associated particle yield from a heavy-ion collision and from a small collision system. The uncertainties of the points are purely statistical. STAR did not provide any systematic uncertainties of the associated particle yields, so this could not be included.
The near side I_{AA} is constant and it agrees with unity within the uncertainty. For the away side I_{AA} there might be a hint for a decreasing I_{AA} with increasing $p_{\mathrm{T,assoc}}$. But this is not significant within the presented statistics.

3. The LHC and the ALICE Detector

The Large Hadron Collider (LHC) is a particle accelerator built at CERN in Switzerland and France, which can collide the accelerated particles at four interaction regions. At the time of writing this thesis the LHC is the particle accelerator with the highest collision energy which has been built by mankind. At present the LHC can run in 3 modes, proton-proton (pp), lead-lead (Pb–Pb) and proton-lead (p–Pb).
One of the experiments at the LHC is ALICE (A Large Ion Collider Experiment). The ALICE collaboration studies the physics of strongly interacting matter at LHC energies in all collision types. A special focus is on Pb–Pb collisions in which a new state of matter is expected, the QGP.
This thesis presents results obtained from ALICE data. In this chapter a brief description of the LHC and its experiments is given. The main focus is on ALICE and its subdetectors.

3.1. The Large Hadron Collider

With a circumference of 26.7 km, the LHC [EB08] is the biggest particle accelerator ever built. The collision energy of $\sqrt{s} = 13\,\text{TeV}$ for pp collisions and $\sqrt{s_{NN}} = 5.1\,\text{TeV}$ for Pb–Pb collisions is the highest energy which has ever been achieved by mankind with a collider.
Before the particles can be accelerated in the LHC, they have to be pre-accelerated. In the acceleration process the magnetic fields and the acceleration procedure have to be adjusted to the energy of the particles. For particles which should be accellerated from zero to multiple TeV this is not feasible in one machine. In Figure 3.1 the schematic acceleration steps for the beam are shown. The proton beam is created and then accelerated through LINAC 2 and the PS BOOSTER to get into the PS (Proton Synchrotron). From here the beam is further accelerated in the SPS (Super Proton Synchrotron) and then injected into the LHC. The lead beam is created and first accelerated in LINAC 3. Afterwards it is accelerated in LEIR (Low Energy Ion Ring) before it is injected into the PS. From this stage on it is accelerated by the SPS and the LHC like the proton beam.
The LHC itself is built underground at a depth between 45 and 170 m, with two counter-rotating beams. In these rings the beams circulate in opposite directions. The rings contain eight interaction regions (IR). Four of them are used for particle collisions and the other four are used for beam maintenance. The experiments at the IR with collisions are; ALICE, ATLAS (A Toroidal LHC ApparatuS), CMS (Compact Muon Solenoid) and LHCb (Large Hadron Collider beauty experiment). The three

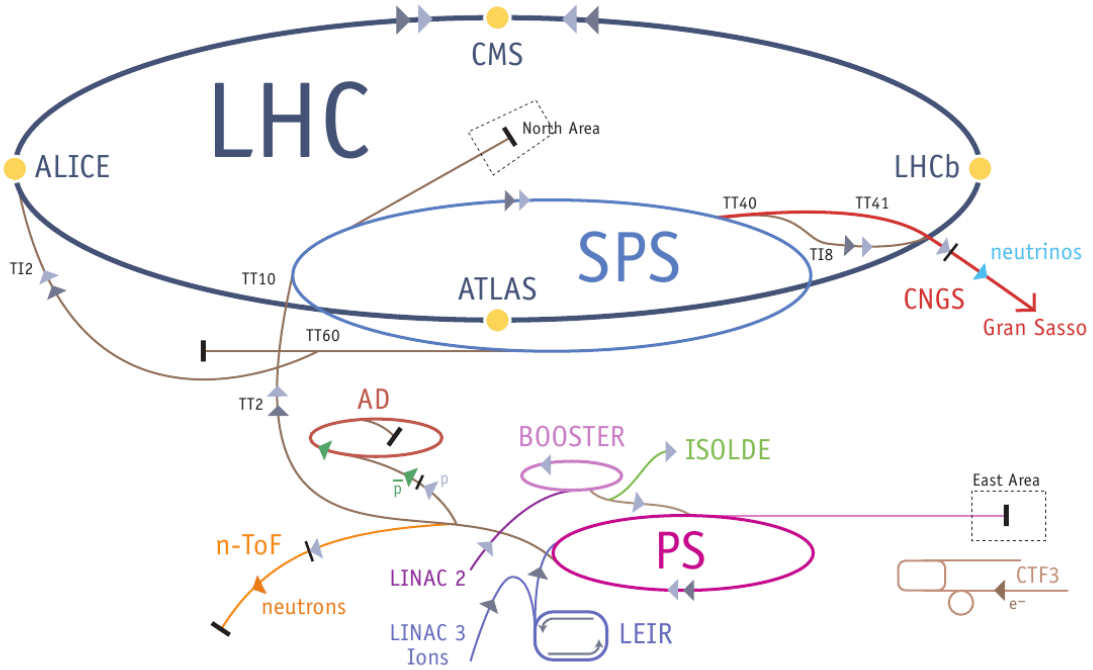

Figure 3.1.: Schematic view of the LHC and its pre-accelerators. The yellow points represent the four big experiments at the LHC. Figure from [Lef09].

smaller experiments, LHCf (Large Hadron Collider forward experiment), MoEDAL and TOTEM (TOTal cross section, Elastic scattering and diffraction dissociation Measurement) are installed close to ATLAS, LHCb and CMS respectively.
In Table 3.1 the experiments and the beam facilities with their corresponding IR are shown. A brief description of the beam facilities is given in Section 3.1.1. A short overview over the experiments is given in Section 3.1.2. The ALICE experiment is explained in more detail in Section 3.2.
The approval of the LHC by the CERN council was given in December 1994. It was built in the existing LEP (Large Electron Positron) tunnel which has been constructed between 1984 and 1989. At the time of the council decision the LEP collider was still to be operated until 2000. At the beginning it was planned to build the LHC in two stages. The second stage would have reached the final energy of 14 TeV. Because of substantial contributions from non-member states, the LHC was finally built in one single stage. The decision for this was approved by the council in December 1996.
In the time between 2000 and 2008 the LHC and the experiments were constructed. The first circulating proton beam occurred on September 10, 2008. Because of a fault in the electrical connection of two superconducting magnets on the 19th September, beam operation stopped again. The incident caused some mechanical damage to the magnets and a leak of liquid helium. After this issue was fixed, the proton beam circulated again on November 20, 2009.

IR	Installation
1	ATLAS, LHCf
2	ALICE
3	beam cleaning
4	RF cavities
5	CMS, TOTEM
6	beam dump
7	beam cleaning
8	LHCb, MoEDAL

Table 3.1.: Description of the interaction regions (IR) of the LHC. The installation column describes the experiment [Lef09] or the beam facility [EB08].

During the following years, until February 2013, the experiments took the LHC Run I data. In February 2013 the beams in the LHC stopped for the LS1 (Long Shutdown 1). The LHC was upgraded in the following 2 years so that it can be operated at the designed higher energy.
The first pp collisions at 13 TeV took place on May 20, 2015. The reason to run with 13 TeV instead of 14 TeV was the reduced time needed to get the magnets ready for the physics runs. The superconducting magnets of the LHC need some training in their final configuration to run stably without the risk of a magnet quench. A magnet quench is a warm up of the magnet, which stops it from superconducting [Cer15].

3.1.1. Design Performance of the LHC

The LHC consists of eight straight sections and eight arcs containing 9600 magnets of different types (dipoles, quadrupoles, sextupoles, etc) [EB08, Lef09]. Most of the 1232 dipoles, with a length of 14.3 m each, are used in the arcs to keep the beam on a curved path. To do so the magnets use a magnetic field of up to 8.33 T at a temperature of 1.9 K. Some further dipoles are used in the insertion tunnel to the LHC. The other kind of magnets are used to focus the beam or to guide the beam in the insertion step or at the interaction regions. The operating temperature of 1.9 K is reached by liquid helium cooling.
The beam acceleration is done with eight cavities per beam, which are located at the interaction region 4. The cavities use a radio frequency (RF) of 400 MHz to create an average electrical field of 5.5 MV/m.
The collider performance can be described by the luminosity which is defined as:

$$\mathcal{L} = f \cdot n_b \frac{N_1 N_2}{A}. \tag{3.1}$$

Here f is the frequency with which the particles are circulating the accelerator ring, n_b the number of bunches in the accelerator, N_1 and N_2 the number of particles per bunch in the different beams. Usually both beams have the same number of particles per bunch. A is the effective beam cross-section. The designed luminosity of the LHC

is $\mathcal{L} = 10^{34}\,\mathrm{cm}^{-2}\mathrm{s}^{-1}$ for pp collisions and $\mathcal{L} = 10^{27}\,\mathrm{cm}^{-2}\mathrm{s}^{-1}$ for Pb–Pb collisions respectively. For high luminosities, multiple particle collisions can happen in one bunch crossing. This effect is called pileup.
The luminosity for Pb–Pb collisions is considerably lower than for pp collisions. Because of the 82 protons per Pb ion, the repulsion of the ions due to the electromagnetic force within one bunch is much stronger in Pb bunches than in proton bunches. Consequently the number of Pb ions per bunch is reduced compared to pp bunches. The design parameters in proton beams are 2808 bunches of $1.1 \cdot 10^{11}$ protons each. In the lead beams up to 592 bunches contain up to $7.0 \cdot 10^{7}$ nuclei each.
At the interaction regions 3 and 7 several collimators are installed to clean the beam. At IR3 particles with a high momentum offset are scattered out of the beam, while at IR7 particles with a large betatron amplitudes are scattered. The betatron amplitude is the deviation of the particle path from the designed particle path in the accelerator. The absorption of the scattered particles is done by secondary and tertiary collimators.
At IR6 the beam dump system is installed. Because of the high energy stored in the LHC during the operation the dumping procedure has to guarantee that the energy is deposited outside of the area critical for the LHC operation. To do so both beams are deflected into separate directions and then absorbed by a dedicated beam dump [EB08].

3.1.2. The Experiments

ALICE (A Large Ion Collider Experiment)

ALICE is the dedicated heavy-ion experiment designed to study the Quark–Gluon Plasma. The experiment is also studying pp collisions which are, among other things, used as a baseline for the Pb–Pb collisions. A further detailed description of the experiment is given in Section 3.2 [ALI08].

ATLAS (A Toroidal LHC ApparatuS) and CMS (Compact Muon Solenoid)

ATLAS and CMS are general purpose detectors designed to cover the widest possible range of physics at the LHC. The biggest discovery up to now is the discovery of a particle consistent with the Standard Model Higgs boson in 2012 [ATL12, CMS12c]. Among other things the detectors are searching for extra dimensions and supersymmetry (SUSY).
While ATLAS and CMS have the same research program, the design of the detectors is different. This allows them to cross check each other [ATL08, CMS08].

LHCb (Large Hadron Collider beauty experiment)

LHCb is designed to investigate the asymmetry of matter and antimatter in B-particle productions. This should help investigate why the universe is made of the matter we observe. Different from the other big experiments at CERN, LHCb does not surround

the interaction region with one detector but only has detectors to measure particles in the forward direction [LHC08b].

LHCf (Large Hadron Collider forward experiment)

LHCf is located at the same interaction region as ATLAS and it investigates particles created very close to the beam direction. This is used to test models which are used to estimate the primary energy of ultra high-energetic cosmic rays [LHC08a].

MoEDAL (Monopole & Exotics Detector At the LHC)

MoEDAL is located at the same interaction region as LHCb and it searches for magnetic monopoles and other highly-ionizing particles. It is a passive detector which is read out offline. This means the detector read out is done after the beams in the LHC stopped. At time of writing this thesis no magnetic monopole has been found [MoE16].

TOTEM (TOTal cross section, Elastic scattering and diffraction dissociation Measurement)

TOTEM is located at the same interaction region as CMS and studies the proton structure and the proton-proton interaction cross section. Like LHCf it measures particles emitted very close to the beam line [TOT08].

3.2. ALICE

ALICE [ALI08] is the dedicated heavy-ion experiment to study the Quark–Gluon Plasma. The experiment is operated by a collaboration of over 1 000 members. The detector is located at interaction region 2 of the LHC in Saint-Genis-Pouilly, France. The detector is $16 \times 16 \times 26\,\mathrm{m}^3$, and weights approximately 10 000 t. The ALICE subdetectors are grouped into the central barrel, the muon arm and the forward detectors. The central barrel, which is inside the magnet, covers a pseudorapidity range of $|\eta| < 0.9$. The muon arm is at $-4.0 < \eta < -2.5$. The forward detectors cover different pseudorapidity ranges and are described below. The positions of the different subdetectors within ALICE are shown in Figure 3.2.

3.2.1. Central Barrel

The central barrel contains the main tracking detectors of ALICE. The detectors with full azimuthal coverage and a pseudorapidity range of $|\eta| < 0.9$ are the Inner Tracking System (ITS), the Time-Projection Chamber (TPC), the Transition Radiation Detector (TRD) and the Time-Of-Flight (TOF) detector. The detectors with limited φ coverage and different pseudorapidity coverages are the High-Momentum Particle

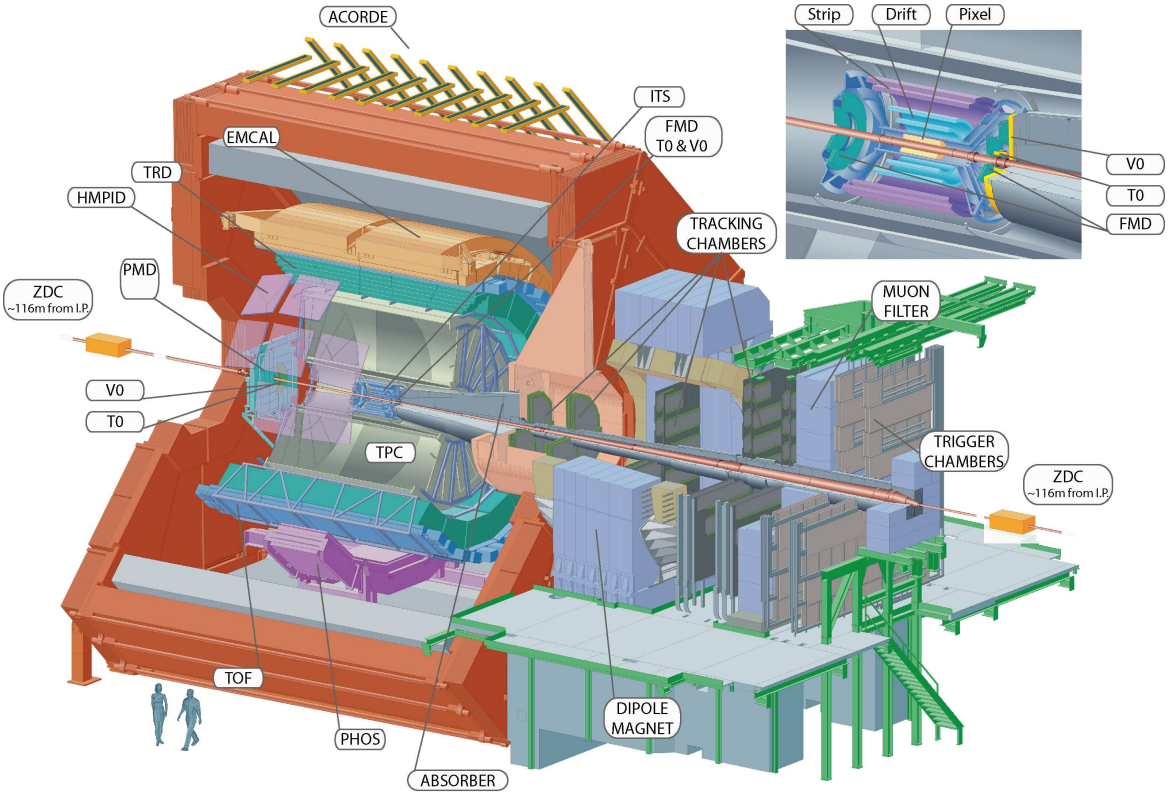

Figure 3.2.: Schematic view of ALICE. Figure adapted from [ALI08].

Identification Detector (HMPID), the PHOton Spectrometer (PHOS) and the ElectroMagnetic Calorimeter (EMCal). During LS1 an additional calorimeter was added to increase the acceptance of the EMCal. The new calorimeter is called the ALICE Di-Jet Calorimeter (ALICE-DCal). It is installed on the opposite side of the beam from the EMCal which allows to measure di-jets with both detectors.
These detectors are contained in a room temperature solenoid magnet, the L3 magnet. The magnet is reused from the L3 experiment which was operated at the LEP collider and located in the same cavern before ALICE. The magnet is built out of an octagonal iron yoke containing an aluminum coil. At the poles it is closed with doors to be able to access the inner volume. The coil has a length of 11.9 m and an inner radius of 5.9 m [L3 90]. On the outside the magnet has a length of 15.8 m and a width of 14.1 m. The magnet has a nominal flux density of 0.50 T with field variations below 2% [ALI08].
The magnet creates a magnetic field, which forces the charged particles which are created in the collision on a curved track. Out of this curvature the momentum of the particle can be calculated.

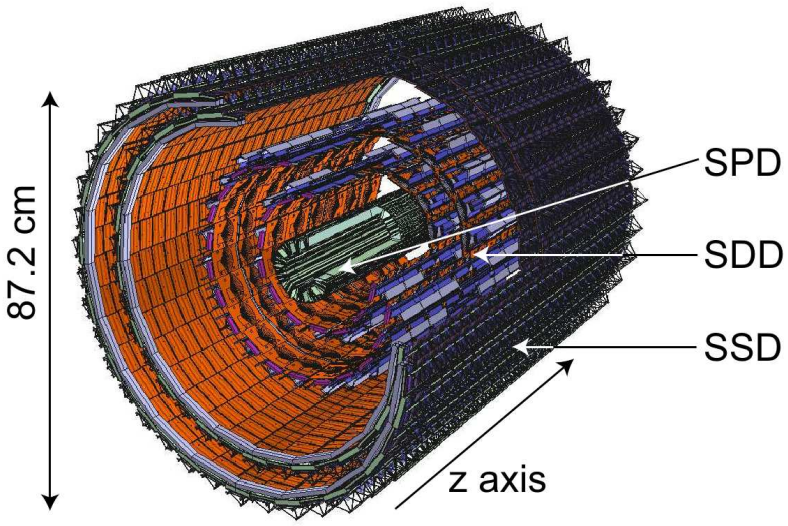

Figure 3.3.: Schematic view of the ITS. Figure from [GO09].

Inner Tracking System (ITS)

The Inner Tracking System (ITS) identifies the primary vertex of the collision with a resolution better than 100 μm. For particles with a momentum less than 200 MeV/c the ITS is the main detector that tracks and identifies the particles. At higher particle energies it still improves the momentum and angle reconstruction of the TPC [ALI08]. The ITS consists of six layers of silicon detectors, which surround the beryllium beam pipe. The beam pipe has a radius of 3 cm and the mechanical support of it is provided by the ITS. This way no relative movement between ITS and beam pipe can take place during operation. The first ITS layer is at a radial distance of 3.9 cm to the nominal interaction region and the last layer is at 43 cm. Along the beam axis all layers cover at least $|\eta| < 0.9$ for collisions which take place within the z vertex $|z_{vtx}| < 5.3$ cm. Azimuthally the ITS has full coverage. To reduce particle scattering and energy loss the material budget was kept low. In terms of radiation length X/X_0, it is less than 8%.
For the six ITS layers three different technologies have been used. In Figure 3.3 the schematic construction of the detector is shown.
The two inner most layers form the Silicon Pixel Detector (SPD), which is optimized to reconstruct the vertex and the impact parameter of the collision. The average distance of the layers to the interaction region are $r = 3.9$ cm and $r = 7.6$ cm. They have a larger pseudorapidity coverage of $|\eta| < 2.0$ (first layer) and $|\eta| < 1.4$ (second layer) so that they provides together with the Forward Multiplicity detector (FMD) a continuous η coverage. With $3.3 \cdot 10^6$ and $6.6 \cdot 10^6$ channels for the first and second layer, each SPD layer has more channels than the other layers combined. With this high amount of channels the vertex determination and impact parameter resolution

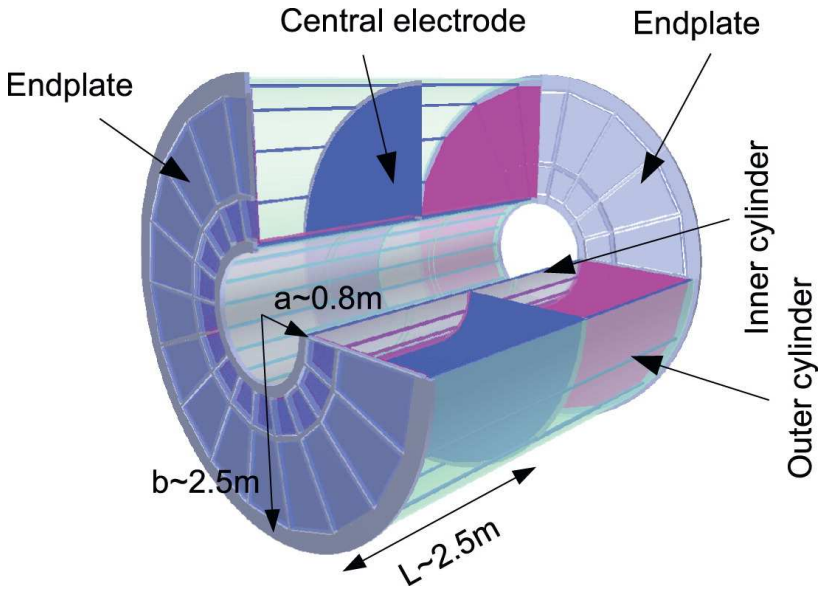

Figure 3.4.: Schematic view of the TPC. Figure from [RSR11].

is improved. The SPD has a digital read out and does not provide any energy loss measurements.
The third and forth layer are the Silicon Drift Detector (SDD). Contrary to the SPD, the SDD has an analog read out and it provides energy loss measurements dE/dx. The first layers is located at an average distance from the interaction region of $r = 15.0\,\text{cm}$ and the second layer is at $r = 23.9\,\text{cm}$. The SDD layers are protected by a heat shield from heat radiation emitted by the SPD.
The outermost layers form the Silicon Strip Detector (SSD). Like the SDD it has an analog read out and it provides energy loss measurements. One layer is located at an average distances from the interaction region of $r = 38.0\,\text{cm}$ and the other one at $r = 43.0\,\text{cm}$. These layers are important to match tracks from the ITS and TPC [ALI08].

Time Projection Chamber (TPC)

The Time Projection Chamber (TPC) is a cylindrical detector assembled around the ITS. A schematic view of it is shown in Figure 3.4. The inner and outer radius of the TPC are 0.6 m and 2.8 m while the sensitive volume is between the radii of 0.8 and 2.5 m. Along the beam axis the central electrode divides the detector into two parts, which are both 2.5 m long. They cover a pseudorapidity of $|\eta| < 0.9$ for tracks with full radial track length and $|\eta| < 1.5$ for tracks with 1/3 radial track length. The detector was filled with $90\,\text{m}^3$ of $Ne/CO_2/N_2$ in the ratio 90/10/5 during the LHC Run I [ALI08]. After run I the gas mixture was changed to Ar/CO_2 in the ratio 90/10 so that the detector response is more stable at high particle fluxes [ALI15a].
The TPC is used to measure charged particle tracks and their momenta. The gas

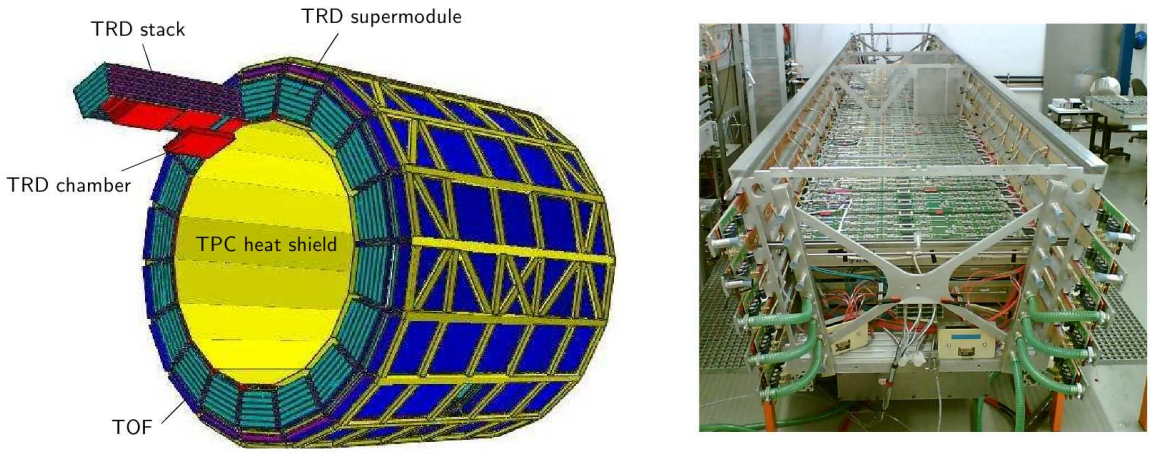

Figure 3.5.: Schematic view of the TRD on the left side. On the right side a picture of one supermodule is shown. Figure from [ALI08].

mixture inside is ionized by charged particles traversing the TPC, and the created electrons drift to one of the end plates on the sides of the TPC. The electrons drift with a velocity of $2.7\,\mathrm{cm}/\mu\mathrm{s}$, which is generated by an electrical field of $400\,\mathrm{V/cm}$. This corresponds to a maximum drift time of $90\,\mu\mathrm{s}$. With this readout time the TPC is the slowest detector of ALICE and thus determines the time a full detector readout needs.
On the end plates 18 detector segments are mounted containing multi-wire proportional chambers to measure the drift electrons. Between neighboring sectors are small inactive areas which add up to a 10% azimuthal angle in which the TPC is not sensitive. This does not reduce the efficiency of detecting particles with the TPC by 10% because the momentum of a charged particle is measured via the curvature of the track. Due to this curvature, a particle track can only partly be within a non-sensitive area. Obviously this is not the case for high p_T tracks which are hardly curved. Within the TPC a large momentum range from $0.1\,\mathrm{GeV}/c$ to $100\,\mathrm{GeV}/c$ can be measured.
The TPC provides good two-track separation even at high particle densities. It is designed for a density of up to 20 000 tracks within the TPC acceptance. These high track densities were never reached during operation. The TPC further contributes to particle identification of the central barrel by measuring the energy loss. With the TPC tracks the vertex position can be determined and the measurement of the ITS can be further improved [ALI08].

Transition Radiation Detector (TRD)

The Transition Radiation Detector (TRD) is assembled in a cylindrical shape around the TPC. The main purpose of the TRD is to distinguish electrons and pions at transverse momenta $p_T > 1\,\mathrm{GeV}/c$. At lower energies, energy loss measurements of the TPC can distinguish these particles.
The TRD can be operated as a fast trigger for high momentum charged particles. This

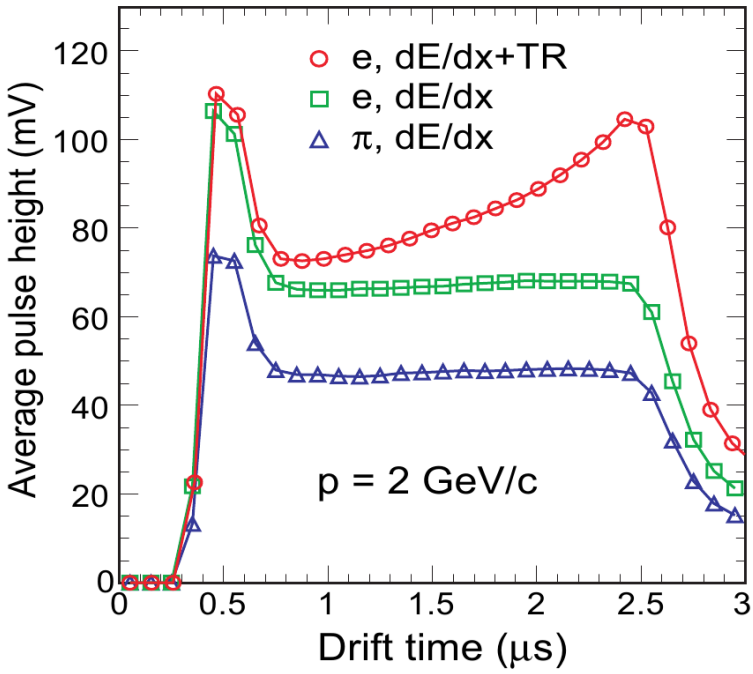

Figure 3.6.: Average pulse height of the current measured in the TRD chamber dependent on the drift time. The results are shown for pions (triangles), electrons without a radiator (squares) and electrons with a radiator (circles). Figure from [ALI08].

can be used to enhance the yield from high p_T decay particles and jets. Together with the electron identification capabilities of the TRD, it can provide a di-electron trigger. In Figure 3.5 on the left side a schematic view of the TRD is shown. It is installed at a radial distance from the beam of 2.90 m to 3.68 m. It consists of 18 supermodules each of 7.8 m length, which are installed around the beam. A picture of one supermodule is shown in Figure 3.5 on the right side. Each supermodule consists of 30 chambers which are arranged in six layers and five stacks.
At the bottom of each TRD chamber a radiator is installed. This radiator consists of many material layers with different dielectric constants. Particles with a high γ factor ($\approx 1\,000$) create transition radiation while they change from one material to another. Electrons fulfill this requirement, pions do not. An electron transversing the radiator produces on average 1.45 x-ray photons. These photons are converted into electrons in the gas directly behind the radiator. The gas mixture is Xe/CO_2 in a ratio of 85/15. Both the electrons and pions from the collision ionize the gas and produce ionization electrons. All produced electrons drift to the anode wires which are mounted on the other side of the chamber. The measured current induced by pions and electrons depends differently on the drift time.
In Figure 3.6 the measured signal is shown for pions and electrons at a momentum of $p = 2\,\mathrm{GeV}/c$. The pion measurement has a peak at the beginning and afterwards

it stays flat. In the electron case the measurement is done once with a radiator and once without it. Without the radiator the shape is the same as for the pions but at a higher average pulse height. In this measurement no transition radiation is created. With the additional radiator, the electrons produce transition radiation which creates an additional peak at a longer drift time. Due to this two peak structure the electrons can be identified [ALI08].
During the LHC Run I 13 TRD supermodules were installed in ALICE. In the LS1 the missing five supermodules were installed so that in Run II the detector covers the full azimuthal acceptance [ALI16].

Time Of Flight detector (TOF)

Outside of the TRD, the Time Of Flight (TOF) detector is a cylindrical detector, which is built at a radial distance from 3.77 m to 3.99 m. The detector is used for the Particle IDentification (PID) of pions, kaons and protons. The pions and kaons can be identified up to 2.5 GeV/c and the protons up to 4 GeV/c with a system time resolution of 80 ps. These measurements are done with a π/K and the K/p separation better than $3\,\sigma$ [ALI14].
The detector is divided into 18 azimuthal segments (in φ) and 5 longitudinal segments (in z), like the TRD. Each of these segments uses so called Multi-gap Resistive-Plate Chambers (MRPC) to measure the particles. In each of these chambers a high electrical field is used, which is uniform over the full sensitive gaseous volume. Due to the high field, every ionization induced by particles transversing the TOF immediately starts a gas avalanche process. The electrons do not first drift towards a region of high electrical field. To achieve this effect the chambers are realized as thin structures with a width of 250 μm.
The TOF measures the time for each particle between its creation in the initial collision and the moment when the particle arrives at the detector. As additional input the collision time from the TZERO detector (see below) is used. The TOF uses the effect that different kind of particles with the same momentum have a different velocity because of the different mass. The momentum of the particles is known from the curvature in the ITS and TPC [ALI08].

3.2.2. Forward Detectors

VZERO detector

The VZERO detector consists of the two separate scintillation detectors V0A and V0C. They are installed on both sides of the interaction region at $2.8 < \eta < 5.1$ (V0A) and $-3.7 < \eta < -1.7$ (V0C). The V0A side is at 340 cm distance from the interaction region, while the V0C is at a distance of 90 cm because it is mounted on the front end of the hadronic absorber of the muon system. Both detectors consist out of four rings containing 32 elementary scintillation counters.
With a time resolution better than 1 ns for the individual scintillation counters, the

VZERO detectors can be used as a trigger. The V0A and V0C detectors can distinguish beam-gas interactions from beam-beam interactions by measuring the time difference between the arrival of charged particles at the detectors. The beam-beam interactions always take place in between the V0A and V0C detectors while beam-gas interactions can occur everywhere. The procedure how events from outside this area are identified is described in Section 4.1 [ALI04].

TZERO detector

The TZERO detector consists out of two separate arrays of Cherenkov counters. They are placed on both sides of the interaction region and contain 12 counters each. Because of the absorber of the muon system the T0C is mounted at a distance of 72.7 cm while the T0A is mounted at a distance of 375 cm. They cover a pseudorapidity range of $4.61 < \eta < 4.92$ (T0A) and $-3.28 < \eta < -2.97$ (T0C).
This detector measures the collision time with a precision of 50 ps. It is used as a reference time for the TOF detector. Further the detector determines the vertex position and creates a trigger if the position is within an accepted window [ALI08].

Zero-Degree Calorimeter (ZDC)

The Zero-Degree Calorimeter (ZDC) is a hadronic calorimeter installed at a distance of 116 m on both sides of the nominal interaction region. It is designed to measure the nucleons of the particle collision which do not participate in the interaction. These particles keep flying very close to the beam path. They are called spectators. The magnetic field of the LHC deflects the protons while the neutrons stay straight. To measure the neutrons the beam pipe is divided into two pipes and the calorimeter (ZN) is placed in between these pipes at an angle of 0 ° from the beam axis. The calorimeter for the protons (ZP) is installed next to the beam pipe at the position to which the protons are deflected to.
On the opposite site of the muon arm two electromagnetic calorimeters (ZEM) are installed on both sides of the beam pipes at a distance of 7 m from the interaction region. The ZEM measures the energy of the particles emitted in the forward direction. The ZDC provides together with the ZEM the centrality information of the event. The centrality information from the ZDC can be used as Level 1 trigger [ALI08].

3.2.3. The ALICE Trigger System

It is not possible to record all collisions in the LHC due to limited available resources like bandwidth and storage capacities. Additionally the detectors have a dead time after a collision is recorded. To measure as many interesting physics events as possible a trigger system is used. This system uses the fast detectors to provide a decision whether an event should be recorded or not. The decision has to be taken within a short time frame so that the data which should be recorded is still available in the detector. In case an event is not recorded the trigger has to be ready for the next

collision.
The trigger system is implemented in several levels of hardware triggers and one last software trigger, the HLT (High Level Trigger). This HLT runs on a computing cluster near the experiment.
Dependent on the trigger level, a different time window is available to get a decision. Due to the detector requirements the first trigger level 0 (L0) has to arrive at the detectors at 1.2 μs. This time is not sufficient to collect the input from all triggers so they are included in the level 1 (L1) trigger which arrives after 6.5 μs. The decision time of the L0 trigger is of the order of 100 ns the rest of the time originates from the trigger generation and cable delays.
The level 2 (L2) trigger decides if the event is finally accepted. This includes a 'past-future protection' which ensures that the events are not spoilt by pile up events. For example to record an event in Pb–Pb collisions, no more than 2 additional peripheral events and no semi-central event are allowed in a time interval of twice the readout time of the slowest detector. This time interval is centered around the event which should be recorded. The slowest detector of ALICE is the TPC with a readout time of 90 μs, which consists mainly out of the drift time of the electrons. This means the above mentioned constrains have to be fulfilled a time window $\pm$90 μs around the triggered event [ALI08].
The so far explained hardware triggers increase the number of recorded events which can be used for physics analysis. The HLT does not affect the events which are recorded by the detector. This trigger can decide if an event is saved based on a quick online analysis. Thus it improves the efficient use of the storage elements. Additionally it compresses the data without loosing information. These compression algorithms reduce the needed storage space and the needed bandwidth to the storage systems. In the current configuration only the data compression is used and not the online analysis [ALI14].
The triggers used in this thesis are the minimum-bias trigger and two centrality triggers. The minimum-bias trigger is designed to identify all events which contain an inelastic scattering of the incoming particles. For this trigger only fast detectors can be used. In ALICE these are the SPD, the VZERO and the ZDC detectors. In pp collisions every event which has either a signal in the SPD or in one of the VZERO detectors is accepted if the VZERO detectors did not detect a beam-gas interaction. In Pb–Pb collisions an additional signal in both ZDC detectors is required to suppress the electromagnetic interactions between the Pb ions.
The centrality triggers select high multiplicity events. The centrality concept is explained in Section 4.2. It describes the geometry of the collision. With the different trigger settings different collision geometries are chosen. For this trigger the multiplicity in the VZERO detectors is measured. Because the multiplicity is correlated with the centrality, this makes it possible to identify more central events in the measurement without determining the final centrality. The different trigger configurations select certain multiplicity ranges in the VZERO detectors which correspond to different centrality ranges [ALI14].

3.2.4. Computing Tools

During the LHC run I from 2010 to 2013 the ALICE experiment collected 7.2 PB of raw data. To analyze this amount of data, a huge amount of computing power is required, which cannot be provided by a single institute. Hence, the collaborating institutes provide computing power and storage capacity for the whole collaboration. For a system of this size the distribution of the data and the analysis on the different computing centers cannot be done manually. Thus the network is organized as a Grid in which the different computing centers are loosely coupled. The analysis jobs are executed in parallel and the user access is realized via central servers at CERN.
In the daily work the Grid structure is hidden from the user by the AliEn (ALICE Environment) interface. This is the top level Grid software used by ALICE [Bag08]. The physics analysis is executed by a framework developed by the ALICE collaboration. This framework is called AliROOT[1]. It is installed on all Grid nodes. Because of the automatically installed framework the users do not need to send their code to the analysis nodes to execute their task. It is sufficient to send the task configuration.
The analysis with the Grid can be done by the user individually or with the help of the LEGO train system [Ali15f, ZG14]. The LEGO trains are the centralized Grid submission system of ALICE. It makes it possible to run the physics analysis on the Grid in a more efficient way than the individual users could do it themselves. This system is further explained in Section 3.2.4 and in the Appendix A.

AliEn

AliEn is an interface managing the ALICE Grid resources. The development of this system started in 2000 and it groups together several services which have been developed earlier. The primary goal of AliEn is to hide the complexity and heterogeneity of the underlying systems from the end-user.
The underlying systems and basic services are [Bag08]:

File Catalogue It contains the location of every file on the ALICE computing sites. The catalogue does not contain the files themselves but the mapping where they can be found. For most of the files in the catalogue multiple replicas are saved at different computing sites to ensure data preservation.

Data Management Tools These tools take care of the data access. Dependent from where in the world a user wants to access a file the easiest to reach replica is used. These tools further execute the copy and delete operations on the files if requested.

Authentication and Authorization This makes sure that only authorized people can access the other AliEn services.

[1]For organizational reasons the AliROOT repository is split into AliROOT and AliPHYSICS. The first one contains the rarely changed code from the framework and the second one contains the user code. In the following both frameworks are referenced with AliROOT.

Workload Management It collects all computing jobs in a central queue and distributes them to the computing sites in an efficient way. The job description is done in the Job Description Language (JDL) which is uniform for the system. This means that the definition is independent of the computing site where the job will run at the end.

Interface to other Grid Implementations This allows AliEn to not only run as a standalone Grid but also to connect to other Grid implementations.

Monitoring Services The monitoring is based on the MonALISA framework. This framework has a hierarchic structure which selects and aggregates important information. Part of this is the monitoring of the other AliEn services.

AliROOT

The physics analysis within ALICE is done with the framework AliROOT. It builds up on top of the ROOT framework which is based on C++. AliROOT is used for simulation, alignment, calibration, reconstruction, visualization and analysis of the experimental data.
AliROOT was developed starting in 1998 [ALI08].The framework contains classes which are used by many people and individual user analysis classes which are used by one person. The user classes are organized in different physics working groups. Due to the high amount of changes in the frameworks no full documentation exists. Several web pages explain the current status and how to use it [ALI15b, Ber15]. Some base classes are explained in [ALI08].
To run on the Grid the framework needs to be tagged, which is usually done once per day. The AliROOT tag is a name for the version of the framework which existed at one certain moment. For the users it is mandatory to submit their code to the framework. With frequent code submission from the users the code repository serves as a bookkeeping system of the code changes. Additionally the installation of the framework on the Grid sites is used as main method to deploy user code on the Grid sites. To use the centralized analysis system, the LEGO trains, the code submission is a prerequisite.

Grid - LEGO trains

The LEGO (Lightweight Environment for Grid Operations) train system is the centralized analysis system of ALICE. It provides the users with an easy access system in form of a webpage to run their analysis. This hides the Grid complexity from the users. At the same time this system can organize the analysis in a way that the resources of ALICE are used in an optimal way. Additionally the system provides a uniform bookkeeping system for all users.
AliEn is a high level job submission management system. But it still requires detailed knowledge about the JDL and the job submission procedure. The analysis and merging jobs have to be submitted individually and every error has to be analyzed. This

means that every user will have to learn these basic concepts of the Grid and the same mistakes are probably repeated for different users. Additionally it is very difficult for the users to test their analysis in an environment which is similar to the one on the Grid.
Apart from the difficulty for the users to execute their analysis, the individual analysis of many users is CPU inefficient. The reason for this is that most of the jobs spend more time on reading the data than on computing the results. This is a problem which originates from the large size of the data and thus the long time necessary to read it from disk.
Both problems are cured with the concept of the LEGO trains [Ali15f, ZG14]. This system collects multiple analyses and executes them together in an efficient way.
Following the concept the users commit their code to the AliROOT repository, which is uploaded to the Grid when it has been tagged. Afterward the user define their task on a website. This is called a train 'wagon'. In this train wagon only parameters about the task have to be defined. The Grid parameters are completely transparent for the user.
For each train, the train operators take care to put multiple train wagons together into one train run. This is one big advantage of the system. Multiple users who want to analyze the same dataset can run together in one train run. In such a train run the data is loaded only once and multiple analysis are executed on them. This improves the CPU efficiency of the analysis jobs.
Before a train run can be executed on the full dataset, it has to be tested in a special test environment. This test environment simulates the environment on the grid sites and runs the code on a reduced number of files. Afterwards the result is validated. Only if this test is successful the train run can start on the Grid.
The train test system identifies many errors in the code which prevents not working trains to run to the Grid. This and the increased CPU efficiency improve the efficient usage of the computing resources within ALICE. Additionally the standardized run procedure makes it easier for experts to have a look at the analysis of a user and to help debug it.
Further technical information about the LEGO train system, which was significantly improved as part of this thesis work, is shown in Appendix A.

4. Event and Track Selection

The events recorded by ALICE are triggered with the trigger system which is explained in Section 3.2.3. A selection is made which events are used for the analysis of this thesis. This selection ensures that the recorded events are from the correct kind of collision. Rejected events can be events which are created by a beam-gas interaction which is described in Section 4.1. Additionally subsets of the events are used which are expected to contain a big or small signature of the QGP. The concepts of the centrality and the longitudinal z-vertex z_{vtx} position are explained in the Sections 4.2 and 4.3. On the basis of these concepts the event cuts used in this thesis are introduced in Section 4.4.
In the events the particle tracks can based on different track cuts. A short overview over the track cuts used for this thesis is given in Section 4.5.

4.1. Beam-Gas-Interactions

In the LHC beam pipe a vacuum of 10^{-13} atm is created. Due to this high vacuum the beam particles rarely interact with gas particles. But these kind of collisions are not completely avoided. Thus they have to be detected so that the events are not used for the analysis.
Beam-gas interactions can happen at any position inside the LHC beam pipe. The beam-beam collisions are only possible at the nominal collision point. The VZERO detectors (see Section 3.2.2) can detect if a collision took place around the nominal interaction area.
All particles created in the collision travel almost with the speed of light to the V0A and V0C detectors independent in which collision and where they have been produced. The small difference to the speed of light can be neglected for the following calculations. Because of the different distance of the VZERO detectors to the nominal interaction point, the signal arrives at the detector after 11.3 (V0A) or 3 ns (V0C). This is illustrated in Figure 4.1 a). In case the collision takes place outside of the VZERO detectors (see Figure 4.1 b) and c)) the time the particles arrive at one of the detectors is negative compared to the nominal bunch-crossing time. This is independent how far away from the V0A or V0C detector this collision happened because the new created particles travel like the colliding particle (proton or Pb-ion) almost at the speed of light. They arrive at the detector at the same time as the proton or Pb-ion would have passed it.
In Figure 4.2 the measured arrival time of the created particles are shown compared to the nominal bunch-crossing time. This is shown for illustration purposes for the V0A

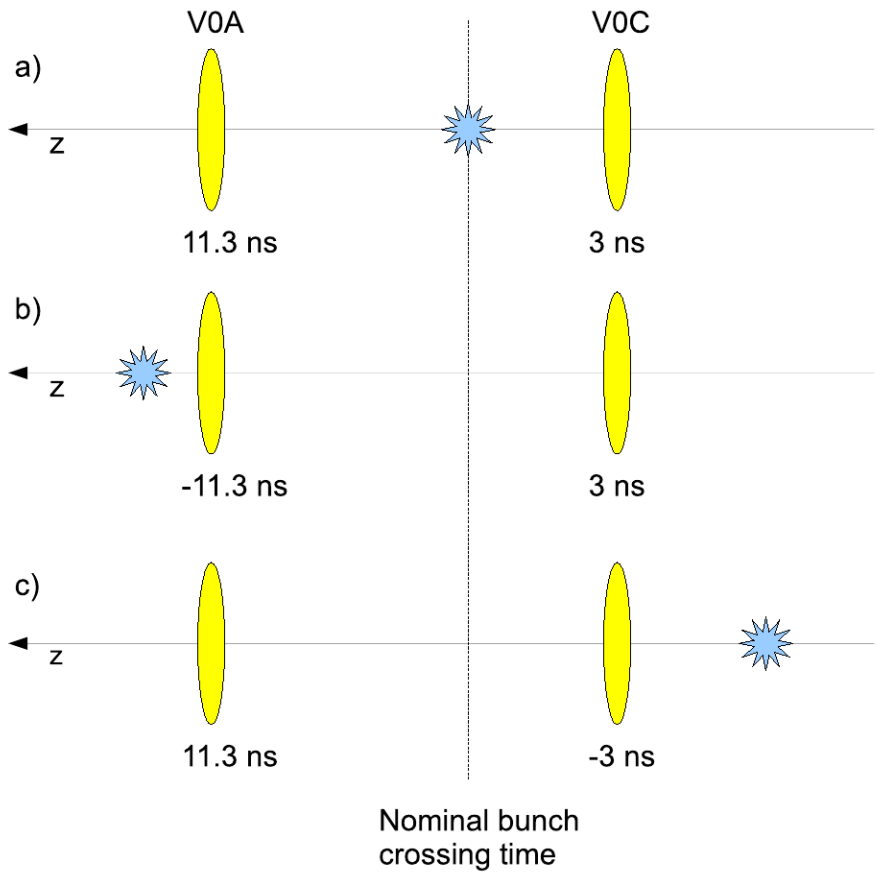

Figure 4.1.: Measurement time of the created particles in the VZERO detectors dependent where the collision took place. In a) a beam-beam collision is shown. The time after which the created particles arrive in the VZERO detectors is both positive. In b) and c) beam-gas collisions outside the interaction area are illustrated. Figure taken from [GO09].

detector. The measurement with the V0C detector is the same. The peak at $-11.3\,\text{ns}$ corresponds to beam-gas interactions outside V0A. This configuration is illustrated in Figure 4.1 b). The particles created in normal beam-beam collisions are shown in the peak at 11.3 ns. The small peaks between -11.3 and 11.3 ns origin from satellite collisions [ALI13c].

4.2. Centrality

In Pb–Pb collisions the Pb-ions can collide in different ways. If the ions collide peripherally most of the nucleons from both nuclei will continue to fly straight without interacting with nucleons from the other nucleus. In central Pb–Pb collisions most of the nucleons will interact with nucleons from the other nucleus. This way a QGP is

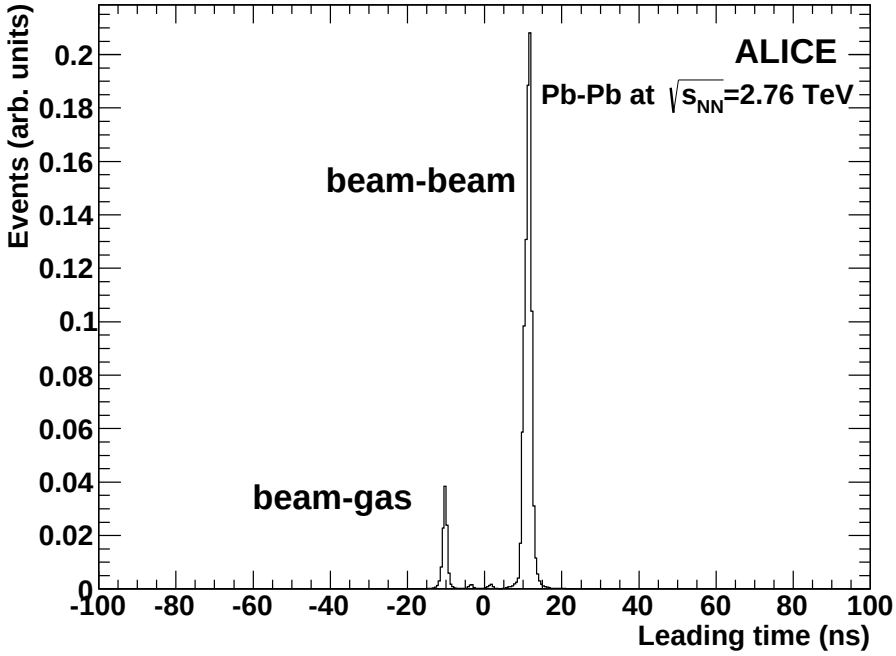

Figure 4.2.: V0A time measurement relative to the nominal bunch-crossing time. The signal at a negative time originates from beam-gas interactions which occurred before the V0A detector. Figure taken from [ALI13c].

created and medium effects are expected. To be able to correlate measurements with the size of the QGP, the characterization of the collision geometry in Pb-Pb collisions is important.
The difference between central and peripheral collisions can be quantified with the impact parameter b which describes the distance between the center of the nuclei at the moment of collision. But this parameter is not directly accessible in a measurement. To describe different collision geometries the centrality concept was introduced [ALI13c]. The centrality C is connected to the impact parameter b and it divides the collisions into groups with similar impact parameters. This is done dependent on the total nuclear interaction cross section σ.

$$C = \frac{\int_0^b d\sigma/db'db'}{\int_0^\infty d\sigma/db'db'} = \frac{1}{\sigma_{AA}} \int_0^b \frac{d\sigma}{db'} db' \tag{4.1}$$

In Equation 4.1 the impact parameter distribution $d\sigma/db'$ is integrated for all impact parameters smaller than b. This is divided by the integral of all possible impact parameters. The ratio defines the centrality of an event with the impact parameter b. The integration of the cross section does not help to directly measure the centrality of a single event because the impact parameter b is not accessible. Instead the particle multiplicity over a given threshold N_{ch}^{THR} can be measured. This can be done because

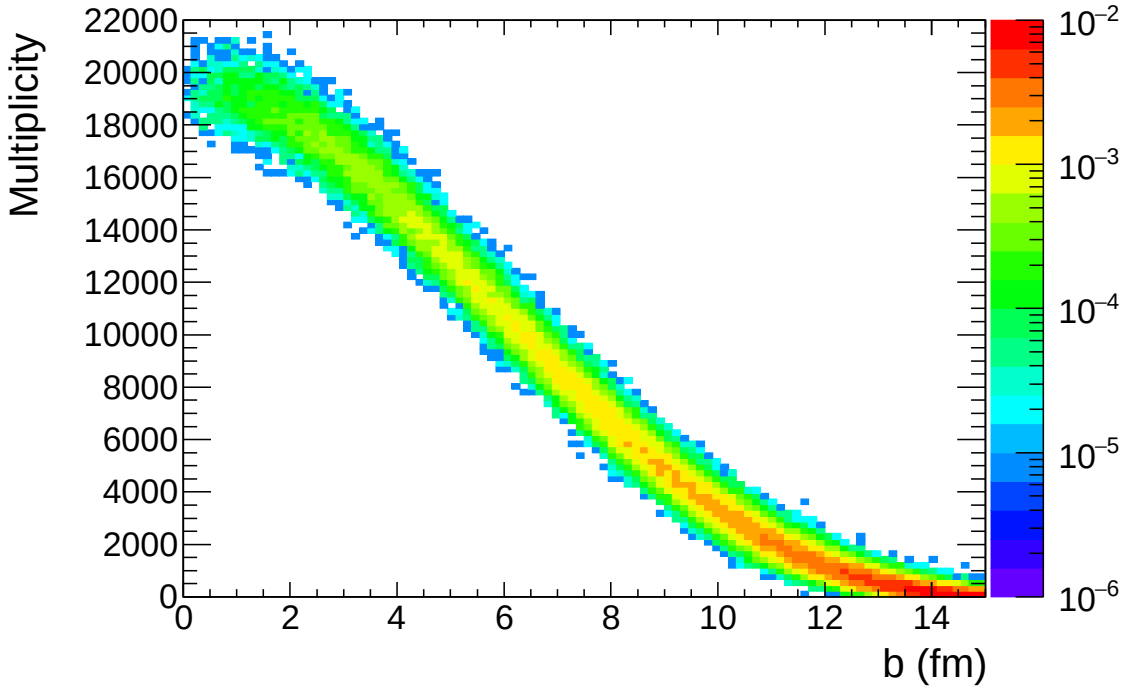

Figure 4.3.: Correlation between the impact parameter and the particle multiplicity in Pb–Pb collisions. The values are calculated with a Glauber Monte Carlo Simulation. Figure taken from [ALI15d].

the multiplicity is directly correlated with the impact parameter. In Figure 4.3 the correlation is shown based on a Glauber Monte Carlo simulation. The Glauber model assumes that a Pb–Pb collision can be simulated as superposition of many nucleon-nucleon collisions. It can be seen that one multiplicity value is correlated with a small distribution of impact parameter values. With this correlation the centrality in Equation 4.1 can be written dependent on the multiplicity.

$$C \approx \frac{1}{\sigma_{AA}} \int_{N_{ch}^{THR}}^{\infty} \frac{d\sigma}{dN'_{ch}} dN'_{ch} \tag{4.2}$$

This equation allows the determination of the centrality out of known quantities. If the charged particle multiplicity could be fully measured for all collision centralities without any background, the hadronic cross section σ would not be necessary. In this case each recorded multiplicity would be compared to all recorded multiplicities. But the charged particle multiplicity has a large background at low multiplicities from non-hadronic collisions. So for the centrality definition, one point in the multiplicity spectrum has to be defined which corresponds to a known point in the hadronic cross section. This point is called the Anchor Point (AP). With the AP all other measured values can be assigned to a centrality class.
With the Glauber model a theoretical multiplicity distribution is created which is fitted to the data. The Glauber model creates a connection between the measured

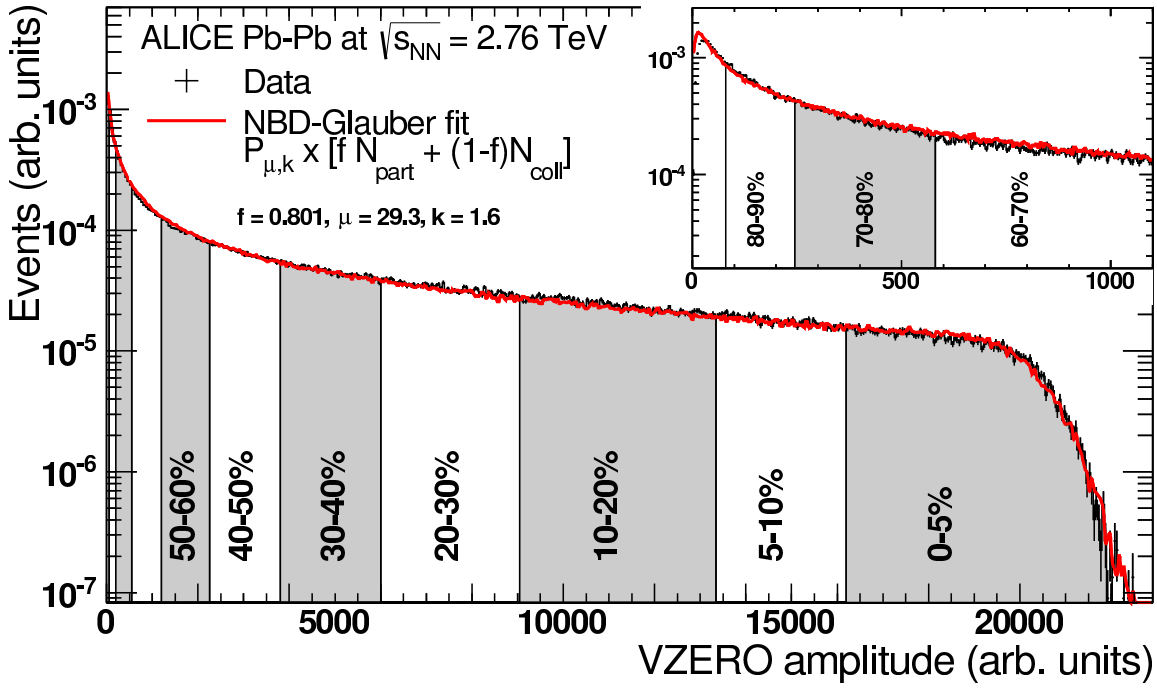

Figure 4.4.: The measured VZERO amplitude distribution with the Glauber fit. The resulting centrality classes are marked. The inset shows a zoom of the low VZERO amplitudes. Low centralities (0–5%) represent central collisions and high centralities (80–90%) represent peripheral collisions. Figure taken from [ALI13c].

distribution and the hadronic cross section σ. From the model an AP can be determined which belongs to a defined point in the hadronic cross section. Due to the high background and big systematic uncertainties for lower multiplicities the AP is defined at 90% of the hadronic cross section.
The multiplicity measurement can be done with the multiplicity signal from every detector. To avoid autocorrelations, it has to be done in a different detector than the physics measurement which should be connected to the centrality. In this thesis the amplitude from the VZERO detector is used to determine the centrality.
All VZERO amplitudes which are bigger than the AP belong to events which have a centrality of 90% or lower (= more central). The events are divided into centrality classes as follows. The highest 5% of amplitudes are put into the centrality class 0–5%. The next highest 5% of the VZERO amplitude are put into the next centrality class (5–10%) and so on. This can be continued until the 85–90% highest VZERO amplitudes are filled into the correspondent centrality bin. More peripheral events are not cathegorized into a centrality because the they are over the AP. In Figure 4.4 the VZERO amplitude distribution with the Glauber fit and the centrality classes is shown [ALI13c].
More central collisions correspond to more nucleons from the Pb ions to interact with

each other. The number of nucleons which interact with at least one other nucleon in the collision is called the number of participants N_{part}. In the heavy-ion collisions these particles participate in N_{coll} nucleon-nucleon collisions. Because a single nucleon can interact with multiple other nucleons the number of participants is not required to be twice the number of collisions. The number of participants and collisions can be calculated out of the Glauber fit with the Glauber model.

4.3. Vertex Selection

The vertex position of the particle collision in the LHC is measured relatively to the nominal collision point. It can deviate in direction of the beam pipe and perpendicular to it. During one fill the collisions are only minimally shifted perpendicular to the beam. This means the collision point in the direction of the beam pipe is the one which has to be carefully monitored for each collision. The distance of the real collision point from the nominal collision point in the beam pipe direction is called the z_{vtx}.
Dependent on the exact z_{vtx}, different parts of the ALICE detector measure more or less particles created in the collision. Because of this effect the detector corrections in the particle correlations are calculated for the individual z_{vtx} bins (see Chapter 5). At large z_{vtx} bins the efficiency to detect particles at the border of the η-acceptance is reduced because parts of the track can be outside of the detector. Additionally the number of collisions is lower at these large z_{vtx} bins compared to the nominal collision point. A maximum distance from the nominal interaction point is defined in which the events are accepted. For the analysis in this thesis it is $|z_{vtx}| < 8\,\text{cm}$.

4.4. Event Selection

ALICE records only events which fulfill a trigger condition. These can be a minimum bias trigger or an advanced trigger condition. For the minimum bias trigger it is checked if a collision between the accelerated particles took place. This includes a rejection of beam-gas interactions. The detection of these events was described in Section 4.1. Additionally to the minimum bias trigger the centrality triggers are used in this thesis.
For the analysis the runs from the LHC 11h dataset are used. This selection bases on the general Quality Assurance (QA) which is used within ALICE. From the 176 runs with interactions in the detector, 107 are selected as good runs. Each of these runs contains between $1.3{\cdot}10^5$ and $4.4{\cdot}10^6$ reconstructed events. By selecting only the events which fulfill the above explained triggers $48.1 \cdot 10^6$ events are used for the analysis of Pb–Pb collisions in this thesis.
In a second event selection only events are accepted which fulfill the centrality and z_{vtx} cuts. For the analysis the centralities 0–7.5% and 30–50% are used and the z_{vtx} has to be less than 8 cm away from the nominal interaction point. This reduces the number of events to $16.6 \cdot 10^6$ events for the 0–7.5% most central events and $8.2 \cdot 10^6$ events for

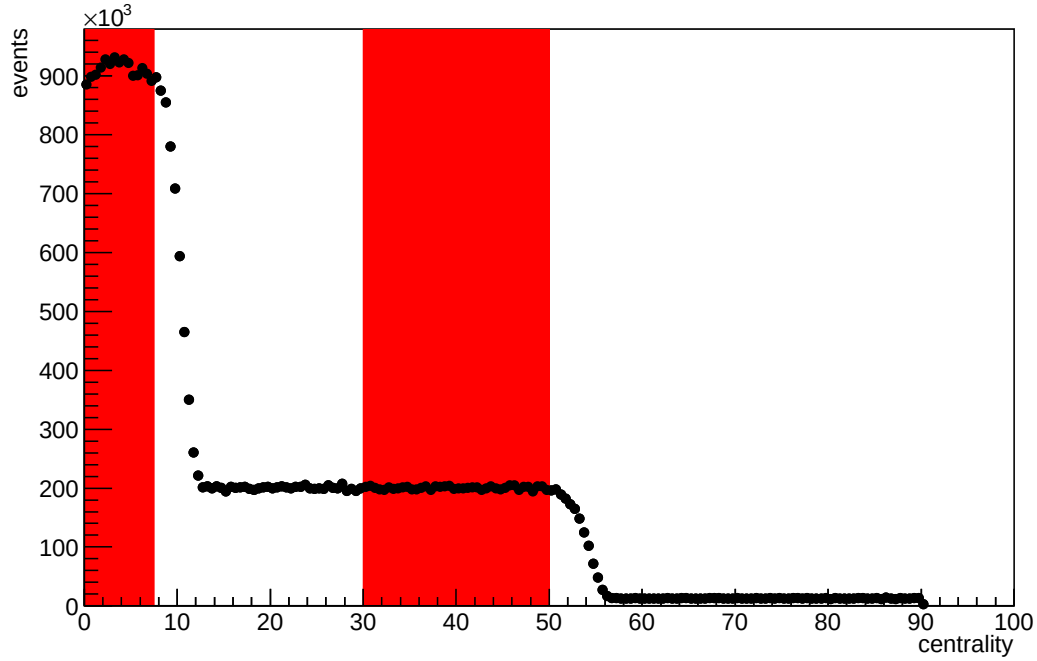

Figure 4.5.: Events which passed the QA and event selection. The areas which are marked with the red boxes are used in the analysis of this thesis.

the 30–50% most central events.
The amount of accepted events per centrality bin is shown in Figure 4.5. For the analysis the centrality ranges marked with the red boxes are used. The increased amount of events at the most central events are created by the centrality triggers for events with centralities $> 7.5\%$ and $> 50\%$.

4.5. Track Selection

ALICE measures at $\sqrt{s_{NN}} = 2.76\,\text{TeV}$ and mid-rapidity an average charged particle multiplicity of $dN_{ch}/d\eta = 1600$ for the 0–5% most central events [ALI11c]. These particles are mainly tracked with the ITS and the TPC, but the TRD and TOF (see Sections 3.2.1) are included in the tracking if a measurement in these detectors is available. This thesis analyzes the tracks obtained with these detectors from the central barrel.
The track reconstruction is done independently from the track cuts. Afterwards all tracks are analyzed and only the ones which fulfill the track cuts are accepted for the analysis. To understand some of the cuts, it is essential to understand the track reconstruction [ALI14].
The ITS and the TPC both read out the signals from their detector cells (for example pads for the TPC). In the SPD (first layers of the ITS) the signal is digital while the

signal in the other detectors is analog. Multiple signals from neighboring detector cells in the same time bin or multiple signals in the same detector cell in consecutive time bins are called a cluster. A track is the estimated trajectory of a particle through these clusters. To identify the clusters which are created by the same particle in different detectors, a fit of the clusters together with the primary interaction vertex is started at large radii of the TPC. In an iterative process more clusters are added to the track at smaller radii. If no more clusters in the TPC can be added to the track, this is extended to the ITS. After all clusters in the ITS have been either rejected or added to the track, it is again extrapolated to the point of closest approach to the primary interaction vertex. From there the track is propagated outwards again. In the ITS and the TPC the tracks are refitted with the clusters found in the previous stage. Further outside the tracks are matched with the measurements from the TRD and the TOF.
In the fit procedure several other fit parameter are determined which can be used for the track cuts. The track cuts are used to reject tracks from other sources than primary particles from the collision and to ensure a good track quality. For the analysis of Pb–Pb collisions in this thesis two different kind of track cuts are used. They are the so-called 'hybrid' and the 'global' track cuts. The first one is used as default track cut while the second one is used to estimate the systematic uncertainty of the analysis. The detailed cuts are shown in Table 4.1.
For all clusters of a track the χ^2 can be defined which determines the quality of the track fit with respect to each cluster. Each cluster has two degrees of freedom (ndf). On the average χ^2 over all clusters of a track, a cut is applied. The average χ^2 has to be smaller than 36 for the ITS clusters and smaller than 4 for the TPC clusters. For the ITS value this means that only outliers are cut out. The constraint on the TPC clusters is equal to $\chi^2/ndf < 2$ which ensures the high track quality. For the track fit a minimum number of 70 crossed pad rows out of 159 is required in the TPC. Additionally the ratio of found clusters per crossed pad row has to be bigger than 0.8. The number of crossed pad rows is determined out of the fit.
For the hybrid track cuts up to 40% of the TPC clusters are allowed to be shared by multiple tracks. In other words this means that minimum 60% of the clusters of a track have to be associated to this track only. This requirement does not exist for the global track cuts.
For the vertex extrapolation a measurement (=hit) in the innermost layers of the ITS, the SPD, is helpful. Due to the non-uniform efficiency of the ITS this introduces a non-uniform particle measurement dependent on φ. The global track cuts require either a hit in the SPD or in the first layer of the SDD. For the hybrid track cuts two categories (bins) have been created. The first one requires a hit in the SPD and the second one does not require any hit in the ITS but it excludes all tracks which have been accepted in the first bin. In case of the second bin the vertex position is added as point to the track improve the momentum resolution. Due to the ITS refit requirement, additional hits in the ITS are required implicitly.
Another criteria for the track selection is a kink in the track. Such a kink can be produces by a particle scattering or a particle decay. After the direction change, the particle no longer represents the properties generated in the collision. Thus the track

track cut	hybrid track cuts		global track cuts
	first bin	second bin	
TPC refit	required	required	required
ITS refit	required	required	required
χ^2 per ITS cluster	< 36	< 36	< 36
χ^2 per TPC cluster	< 4	< 4	< 4
minimum crossed pad rows in the TPC	70	70	70
minimum crossed pad rows over all possible clusters in the TPC	>0.8	>0.8	>0.8
maximum shared TPC clusters	0.4	0.4	1
ITS hits	1 hit in SPD	not required	1 hit in SPD or in the first SDD layer
vertex point is included in track reconstruction	no	yes	no
kink daughters	rejected	rejected	rejected
DCA longitudinal to the vertex	$< 3.2\,\mathrm{cm}$	$< 3.2\,\mathrm{cm}$	$< 2\,\mathrm{cm}$
DCA transversal to the vertex	$< 2.4\,\mathrm{cm}$	$< 2.4\,\mathrm{cm}$	$< 0.0105\,\mathrm{cm}$ $+0.0350\,\mathrm{cm} \cdot p_T^{-1.1}$
special	-	not accepted in first bin	-

Table 4.1.: Track cuts for the 'hybrid' and 'global' track cuts.

after the kink, which is called the daughter, is not used in the analysis.
Particles from secondary vertices can be further sorted out by requiring the Distance of Closest Approach (DCA) between the track and the primary vertex position to be below a certain threshold. The hybrid track cuts use a constant cut of 3.2 cm for the longitudinal (z) and 2.4 cm for the transversal (xy) DCA. The cuts for the global track cuts are tighter because the required hit in the SPD or the first layer of the SDD improves the quality of the fit close to the vertex and thus the measurement of the DCA. In the longitudinal direction a constant cut of 2 cm is applied, while in the transversal direction it is dependent on the track momentum. The DCA has to be below $0.0105\,\mathrm{cm} + 0.0350\,\mathrm{cm} \cdot p_T^{-1.1}$ [ALI06].
Tracks fulfilling the global track cuts have a good track quality and a non-uniform φ distribution. The tracks obtained with the hybrid track cuts have a uniform φ distribution, at the price of a mixed track quality. The transverse momentum resolution of both track cuts are comparable up to $\approx 10\,\mathrm{GeV}/c$. Afterwards the hybrid track cuts are significantly worse. Both track cuts are standard cuts used within the ALICE collaboration. More details can be found in Ref. [ALI15e].

Additionally to the so far mentioned track cuts for this thesis all tracks have to be fully contained in the TPC which limits the pseudo-rapidity to $|\eta| < 0.9$.
The analysis of pp events was done with a modified version of the hybrid track cuts. Additionally to the particles which fulfill the here mentioned hybrid track cuts, TPC stand alone tracks were accepted. For these additional tracks the ITS refit was not done and the tracks were estimated from TPC clusters only.

5. Two Particle Correlations

Two particle angular correlations [1] can be used to characterize jet and collective effects. In 1+1 correlations a trigger particle is used as a proxy to find jets. All other particles in the event are analyzed relative to this trigger particle. By doing this for many events, the sample averaged properties (yields) of associated particles can be investigated. With this method jets can be analyzed at lower energies compared to the analysis with jet finders.
In this chapter the correlation method is explained in detail. The measurement of the 1+1 yield is identical for different z-vertex cuts z_{vtx} and centralities C. For simplicity reasons the calculations are presented independent of these variables.
For the development of the measurement method a toy event generator was used. This toy generator is explained in Section 5.1 and afterwards it is used to illustrate the 1+1 correlations which are explained in the following sections.
In the Sections 5.2 and 5.3 the measurement of the correlated yield and the correction of efficiency and acceptance effects are described. An additional single particle efficiency correction is presented afterwards in Section 5.4. This is followed by the background correction in Section 5.5. The last two Sections 5.6 and 5.7 explain two methods by which the correlated yield is measured. The first one is the standard method which is used in this thesis and the second one is used for the estimation of the systematic uncertainty.

5.1. Toy Event Generator

The toy event generator was developed to investigate the different contributions in the 2+1[2] associated particle yield. It is used as well to illustrate the 1+1 correlations. The generated events from the toy generator are analyzed using the correlation method. By changing the composition of the initial events, different yield contributions can be analyzed. Because in the events from the toy generator the signal can be definitely distinguished from the background, this can be compared to the obtained signal after using the correlation techniques and the background subtraction.
In the toy generator events are generated with simplified particles. They are defined by a transverse momentum p_T, a pseudo-rapidity η and an azimuthal angle φ.
The event generation is divided into several parts. First the number of mini-jets is defined. This number can be random or the same for every event. For the illustrations

[1] In the following they are denoted by 1+1 correlations (see Section 2.7).
[2] The 2+1 correlations method was introduced in Section 2.8. It will be explained in more detail in Chapter 6.

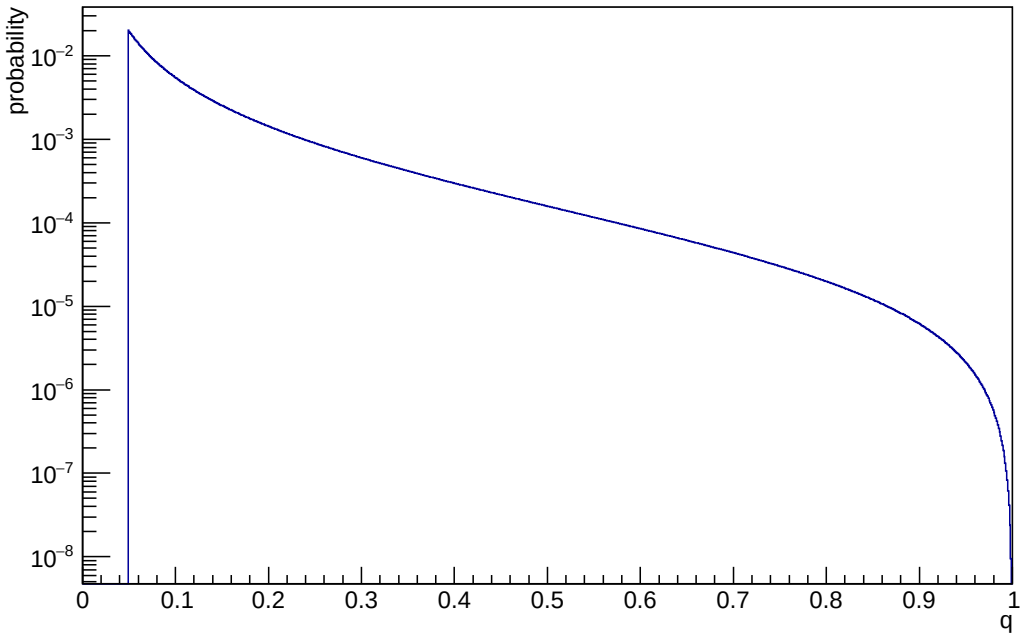

Figure 5.1.: KKP jet fragmentation function [KKP00] used in the toy event generator. On the x-axis the relative transverse momentum of a jet particle compared to the jet momentum is shown. The used KKP fragmentation function is split into several jet momentum bins from 0 to 120 GeV. For each jet momentum bin it is normalized to one. Here the average over all these jet momentum bins is shown.

in this chapter five mini-jets have been used. By increasing this number, the background for the analysis is increased. Each mini-jet has a transverse momentum which is determined randomly from a jet transverse momentum spectrum. This function is defined in the range between 5 and 120 GeV and it follows the power law $f(p_T) = p_T^{-5.1}$. The jet-axis is placed at random φ and η. The position of η can be outside of the defined detector acceptance. Each jet has an away side jet which is back-to-back in φ. The η variable of the away side jet is also random. One or even both jets of a di-jet can be outside of the acceptance.
Both jets can either have the same transverse momentum or the away side jet has half the transverse momentum of the near side jet. This simulates a quenching effect. For the quenched jet the lost energy is not redistributed to other particles in the event.
Each jet is fragmented into several particles with the KKP fragmentation function which is shown in Figure 5.1. This fragmentation function has been fitted to hadron distributions measured in e^+e^- annihilations. A random number q is generated following this distribution and this number is multiplied with the jet transverse momentum. The result is the particle transverse momentum. Due to the minimum $q = 0.05$, the minimum transverse momentum of a particle is 5% of the jet transverse momentum.

The procedure to determine the transverse momentum of the next particle is repeated until the momenta of all particles add up to the jet transverse momentum. During each random number generation the maximum possible q is the q which would create a new particle transverse momentum equal to the jet transverse momentum minus all already created particle transverse momenta. If this is less than 5%, one last particle is created which contains the left over transverse momentum. A more detailed description of the fragmentation function can be found in Ref. [KKP00].
Each particle in the jet gets an azimuthal angle φ and a pseudo-rapidity η. Independent of each other, the values are determined randomly from a Gaussian function which is centered around the jet axis. The width of the Gaussian is equal to the jet radius. It is identical for both variables and it can be changed in the simulation. A typical radius in the simulation is 0.3. In real events the angle is smaller for particles with a high q. This effect is neglected in these simulations.
All mini-jets are simulated independent of each other. To guarantee enough events for the analysis afterwards, at this point the particles are checked if at least one of them has the required trigger momentum. If all particles have a smaller transverse momentum, the event is discarded. This does not bias the particle correlation analysis because events which do not contain a trigger are not included in the analysis. The mixed events would be biased with this dataset. So a special dataset was created without this bias. This optimization makes it possible to run the analysis on a standard computer.
Additionally to the jet particles uncorrelated background particles can be introduced to the event. These particles are following a flat φ and η distribution in the event.
It is possible to modulate all particles in the event with elliptic flow. The flow feature can be deactivated which makes it possible to identify the influence of the flow on the correlation yield. With the activated flow the particles in an event are shifted towards $\cos[2(\varphi - \Psi)]$. The angle of the flow reaction plane Ψ is determined randomly with no preference in any direction. The flow does not influence the direction of the jets. But the Gaussian distribution of the particles in the jet is modulated with the flow function.

5.2. Correlations within the Same Event

In the 1+1 correlations particles within a certain transverse momentum range $p_{\mathrm{T,trig}}$ are defined as trigger particles. In every event all particles which have the trigger momentum are identified. If at least one trigger particle was found in an event, all particles in that event with a transverse momentum $p_{\mathrm{T,assoc}}$ are filled into a histogram. These particles are called the associated particles. The angular difference $\Delta\varphi$ and $\Delta\eta$ between the trigger and the associated particles are filled into a histogram.
For a better readability the integration of the differential particle yield over the trigger and associated transverse momentum range is not written in the formulas. The

integration is denoted with brackets around the transverse momentum variable.

$$N([p_T]) = \int_{p_{T,min}}^{p_{T,max}} \frac{dN(p_T)}{dp_T} dp_T \tag{5.1}$$

The number of trigger particles N_{trig} in the 1+1 correlations analysis is the sum of all found trigger particles within the transverse momentum bin $p_{\mathrm{T,trig}}$.

$$N_{trig}(p_{\mathrm{T,trig}}) = \int_0^{2\pi} d\varphi \int_{-\eta_{max}}^{\eta_{max}} d\eta \; \epsilon(p_{\mathrm{T,trig}}, \varphi, \eta) \frac{d^2N}{d\varphi d\eta}([p_{\mathrm{T,trig}}], \varphi, \eta) \tag{5.2}$$

The measured number of trigger particles is lower than the true number because of the limited detector efficiency and the limited detector acceptance. These effects are combined in the detector effects $\epsilon(p_{\mathrm{T,trig}}, \varphi, \eta)$. The single particle efficiency, which is dependent on p_T, is corrected before the integration over p_T is executed. This correction is more precise in p_T than the $p_{\mathrm{T,trig}}$ and $p_{\mathrm{T,assoc}}$ binning which is mentioned in the rest of this chapter.
The particle correlations are described with the following definition of the angular differences and angular sums. These variables are based on the angular positions of the trigger (φ_1, η_1) and the associated particle (φ_2, η_2).

$$\begin{aligned} \Delta\varphi &= \varphi_1 - \varphi_2 \\ \Delta\eta &= \eta_1 - \eta_2 \\ \varphi_0 &= \varphi_1 + \varphi_2 \\ \eta_0 &= \eta_1 + \eta_2 \end{aligned} \tag{5.3}$$

The particle correlations are measured in the same event yield $\frac{d^2N^{same}}{d\Delta\varphi d\Delta\eta}$ which depends on the angular differences $\Delta\varphi$ and $\Delta\eta$. This yield includes the particle pair distribution $\frac{d^4N}{d\varphi_1 d\eta_1 d\varphi_2 d\eta_2}$ and the detector effects ϵ which are dependent on the particle positions φ_1, η_1,φ_2, η_2. In the correlation measurement the particle pair distribution should be extracted. The procedure is explained in this chapter.
In the same event yield in Equation 5.4 the integration of the particle pair distribution is indicated with the bracket syntax from Equation 5.1.

$$\begin{aligned} &\frac{d^2N^{same}}{d\Delta\varphi d\Delta\eta}(p_{\mathrm{T,trig}}, p_{\mathrm{T,assoc}}, \Delta\varphi, \Delta\eta) \\ &= \int_0^{2\pi} d\varphi_1 \int_{-\eta_{max}}^{\eta_{max}} d\eta_1 \; \epsilon(p_{\mathrm{T,trig}}, \varphi_1, \eta_1) \\ &\cdot \int_0^{2\pi} d\varphi_2 \int_{-\eta_{max}}^{\eta_{max}} d\eta_2 \; \epsilon(p_{\mathrm{T,assoc}}, \varphi_2, \eta_2) \frac{d^4N_{assoc,same}}{d\varphi_1 d\eta_1 d\varphi_2 d\eta_2}([p_{\mathrm{T,trig}}], [p_{\mathrm{T,assoc}}], \varphi_1, \eta_1, \varphi_2, \eta_2) \\ &\cdot \delta(\Delta\varphi - (\varphi_1 - \varphi_2)) \; \delta(\Delta\eta - (\eta_1 - \eta_2)) \end{aligned} \tag{5.4}$$

In the same event yield the particle pair distribution can be rewritten to depend on the angular sums (φ_0 and η_0) and angular differences ($\Delta\varphi$ and $\Delta\eta$). The angular sums

describe the position of a particle pair in the detector and the angular difference the relative position of the particles to each other. The same event yield is independent of φ_0 because the physics is invariant in all azimuthal directions of the detector. For the pseudo-rapidity η_0 no dependence is assumed which is a decent approximation at mid-rapidity[3]. Consequently the dependence of the same event yield on the angular sums is neglected. After the integration over the δ functions, the particle distributions are not dependent on the remaining integrals. Thus they can be put in front of the integrals. Within the integration the detector effects ϵ remain.

$$
\begin{aligned}
&\frac{d^2N^{same}}{d\Delta\varphi d\Delta\eta}(p_{\mathrm{T,trig}}, p_{\mathrm{T,assoc}}, \Delta\varphi, \Delta\eta) \\
=&\int_0^{2\pi} d\varphi_1 \int_{-\eta_{max}}^{\eta_{max}} d\eta_1 \; \epsilon(p_{\mathrm{T,trig}}, \varphi_1, \eta_1)\epsilon(p_{\mathrm{T,assoc}}, \varphi_1 - \Delta\varphi, \eta_1 - \Delta\eta) \\
&\cdot \frac{d^2N_{assoc,same}}{d\Delta\varphi d\Delta\eta}([p_{\mathrm{T,trig}}], [p_{\mathrm{T,assoc}}], \Delta\varphi, \Delta\eta) \\
=&\frac{d^2N_{assoc,same}}{d\Delta\varphi d\Delta\eta}([p_{\mathrm{T,trig}}], [p_{\mathrm{T,assoc}}], \Delta\varphi, \Delta\eta) \\
&\cdot \int_0^{2\pi} d\varphi_1 \int_{-\eta_{max}}^{\eta_{max}} d\eta_1 \; \epsilon(p_{\mathrm{T,trig}}, \varphi_1, \eta_1)\epsilon(p_{\mathrm{T,assoc}}, \varphi_1 - \Delta\varphi, \eta_1 - \Delta\eta) \\
=&\frac{d^2N_{assoc,same}}{d\Delta\varphi d\Delta\eta}([p_{\mathrm{T,trig}}], [p_{\mathrm{T,assoc}}], \Delta\varphi, \Delta\eta)(\epsilon(p_{\mathrm{T,trig}}) * \epsilon(p_{\mathrm{T,assoc}}))\,(\Delta\varphi, \Delta\eta)
\end{aligned}
\tag{5.5}
$$

The Equation 5.5 rewrites the φ and η integration over the detector effects as convolution over the variables $\Delta\varphi$ and $\Delta\eta$.
The description of the same event yield with detector effects in Equation 5.5 can only be further simplified with an explicit function for the detector effect. In ALICE the biggest effect in ϵ is the limited detector acceptance. The convolution of two constant distributions within a limited range (describing the detector acceptance) is a triangle in $\Delta\eta$. An example is given in the following, assuming that there is no effect dependent on p_{T}, and φ.

$$
\epsilon(\eta) = \begin{cases} A & \text{for } |\eta| < \eta_{max} \\ 0 & \text{for } |\eta| > \eta_{max} \end{cases} \tag{5.6}
$$

Within the acceptance of the detector $|\eta| < \eta_{max}$ the efficiency is constant and equal to A. With this the yield in Equation 5.5 can be integrated.

[3]The pseudo-rapidity η of a jet with a small transverse momentum $p_{\mathrm{T,jet}}$ compared to the collision energy $\sqrt{s_{NN}}$ is strongly influenced by the initial momenta of the scattering partons. The system of two scattering partons moves as a whole which shifts the η position of the resulting jets. This shift is different for every jet. The resulting η distribution of the jets is flat at mid-rapidity. Any correlated effect of the jet with the η position in the detector is lost and a jet can be found at any η. So the probability of finding a correlated particle pair is constant for every η_0 as well.

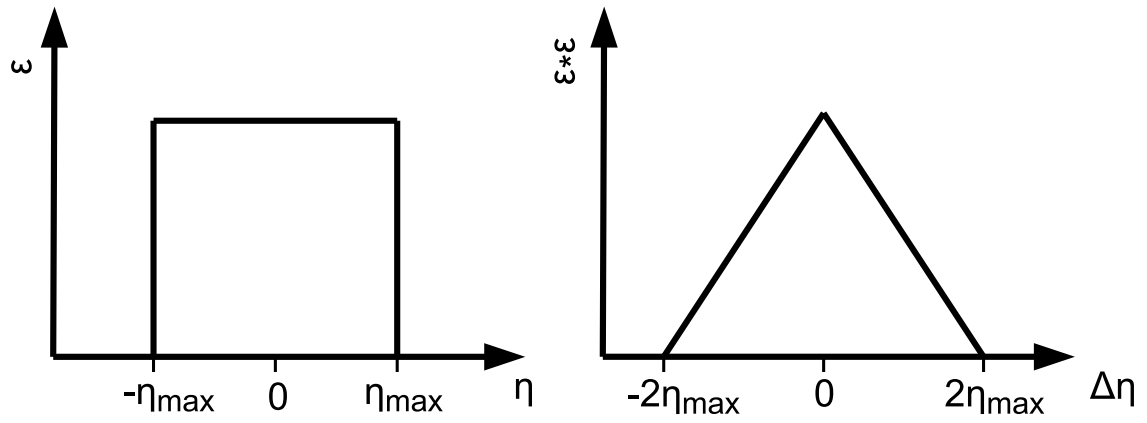

Figure 5.2.: On the left side the limited η range is shown. Only in the area with high efficiency can a particle be detected. On the right side the probability of finding a trigger-associated particle pair is shown. This is equal to the convolution of two efficiency functions from the left side. For small $\Delta\eta$ the probability of finding a particle pair is maximal.

$$
\begin{aligned}
\frac{d^2N^{same}}{d\Delta\varphi d\Delta\eta}(\Delta\eta) &= \frac{d^2N_{assoc,same}}{d\Delta\varphi d\Delta\eta}(\Delta\eta)\int_{-\eta_{max}}^{\eta_{max}} d\eta_1 \epsilon(\eta_1)\epsilon(\eta_1-\Delta\eta) \\
&= \frac{d^2N_{assoc,same}}{d\Delta\varphi d\Delta\eta}(\Delta\eta)\begin{cases}\int_{-\eta_{max}}^{\Delta\eta+\eta_{max}} A\cdot A\; d\eta_1 & \text{for} \quad -2\eta_{max}<\Delta\eta<0 \\ \int_{\Delta\eta-\eta_{max}}^{\eta_{max}} A\cdot A\; d\eta_1 & \text{for} \quad 0<\Delta\eta<2\eta_{max}\end{cases} \\
&= \frac{d^2N_{assoc,same}}{d\Delta\varphi d\Delta\eta}(\Delta\eta)\begin{cases}A^2(2\eta_{max}+\Delta\eta) & \text{for} \quad -2\eta_{max}<\Delta\eta<0 \\ A^2(2\eta_{max}-\Delta\eta) & \text{for} \quad 0<\Delta\eta<2\eta_{max}\end{cases} \\
&= \frac{d^2N_{assoc,same}}{d\Delta\varphi d\Delta\eta}(\Delta\eta)A^2(2\eta_{max}-|\Delta\eta|) \qquad (5.7)
\end{aligned}
$$

The calculation shows the convolution of the flat efficiency within a limited range. The result has the expected triangular shape in $\Delta\eta$. In Figure 5.2 the limited η range from Equation 5.6 is shown on the left side. On the right side the probability of finding a trigger-associated particle pair in arbitrary units is shown. This is a pure effect from the acceptance of the detector. Additional effects containing physics information like the correlated yield would be multiplicative on top of this signature.
An example of the same event yield is shown in Figure 5.3 in the left panel. The triangular shape of the yield in $\Delta\eta$ dominates the yield. Additional minor detector effects depend on the angle φ, the trigger momentum $p_{\mathrm{T,trig}}$ and associated momentum $p_{\mathrm{T,assoc}}$. The area at $|\Delta\varphi| < \pi/2$ is called the near side, the area at $|\Delta\varphi| > \pi/2$ is called the away side. On the near side around $\Delta\varphi = \Delta\eta = 0$ a peak is visible which is created by particles from the same jet as the trigger particle.
These effects can be corrected by the mixed event correction which is described in Section 5.3.

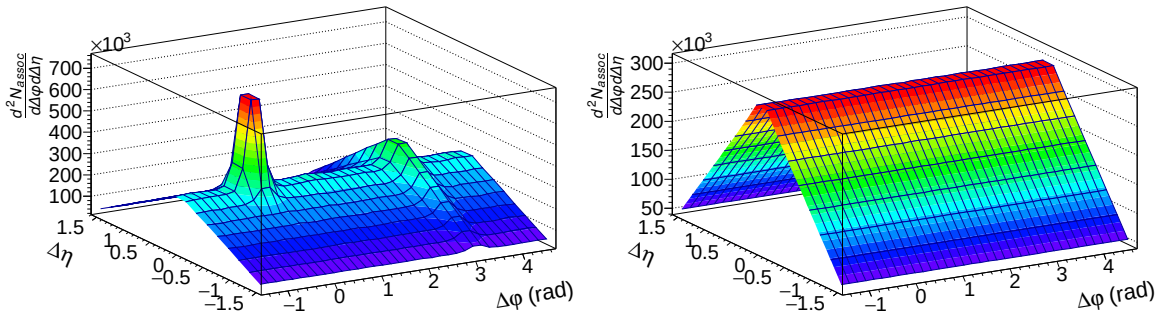

Figure 5.3.: Schematic plot for the same event (left panel) and the mixed event (right panel) yield. The events used to calculate this yield were produced with the toy event generator.

In this thesis all charged particles are used for the correlations. The analysis can be extended to use identified particles for the correlations.

5.3. Correlations within the Mixed Event

The mixed event is used to extract the $\frac{d^2N_{assoc,same}}{d\Delta\varphi d\Delta\eta}$ yield from the same event yield. This means the same event yield is corrected for the pair acceptance and efficiency effects. The mixed event is created by taking the trigger particle and the associated particles from different events. Apart from this, the mixed and same event measurements are created via the same procedure.
The events used for the mixing have the same centrality C and z-vertex z_{vtx}. Of course the trigger momentum $p_{\mathrm{T,trig}}$ and the associated momentum $p_{\mathrm{T,assoc}}$ are kept identical to the ones in the same event analysis. This means that the $\Delta\varphi$-$\Delta\eta$ distribution of uncorrelated particle pairs with $p_{\mathrm{T,trig}}$, $p_{\mathrm{T,assoc}}$ is identical to the distribution in the same event. But correlated particle pairs are not measured in the mixed event.
The probability of finding a trigger or associated particle in the mixed event analysis $\frac{d^2N}{d\varphi_1 d\eta_1}([p_{\mathrm{T}}])$ is independent of the probability of finding the other particle. Averaged over many events it is not dependent on the angular positions φ and η. The δ functions are used again to project the yield on $\Delta\varphi$ and $\Delta\eta$.

$$
\begin{aligned}
&\frac{d^2N^{mixed}}{d\Delta\varphi d\Delta\eta}(p_{\mathrm{T,trig}}, p_{\mathrm{T,assoc}}, \Delta\varphi, \Delta\eta) \\
&\quad = \int_0^{2\pi} d\varphi_1 \int_{-\eta_{max}}^{\eta_{max}} d\eta_1 \; \epsilon(p_{\mathrm{T,trig}}, \varphi_1, \eta_1) \frac{d^2N}{d\varphi_1 d\eta_1}([p_{\mathrm{T,trig}}]) \\
&\quad\quad \cdot \int_0^{2\pi} d\varphi_2 \int_{-\eta_{max}}^{\eta_{max}} d\eta_2 \; \epsilon(p_{\mathrm{T,assoc}}, \varphi_2, \eta_2) \frac{d^2N}{d\varphi_2 d\eta_2}([p_{\mathrm{T,assoc}}]) \\
&\quad\quad \cdot \delta(\Delta\varphi - (\varphi_1 - \varphi_2)) \; \delta(\Delta\eta - (\eta_1 - \eta_2))
\end{aligned}
$$

$$
\begin{aligned}
=&\frac{d^2N}{d\varphi_1 d\eta_1}([p_{\mathrm{T,trig}}])\frac{d^2N}{d\varphi_2 d\eta_2}([p_{\mathrm{T,assoc}}]) \\
&\cdot\int_0^{2\pi} d\varphi_1 \int_{-\eta_{max}}^{\eta_{max}} d\eta_1\ \epsilon(p_{\mathrm{T,trig}},\varphi_1,\eta_1)\epsilon(p_{\mathrm{T,assoc}},\varphi_1-\Delta\varphi,\eta_1-\Delta\eta) \\
=&\frac{d^2N}{d\varphi_1 d\eta_1}([p_{\mathrm{T,trig}}])\frac{d^2N}{d\varphi_2 d\eta_2}([p_{\mathrm{T,assoc}}])(\epsilon(p_{\mathrm{T,trig}})*\epsilon(p_{\mathrm{T,assoc}}))\,(\Delta\varphi,\Delta\eta) \qquad (5.8)
\end{aligned}
$$

The difference between the same event in Equation 5.5 and the mixed event in Equation 5.8 is the correlated yield $\frac{d^2N_{assoc,same}}{d\Delta\varphi d\Delta\eta}(p_{\mathrm{T,trig}},p_{\mathrm{T,assoc}},\Delta\varphi,\Delta\eta)$. In the mixed events it consists only of random combinations which is the background of the same event. The dependency of the mixed event yield on the angular differences $\Delta\varphi$ and $\Delta\eta$ is fully contained in the detector effects ϵ.
To obtain the associated particles in the mixed event analysis any event combination can be used. This means if N events are measured, $N\cdot(N-1)/2$ event combinations can be analyzed for the mixed events which is much larger than the N events analyzed in the same event analysis. This makes it possible to increase the statistics so that the statistical uncertainty is significantly below the uncertainty of the same event. The obtained yield from multiple considered events for the associated particles has to be divided by the number of events which were used for the mixing. This way the associated particles of each trigger represent the particles from one event.
The mixed event analysis is normalized with the factor $\alpha(p_{\mathrm{T,trig}},p_{\mathrm{T,assoc}})$ so that the mixed event yield is unity, $\frac{d^2N^{mixed}}{d\Delta\varphi d\Delta\eta}(p_{\mathrm{T,trig}},p_{\mathrm{T,assoc}},0,0)=1$. At $\Delta\varphi=\Delta\eta=0$ the $\Delta\varphi$ and $\Delta\eta$ dependent acceptance is one by definition. Further efficiency effects dependent on the different p_T between trigger and associated particle are neglected. With the normalization of the mixed event the integral over the detector effects is normalized to one.

$$
\alpha(p_{\mathrm{T,trig}},p_{\mathrm{T,assoc}})=\left(\frac{d^2N}{d\varphi_1 d\eta_1}([p_{\mathrm{T,trig}}])\frac{d^2N}{d\varphi_2 d\eta_2}([p_{\mathrm{T,assoc}}])\right)^{-1} \qquad (5.9)
$$

Because of a limited resolution of the $\Delta\eta$ bins a bin width correction has to be applied. This correction assumes that the yield at $\Delta\eta=0$ has to be 1 and not over the full bin width $b_{\Delta\eta}$ close to $\Delta\eta=0$. The correction factor is the finite bin correction fbc.

$$
fbc=1-\frac{1}{2\cdot\eta_{max}}\cdot\frac{b_{\Delta\eta}}{2} \qquad (5.10)
$$

Here η_{max} means the cut which is applied on the tracks in η. The maximum possible $\Delta\eta$ correlation value is $\Delta\eta_{max}=2\cdot\eta_{max}$. The first ratio represents the slope of the triangle from 1 at $\Delta\eta=0$ to 0 at $\Delta\eta=2\cdot\eta_{max}$. The second ratio is the half bin width which is the distance the middle of the bin is away from $\Delta\eta=0$. The product is subtracted from 1 to get the nominal value at the bin center closest to $\Delta\eta=0$. The mixed yield is assumed to be flat in $\Delta\varphi$ around $\Delta\varphi=0$ so that no further correction has to be applied there.
The associated particle yield corrected for detector effects can be obtained by dividing

Equation 5.5 by 5.8 and scaling with the α factor.

$$\frac{\frac{d^2N^{same}}{d\Delta\varphi d\Delta\eta}(p_{\mathrm{T,trig}}, p_{\mathrm{T,assoc}}, \Delta\varphi, \Delta\eta)}{\frac{d^2N^{mixed}}{d\Delta\varphi d\Delta\eta}(p_{\mathrm{T,trig}}, p_{\mathrm{T,assoc}}, \Delta\varphi, \Delta\eta)} \cdot \frac{1}{\alpha(p_{\mathrm{T,trig}}, p_{\mathrm{T,assoc}})} \tag{5.11}$$

$$\begin{aligned}
=&\frac{\frac{d^2N_{assoc,same}}{d\Delta\varphi d\Delta\eta}([p_{\mathrm{T,trig}}], [p_{\mathrm{T,assoc}}], \Delta\varphi, \Delta\eta)}{\frac{d^2N}{d\varphi_1 d\eta_1}([p_{\mathrm{T,trig}}])\frac{d^2N}{d\varphi_2 d\eta_2}([p_{\mathrm{T,assoc}}])} \\
&\cdot \frac{(\epsilon(p_{\mathrm{T,trig}}) * \epsilon(p_{\mathrm{T,assoc}}))\,(\Delta\varphi, \Delta\eta)}{(\epsilon(p_{\mathrm{T,trig}}) * \epsilon(p_{\mathrm{T,assoc}}))\,(\Delta\varphi, \Delta\eta)} \cdot \frac{d^2N}{d\varphi_1 d\eta_1}([p_{\mathrm{T,trig}}])\frac{d^2N}{d\varphi_2 d\eta_2}([p_{\mathrm{T,assoc}}]) \\
=&\frac{d^2N_{assoc,same}}{d\Delta\varphi d\Delta\eta}([p_{\mathrm{T,trig}}], [p_{\mathrm{T,assoc}}], \Delta\varphi, \Delta\eta)
\end{aligned} \tag{5.12}$$

The convolutions in the numerator and denominator are identical. This means that the results of the convoluted detector effects cancel out. The $\alpha(p_{\mathrm{T,trig}}, p_{\mathrm{T,assoc}})$ factor is adjusted so that it cancels out the particle yield from the mixed event. This leaves the associated particle yield from the same event $\frac{d^2N_{assoc,same}}{d\Delta\varphi d\Delta\eta}([p_{\mathrm{T,trig}}], [p_{\mathrm{T,assoc}}], \Delta\varphi, \Delta\eta)$. This can be divided by the number of triggers from Equation 5.2 to obtain the associated yield per trigger particle.

$$\frac{1}{N_{trig}(p_{\mathrm{T,trig}})}\frac{d^2N_{assoc,same}}{d\Delta\varphi d\Delta\eta}([p_{\mathrm{T,trig}}], [p_{\mathrm{T,assoc}}], \Delta\varphi, \Delta\eta) \tag{5.13}$$

An example for the mixed event is shown in Figure 5.3 in the right panel. The triangle which can also be seen in the same event yield in the left panel is well reproduced. By applying the mixed event correction the associated per trigger yield is obtained and shown in Figure 5.4.
The important remark about this method is that it only works if the measured particle correlations are independent of the position in the detector. This is assumed in all calculations by projecting the yield on the $\Delta\varphi$ and $\Delta\eta$ variables.
The associated per trigger particle yield has several contributions from different sources (jet, flow, combinatorics). They are discussed in Section 5.5.

5.4. Single Particle Efficiency Correction

The detector effects ϵ contain the single particle efficiency and acceptance effects. Two particle acceptance effects are created by the correlation of two particles which has been described in the last sections. These effects are corrected in the mixed event method.
The probability of detecting an associated particle at the position of the trigger particle is ϵ. This is a single particle efficiency because the measurement of the trigger particle proofs that particles can be detected at this angular position.
Every real detector has a finite efficiency. This can be due to a limited phase space coverage by the detector because of the support frame, cables, holes in the detector

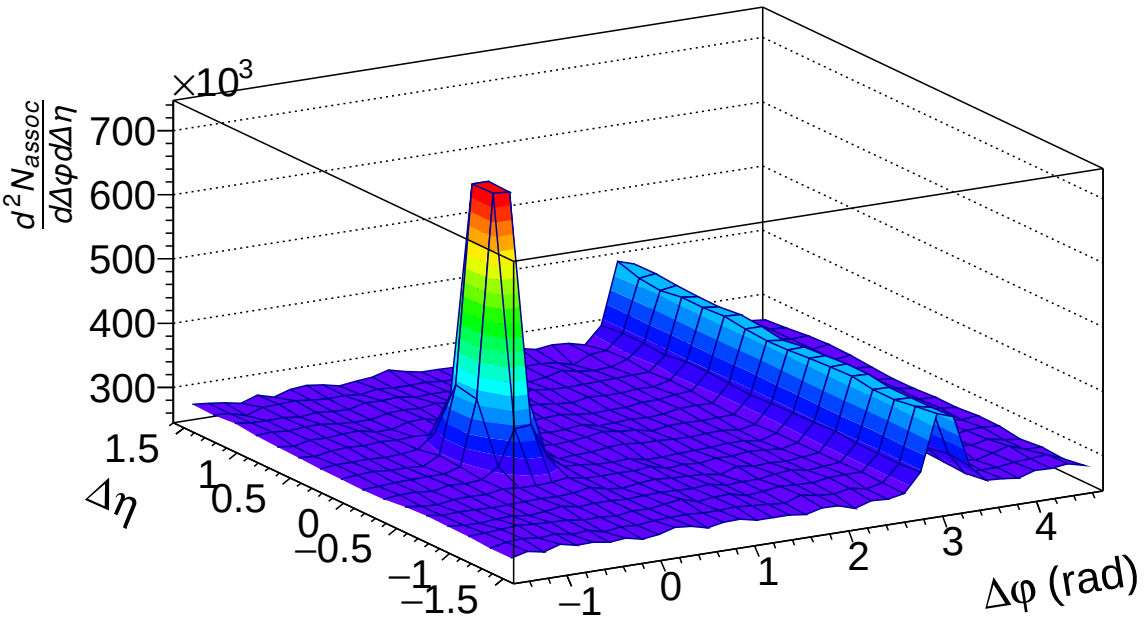

Figure 5.4.: The associated particle yield. This is obtained by divided by the same event yield by the mixed event yield which are both shown in Figure 5.3. This way the limited acceptance of ALICE is corrected.

or broken channels. Some particles might not have enough energy to reach the detector. Independent of the reason, the detection efficiency can be corrected by scaling each detected particle with the inverse single-particle efficiency. This efficiency is the probability of measuring a particle with a certain transverse momentum at a defined position in the detector. It is determined in MC simulations. For each dataset measured with ALICE a correspondent MC simulation exists which allows the extraction of the single-particle efficiency. The efficiency is determined dependent on the angle η, the particle momentum p_{T}, the centrality C and the z-vertex z_{vtx}.
The single particle efficiency correction is applied on the particle level for every correlation measurement. Each measured particle is immediately multiplied by its inverse single-particle efficiency. This way the measured particle distribution is independent of the position in the detector.
In case of particle correlations this means that the measured associated particle yield is scaled with the inverse detection efficiency of the associated particle and the trigger particle. The trigger particles are only scaled with the inverse efficiency of the trigger particles. The MC correction uses a finer binning than the trigger and associated momentum binning in the correlation analysis. By applying the efficiency correction before doing the particle correlations, the weighting of particles with different momenta within one trigger or associated momentum bin is done correctly.
After this correction, the same and mixed event yields do still contain the pair effi-

ciency. This is the efficiency to measure a particle pair. The main contribution are acceptance effects. By dividing the same and mixed events this pair acceptance drops out. This was shown in Section 5.3. Another pair efficiency is a modified efficiency to measure two particles close to each other. But this is a small effect which is not significant within the systematic uncertainties of the measurements in this thesis.
The application of the single particle efficiency correction is identical for the number of trigger particles ($\frac{d^2N}{d\varphi d\eta}([p_{\mathrm{T,trig}}], \varphi, \eta)$ in Equation 5.2) and the correlated yield ($\frac{d^2N_{assoc,same}}{d\Delta\varphi d\Delta\eta}$ in Equation 5.5). So the effect from the efficiency correction on the trigger particles cancels out when the per trigger yield is determined.

5.5. Background

Not all particles in an event are correlated with the trigger particle. Uncorrelated particles show a flat background in the $\Delta\varphi$ - $\Delta\eta$ plot. The probability of finding such a particle combination can be described as the product of the probabilities to find the single particles. The particle pairs which are created by real correlations cannot be written as product because the correlation is defined as the particles in the event additionally to these random combinations.

$$\begin{aligned}
&\frac{d^2N_{assoc,same}}{d\Delta\varphi d\Delta\eta}([p_{\mathrm{T,trig}}], [p_{\mathrm{T,assoc}}], \Delta\varphi, \Delta\eta) \\
= &\underbrace{\frac{d^2N}{d\varphi_1 d\eta_1}([p_{\mathrm{T,trig}}])\frac{d^2N}{d\varphi_2 d\eta_2}([p_{\mathrm{T,assoc}}])}_{\substack{\textit{trigger and associated particle are not correlated} \\ \rightarrow \textit{the yield is isotrop}}} \\
&+ \underbrace{\frac{d^2N_{assoc}}{d\Delta\varphi d\Delta\eta}([p_{\mathrm{T,trig}}], [p_{\mathrm{T,assoc}}], \Delta\varphi, \Delta\eta)}_{\textit{correlated yield}}
\end{aligned} \tag{5.14}$$

The flat background is not the only background. Pb-Pb events are affected by the elliptic flow. This can be described by multiplying the particle distribution in each event with a collective flow term $(1 + 2\nu_2 \cos 2(\varphi - \Psi))$. This does not influence the calculation of the mixed events because the reaction plane angle Ψ is distributed isotropically over all events. But in the same event a small effect can appear if the trigger particle is affected by the flow. The finally measured correlation yield can have a flow ridge at $|\Delta\varphi| \sim 0$ and $|\Delta\varphi| \sim \pi$. In Equation 5.14 this is part of $\frac{d^2N_{assoc,same}}{d\Delta\varphi d\Delta\eta}$. So in the jet yield extraction this has to be taken into account.
The jet correlations can be split into two components. The near side jet ($|\Delta\varphi| \sim 0$) and the away side jet ($|\Delta\varphi| \sim \pi$).

- $\frac{d^2N_{jet,near}}{d\Delta\varphi d\Delta\eta}([p_{\mathrm{T,trig}}], [p_{\mathrm{T,assoc}}], \Delta\varphi, \Delta\eta)$
  jet particles on the near side focused in one peak($|\Delta\varphi| \sim 0$, $|\Delta\eta| \sim 0$)

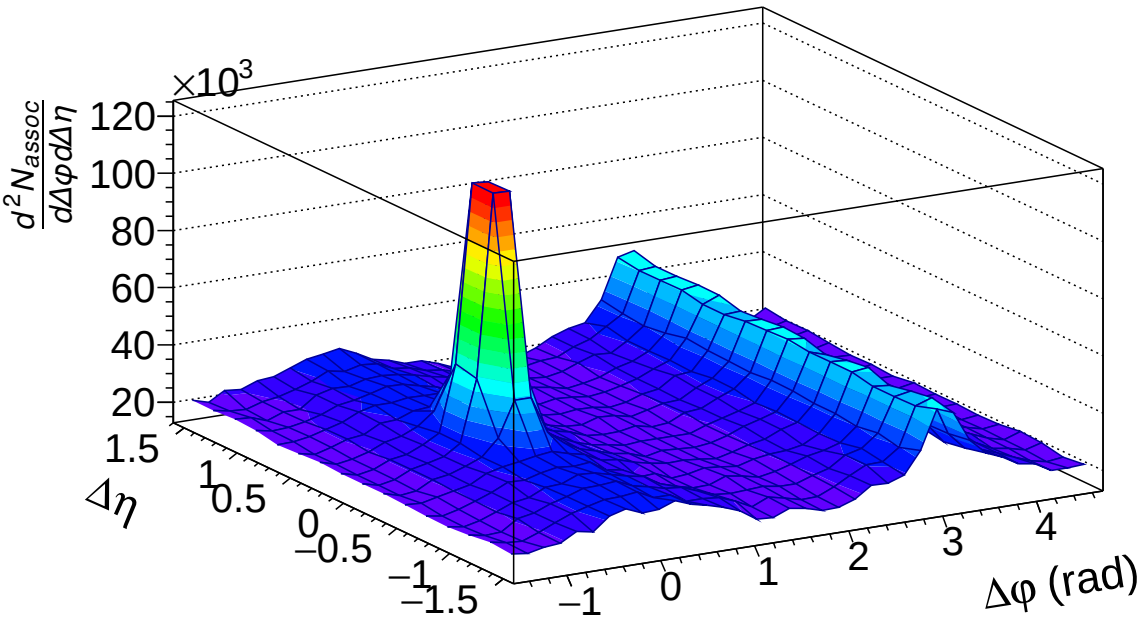

Figure 5.5.: The associated particle yield of 1+1 correlations. The near side jet correlations are visible as peak around $\Delta\varphi = \Delta\eta = 0$. The away side jets are contained in the ridge on the away side at $\Delta\varphi \approx \pi$. The same ridge contains part of the flow signal. The rest of the flow forms the ridge at $\Delta\varphi \approx 0$.

- $\frac{d^2N_{jet,away}}{d\Delta\varphi d\Delta\eta}([p_{\mathrm{T,trig}}], [p_{\mathrm{T,assoc}}], \Delta\varphi)$
  jet particles on the away side in a ridge ($|\Delta\varphi| \sim \pi$)
- $\frac{d^2N_{flow}}{d\Delta\varphi d\Delta\eta}([p_{\mathrm{T,trig}}], [p_{\mathrm{T,assoc}}], \Delta\varphi)$
  particles affected by flow

$$\begin{aligned}
&\frac{d^2N_{assoc}}{d\Delta\varphi d\Delta\eta}([p_{\mathrm{T,trig}}], [p_{\mathrm{T,assoc}}], \Delta\varphi, \Delta\eta) \\
=&\frac{d^2N_{jet,near}}{d\Delta\varphi d\Delta\eta}([p_{\mathrm{T,trig}}], [p_{\mathrm{T,assoc}}], \Delta\varphi, \Delta\eta) \\
&+ \frac{d^2N_{jet,away}}{d\Delta\varphi d\Delta\eta}([p_{\mathrm{T,trig}}], [p_{\mathrm{T,assoc}}], \Delta\varphi) \\
&+ \frac{d^2N_{flow}}{d\Delta\varphi d\Delta\eta}([p_{\mathrm{T,trig}}], [p_{\mathrm{T,assoc}}], \Delta\varphi)
\end{aligned} \tag{5.15}$$

In Figure 5.5 an example of the associated particle yield is shown. In this figure the different correlation distributions can be seen. The flat background consists of particles from the uncorrelated background. On the near side a clear peak can be

identified which contains the near side jet particles $\frac{d^2N_{jet,near}}{d\Delta\varphi d\Delta\eta}$. The jet peak is focused in $\Delta\varphi$ and $\Delta\eta$. Independent of $\Delta\eta$ a ridge can be seen on the away side which contains the away side jet particles. The flow $\frac{d^2N_{flow}}{d\Delta\varphi d\Delta\eta}$ creates an additional ridge on the near side and part of the away side ridge. While the flow ridge on the near side can be identified at large $\Delta\eta$, this is impossible on the away side because the away side jet ridge overlays the flow ridge.

5.6. Peak Yield Extraction using a Fit

The correlation plot is projected from the two dimensional $\Delta\varphi$-$\Delta\eta$ to the one dimensional $\Delta\eta$ plot within $|\Delta\varphi| < \pi/6$. This range is sufficient for all trigger configurations and associated momenta. In the new plot the collective effects, which have a ridge structure in the two dimensional plot, are equal to a constant background.
The peak is fitted within $|\Delta\eta| < 1.4$ with a Gaussian distribution on top of a constant background.

$$f(\Delta\eta) = a + \frac{Y}{\sqrt{2\pi}\sigma}\mathrm{e}^{-\frac{1}{2}(\Delta\eta/\sigma)^2} \tag{5.16}$$

In this fit the background is modeled by a term a which is constant in $\Delta\eta$. The Gaussian is fixed to be centered at $\Delta\eta = 0$ and the width c has to be within a reasonable range $(0.07 - 0.5)$. This avoids the peak being very sharp and modeling only one point. Additionally it avoids the Gaussian being too broad so that it is like another constant line. The Gaussian can describe a thin peak which covers two bins (high $p_{\mathrm{T,assoc}}$) and it can describe peaks which cover almost all bins (low $p_{\mathrm{T,assoc}}$).
The parameter Y is the integral of the Gaussian. In this method the fluctuations have a smaller influence compared to the bin counting method. But the resulting yield does still contain a statistical uncertainty for the peak yield of the same order as for the bin counting method. The advantage of this method is the reduced systematic uncertainty because the background is not subtracted in a separate step. The fit of the baseline a contains smaller fluctuations than the $\Delta\eta$ gap subtraction which is described in the next section.

5.7. Peak Yield Extraction using direct Bin Counting

Before the peak yield can be integrated by adding up the bin content, the background has to be subtracted with the $\Delta\eta$ gap method. For this the per trigger yield is sampled at large $\Delta\eta$ and the resulting yield is subtracted from the yield at small $\Delta\eta$. It is important to separate the peak area from the area in which the background is estimated to suppress the jet influence in the background sample. Because of the ALICE detector acceptance $\eta_{max} = 0.9$, the maximum $\Delta\eta$ is 1.8. The largest 2 bins are excluded because of poor statistics due to the small phase space from which these angular differences can be obtained. This means that the background yield is sampled at $0.8 < |\Delta\eta| < 1.4$ and then subtracted from the yield at $|\Delta\eta| < 0.6$.

$p_{\mathrm{T,assoc}}$	$\lvert\Delta\varphi\rvert$	$\lvert\Delta\eta\rvert$
1.0-5.0	$\pi/6$	0.6
5.0-8.0	$\pi/9$	0.6

Table 5.1.: Integration area for the jet peak in 1+1 particle correlations with the bin counting method.

After the background subtraction the yield from Equation 5.13 contains only the yield from the near side jet. The peak yield can be obtained from the bins around $\Delta\varphi = \Delta\eta = 0$. To further reduce the background the peak area is projected on $\Delta\varphi$ within $|\Delta\eta| < 0.6$. This range can be varied dependent on $p_{\mathrm{T,assoc}}$ because the peak width changes. But the influence was found to be small.
After the projection a constant baseline is subtracted. It is fitted at $1.0 < |\Delta\varphi| < 1.4$. This area has the same distance to the jet peak at $\Delta\varphi = 0$ as the area which is used for the $\Delta\eta$ gap subtraction and it is sufficiently far enough away from the away side ridge. The baseline yield is subtracted from every bin. The yield is expected to be very small because the $\Delta\eta$ gap subtraction should remove any background. This baseline subtraction guarantees that no residual baseline is left. This baseline has a smaller uncertainty because it is created from more $\Delta\eta$ bins than the $\Delta\eta$ gap subtraction.
The peak yield can be integrated from all bins within a defined $\Delta\varphi$ by summing up the bin content. To reduce the influence from fluctuations in bins with no jet yield, the number of bins is kept as small as possible. The used integration area is shown in Table 5.1.

6. Two Plus One Particle Angular Correlations

To be able to analyze the away side jet yield in 1+1 correlations at $\Delta\varphi \approx \pi$ in more detail the two plus one particle angular correlations have been developed. This method searches for the associated per trigger yield of back-to-back trigger particles. The trigger particles stand as proxies for back-to-back jets. At low energies it is difficult to identify these jets with jet finders.
In this chapter the 2+1 correlations are explained in detail. The technical details of the correlation measurement are explained in the Sections 6.1 and 6.2. The 2+1 correlations contain an additional layer of combinatorial background compared to the 1+1 correlations which is explained in Section 6.4. After this background is subtracted the signal is extracted the same way as in 1+1 correlations. This is explained in more detail in Section 6.6.
In Section 6.5 the statistical uncertainties are discussed and the dependence on the centrality is investigated.
In 2+1 correlations it is possible to compare the associated particle yield of back-to-back jets. Derived measurements which contain these comparison are described in the closing Section 6.7.

6.1. Correlations within the Same Event

The procedure to obtain the 2+1 same event yield is similar as for the 1+1 correlations. Instead of one particle, two particles are taken as trigger with the transversal momenta $p_{\mathrm{T1,trig}}$ and $p_{\mathrm{T2,trig}}$. The number of 2+1 trigger particles can be calculated with the integrated 1+1 correlated yield within $|\Delta\varphi - \pi| < \alpha$.

$$\begin{aligned} & N^{2+1}_{trig}(p_{\mathrm{T1,trig}}, p_{\mathrm{T2,trig}}, \alpha) \\ = & \int_0^{2\pi} d\varphi_1 \int_{-\eta_{max}}^{\eta_{max}} d\eta_1 \; \epsilon(p_{\mathrm{T1,trig}}, \varphi_1, \eta_1) \int_{\varphi_1+\pi-\alpha}^{\varphi_1+\pi+\alpha} d\varphi_2 \int_{-\eta_{max}}^{\eta_{max}} d\eta_2 \; \epsilon(p_{\mathrm{T2,trig}}, \varphi_2, \eta_2) \\ & \cdot \frac{d^4 N_{assoc,same}}{d\varphi_1 d\eta_1 d\varphi_2 d\eta_2}([p_{\mathrm{T1,trig}}], [p_{\mathrm{T2,trig}}], \varphi_1, \eta_1, \varphi_2, \eta_2) \end{aligned} \tag{6.1}$$

Like for the 1+1 analysis described in Chapter 5 the associated yield of the 2+1 correlations cannot be directly measured. Instead the same event yield is measured. But in 2+1 correlations there are two correlation measurements. In this chapter all examples are presented for the trigger 1 associated yield.

The trigger 1 associated yield of the same event yield is defined as follows.

$$\begin{aligned}
&\frac{d^2N^{same}_{T1assoc}}{d\Delta\varphi d\Delta\eta}(p_{\mathrm{T1,trig}}, p_{\mathrm{T2,trig}}, p_{\mathrm{T,assoc}}, \Delta\varphi, \Delta\eta, \alpha) \\
=&\int_0^{2\pi} d\varphi_1 \int_{-\eta_{max}}^{\eta_{max}} d\eta_1 \; \epsilon(p_{\mathrm{T1,trig}}, \varphi_1, \eta_1) \cdot \int_{\varphi_1+\pi-\alpha}^{\varphi_1+\pi+\alpha} d\varphi_2 \int_{-\eta_{max}}^{\eta_{max}} d\eta_2 \; \epsilon(p_{\mathrm{T2,trig}}, \varphi_2, \eta_2) \\
&\cdot \int_0^{2\pi} d\varphi_3 \int_{-\eta_{max}}^{\eta_{max}} d\eta_3 \; \epsilon(p_{\mathrm{T,assoc}}, \varphi_3, \eta_3) \\
&\cdot \frac{d^6N_{T1assoc,same}}{d\varphi_1 d\eta_1 d\varphi_2 d\eta_2 d\varphi_3 d\eta_3}([p_{\mathrm{T1,trig}}], [p_{\mathrm{T2,trig}}], [p_{\mathrm{T,assoc}}], \varphi_1, \eta_1, \varphi_2, \eta_2, \varphi_3, \eta_3) \\
&\cdot \delta(\Delta\varphi - (\varphi_1 - \varphi_3)) \; \delta(\Delta\eta - (\eta_1 - \eta_3))
\end{aligned} \tag{6.2}$$

The integration over the position of trigger 2 can be rewritten as dependence over $\Delta\varphi_{12}$, $\Delta\eta_{12}$, φ_0^{12} and η_0^{12} which are defined as the difference and the sum of the particle positions (see Equation 5.3). As in the 1+1 correlations the dependence on the sums φ_0^{12} and η_0^{12} can be neglected. Additionally there is no dependence on $\Delta\eta_{12}$ because the trigger particles are not correlated in η.
As an approximation the dependence on $\Delta\varphi_{12}$ is neglected as well. This assumes that the 1+1 away side yield (= the distribution of trigger 2) is constant within the limited integration area of trigger 2. Due to the correlations of the trigger particles, the particle yield of trigger 2 is larger within the integrated area than outside of it.
The dependence of the same event yield on the position of trigger 1 and the associated particles is rewritten with the new variables $(\Delta\varphi, \Delta\eta, \varphi_0, \eta_0)$ as well. Like in the 1+1 correlations the dependence on φ_0 and η_0 is neglected[1].
In the final yield the 2+1 associated yield is formulated very similar to the 1+1 correlation yield. The probability of finding a trigger in 1+1 correlations $\frac{d^2N_{assoc,same}}{d\Delta\varphi d\Delta\eta}$ is changed to the probability of finding a trigger pair $\frac{d^2N_{T1assoc}}{d\Delta\varphi d\Delta\eta}$. Additionally to the convolution of the trigger 1 and the associated particle efficiency, the yield is integrated over the position of trigger 2 and the correspondent efficiency.

$$\begin{aligned}
&\frac{d^2N^{same}_{T1assoc}}{d\Delta\varphi d\Delta\eta}(p_{\mathrm{T1,trig}}, p_{\mathrm{T2,trig}}, p_{\mathrm{T,assoc}}, \Delta\varphi, \Delta\eta, \alpha) \\
=&\frac{d^2N_{T1assoc,same}}{d\Delta\varphi d\Delta\eta}([p_{\mathrm{T1,trig}}], [p_{\mathrm{T2,trig}}], [p_{\mathrm{T,assoc}}], \Delta\varphi, \Delta\eta) \\
&\int_0^{2\pi} d\varphi_1 \int_{-\eta_{max}}^{\eta_{max}} d\eta_1 \int_{\pi-\alpha}^{\pi+\alpha} d\Delta\varphi_{12} \int_{-2\eta_{max}}^{2\eta_{max}} d\Delta\eta_{12} \; \epsilon(p_{\mathrm{T2,trig}}, \varphi_1 - \Delta\varphi_{12}, \eta_1 - \Delta\eta_{12}) \\
&\cdot \epsilon(p_{\mathrm{T1,trig}}, \varphi_1, \eta_1)\epsilon(p_{\mathrm{T,assoc}}, \varphi_1 - \Delta\varphi, \eta_1 - \Delta\eta)
\end{aligned} \tag{6.3}$$

This formulation of the same event yield factorizes the acceptance and efficiency variables ϵ for all involved particles. The yield can be corrected for these effects with the mixed event method.

[1] This is exact for φ and an approximation in η like before in the 1+1 correlations.

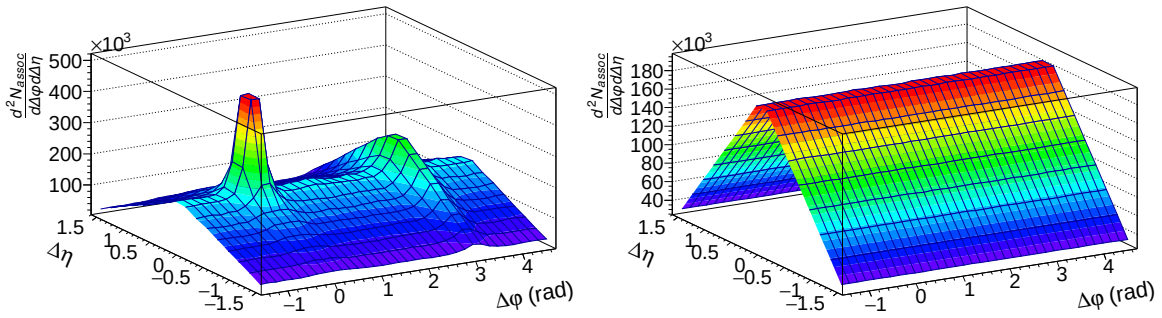

Figure 6.1.: Schematic plot for the same event (left panel) and mixed event (right panel) trigger 1 associated yield. The events used to calculate this yield were produced with the toy event generator.

The efficiency integral in Equation 6.3 creates a structure like the efficiency convolution in the 1+1 correlations (Equation 5.5) because trigger 1 and the associated particles form the same kind of correlation. The required existence of the second trigger particle creates an additional effect. The acceptance and efficiency effect $\epsilon(p_{\mathrm{T2,trig}}, \varphi_1 - \Delta\varphi_{12}, \eta_1 - \Delta\eta_{12})$ is integrated out over all possible η positions and over a defined φ range. Because the phase space of this integration is the same for all trigger 1, there is no strong acceptance effect like from the limited η acceptance in two particle correlations.
In the left panel of Figure 6.1 an example for the same event yield for the trigger 1 associated particles is shown. The simulation of these event did not contain particle flow. The triangular shape in $\Delta\eta$, which is created out of the convolution of a constant acceptance in a limited range, can clearly be seen. The yield is very similar to the 1+1 yield in the left panel of Figure 5.3, but it contains the additional requirement of a second trigger particle.

6.2. Correlations within the Mixed Event

The mixed event of the 2+1 analysis is defined similarly to the 1+1 mixed event. The trigger particles are taken from one event and the associated particles are taken from another event. An alternative mixed event could be created out of three events. In this case the trigger particles would be from two different events. In this section the calculation of the first method will be shown. At the end it will be clear that only the first method is mathematically correct.
For higher statistics multiple events are used to obtain the associated particles. The resulting yield is scaled down with the number of used events.
Because no correlation exists between the particles from the first and second event these yields can be factorized in the formulation of the mixed event yield. The probability of finding an associated particle in the mixed event is independent of the position in the event. Thus this dependence can be dropped. This assumes that there is no

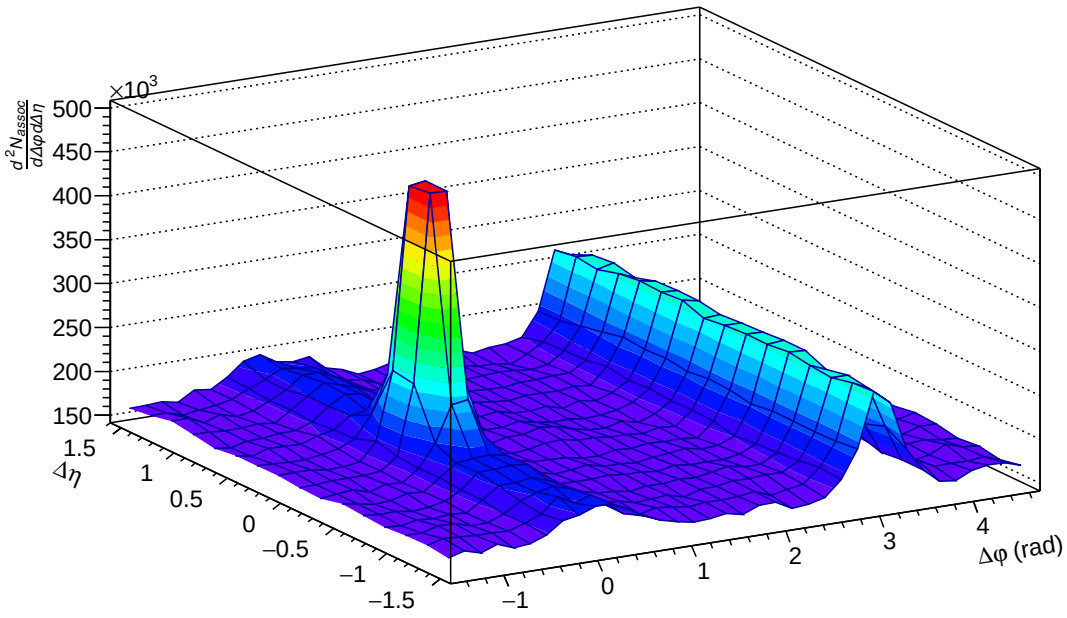

Figure 6.2.: Same event divided by the mixed event (Figure 6.1). This way the efficiency and acceptance effects ϵ on the same event yield are corrected. This division is done separately for the trigger 1 and trigger 2 associated particle yield. For the event generation of the used simulation no flow effects are used. The near side ridge is an effect from uncorrelated trigger particles.

physics effect dependent on η as before in the 1+1 mixed event.
The 2+1 mixed event yield is defined analog to the 1+1 mixed event. Instead of a single particle trigger distribution, the trigger pair yield $\frac{d^4N}{d\varphi_1 d\eta_1 d\varphi_2 d\eta_2}([p_{\mathrm{T1,trig}}], [p_{\mathrm{T2,trig}}], \Delta\varphi_{12})$ is used. This yield cannot be split in two distributions because it contains the correlated trigger yield. The dependence on $\Delta\eta_{12}$, φ_0^{12} and η_0^{12} is neglected as it was done in the 1+1 correlations. Additionally the dependence on $\Delta\varphi_{12}$ is neglected the same way as before for the same event (the yield is assumed to be constant within the trigger 2 integration area).

$$
\begin{aligned}
&\frac{d^2N^{mixed}_{T1assoc}}{d\Delta\varphi d\Delta\eta}(p_{\mathrm{T1,trig}}, p_{\mathrm{T2,trig}}, p_{\mathrm{T,assoc}}, \Delta\varphi, \Delta\eta, \alpha) \\
=&\int_0^{2\pi} d\varphi_1 \int_{-\eta_{max}}^{\eta_{max}} d\eta_1 \; \epsilon(p_{\mathrm{T1,trig}}, \varphi_1, \eta_1) \\
&\cdot \int_{\varphi_1+\pi-\alpha}^{\varphi_1+\pi+\alpha} d\varphi_2 \int_{-\eta_{max}}^{\eta_{max}} d\eta_2 \; \epsilon(p_{\mathrm{T2,trig}}, \varphi_2, \eta_2) \frac{d^4N}{d\varphi_1 d\eta_1 d\varphi_2 d\eta_2}([p_{\mathrm{T1,trig}}], [p_{\mathrm{T2,trig}}]) \\
&\cdot \int_0^{2\pi} d\varphi_3 \int_{-\eta_{max}}^{\eta_{max}} d\eta_3 \; \epsilon(p_{\mathrm{T,assoc}}, \varphi_3, \eta_3) \frac{d^2N}{d\varphi_3 d\eta_3}([p_{\mathrm{T,assoc}}]) \\
&\cdot \delta(\Delta\varphi - (\varphi_1 - \varphi_3)) \; \delta(\Delta\eta - (\eta_1 - \eta_3)) \qquad (6.4) \\
=&\frac{d^2N}{d\Delta\varphi_{12} d\Delta\eta_{12}}([p_{\mathrm{T1,trig}}], [p_{\mathrm{T2,trig}}]) \frac{d^2N}{d\Delta\varphi d\Delta\eta}([p_{\mathrm{T,assoc}}]) \\
&\int_0^{2\pi} d\varphi_1 \int_{-\eta_{max}}^{\eta_{max}} d\eta_1 \int_{\pi-\alpha}^{\pi+\alpha} d\Delta\varphi_{12} \int_{-2\eta_{max}}^{2\eta_{max}} d\Delta\eta_{12} \; \epsilon(p_{\mathrm{T2,trig}}, \varphi_1 - \Delta\varphi_{12}, \eta_1 - \Delta\eta_{12}) \\
&\cdot \epsilon(p_{\mathrm{T1,trig}}, \varphi_1, \eta_1) \epsilon(p_{\mathrm{T,assoc}}, \varphi_1 - \Delta\varphi, \eta_1 - \Delta\eta) \qquad (6.5)
\end{aligned}
$$

The mixed event yield is transformed so that the efficiency integrals are isolated. The trigger particle yield $\frac{d^2N}{d\Delta\varphi_{12} d\Delta\eta_{12}}([p_{\mathrm{T1,trig}}], [p_{\mathrm{T2,trig}}])$ is calculated per $\Delta\varphi_{12}$ and $\Delta\eta_{12}$ bin but it is not dependent on these bins. So it can be written in front of the efficiency integrals.
The 2+1 mixed event yield is normalized with the factor α_N.

$$
\alpha_N(p_{\mathrm{T1,trig}}, p_{\mathrm{T2,trig}}, p_{\mathrm{T,assoc}}) = \frac{1}{\frac{d^2N}{d\Delta\varphi_{12} d\Delta\eta_{12}}([p_{\mathrm{T1,trig}}], [p_{\mathrm{T2,trig}}]) \frac{d^2N}{d\varphi_3 d\eta_3}([p_{\mathrm{T,assoc}}])} \qquad (6.6)
$$

After normalizing the mixed event yield from Equation 6.5, the acceptance and detector effects in Equation 6.3 can be corrected. This is done like for the 1+1 correlations in Equation 5.11 by dividing the same and mixed events.

$$
\begin{aligned}
&\frac{\frac{d^2N^{same}_{T1assoc}}{d\Delta\varphi d\Delta\eta}(p_{\mathrm{T1,trig}}, p_{\mathrm{T2,trig}}, p_{\mathrm{T,assoc}}, \Delta\varphi, \Delta\eta, \alpha)}{\frac{d^2N^{mixed}_{T1assoc}}{d\Delta\varphi d\Delta\eta}(p_{\mathrm{T1,trig}}, p_{\mathrm{T2,trig}}, p_{\mathrm{T,assoc}}, \Delta\varphi, \Delta\eta, \alpha)} \cdot \frac{1}{\alpha_N(p_{\mathrm{T1,trig}}, p_{\mathrm{T2,trig}}, p_{\mathrm{T,assoc}})} \\
=&\frac{\frac{d^2N_{T1assoc,same}}{d\Delta\varphi d\Delta\eta}([p_{\mathrm{T,trig}}], [p_{\mathrm{T,assoc}}], \Delta\varphi, \Delta\eta)}{\frac{d^2N}{d\Delta\varphi_{12} d\Delta\eta_{12}}([p_{\mathrm{T1,trig}}], [p_{\mathrm{T2,trig}}]) \frac{d^2N}{d\varphi_3 d\eta_3}([p_{\mathrm{T,assoc}}])} \\
&\frac{\int_0^{2\pi} d\varphi_1 \int_{-\eta_{max}}^{\eta_{max}} d\eta_1 \int_{\pi-\alpha}^{\pi+\alpha} d\Delta\varphi_{12} \int_{-2\eta_{max}}^{2\eta_{max}} d\Delta\eta_{12} \; \epsilon(p_{\mathrm{T2,trig}}, \varphi_1 - \Delta\varphi_{12}, \eta_1 - \Delta\eta_{12})}{\int_0^{2\pi} d\varphi_1 \int_{-\eta_{max}}^{\eta_{max}} d\eta_1 \int_{\pi-\alpha}^{\pi+\alpha} d\Delta\varphi_{12} \int_{-2\eta_{max}}^{2\eta_{max}} d\Delta\eta_{12} \; \epsilon(p_{\mathrm{T2,trig}}, \varphi_1 - \Delta\varphi_{12}, \eta_1 - \Delta\eta_{12})} \\
&\frac{\epsilon(p_{\mathrm{T1,trig}}, \varphi_1, \eta_1) \epsilon(p_{\mathrm{T,assoc}}, \varphi_1 - \Delta\varphi, \eta_1 - \Delta\eta)}{\epsilon(p_{\mathrm{T1,trig}}, \varphi_1, \eta_1) \epsilon(p_{\mathrm{T,assoc}}, \varphi_1 - \Delta\varphi, \eta_1 - \Delta\eta)} \\
&\frac{d^2N}{d\Delta\varphi_{12} d\Delta\eta_{12}}([p_{\mathrm{T1,trig}}], [p_{\mathrm{T2,trig}}]) \frac{d^2N}{d\varphi_3 d\eta_3}([p_{\mathrm{T,assoc}}]) \\
=&\frac{d^2N_{T1assoc,same}}{d\Delta\varphi d\Delta\eta}([p_{\mathrm{T,trig}}], [p_{\mathrm{T,assoc}}], \Delta\varphi, \Delta\eta) \qquad (6.7)
\end{aligned}
$$

The integrals over the same and mixed event detector effects ϵ cancel out. If the mixed event method would have been created from three events, the integral in the mixed event would be different and the detector effects would not cancel out.
The associated yield can be divided by the number of trigger particles from Equation 6.1 to obtain the per trigger yield.

$$\frac{1}{N_{trig}^{2+1}(p_{\mathrm{T1,trig}}, p_{\mathrm{T2,trig}}, \alpha)} \frac{d^2 N_{T1assoc,same}}{d\Delta\varphi d\Delta\eta}([p_{\mathrm{T1,trig}}], [p_{\mathrm{T2,trig}}], [p_{\mathrm{T,assoc}}], \Delta\varphi, \Delta\eta) \quad (6.8)$$

This is the per trigger associated yield of the trigger 1 associated particles in 2+1 correlations. The same calculation can be done for the trigger 2 associated yield.
In the right panel of Figure 6.1 the mixed event yield for the 2+1 correlations for trigger 1 associated particles is shown. It is very similar to the 1+1 mixed event yield in the right panel of Figure 5.3, but it contains the additional requirement of a second trigger particle. The 2+1 mixed event yield contains the acceptance and efficiency effects which can be seen in the same event yield in the left panel of Figure 6.1 as well. There the correlation effects can be seen multiplicative on top of the background. After dividing the same and mixed event the background is flat. This is shown in Figure 6.2. The simulated events which are used for these correlations do not contain any flow effect. The ridge like structure at $\Delta\varphi \approx 0$ is created by the away side jets of trigger 2 which are not correlated with the trigger 1 and thus they are found at all $\Delta\eta$ positions.
In case the mixed event yield would have been created from three events, the correlated yield $\frac{d^4N}{d\varphi_1 d\eta_1 d\varphi_2 d\eta_2}([p_{\mathrm{T1,trig}}], [p_{\mathrm{T2,trig}}])$ could be factorized in a yield for trigger 1 and a yield for trigger 2. Consequently the transverse momentum distribution of trigger 2 would change. So the composition of the acceptance and efficiency factors ϵ in Equation 6.5 would change. With these changes the cancellation of the efficiency and acceptance factors would not be exact anymore.

6.3. Efficiency Correction

The 2+1 efficiency correction is identical to the 1+1 efficiency correction presented in Section 5.4. But the efficiency correction is done for three particles instead of two. The number of trigger particles is scaled with the inverse efficiencies from both trigger particles. The associated yield is scaled additionally to these two efficiencies with the inverse detection efficiency of the associated particle.
Due to this correction the same and mixed event particle yields are flat in φ and η. This makes it possible to execute the mixed event correction.

6.4. Background from Uncorrelated Trigger Combinations

In the 2+1 measurements many correlations are measured which do not represent the expected associated yield from correlated trigger particles. The measured yield can be divided into five different contributions dependent which particle is correlated with which other particle in the measurement.

$$
\begin{aligned}
&\frac{d^2N_{T1assoc,same}}{d\Delta\varphi d\Delta\eta}([p_{\mathrm{T1,trig}}],[p_{\mathrm{T2,trig}}],[p_{\mathrm{T,assoc}}],\Delta\varphi,\Delta\eta) \\
&= \underbrace{\frac{d^2N}{d\varphi_1 d\eta_1}([p_{\mathrm{T1,trig}}],\varphi_1,\eta_1)\cdot\frac{d^2N}{d\varphi_2 d\eta_2}([p_{\mathrm{T2,trig}}],\varphi_1,\eta_1)\cdot\frac{d^2N}{d\varphi_3 d\eta_3}([p_{\mathrm{T,assoc}}],\varphi_3,\eta_3)}_{\substack{=\mu_1,\ \textit{triggers are uncorrelated}\\ \textit{and the associated particles are not correlated with any trigger particle}}} \\
&+ \underbrace{\frac{d^4N}{d\varphi_1 d\eta_1 d\varphi_2 d\eta_2}([p_{\mathrm{T1,trig}}],[p_{\mathrm{T2,trig}}],\varphi_1,\eta_1,\varphi_2,\eta_2)\cdot\frac{d^2N}{d\varphi_3 d\eta_3}([p_{\mathrm{T,assoc}}],\varphi_3,\eta_3)}_{\substack{=\mu_2,\ \textit{triggers are correlated}\\ \textit{and the associated particles are not correlated with any trigger particle}}} \\
&+ \underbrace{\frac{d^2N}{d\varphi_2 d\eta_2}([p_{\mathrm{T2,trig}}])\cdot\frac{d^4N}{d\varphi_1 d\eta_1 d\varphi_3 d\eta_3}([p_{\mathrm{T1,trig}}],[p_{\mathrm{T,assoc}}],\varphi_1,\eta_1,\varphi_3,\eta_3)}_{\substack{=\mu_3,\ \textit{trigger particles are not correlated,}\\ \textit{associated particles are correlated with trigger}1}} \\
&+ \underbrace{\frac{d^2N}{d\varphi_1 d\eta_1}([p_{\mathrm{T1,trig}}])\cdot\frac{d^4N}{d\varphi_2 d\eta_2 d\varphi_3 d\eta_3}([p_{\mathrm{T2,trig}}],[p_{\mathrm{T,assoc}}],\varphi_2,\eta_2,\varphi_3,\eta_3)}_{\substack{=\mu_4,\ \textit{trigger particles are not correlated,}\\ \textit{associated particles are correlated with trigger}2}} \\
&+ \underbrace{\frac{d^6N_{T1assoc}}{d\varphi_1 d\eta_1 d\varphi_2 d\eta_2 d\varphi_3 d\eta_3}([p_{\mathrm{T1,trig}}],[p_{\mathrm{T2,trig}}],[p_{\mathrm{T,assoc}}],\varphi_1,\eta_1,\varphi_2,\eta_2,\varphi_3,\eta_3)}_{\substack{=\mu_5,\ \textit{trigger particles are correlated}\\ \textit{associated particles are correlated with both triggers}}}
\end{aligned}
\tag{6.9}
$$

The aim of the measurement is to extract the correlated associated particle yield from correlated trigger particles. This is the yield μ_5.
The background yields have different contributions. Independent if the trigger particles are correlated or not, the associated particles can be uncorrelated with both trigger particles. In this case the associated particle yield is constant. This background existed already in the 1+1 correlations. In Equation 6.9 the constant background is called μ_1 and μ_2 dependent if the trigger particles are correlated. Independent of this the associated yield has the same shape.
If the trigger particles are not correlated the associated particles can be correlated with one of the trigger particles. In case of a correlation of trigger 1 with the associated particles this is called μ_3, in case of trigger 2 μ_4. At small angular distances $\Delta\varphi \approx 0$ and $\Delta\eta \approx 0$ (near side) this yield looks very similar to the real 2+1 correlation yield because a peak structure is measured. This is observed for both trigger

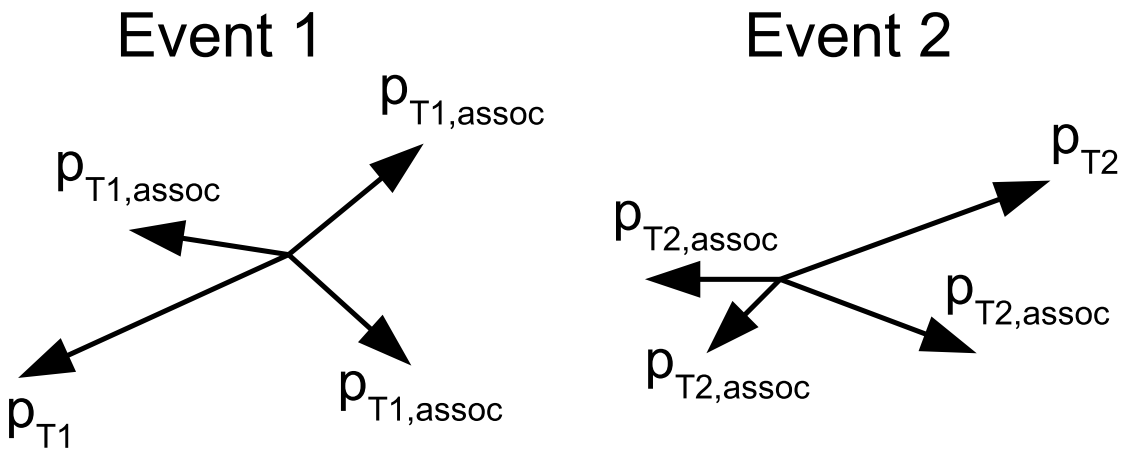

Figure 6.3.: Schematic overview over the mixed combinatorics method. The events are projected in the azimuthal plane. The length of the vector indicates the momentum. The particle marked with p_{T1} is a candidate for a trigger 1, the particle marked with p_{T2} is a candidate for trigger 2. Because both are back-to-back, the trigger combination is accepted for the mixed combinatorics and the other particles in the events are taken as associated particles for the correspondent trigger.

particles. But it does not originate from a di-jet, so this associated particle yield has to be subtracted.
In a single background trigger pair the background yields μ_1, μ_3 and μ_4 appear together. In other words this means, if the trigger particles are not correlated, both trigger particles have other particles in the events which are correlated with them. Additionally each event has particles which are not correlated with any trigger at all. For the trigger 1 associated particle yield it is important to subtract the background yield μ_3 because it has the same peak structure as the 2+1 yield. But for the trigger 2 associated yield, the background yield μ_4 has to be subtracted. There are different methods how this background subtraction can be executed. In the Section 6.4.1 the concept of the correction is introduced with the mixed combinatorics method. Afterwards in Section 6.4.2 an alternative method is presented which is mainly used to determine the rate of background trigger pairs. The difference between these two methods is discussed and evaluated in Section 6.4.3. One method is chosen for the determination of the background trigger pairs. At the end in Section 6.4.4 an alternative approach is introduced to determine the background particle yield if the number of background pairs is known.

6.4.1. Mixed Combinatorics Method

The mixed combinatorics method uses multiple events to describe the yield of the uncorrelated triggers. In Figure 6.3 the mixed combinatorics method is illustrated. The

schematic events show the projection on the φ plane. Trigger 1 is taken from event 1 and a trigger 2 from event 2. Both have to be back-to-back in φ. Because the triggers are from different events, it is guaranteed that they are not correlated.
The number of found trigger combinations $N_{trig}^{mixedComb}$ is equal to the number of uncorrelated trigger combinations found in the normal 2+1 same event.

$$\begin{aligned}
&N_{trig}^{mixedComb}(p_{\mathrm{T1,trig}}, p_{\mathrm{T2,trig}}, \alpha) \\
=&\int_0^{2\pi} d\varphi_1 \int_{-\eta_{max}}^{\eta_{max}} d\eta_1 \; \epsilon(p_{\mathrm{T1,trig}}, \varphi_1, \eta_1) \frac{d^2N}{d\varphi_1 d\eta_1}([p_{\mathrm{T1,trig}}], \varphi_1, \eta_1) \\
&\cdot \int_{\varphi_1+\pi-\alpha}^{\varphi_1+\pi+\alpha} d\varphi_2 \int_{-\eta_{max}}^{\eta_{max}} d\eta_2 \; \epsilon(p_{\mathrm{T2,trig}}, \varphi_2, \eta_2) \frac{d^2N}{d\varphi_2 d\eta_2}([p_{\mathrm{T2,trig}}], \varphi_2, \eta_2)
\end{aligned} \tag{6.10}$$

After the two triggers of a trigger combination were found in two separate events, the associated yield is filled in two steps. The particles from event 1 are used as associated particles for trigger 1. Accordingly the particles from event 2 are used for the calculation of the trigger 2 associated yield. This way the associated yield of trigger particles is recorded which do not have a second correlated trigger in the same event but the acceptance allows them to find an uncorrelated trigger.
The mixed combinatorics same event yield is defined the same way as the normal same event yield in Equation 6.2. But the trigger 2 yield is not correlated with the trigger 1 or the associated particle yield. This mixed combinatorics yield is measured as a same event yield like the normal same event yield. It has to be corrected with the mixed event method as well. To simplify the explanations here the yield is described after the mixed event correction.

$$\begin{aligned}
&\frac{d^2N_{T1assoc,mixedComb}}{d\Delta\varphi d\Delta\eta}([p_{\mathrm{T1,trig}}], [p_{\mathrm{T2,trig}}], [p_{\mathrm{T,assoc}}], \Delta\varphi, \Delta\eta, \alpha) \\
=&\frac{d^2N}{d\varphi_1 d\eta_1}([p_{\mathrm{T1,trig}}], \varphi_1, \eta_1) \cdot \frac{d^2N}{d\varphi_2 d\eta_2}([p_{\mathrm{T2,trig}}], \varphi_1, \eta_1) \cdot \frac{d^2N}{d\varphi_3 d\eta_3}([p_{\mathrm{T,assoc}}], \varphi_3, \eta_3) \\
&+ \frac{d^2N}{d\varphi_2 d\eta_2}([p_{\mathrm{T2,trig}}]) \cdot \frac{d^4N}{d\varphi_1 d\eta_1 d\varphi_3 d\eta_3}([p_{\mathrm{T1,trig}}], [p_{\mathrm{T,assoc}}], \varphi_1, \eta_1, \varphi_3, \eta_3) \\
=&\mu_1 + \mu_3
\end{aligned} \tag{6.11}$$

This yield contains the background yield μ_3 which should be subtracted from the trigger 1 associated same event yield. The additional flat background μ_1 is helpful in the subtraction but not important because it can be subtracted with other methods afterwards.
The resulting 2+1 per trigger associated yield is computed out of the difference between the same event yield and the mixed combinatorics yield. The yield $\frac{d^2N_{T1assoc,same}}{d\Delta\varphi d\Delta\eta}$

represents the associated particle yield after the mixed event correction.

$$
\begin{aligned}
&\frac{1}{N_{trig}}\frac{d^2N_{T1assoc}}{d\Delta\varphi d\Delta\eta}([p_{\mathrm{T1,trig}}],[p_{\mathrm{T2,trig}}],[p_{\mathrm{T,assoc}}],\Delta\varphi,\Delta\eta,\alpha)\\
=&\frac{1}{N_{trig}^{2+1}-N_{trig}^{mixedComb}}\left[\frac{d^2N_{T1assoc,same}}{d\Delta\varphi d\Delta\eta}([p_{\mathrm{T1,trig}}],[p_{\mathrm{T2,trig}}],[p_{\mathrm{T,assoc}}],\Delta\varphi,\Delta\eta,\alpha)\right.\\
&\left.-\frac{d^2N_{T1assoc,mixedComb}}{d\Delta\varphi d\Delta\eta}([p_{\mathrm{T1,trig}}],[p_{\mathrm{T2,trig}}],[p_{\mathrm{T,assoc}}],\Delta\varphi,\Delta\eta,\alpha)\right]\\
=&\mu_2+\mu_4+\mu_5
\end{aligned}
\tag{6.12}
$$

This resulting yield contains the constant background μ_2 and the trigger 2 associated yield μ_4. The constant background will be subtracted later and it can be neglected for the discussion here. The trigger 2 associated background can be split into two parts. The near side associated yield and the away side associated yield (in both cases with respect to trigger 2). The near side associated yield of trigger 2 is on the away side of trigger 1 and it does not matter because only the near side of the trigger 1 associated yield will be analyzed. The away side associated yield of trigger 2 can be seen as a near side ridge relative to trigger 1. This means even after the mixed combinatorics correction the associated yield contains some kind of correlated background. This background can be subtracted in a separate background subtraction which is further described in Section 6.6.
In this section the background subtraction for the trigger 1 associated yield was explained. The same calculations can be done for the trigger 2 associated yield. The yield correction is taken from the trigger 2 associated yield in event 2 of the mixed combinatorics.
The mixed combinatorics method is mathematically a good method to subtract the background. But it has some disadvantages. Several effects exist which cause the number of triggers from the mixed combinatorics method to be on average higher or lower than the background trigger rate in the same event. The effect which causes less trigger 2 dominates. All these effects are explained in detail in Section 6.4.3.
Another problem is connected with the implementation of the code. For the event mixing, buffers are used which are filled separately for each centrality and z-vertex bin. The calculation of the mixed combinatorics can only start as soon as the buffers are filled with some events. To get the correct amount of uncorrelated trigger pairs, the same event analysis can only start in the moment when the mixed combinatorics start. The 2+1 method is used for big datasets, which are analyzed with highly parallelized computing methods. This means that a lot of buffers are separately filled and used for the analysis. Because of the high number of buffers, a not negligible part of the available data is not analyzed for 2+1 correlations if the analysis would start after the buffers are filled. This would increase the statistical uncertainty of the analysis.

6.4.2. Background Same Method

As an alternative to the mixed combinatorics method, the background same method is introduced.
The trigger 1 particle is obtained as usual. But the trigger 2 is not taken from the angular difference $|\Delta\varphi - \pi| < \alpha$ but from $|\Delta\varphi \pm \pi/2| < \alpha/2$. The new areas have half the size compared to the same event trigger 2 area. But to compensate for this, two areas are used. The areas are located as far away from the trigger 1 and the correlated away side particles as possible. This way the background same trigger particles are uncorrelated with the trigger particles of the same event measurement.
The background same yield is expected to be identical to the mixed combinatorics yield presented in Equation 6.11 if the considered area around the trigger particles is small enough[2]. If in the same event a regular trigger 2 and a background same trigger 2 is found, the phase space can be defined with the minimum distance d in φ between these triggers.

$$\begin{aligned} d &= \pi/2 - \alpha - \alpha/2 \\ &= \pi/2 - \pi/8 - \pi/16 \\ &= 5/16\pi = 0.98. \end{aligned}$$

This calculation assumes the same event trigger 2 and the background same trigger 2 being both at the border of their accepted areas. If no particle in an event should have the chance to be double counted as possibly belonging to the same event trigger 2 jet and to the background same trigger 2 jet, the maximum integration area in $\Delta\varphi$ has to be $d/2$. This is equal to a maximum integration area of $|\Delta\varphi| < 0.49$. This area is slightly smaller than the used integration area in the peak yield extraction (see Section 5.6).
In a further analysis (see Section 6.4.3) it was found out that the number of trigger particles from the background same method is slightly too big because it contains trigger particles which are correlated with the trigger 1. The effect is observed to be small in the Pb–Pb data analysis and it is considered in the analysis of the systematic uncertainty in Chapter 8. There the effect is identified to be negligible.

6.4.3. Background Components

To validate the background subtraction, the method is employed on HIJING events. It is observed that the number of background trigger combinations found with the background same and mixed combinatorics methods events are not identical. In central events[3] they deviate in the order of 6%. The effect increases to 15% for the 40–50% most central events.

[2] In Section 6.4.3 it will be shown that there is actually a small difference between the triggers found in both methods. Accordingly there is a difference in the yields.
[3] In Section 2.5 the HIJING event generation has been introduced. Central events are created out of a super-position of three events with the centrality 30–50%.

In the following the background trigger combinations are analyzed and the sources of the background are identified. At the beginning the background is analyzed in a theoretical way. Background contributions from different sources are identified as separate background components. Afterwards the actual background components in HIJING events are determined and presented. The background analysis can be presented better based on HIJING events than on the data analysis because of the smaller statistical uncertainties. But at the end the effects which were observed in HIJING events are discussed for the data analysis as well.
For the theoretical calculation of the background trigger combinations an average event is assumed which contains a di-jet trigger pair (T1 - T2) with the probability $\frac{N_1}{N_1+N_0}$. Here N_1 is the number of events which contain a di-jet and N_0 is the number of events which do not contain a di-jet. Events with more than one di-jet trigger pair are neglected. This approximation is valid because the probability for a di-jet is very low. Additionally each event contains m T2 and n T1 which are not correlated with any other particle in the event.

$$m = \int_0^{2\pi} d\varphi \int_{-\eta_{max}}^{\eta_{max}} d\eta \frac{d^2N}{d\varphi d\eta} ([p_{\mathrm{T2}}], \varphi, \eta) \tag{6.13}$$

$$n = \int_0^{2\pi} d\varphi \int_{-\eta_{max}}^{\eta_{max}} d\eta \frac{d^2N}{d\varphi d\eta} ([p_{\mathrm{T1}}], \varphi, \eta) \tag{6.14}$$

In practice m and n are measured in the 1+1 measurement by dividing the number of triggers by the number of events. This measurement includes particles which are part of a (T1 - T2) pair. But the number of correlated trigger pairs is low compared to the uncorrelated particles with the same transverse momentum, so it can be neglected. The factor m describes the amount of background trigger 2 and not the rate of trigger 2 which are correlated with a potential trigger 1. If m is measured in the described way, it is correct for a random event in a dataset. But in case a trigger 1 is present in the event, the event selection is biased and the average probability of finding a trigger 2 is biased to m_{T1}. This rate is slightly higher than m. The difference between m and m_{T1} is explained in the text further below.
Additionally to the back-to-back correlated trigger particles (T1 - T2) and the isotropic distribution of trigger particles (m and n), the trigger particles can be correlated under angles other than π. For the background estimation the particles which are perpendicular to each other (T1 $\perp$ T2) are important. The number of events which contain such a correlation is called M_1.
For an easier understanding the expected trigger combinations are calculated for a reduced event content. The probability of having an event one which contains a trigger 1 is multiplied with the probability of having an event two which has a trigger 2. This calculation is done for the background same and the mixed combinatorics method. In the background same method the same event has to contain both trigger particles, while in the mixed combinatorics method two events are requested to have a trigger particle each. In both cases these triggers have to be at the correct angular difference to each other so that they qualify for a trigger pair.

Type A Background
In events with exactly 1 back-to-back trigger particle (T1 - T2) no background trigger combination is measured in the background same method. In the mixed combinatorics method the (T1 - T2) trigger combinations in the two events can be arranged in a way that a background trigger combination is measured. The amount of background triggers is equal to the squared probability of having an event with a (T1 - T2) trigger combination $\left(\frac{N_1}{N_1+N_0}\right)^2$ multiplied by the phase space factor $\frac{\alpha}{\pi}$. The phase space factor is the probability that the angular difference of the trigger particles fulfills the trigger condition. In the mixed combinatoric method this means $\Delta\varphi \approx \pm\pi$. In this thesis $\alpha = \pi/8$ is used which results in $\frac{\alpha}{\pi} = 1/8$. The described background in the mixed combinatorics method is called background component A.

Type B Background
In events which contain additionally m trigger 2 particles both background methods result in an additional background component which is called component B. The chance for the trigger 1 from the (T1 - T2) trigger combination $\frac{N_1}{N_1+N_0}$ is multiplied with the chance for the trigger 2 to be at the correct phase space $m\frac{\alpha}{\pi}$. But in the background same analysis the events are biased, because every event has one particle which fulfills the trigger 1 requirement. In these events the probability of finding a particle which fulfills the trigger 2 requirement m_{T1} is higher than the probability in an average event m.

Type C Background
Another type of events is assumed which contains n trigger 1 and m trigger 2. None of the triggers is correlated with any of the other triggers. The component C is calculated by multiplying the probability for an event with a trigger 1 with the probability for an event with a trigger 2. Again events which have a trigger 1 have an increased chance for a trigger 2 compared to events which do not contain a trigger 1.

Type D Background
One last event configuration is considered which contains a perpendicular trigger combination (T1 $\perp$ T2) . In the background same method the probability for such an event $\frac{M_1}{M_1+M_0}$ represents directly the amount of background triggers and it is called component D. In the mixed combinatorics method this probability has to be squared and multiplied with the phase space factor $\frac{\alpha}{\pi}$. This is a very small probability because already the probability for a perpendicular correlated trigger pair is small.

All these background trigger combinations are summarized in Table 6.1 and the background components are indicated. To compare the size of these components they are measured in HIJING events.
For the measurement of m_{T1} the 1+1 per trigger associated particle yield is measured with the 2+1 trigger 1 transverse momentum as trigger momentum and the 2+1 trigger 2 transverse momentum as associated particle momentum. The associated particle

Event Content	Background Same	Mixed Combinatorics
$\frac{N_1}{N_1+N_0}$(T1 - T2)	0	$\underbrace{\left(\frac{N_1}{N_1+N_0}\right)^2 \cdot \frac{\alpha}{\pi}}_{\text{A}}$
mT2 $\oplus$ $\frac{N_1}{N_1+N_0}$(T1 - T2)	$\frac{N_1}{N_1+N_0} m_{T1} \frac{\alpha}{\pi}$	$\underbrace{\frac{N_1}{N_1+N_0} m \frac{\alpha}{\pi}}_{\text{B}} + \left(\frac{N_1}{N_1+N_0}\right)^2 \cdot \frac{\alpha}{\pi}$
mT2 $\oplus$ nT1	$n m_{T1} \frac{\alpha}{\pi}$	$\underbrace{n m \frac{\alpha}{\pi}}_{\text{C}}$
$\frac{M_1}{M_1+M_0}$(T1 $\perp$ T2)	$\underbrace{\frac{M_1}{M_1+M_0}}_{\text{D}}$	$\underbrace{\left(\frac{M_1}{M_1+M_0}\right)^2 \cdot \frac{\alpha}{\pi}}_{\approx 0}$

Table 6.1.: The number of background trigger combinations is calculated for the background same and the mixed combinatorics method dependent on the event content. (T1 - T2) stands for a trigger pair which is back-to-back in φ. Respectively (T1 $\perp$ T2) is a trigger pair with perpendicular trigger particles in φ. Four sources of background trigger combinations are identified and labeled from A to D.

yield has to be integrated at a phase space which does not contain any correlations between the triggers. This is done at $1.0 < |\Delta\eta| < 1.4$ and $|\Delta\varphi| < 0.51$. Afterwards this yield is scaled to the full detector acceptance ($|\Delta\eta| < 1.8$ and full $\Delta\varphi$ acceptance). The result is m_{T1}.
The ratio $m_{bias} = \frac{m_{T1}}{m}$ shows the strength of this bias effect for the different centralities. It is shown in Figure 6.4. At the same centrality, m_{bias} is almost constant for the different trigger configurations.
This bias effect can be explained with an event bias towards higher average centralities. The average number of nucleon-nucleon collisions $\langle N_{coll} \rangle$ is higher in events which have a trigger 1 compared to events which do not require a trigger 1. The average number of nucleon-nucleon collisions for events with a trigger 1 is called $\langle N_{coll}^{T1} \rangle$. This bias effect can be interpreted as a slightly higher average centrality within a centrality bin. The change of the average number of collisions is the bias factor f_{bias}.

$$f_{bias} = \frac{\langle N_{coll}^{T1} \rangle}{\langle N_{coll} \rangle} \tag{6.15}$$

The particle yield in every transverse momentum bin of these biased events is expected to be increases by this bias factor compared to the unbiased events. This means the value should be equal to m_{bias}. In Table 6.2 f_{bias} is shown for the trigger 1 momentum $8 < p_{\mathrm{T1,trig}} < 12\,\mathrm{GeV}/c$. This is compared to the value of m_{bias} from Figure 6.4. For

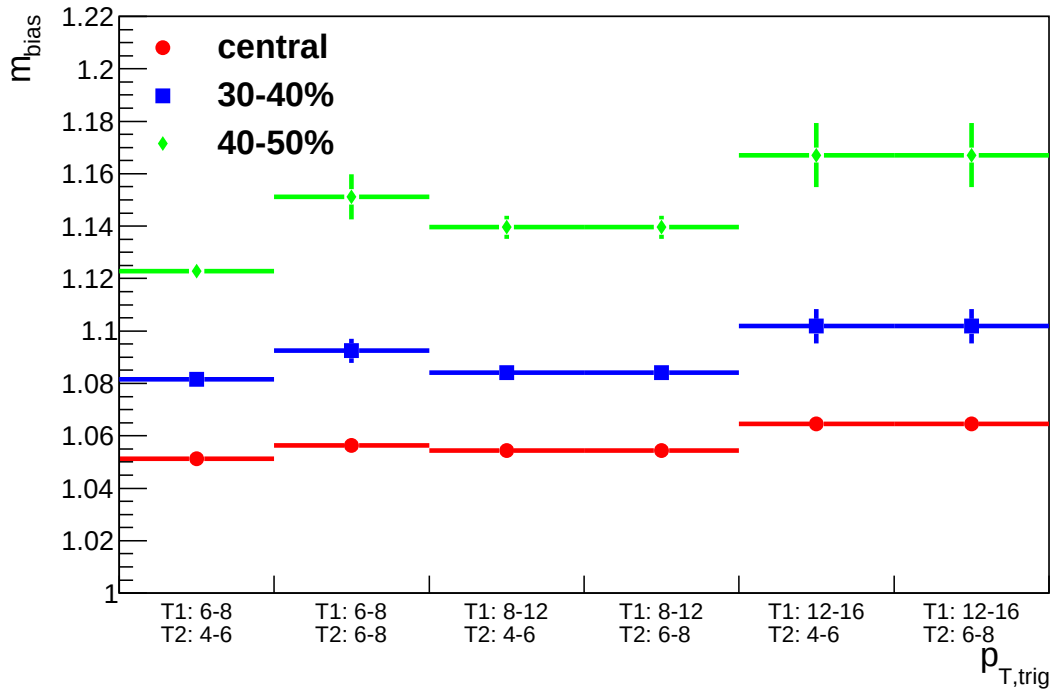

Figure 6.4.: Ratio between the background trigger 2 in HIJING events with trigger 1 and all HIJING events. This shows the trigger bias towards more trigger 2 in an event with a trigger 1.

the central events this comparison is difficult because the bias exists only for one of the three events which are super-positioned to create these events.
For the non-central events the bias in N_{coll} explains m_{bias} qualitatively. Both observables have the same dependence on the centrality and they have a similar magnitude. Although f_{bias} underestimates m_{bias} slightly. This difference can be explained by a scaling factor between the changed particle content in the event and the bias of N_{coll}. The analysis in central events does not contradict these conclusions. Due to the different generation procedure for the events the N_{coll} bias might be affected. In a cross check with HIJING events from the centrality 0–5% the correlation of the bias effects

centrality	$\langle N_{coll} \rangle$	f_{bias}	m_{bias}
central	375.7	1.015	1.054 ± 0.001
30–40%	159.6	1.067	1.084 ± 0.002
40–50%	91.7	1.111	1.140 ± 0.004

Table 6.2.: $\langle N_{coll} \rangle$ in all events of a certain centrality and the ratio to $\langle N_{coll}^{T1} \rangle$ which is only measured in events with a trigger 1 of $8 < p_{\mathrm{T1,trig}} < 12\,\mathrm{GeV}/c$. If not otherwise specified the statistical error of all shown observables are smaller than the shown precision.

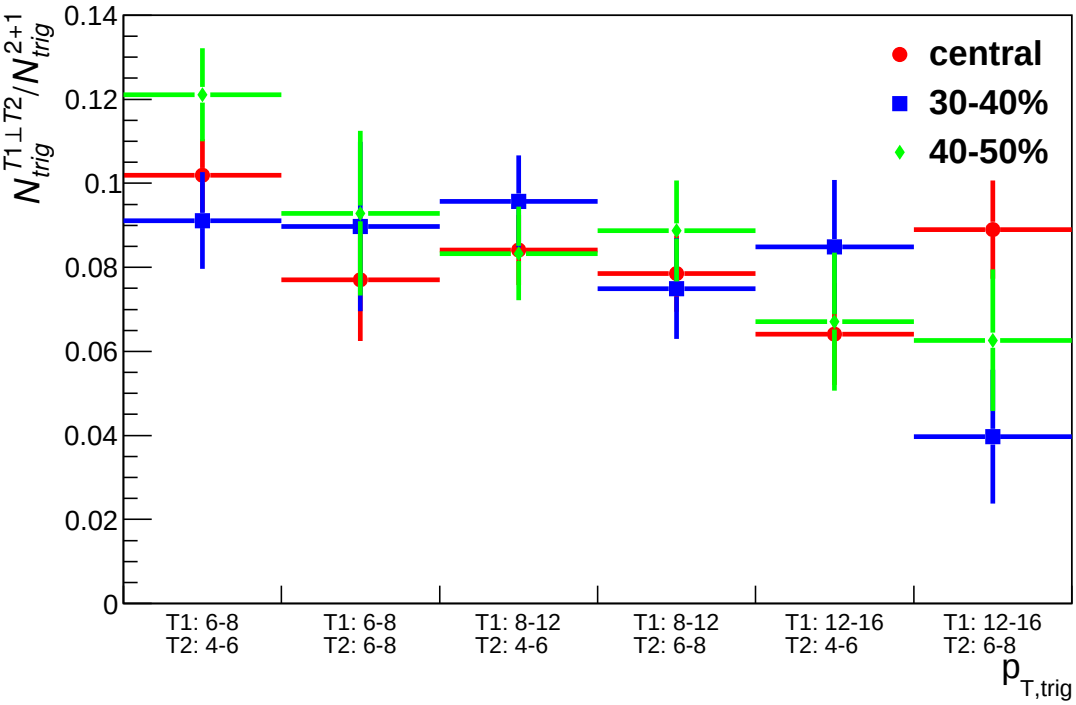

Figure 6.5.: Estimation of the correlated trigger 2 yield perpendicular to the trigger 1 in HIJING events. This yield is divided by the found trigger yield back-to-back with the trigger particle.

was verified.
To calculate the background component D the rate of perpendicular trigger combinations $\frac{M_1}{M_1+M_0}$ is needed. It is measured in 1+1 correlations at large $\Delta\eta$ which is called $Y_{large\Delta\eta}$ and at $\Delta\varphi \approx \pi/2$ which is called $Y_{\pi/2}$. For the large $\Delta\eta$ area the integration is done within $1.0 < |\Delta\eta| < 1.4$ and $|\Delta\varphi| < 0.51$. This range is identical to the range used before to extract m_{T1}. The yield at $\approx \pi/2$ is integrated within $1.40 < \Delta\varphi < 1.73$ and $|\Delta\eta| < 1.4$. Both yields are normalized to the same phase space and the difference is calculated. This difference is compared to the away side peak yield Y_{peak} which is measured at $2.80 < \Delta\varphi < 3.48$ and $|\Delta\eta| < 1.4$. The factor obtained out of this ratio is called r and it represents the amount of correlated trigger 2 at $\pi/2$ compared to the correlated trigger 2 at π.

$$r = \frac{N_{trig}^{T1\perp T2}}{N_{trig}^{2+1}} = \frac{Y_{\pi/2} - Y_{large\Delta\eta}}{Y_{peak} - Y_{large\Delta\eta}} \tag{6.16}$$

After the $Y_{\pi/2}$ yield was scaled to the correct phase space, the background is subtracted with the estimation from the large $\Delta\eta$ area. In Figure 6.5 the ratio r is shown for all trigger configurations which are used in this thesis.
With this new factor r the number of perpendicular trigger combinations can be expressed with the number of back-to-back trigger combinations. The sum of events with

a perpendicular trigger combination and without it M_1+M_0 is equal to all events. The same number id described with the number of events with and without a back-to-back trigger pair $N_1 + N_0$.

$$\frac{M_1}{M_1 + M_0} = \frac{rN_1}{N_1 + N_0} \tag{6.17}$$

With the described coefficients all components shown in Table 6.1 can be calculated. In Figure 6.6 the components are shown for the background same and mixed combinatorics methods in HIJING events at the example centrality of 30–40%. In this centrality the components B and C differ between background same and mixed combinatorics by roughly 8% ($m_{bias} \approx 1.08$).
It can be seen that the component A has basically no contribution. In the simple toy event generator (see Section 5.1) this component was predicted to be dominant. But in the toy generator the back-to-back trigger rate per event was much higher. The component D is small but not negligible.
With these background components, the ratio between the trigger obtained from mixed combinatorics $N_{trig}^{mixedComb}$ and the trigger from background same N_{trig}^{BGsame} can be calculated.

$$\frac{N_{trig}^{mixedComb}}{N_{trig}^{BGsame}} = \frac{B_{mixedComb} + C_{mixedComb}}{D + B_{BGsame} + C_{BGsame}} \tag{6.18}$$

The result of this components calculation is compared in Figure 6.7 with the result obtained from the measurement in HIJING events. The measured values agree with the expected values from the components calculation within the uncertainties. The trigger configuration $6 < p_{\mathrm{T1,trig}} < 8\,\mathrm{GeV}/c$ and $6 < p_{\mathrm{T2,trig}} < 8\,\mathrm{GeV}/c$ cannot be compared because the estimation of m is wrong. Due to the overlapping trigger momentum bins, the maximum possible trigger 2 momentum in each event is equal to the trigger 1 momentum found in that event and not $8\,\mathrm{GeV}/c$.
The conclusion from the calculations in this section is that no background method is perfect for estimating the background trigger combinations. The background same method contains the additional background component D which is not a real background. Because of this, the background same triggers overestimate the number of background trigger combinations in the same event. The mixed combinatorics method underestimates the components B and C because of the missing bias. In the same event measurement, the background rate of uncorrelated trigger 2 is increased by m_{bias} compared to the rate in the mixed combinatorics.
The estimation of m_{bias} or component D is not possible in the data analysis because the 1+1 correlations contain a flow signal which prevents the measurement of a baseline at large $\Delta\eta$. But in the data analysis the background trigger estimations from the mixed combinatorics and the background same method do deviate less from each other than in HIJING events.
In the data events the rate of perpendicular jets $\frac{M_1}{M_0+M_1}$ is at least 50%[4] smaller than

[4]This value is estimated from the $N_{trig}^{mixedComb}/N_{trig}^{BGsame}$ ratio in the data analysis which is closer to unity. This ratio is presented in Figure 8.8 in the systematic uncertainty analysis.

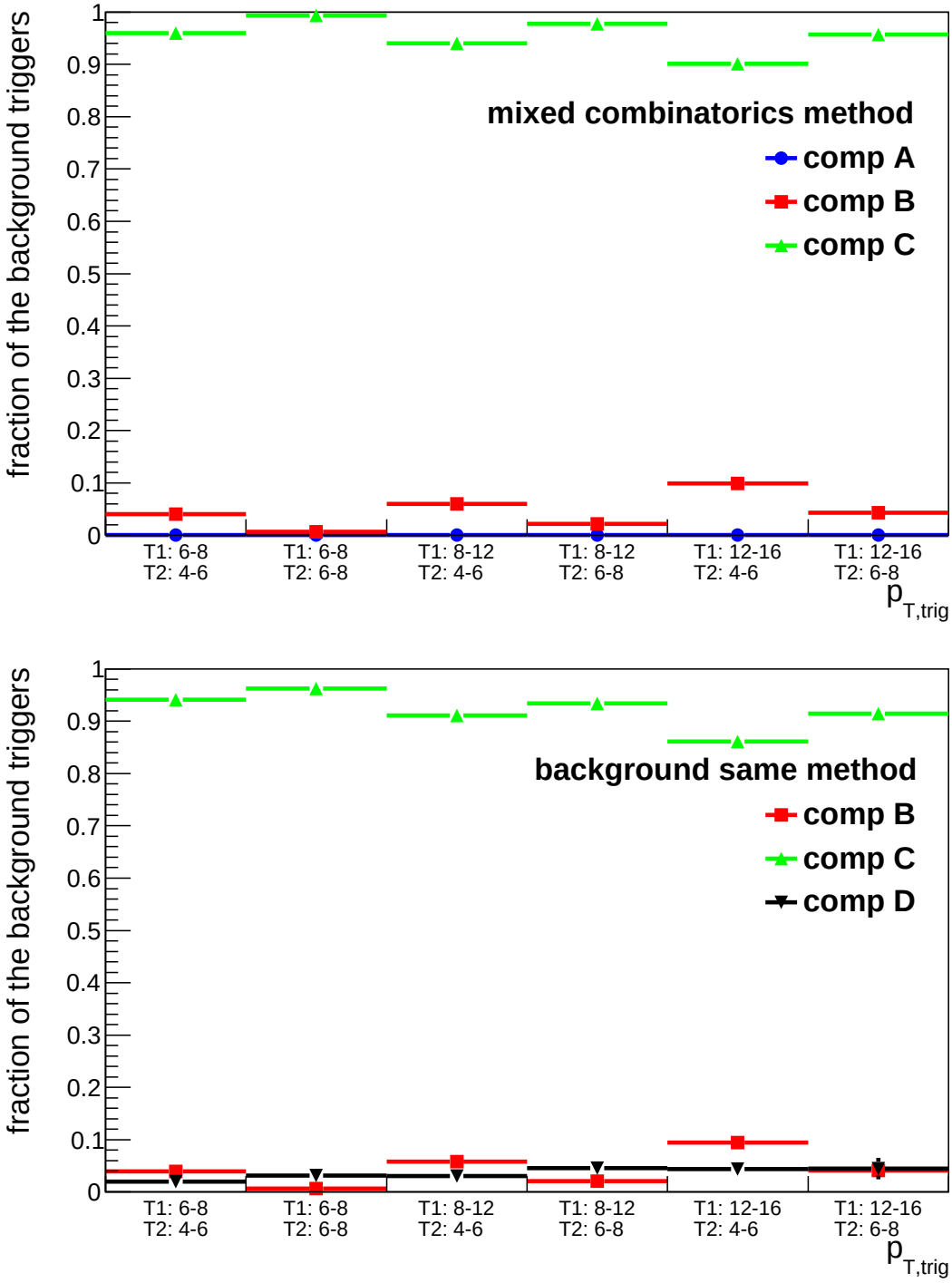

Figure 6.6.: Background components for the background same and the mixed combinatorics method in HIJING events at the centrality 30–40%. The full background of all trigger configurations is normalized to one so that the components can be compared with each other.

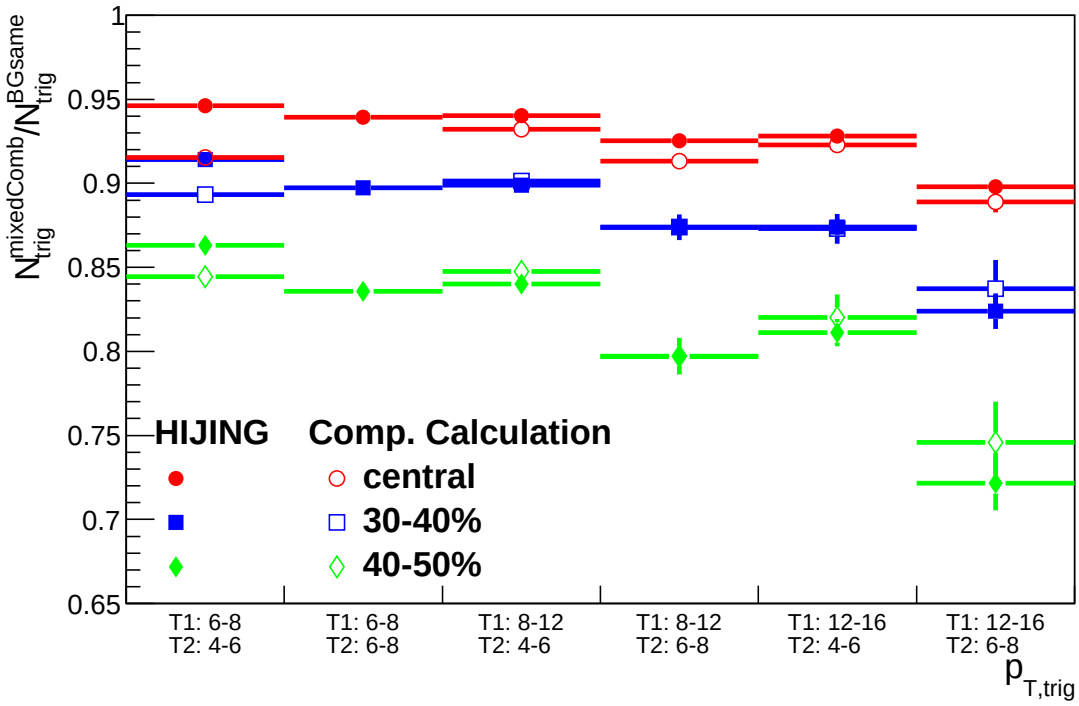

Figure 6.7.: Ratio of the found trigger combinations in the mixed combinatorics and background same method. The ratio is presented for HIJING events and the calculation is based on the background components. The background components calculations include parameters which have been obtained from other measurements in HIJING events. These measurements have been presented in this section. The reason for the deviation at the trigger configuration $6 < p_{\mathrm{T1,trig}} < 8\,\mathrm{GeV}/c$ and $6 < p_{\mathrm{T2,trig}} < 8\,\mathrm{GeV}/c$ is explained in the text.

in HIJING events. Qualitatively this can be observed by comparing the width of the away side jets in 1+1 correlations. In Figure 6.8 the $\Delta\varphi$ distribution of particles with a trigger 2 transverse momentum relative to trigger 1 is shown for the example trigger momentum $8 < p_{\mathrm{T1,trig}} < 12\,\mathrm{GeV}/c$ and the associated momentum $4 < p_{\mathrm{T,assoc}} < 6\,\mathrm{GeV}/c$. The distribution of the other trigger momenta follow the same trend. The background same method takes the trigger 2 from $\Delta\varphi \approx \pi/2$, which is illustrated with the green boxes. Both distributions, from data and HIJING, are normalized so that the average yield at $1.0 < |\Delta\varphi| < 1.4$ is zero because they have a different baseline. In both centralities the away side distribution from HIJING events is broader and it has a bigger contribution to the background same yield than the data distribution.
So the component D has a smaller contribution to the background in the analysis of data than in the analysis of HIJING events. Because of this smaller effect, the background trigger number is determined with the background same method, consistently

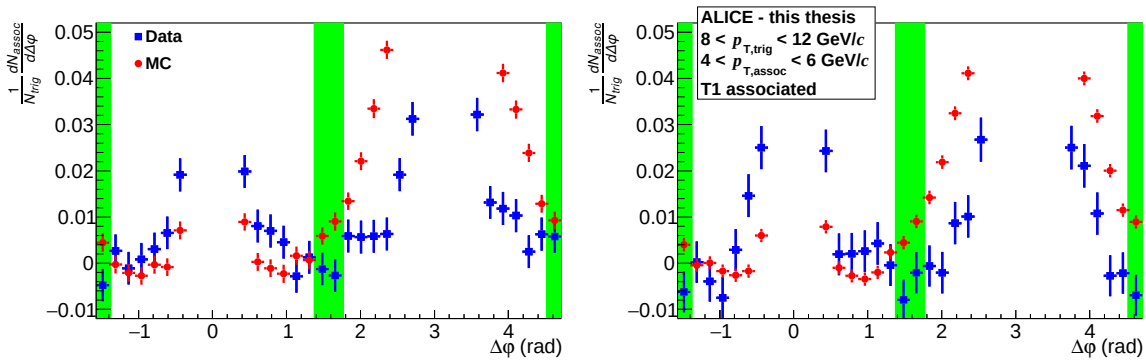

Figure 6.8.: 1+1 correlations from ALICE data and HIJING simulations in the 0–7.5% (left panel) and 30–50% (right panel) most central events. The trigger transverse momentum ranges are adjusted so that the distribution of the 2+1 trigger 2 are shown for a possible trigger 1. The distribution is normalized to 0 between $1.0 < \Delta\varphi < 1.4$. The green boxes show the area which is used to find the background same trigger particles for the 2+1 correlations.

in the analysis of data and HIJING events.

6.4.4. Scaled 1+1 Events

The background estimation from the background same and the mixed combinatorics methods have been shown to return good results. The number of background triggers and the per trigger background yield can be determined with both methods. In this section a method is introduced which improves the measurement of the per trigger yield.

The trigger 1 or trigger 2 associated yields which are obtained in the mixed combinatorics and in the background same method are expected to be identical to the 1+1 yield. In both correction methods uncorrelated trigger pairs are taken and the associated yield of one trigger particle is used for the correction. Because the trigger particles do not have a correlated trigger 2, the resulting yield per trigger in the 1+1 analysis is identical to the per trigger yield in the 2+1 background measurements. But the 1+1 method has much more statistics.

Some of the trigger particles in 1+1 correlations fulfill the requirements for 2+1 correlations as well. This means the 1+1 associated particle yield contains part of the 2+1 correlated signal yield. But this kind of signal yield is contained in the 2+1 background yield as well. One trigger from a correlated trigger pair can be matched with an uncorrelated second trigger. Consequently this yield has to be subtracted in the background subtraction because it was added due to an uncorrelated trigger combination.

In this background correction the per trigger 1+1 yield has to be scaled to the correct number of triggers to be usable for the subtraction. This number can be obtained

from the background same or the mixed combinatorics method. For the background subtraction in this thesis the background same trigger particles N_{trig}^{BGsame} have been chosen as background trigger estimation. The scaled 1+1 yield is subtracted from the same event yield.

$$\begin{aligned}
&\frac{1}{N_{trig}}\frac{d^2N_{T1assoc}}{d\Delta\varphi d\Delta\eta}([p_{\mathrm{T1,trig}}],[p_{\mathrm{T2,trig}}],[p_{\mathrm{T,assoc}}],\Delta\varphi,\Delta\eta,\alpha)\\
=&\frac{1}{N_{trig}^{2+1}-N_{trig}^{BGsame}}\left[\frac{d^2N_{T1assoc,same}}{d\Delta\varphi d\Delta\eta}([p_{\mathrm{T1,trig}}],[p_{\mathrm{T2,trig}}],[p_{\mathrm{T,assoc}}],\Delta\varphi,\Delta\eta,\alpha)\right.\\
&\left.-\frac{N_{trig}^{BGsame}}{N_{trig}^{1+1}}\frac{d^2N_{assoc,1+1}}{d\Delta\varphi d\Delta\eta}([p_{\mathrm{T1,trig}}],[p_{\mathrm{T,assoc}}],\Delta\varphi,\Delta\eta,\alpha)\right]
\end{aligned}\tag{6.19}$$

The background measurement for trigger 2 works the same way. But the p_T of the 1+1 measurement has to be adjusted to $p_{\mathrm{T2,trig}}$. The number of background triggers is identical to the number obtained for trigger 1 in the background same method.
The statistical uncertainty of the associated yield in Equation 6.19 contains several contributions. For a better readability the dependencies of the yields are not shown in the following equation. The uncertainty of the same event yield or the 1+1 yield are indicated with a σ in front of the yield like the uncertainty of the trigger numbers.

$$\begin{aligned}
&\sigma\left(\frac{1}{N_{trig}}\frac{d^2N_{T1assoc}}{d\Delta\varphi d\Delta\eta}([p_{\mathrm{T1,trig}}],[p_{\mathrm{T2,trig}}],[p_{\mathrm{T,assoc}}],\Delta\varphi,\Delta\eta,\alpha)\right)\\
=&\frac{1}{N_{trig}^{2+1}-N_{trig}^{BGsame}}\left[\left(\sigma\left(\frac{d^2N_{T1assoc,same}}{d\Delta\varphi d\Delta\eta}\right)\right)^2+\left(\frac{N_{trig}^{BGsame}}{N_{trig}^{1+1}}\sigma\left(\frac{d^2N_{assoc,1+1}^{T1assoc}}{d\Delta\varphi d\Delta\eta}\right)\right)^2\right.\\
&+\left(\frac{\sigma(N_{trig}^{2+1})}{N_{trig}^{2+1}-N_{trig}^{BGsame}}\left[\frac{d^2N_{T1assoc,same}}{d\Delta\varphi d\Delta\eta}-\frac{N_{trig}^{BGsame}}{N_{trig}^{1+1}}\frac{d^2N_{assoc,1+1}}{d\Delta\varphi d\Delta\eta}\right]\right)^2\\
&+\left(\frac{\sigma(N_{trig}^{BGsame})}{N_{trig}^{2+1}-N_{trig}^{BGsame}}\left[\frac{d^2N_{T1assoc,same}}{d\Delta\varphi d\Delta\eta}-\frac{N_{trig}^{2+1}}{N_{trig}^{1+1}}\frac{d^2N_{assoc,1+1}}{d\Delta\varphi d\Delta\eta}\right]\right)^2\\
&\left.+\left(\frac{N_{trig}^{BGsame}\sigma(N_{trig}^{1+1})}{(N_{trig}^{1+1})^2}\frac{d^2N_{assoc,1+1}}{d\Delta\varphi d\Delta\eta}\right)^2\right]^{1/2}
\end{aligned}\tag{6.20}$$

The uncertainty contribution proportional to the uncertainty of the 1+1 trigger particles or the 1+1 yield can be neglected because the statistics in this measurement is much higher than all the other contributions in this calculation.
The influence of the other uncertainty contributions vary dependent on the trigger conditions. For low trigger momenta $p_{\mathrm{T,trig}}$, the uncertainty of the same event yield is small because the statistics are big. But the numbers for N_{trig}^{2+1} and N_{trig}^{BGsame} are much bigger than the difference between them. This creates a big contribution which is proportional to $\sigma\left(N_{trig}^{2+1}\right)$ and $\sigma\left(N_{trig}^{BGsame}\right)$.
For high trigger momenta $p_{\mathrm{T,trig}}$, the number of background triggers N_{trig}^{BGsame} is low

and the difference $N_{trig}^{2+1} - N_{trig}^{BGsame}$ is big compared to the uncertainty of these trigger numbers. But in this case the statistics of the same event yield is small and $\sigma\left(\frac{d^2N_{T1assoc,same}}{d\Delta\varphi d\Delta\eta}\right)$ has a big contribution to the statistical uncertainty.
The scaled 1+1 events cannot be used for the background subtraction in a trigger configuration with overlapping trigger momentum bins. In this thesis this is the case for the trigger configuration $6 < p_{\mathrm{T1,trig}} < 8\,\mathrm{GeV}/c$ and $6\,\mathrm{GeV}/c < p_{\mathrm{T2,trig}} < p_{\mathrm{T1,trig}}$. Because of the requirement that the trigger 2 transverse momentum has to be smaller than the trigger 1 transverse momentum, the p_T spectrum of the 2+1 triggers is different than the p_T spectrum of the triggers in 1+1 correlations. For this trigger configuration the mixed combinatorics yield is used.

6.5. Uncertainty as a Function of Jets per Event

In the calculation of the statistical uncertainty in the last section it is not immediately clear how the number of independent jets per event influence the statistical uncertainty.
With the toy event generator, which was explained in Section 5.1, this was analyzed. By comparing two simulations with the same amount of events and a different number of jets per event, the simulation with more jets per event contains more trigger combinations. This decreases the statistical uncertainty of the same event yield. At the same time a higher percentage of these trigger pairs are uncorrelated trigger combinations. Thus the uncertainty proportional to ΔN_{trig}^{same} and ΔN_{trig}^{BGsame} rises, because the uncertainty of these values is not negligible compared to the difference of the values.
For different numbers of jets per event several datasets have been produced with the same number of events. In Table 6.3 the trigger numbers and the statistical uncertainty of the yield are shown. The relative uncertainties from the table are illustrated in Figure 6.9. Without doing the background event subtraction, the uncertainty of the extracted yield is smaller for events with more jets per event. After doing the subtraction, the events with less jets per event have a smaller uncertainty because of less uncorrelated trigger combinations although the absolute number of found correlated triggers is smaller as well. The relative uncertainty can be further reduced for all measurements by using more events.

6.6. Yield Extraction in the 2+1 Analysis

After the subtraction of the background events with the scaled 1+1 events, the associated particle yield still contains the backgrounds given in Equation 6.12. This yield does still contain the constant background μ_2 which exists as well in 1+1 correlations (see Section 5.5). Additionally the residual background contribution from associated particles correlated to trigger 2 but not correlated to trigger 1 μ_4 is contained (see Section 6.4.1). Fortunately this background distribution is independent of $\Delta\eta$ because there is no η correlation between the trigger particles (neither if they are correlated

number of jets	trigger same	uncertainty before BG corr (%)	trigger background	correlated triggers (%)	uncertainty after BG corr (%)
5	6405	0.9	2629	59.0	1.8
10	19295	0.6	11585	40.0	2.6
20	65551	0.5	48629	25.9	5.2
30	137069	0.4	112844	17.7	10.8
40	232575	0.3	208082	10.5	20.5

Table 6.3.: Relative statistical uncertainties of the 2+1 peak yield dependent on the number of jets in an event. For each number of jets 50 000 events were simulated with the toy event generator. For events with many jets this results in more absolute found trigger combinations but at the same time into a higher background rate. The uncertainties are extracted from the trigger 1 associated yield for a trigger momentum of $8 < p_{\mathrm{T1,trig}} < 12\,\mathrm{GeV}/c$ and $4 < p_{\mathrm{T2,trig}} < 8\,\mathrm{GeV}/c$. The associated particles are all particles which have a smaller transverse momentum than trigger 1 $p_{\mathrm{T,assoc}} < p_{\mathrm{T1,trig}}$. The relative statistical uncertainty is computed with the ratio out of the associated particle yield uncertainty and the associated particle yield itself.

nor if they are not correlated). This residual background appears in the correlation as ridge like the particles which were affected by particle flow. These two ridges overlay with each other and cannot be distinguished.
It is necessary to subtract all kind of background in the 2+1 correlations before the peak yield can be measured. The yield extraction works in 2+1 correlations the same way as in 1+1 correlations.
In Section 5.6 the fitting method is described. It is applied in the 2+1 correlations the same way as in the 1+1 correlations. The constant background does represent additionally the background due to μ_4 for the trigger 1 associated particles and the background due to μ_3 for the trigger 2 associated particles.
Before the bin counting method is used the background has to be subtracted with the $\Delta\eta$ gap method first. This is done the same way as for the 1+1 method which was explained in Section 5.7. For consistency reasons, the same integration range is used in 2+1 correlations as in 1+1 correlations.

6.7. Observables of the 2+1 Correlation Measurements

With the methods explained so far in this chapter the background corrected per trigger associated particle yield can be measured. To quantify if this yield is affected by medium effects it has to be compared to a baseline. In the following sections two measurements are presented which can be used as baselines.

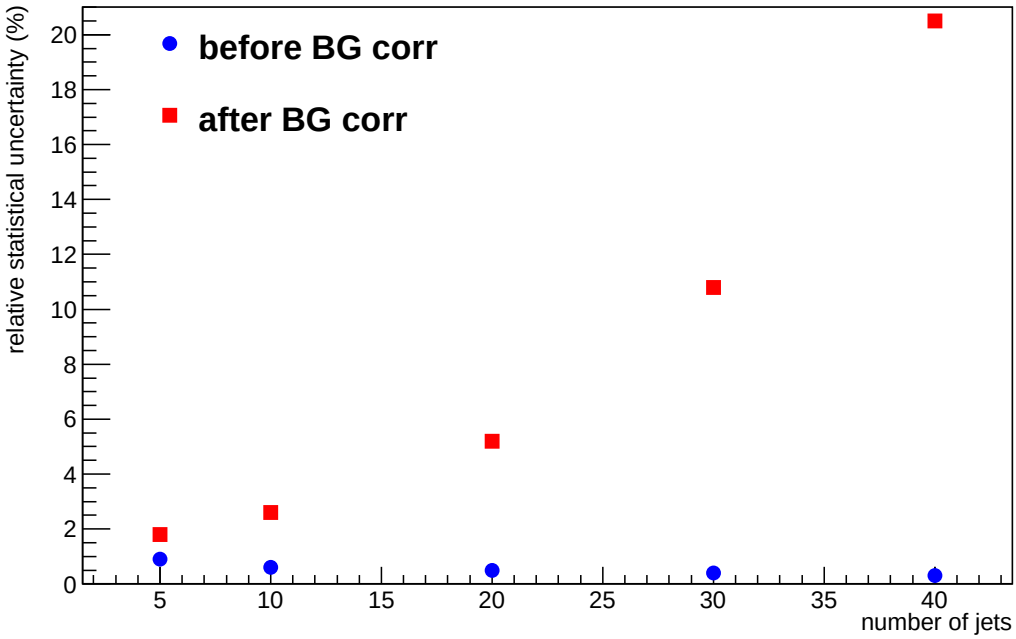

Figure 6.9.: Statistical uncertainties before and after the background correction from Table 6.3. The uncertainties are measured in events from the toy event generator in the near side peak of the trigger 1 correlations.

6.7.1. Ratio of the Yield from PbPb and pp Events

In Section 2.7 the results of the I_{AA} and I_{CP} from 1+1 correlations in ALICE were presented. The same analysis can be repeated with the associated particle yield from 2+1 correlations. This is done by dividing the 2+1 yield obtained from central Pb–Pb events by the 2+1 yield obtained from pp events (or from Pb–Pb events at 30–50% centrality). For the division the trigger 1 or the trigger 2 near side associated yield is used.
One advantage of the calculation with the 2+1 yield compared to the 1+1 yield is that the former away side yield can be described with the near side yield of trigger 2. This way the flow effects can be subtracted from the trigger 2 associated yield which makes it possible to determine the observables at lower $p_{\mathrm{T,assoc}}$.
The biggest problem of the 2+1 analysis is the small statistics. With the presented statistics, the 2+1 correlations can be performed up to 50% in centrality. Thus the I_{CP} is calculated

$$I_{CP} = \frac{\text{Pb–Pb(0–7.5\%)}}{\text{Pb–Pb(30–50\%)}}. \tag{6.21}$$

Instead of two Pb–Pb yields at different centralities the pp yield can be used as baseline. The ratio is called I_{AA} and it can be calculated for both Pb–Pb centralities.

$$I_{AA} = \frac{\text{Pb–Pb(0–7.5\%)}}{\text{pp}} \qquad I_{AA} = \frac{\text{Pb–Pb(30–50\%)}}{\text{pp}} \tag{6.22}$$

6.7.2. Ratio of the Trigger 1 and Trigger 2 Peak Yield R_{T1T2}

To study a potential effect of different path lengths through the medium of the particles associated to trigger 1 or trigger 2, a new observable is introduced. The ratio between the associated particle yield of trigger 1 and trigger 2 is called R_{T1T2}.

$$R_{T1T2} = \frac{\text{T1 assoc}}{\text{T2 assoc}} \tag{6.23}$$

This ratio compares the associated particle yield for correlated trigger particles. It can be used to quantify path length effects in the QGP. Because of the common origin of the triggers it is expected that unquenched jets have the same transverse momentum. There are two options how a trigger configuration can be created out of two unquenched jets. One explanation is a different path length in the QGP for the trigger 1 associated and the trigger 2 associated particles. Due to the different path length the particles are quenched differently. Even if both jets fragment identically, a trigger pair can be measured, because one jet has less energy due to the longer path length in the medium. Alternatively the trigger requirement can be fulfilled by a different jet fragmentation. How strong each of these effects contributes is dependent where the triggers were produced.
The jets can originate from the surface of the fireball and both fragment into the vacuum. A trigger combination can be found in these jets only due to different jet fragmentations. In a second scenario for each jet which travels through the QGP an energy loss is expected. If the path lengths of the jets in the QGP are different, the resulting jet energy in the detector is expected to be different due to a different energy loss. In these two jets particles on a different transverse momentum scale are expected. If a trigger combination is contained in these two jets, the jet with a smaller energy loss is more likely to contain the trigger 1 and the more quenched jet a trigger 2. From the measurement of a trigger combination itself it is not possible to identify which scenario caused the energy difference.
Assuming that no energy would be lost to the medium, the jet containing trigger 2 would have more energy available to produce low energetic particles than the jet containing the trigger 1. This additional available energy is the difference of the trigger momenta. If this effect dominates, R_{T1T2} would be negative.
But with a stronger energy loss of all particles in the second jet (trigger 2 and the associated particles) compared to the first jet, the associated particle yield of trigger 2 is expected to be smaller than the trigger 1 associated particle yield. This leads to

a positive R_{T1T2}. These two effects are superimposed in R_{T1T2}. So this observable can identify a strong energy loss. But a small energy loss may be shadowed by the asymmetry of the trigger particles.

7. Two plus One Particle Correlations in HIJING Events

The physics content of HIJING events is well known. So they were analyzed with the 2+1 correlation method to crosscheck and improve the method. One major improvement obtained from the HIJING analysis is the understanding of the background composition which was presented in Section 6.4.3. Additionally the HIJING events can be used to do the 2+1 analysis without the presence of a quenching signal. The results are presented in this section.
In Section 7.1 the number of found correlated trigger particles per event is presented for all used trigger configurations. This is compared with the purity (signal trigger per background triggers). Afterwards in Section 7.2 the background subtraction is demonstrated with one example trigger configuration and one example associated momentum $p_{\mathrm{T,assoc}}$. The projection on $\Delta\eta$ is compared for several analysis configurations. The obtained integrals from the Gaussian fits are presented in Section 7.3 for multiple centralities and both trigger particles. These yields are compared with each other in more detail in the Sections 7.4 and 7.5.

7.1. Trigger Combinations

For the analysis in this thesis $5{\cdot}10^7$ HIJING events were simulated for central collisions[1] and at centrality 30–50%.
The number of found trigger pairs per event (trigger rate) for each trigger configuration and centrality is shown in the lower panel of Figure 7.1. The trigger rate is large at small trigger p_{T} and decreases with increasing trigger p_{T}. At the highest trigger p_{T} the trigger rate is the smallest and thus the statistical uncertainty is the largest.
In the top panel of the same figure the purity is shown. It indicates the relative amount of trigger pairs which are emitted by the same source (the triggers are correlated) compared to all found trigger pairs. The other trigger pairs are randomly combined and do not originate from the same hard collision. For low trigger p_{T} the purity is small and it increases with increasing trigger p_{T}. The statistical uncertainty of the final yield increases with lower trigger rates.
The trigger combination at $6 < p_{\mathrm{T1,trig}} < 8\,\mathrm{GeV}/c$ and $6\,\mathrm{GeV}/c < p_{\mathrm{T2,trig}} < p_{\mathrm{T1,trig}}$ has a small trigger rate and a low purity. This trigger configuration originates preferentially from di-jets which have the same energy in both jets. Due to the small phase space of

[1] In Section 2.5 the HIJING event generation has been introduced. Central events are created out of a super-position of three events with the centrality 30–50%.

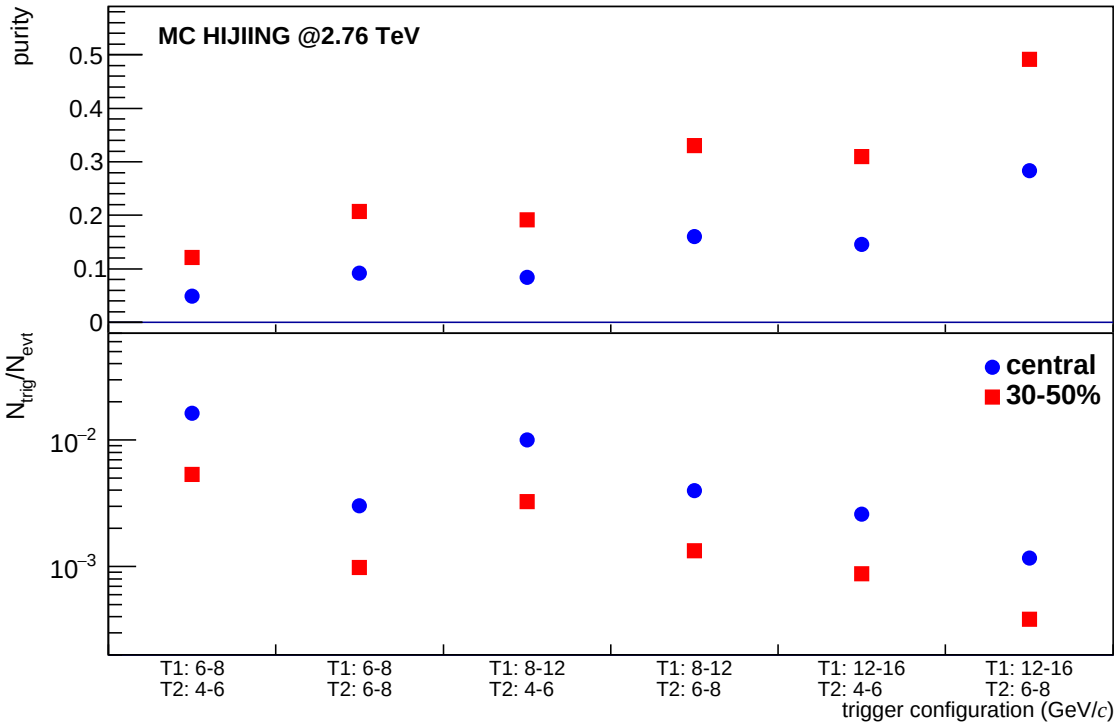

Figure 7.1.: The lower panel shows the trigger rate in HIJING events which represents the number of found correlated trigger combinations per event. The upper panel shows the purity of the trigger combinations. It indicates the relative amount of correlated trigger particles in all found trigger combinations.

the second trigger particle the abundance is small. Nevertheless, all $p_{\mathrm{T,assoc}}$ bins allow the extraction of the signal and the calculation of the I_{CP} and the R_{T1T2}.

7.2. Signal Extraction

The 2+1 particle correlations are measured in HIJING following the method described in Chapter 6. To illustrate the procedure, the 2+1 yield after mixed event correction is shown in Figure 7.2a. It contains the yield from many uncorrelated trigger combinations. This is corrected by subtracting the scaled 1+1 yield which is illustrated in Figure 7.2b. These particle yields correspond to $5.9 \cdot 10^6$ and $5.4 \cdot 10^6$ trigger combinations. The difference is shown in 7.2c and it represents the associated particle yield from $5 \cdot 10^5$ correlated trigger particles. This number of trigger particles is the difference between the number of trigger particles from the same event and the background same event which were mentioned before.
This is the standard background subtraction which is used for all trigger configurations but not for the configuration $6 < p_{\mathrm{T1,trig}} < 8\,\mathrm{GeV}/c$ and $6 < p_{\mathrm{T2,trig}} < 8\,\mathrm{GeV}/c$. In this special trigger configuration the mixed combinatorics event yield has to be used instead of the 1+1 yield because both trigger particles are from the same transverse

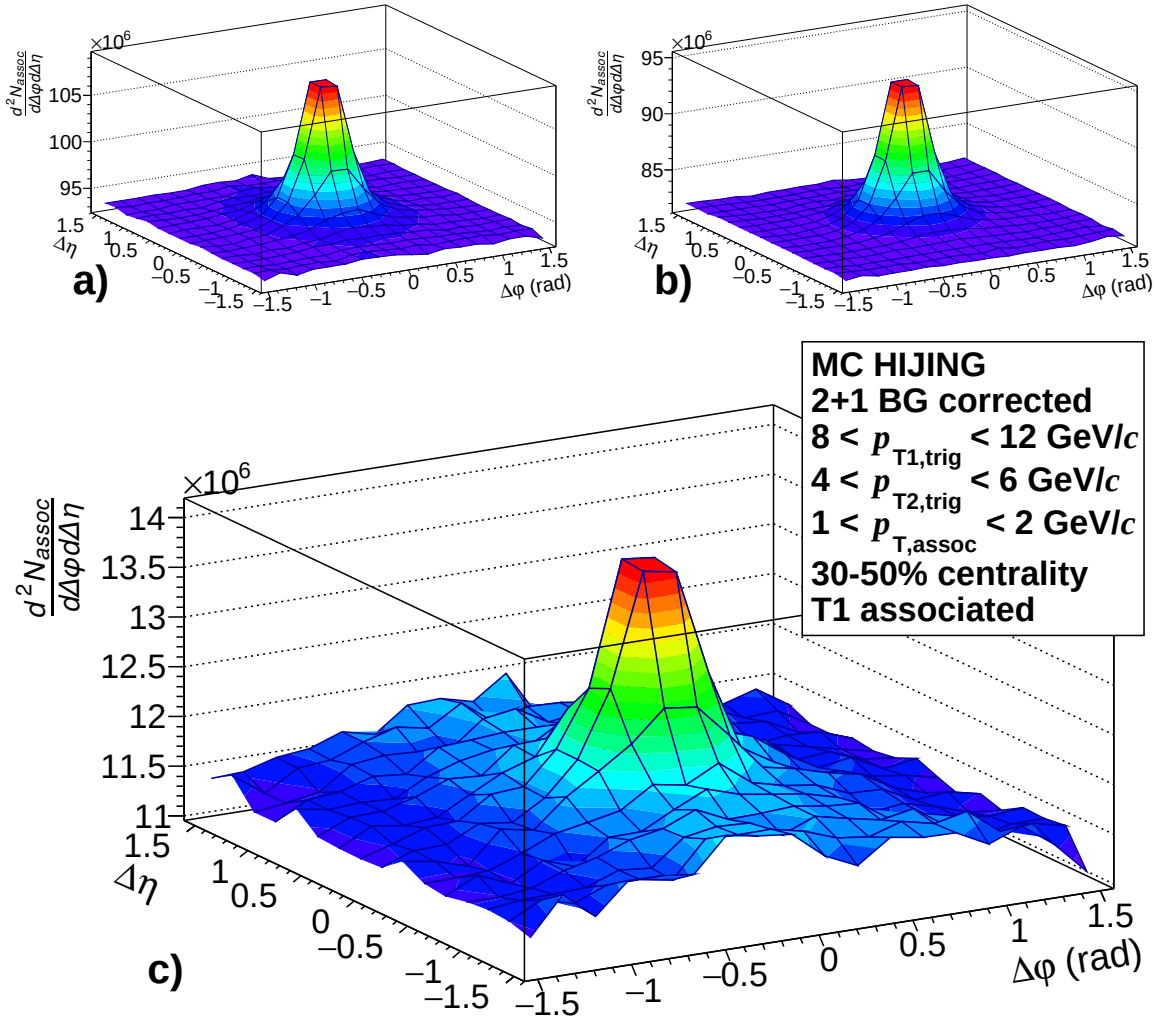

Figure 7.2.: The background correction with scaled 1+1 events is illustrated. In a) the same event and in b) the scaled 1+1 yield are shown which are subtracted from each other. The difference is shown in c). The scaled 1+1 yield measured the associated particles with the same $p_{T,assoc}$ relative to all trigger 1 without requiring a trigger 2.

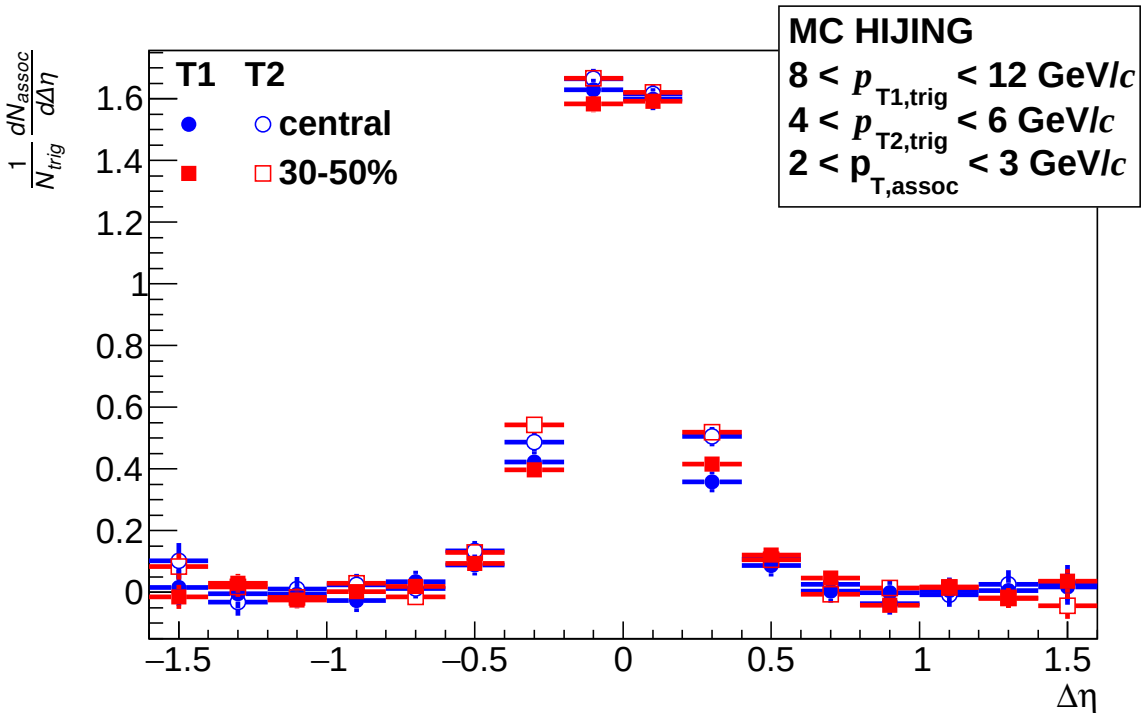

Figure 7.3.: The associated particle yield of 2+1 correlations is shown for both trigger particles from central events and from the 30–50% most central events. The baseline of all plots is estimated at $1.0 < |\Delta\eta| < 1.4$ and subtracted from each point of the corresponding distribution.

momentum bin.
Since the subtracted background is large the resulting yield has large statistical uncertainties compared to the same event yield before. In the next analysis step the peak is projected on the $\Delta\eta$ axis for $|\Delta\varphi| < \pi/6$. This is shown in the following for several analysis configurations.
In Figure 7.3 the associated particle yields from different trigger particles and centralities are shown. These yields are obtained with the trigger configuration $8 < p_{\mathrm{T1,trig}} < 12\,\mathrm{GeV}/c$ and $4 < p_{\mathrm{T2,trig}} < 6\,\mathrm{GeV}/c$ with the associated momentum $2 < p_{\mathrm{T,assoc}} < 3\,\mathrm{GeV}/c$. The baseline under the peaks is subtracted so that the peaks can be directly compared. It is estimated in the range $1.0 < |\Delta\eta| < 1.4$.
The associated peak yield is expected to be identical for different centralities because HIJING events do not contain any medium effects. Within the uncertainties the yield agrees for the two shown centralities. The yield ratios between two centralities are further compared in Section 7.4.
The trigger 2 associated yield is expected to be slightly larger than the trigger 1 associated yield. This bias is created due to the trigger bias (see Section 6.7.2) and no other effects are expected in HIJING events. Indeed the trigger 2 associated yield is observed to be a bit larger than the trigger 1 associated yield in central events. But

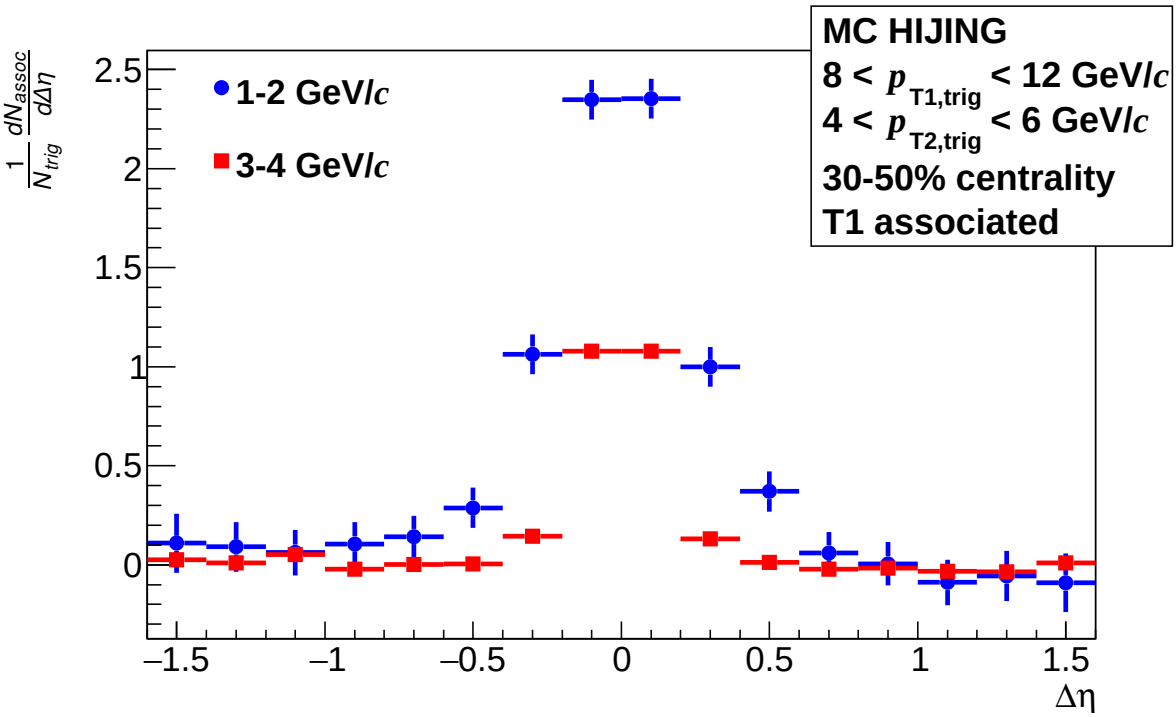

Figure 7.4.: The associated particle yield of trigger 1 is compared for two associated momenta. For illustration purposes the baseline is subtracted from both plots.

this difference is small. It is further analyzed in Section 7.5 with more trigger configurations and $p_{\mathrm{T,assoc}}$ bins.
For both centralities the same amount of events were simulated. But it can be observed that the statistical uncertainty of the yield from the more peripheral events is smaller. This is expected due to the smaller multiplicity in the events (see Section 6.5).
In Figure 7.4 the associated particle yield of the same trigger configuration is compared for different $p_{\mathrm{T,assoc}}$. By increasing $p_{\mathrm{T,assoc}}$ the peak yield and the peak width are reduced. This dependency exists at all trigger configurations, centralities and trigger particles. At higher $p_{\mathrm{T,assoc}}$ the uncertainty of the yield is reduced because there are less background particles.
The trigger 1 associated particle yield at $1 < p_{\mathrm{T,assoc}} < 2\,\mathrm{GeV}/c$ for different trigger configurations is shown in Figure 7.5. It is increased if one of the trigger p_{T} is increased. But this yield increase is not significant within the uncertainty. A similar dependency can be observed for all $p_{\mathrm{T,assoc}}$.

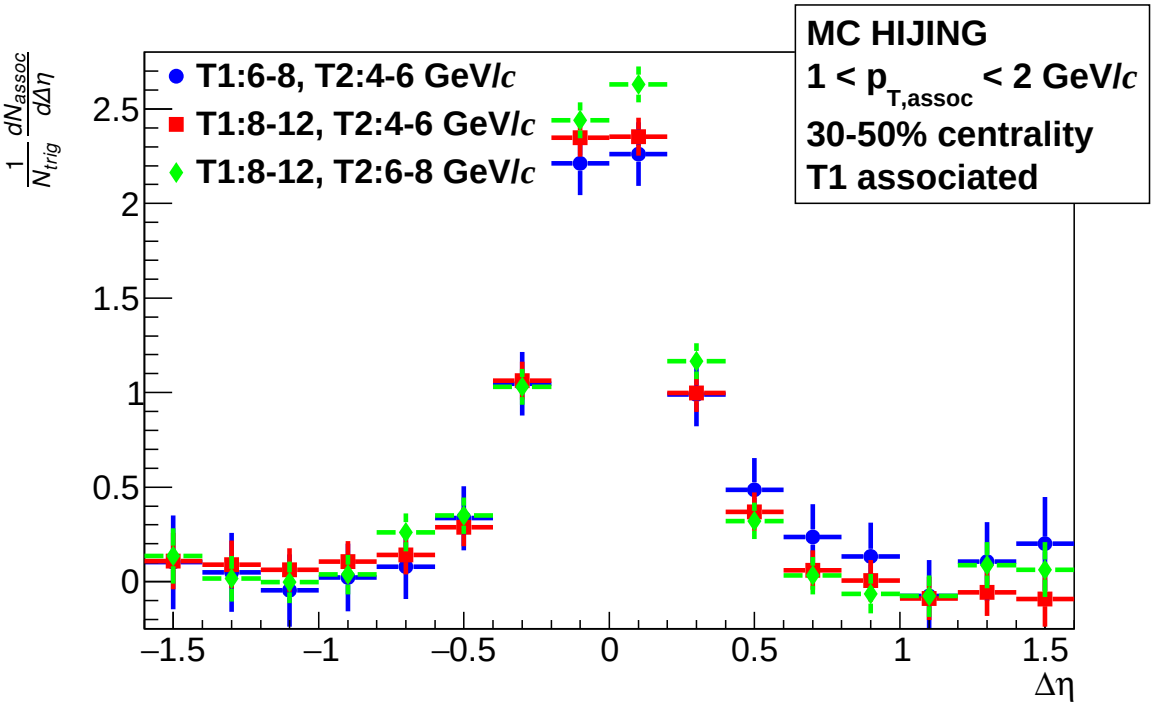

Figure 7.5.: The associated particle yield of trigger 1 is shown for multiple trigger configuration from central events. The associated momentum is $1 < p_{\mathrm{T,assoc}} < 2\,\mathrm{GeV}/c$. For illustration purposes the baseline is subtracted from all plots.

7.3. The Integrated Correlation Peaks in HIJING

The peak yields from correlated trigger particles are integrated with Gaussian fits (see Equation 5.16). The integral Y measures the associated particle yield per trigger. In Figure 7.6 the associated particle yield is shown for the different centralities (central or 30–50%) and the different associated triggers (trigger 1 or trigger 2) for six trigger configurations. For each trigger configuration the trigger 1 associated yield is shown on the left side of the dashed line and the trigger 2 associated yield on the right side. The panel on the top left of the Figure corresponds to the lowest trigger p_{T} and the panel on the lower right to the highest trigger p_{T}.
The trigger 2 associated particle yield is measured for momenta smaller than this p_{T}. For the trigger 1 associated particles a similar constraint is used. The minimum $p_{\mathrm{T1,trig}}$ has to be greater then the maximal measured $p_{\mathrm{T,assoc}}$. In the top row of the panels the trigger 1 momentum is $6 < p_{\mathrm{T1,trig}} < 8\,\mathrm{GeV}/c$, this means the highest associated momentum bin is $5 < p_{\mathrm{T,assoc}} < 6\,\mathrm{GeV}/c$. For all other panels the minimum $p_{\mathrm{T1,trig}}$ is larger or equal $8\,\mathrm{GeV}/c$ which is the maximum measured $p_{\mathrm{T,assoc}}$.
The associated particle yield depends strongly on $p_{\mathrm{T,assoc}}$. At the same time no strong dependency is observed on the trigger p_{T}, the centrality or which of the two trigger particles is used for the correlation analysis. Possibly existing dependencies on the

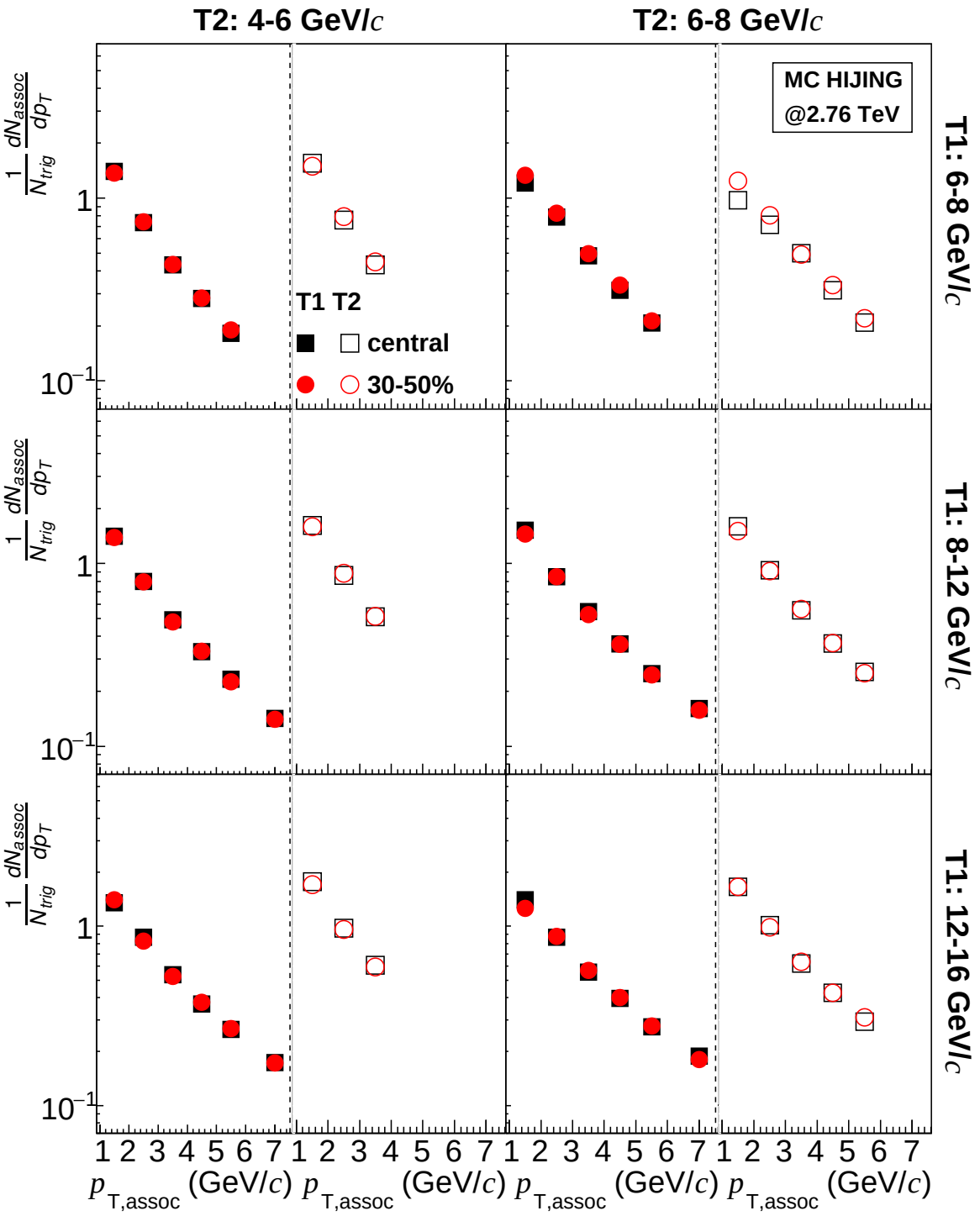

Figure 7.6.: The integrated per trigger 2+1 peak yield is shown for all trigger 1 and trigger 2 associated particles from central events and centrality 30–50%. All events are generated with the HIJING generator.

centrality and the trigger particle are analyzed in the next sections.

7.4. Centrality Dependence of the Particle Yield

The HIJING simulations do not include any medium effects. The only effect which the different centralities have on the event are the changed particle multiplicities. The structure of a single jet is not affected. So the same associated particle yield is expected at both centralities. The I_{CP}, the ratio between the associated particle yield from central events and the centrality 30–50% (see Equation 6.21), is expected to be unity. It is shown in Figure 7.7 for the 2+1 analysis in HIJING events. The plots for the different trigger configurations are arranged the same way as in Figure 7.6 for the integrated peak yield.
For all trigger configurations except one the I_{CP} is compatible with unity. No general dependency of the I_{CP} on $p_{\mathrm{T,assoc}}$ can be observed. In some plots the I_{CP} is for all points slightly above or below unity. This can be caused by a statistical fluctuation in the background subtraction. If the number of background triggers is fluctuating, all points for the corresponding trigger configuration are shifted.
The trigger configuration $6 < p_{\mathrm{T1,trig}} < 8\,\mathrm{GeV}/c$ and $6\,\mathrm{GeV}/c < p_{\mathrm{T2,trig}} < p_{\mathrm{T1,trig}}$ deviates from the described behavior. For all associated momenta except $3 < p_{\mathrm{T,assoc}} < 4\,\mathrm{GeV}/c$ the I_{CP} is below unity. The analysis at this trigger configuration may contain a systematic effect due to the identical momentum bin for both trigger particles. The background subtraction is different from the subtraction of the other trigger configurations. Probably one of these two reasons causes the the I_{CP} to be systematically below unity.
The measured constant I_{CP} at unity for most of the trigger configurations fulfills the expectations. This is a successful test of the 2+1 correlation method.

7.5. Trigger Dependence of the Particle Yield

In Figure 7.8 the ratio between the associated particle yield of the first and second trigger particle R_{T1T2} (see Equation 6.23) is shown. The statistical uncertainty of the yields from central events is bigger than the uncertainty of the yield from the 30–50% most central events due the lower purity.
For almost all trigger configurations R_{T1T2} is below unity. This lowering is created by the difference of the trigger p_{T} (see Section 6.7.2). The effect is stronger for larger transverse momentum differences between the trigger particles. At small trigger p_{T} differences ($6 < p_{\mathrm{T1,trig}} < 8\,\mathrm{GeV}/c$, $4 < p_{\mathrm{T2,trig}} < 6\,\mathrm{GeV}/c$ and $8 < p_{\mathrm{T1,trig}} < 12\,\mathrm{GeV}/c$, $6 < p_{\mathrm{T2,trig}} < 8\,\mathrm{GeV}/c$) R_{T1T2} is in agreement with unity for some $p_{\mathrm{T,assoc}}$. On average it is still below unity.
The analysis with HIJING events has shown that R_{T1T2} is systematically below unity. This means that there are more associated particles around trigger 2 than there are around trigger 1. With an increasing p_{T} difference between the trigger particles the

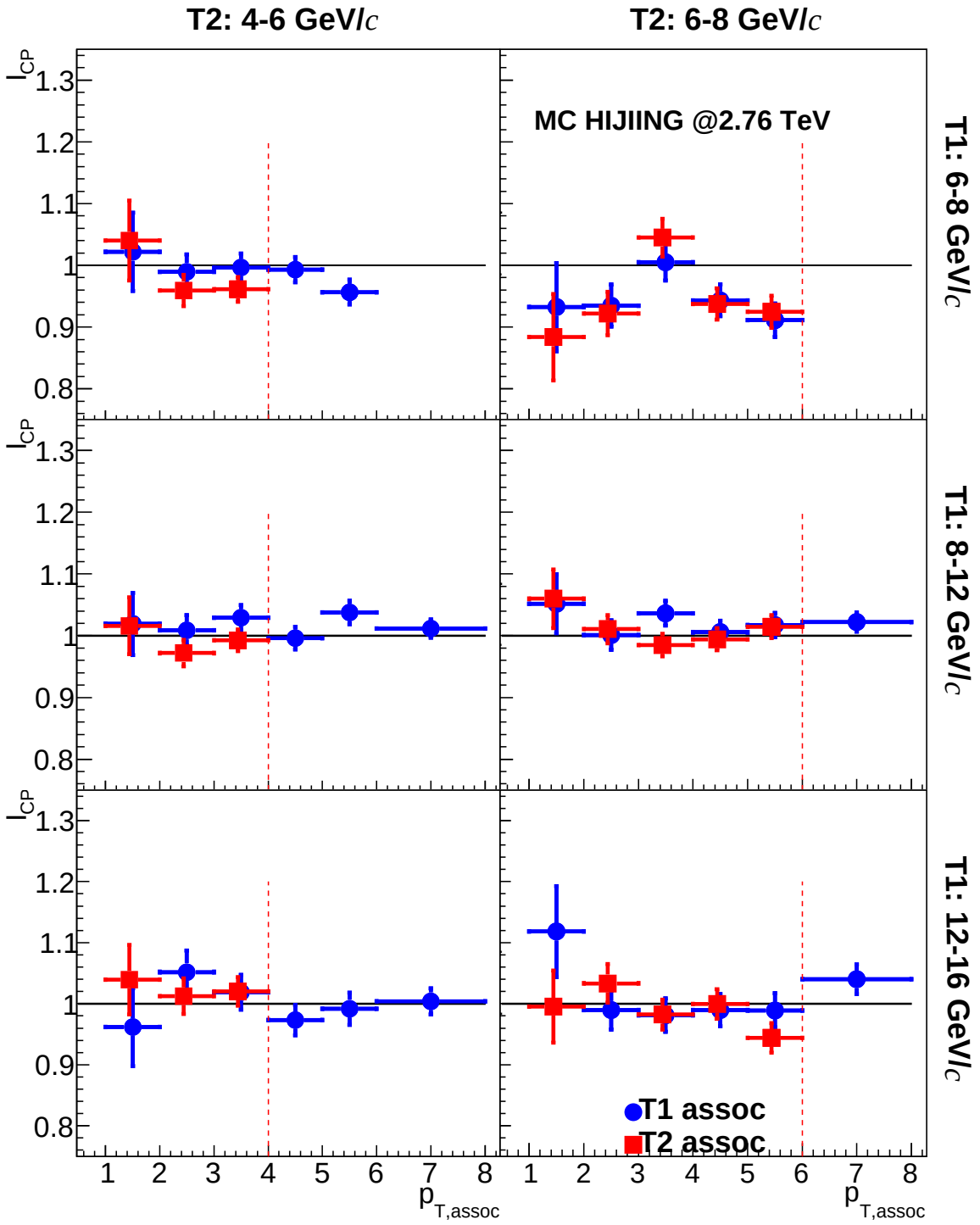

Figure 7.7.: I_{CP} of the per trigger associated yield shown in Figure 7.6. The red line indicates the minimum $p_{\mathrm{T2,trig}}$. At higher $p_{\mathrm{T,assoc}}$ only trigger 1 associated particles are measured and thus the I_{CP} can only be calculated for the trigger 1 associated particles.

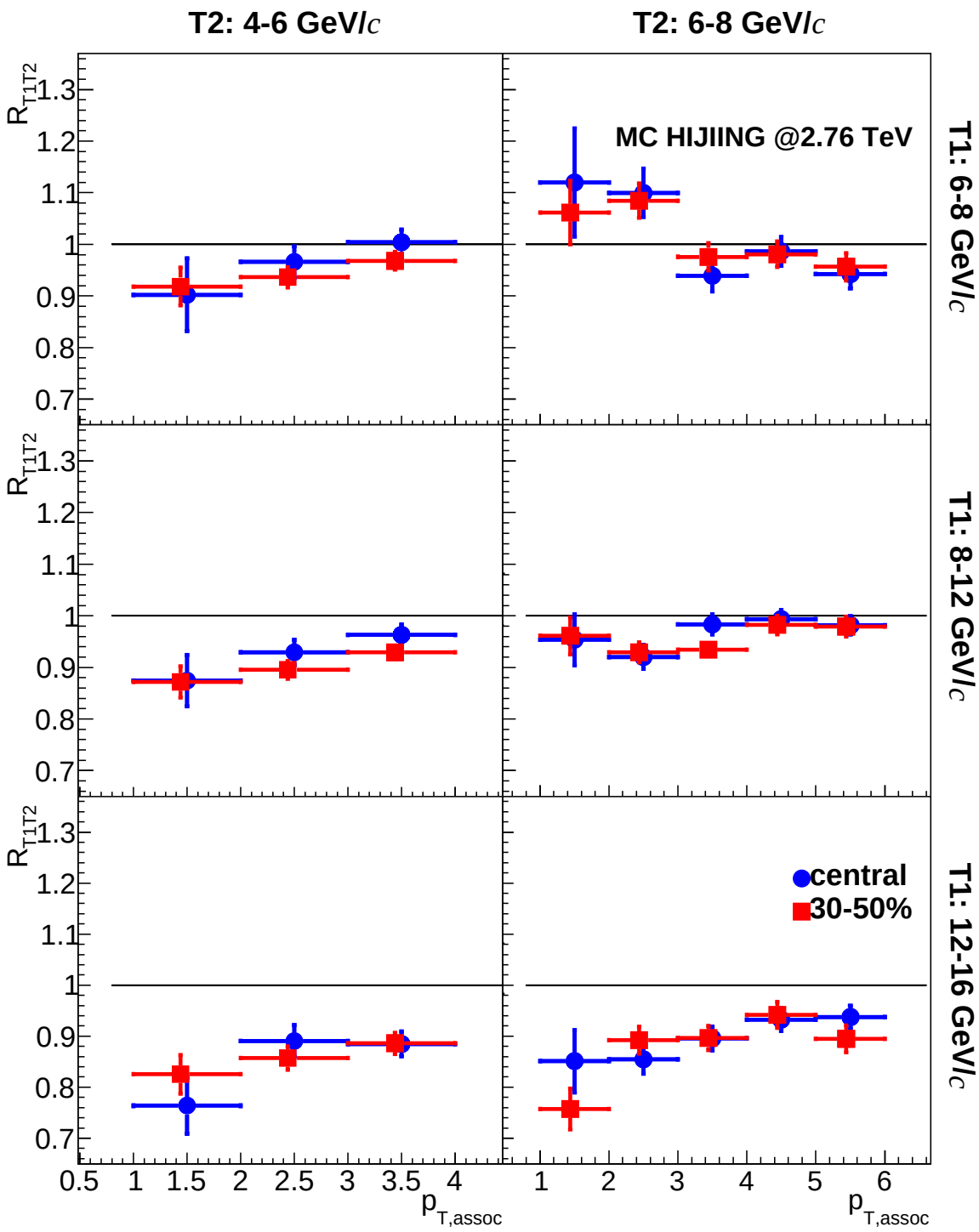

Figure 7.8.: R_{T1T2} of the 2+1 associated per trigger yield in HIJING simulations. The per trigger yield itself is shown in Figure 7.6.

effect gets larger. This sets a baseline for the R_{T1T2} analysis in data.

7.6. Summary

The 2+1 correlations can be measured in HIJING events. The associated particle yield is very similar for different trigger configurations and centralities.
The agreement of the I_{CP} with unity in all trigger configurations, but the one with symmetric trigger p_{T} ranges, shows that no multiplicity dependency exists in the 2+1 correlation measurements. This validates the 2+1 correlations method.
R_{T1T2} is systematically below unity. At larger p_{T} differences between the trigger particles, R_{T1T2} is smaller. The effect is created by the trigger bias which requires more energy for trigger 1 than for trigger 2. Accordingly more energy is available for associated particles of trigger 2.
The 2+1 correlations in HIJING events provide an analysis without any medium effects. This analysis provides a baseline which can be used to compare the results obtained in data. If they show a different behavior this may indicate medium effects which are not modeled in HIJING.

8. Systematic Uncertainties

In this chapter the systematic uncertainties of the 2+1 analysis are discussed for the integrated peak yield Y, I_{CP}, I_{AA} and R_{T1T2}. The last three observables are derived from the integrated peak yield. The existence of systematic uncertainties in an observable are analyzed with the Barlow checks [Bar02]. In such a check the observable is calculated twice. These calculations are slightly different to check if this causes a systematic effect on the observable. If the result agrees within the uncertainties the Barlow check is passed and no systematic uncertainty is assigned.
The Barlow criteria are checked for the peak yield estimation. If this check is successful, no systematic uncertainty is observed within the available statistics. In this case the derived observables do not contain a systematic uncertainty either. If the Barlow check is failed the derived observables are analyzed with the Barlow criteria as well.
The Barlow check procedure is described in Section 8.1. All analyzed sources of systematic uncertainties are described in Section 8.2. This is followed up with the estimation of the systematic uncertainty for one source of the systematic uncertainties which failed the Barlow check in Section 8.3.

8.1. Check of the Barlow Criteria

The Barlow criteria are used to identify a systematic uncertainty. In this example the z_{vtx} cut is used as possible uncertainty source. First the 2+1 analysis is run with the standard configuration. Then the analysis is repeated with a reduced z-vertex range $|z_{vtx}| < 4\,\mathrm{cm}$.
In Figure 8.1 the per trigger peak yield is fit for a z-vertex of $|z_{vtx}| < 4\,\mathrm{cm}$ and $|z_{vtx}| < 8\,\mathrm{cm}$. For the shown examples the peak was fitted to $Y_{z4} = 3.15 \pm 0.54$ (reduced z-vertex) and $Y_{z8} = 3.19 \pm 0.45$ (standard measurement). Out of these values the ratio $Y_{z4}/Y_{z8} = 0.99 \pm 0.09$ is calculated. The statistical fluctuations from Y_{z4} are fully contained in Y_{z8}, because the data sample with $|z_{vtx}| < 4\,\mathrm{cm}$ is a subsample of the full dataset. So the uncertainty of the ratio has to be calculated with taking into account the correlation $\rho = \sigma(Y_{z8})/\sigma(Y_{z4})$ [Bar02].

$$\sigma\left(\frac{Y_{z4}}{Y_{z8}}\right) = \frac{Y_{z4}}{Y_{z8}}\sqrt{\left(\frac{\sigma(Y_{z4})}{Y_{z4}}\right)^2 + \left(\frac{\sigma(Y_{z8})}{Y_{z8}}\right)^2 - \frac{2\sigma(Y_{z8})^2}{Y_{z4}Y_{z8}}} \tag{8.1}$$

The standard rules for the uncertainty propagation are used for the ratio. The same calculation for the ratio and the uncertainty is repeated for all associated particle

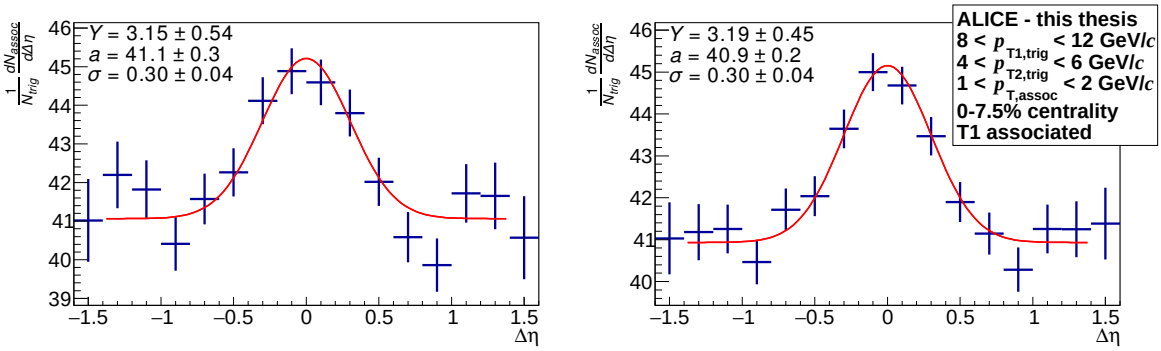

Figure 8.1.: 2+1 peak yield measurement for $|z_{vtx}| < 4\,\mathrm{cm}$ (left panel) and $|z_{vtx}| < 8\,\mathrm{cm}$ (right panel).

transverse momentum ranges of this trigger configuration. In Figure 8.2 the ratios between the yields from the different z-vertex ranges are shown as function of $p_{\mathrm{T,assoc}}$. Following the Barlow criteria [Bar02] no systematic uncertainty exists if the points are within their statistical uncertainty compatible with unity. This check is performed by checking how many standard deviations σ the ratio deviates from unity. If a point agrees with unity within a 1σ uncertainty this passes the Barlow 1σ check. Statistical fluctuations on the 2σ level are common. If many separate checks are performed, some 3σ deviations from unity are expected. Higher order deviations should be analyzed in detail if they are caused by a systematic effect.
In the example in Figure 8.2 for the momentum bin $3 < p_{\mathrm{T,assoc}} < 4\,\mathrm{GeV}/c$ a significant deviation from unity is observed. The value is 1.17 ± 0.05 which represents a 4σ deviation from unity. This bin has been further analyzed and it was found out that the baseline of the Gaussian fit changed considerably. It is not clear how the change of the z_{vtx} cut caused this. But the other $p_{\mathrm{T,assoc}}$ bins show a good agreement with unity and no consistent deviation.
The same plots have been created for all trigger configurations and they are shown in Figure 8.3. In two plots a systematic deviation from unity appears. These plots belong to the trigger configurations $6 < p_{\mathrm{T1,trig}} < 8\,\mathrm{GeV}/c$, $4 < p_{\mathrm{T2,trig}} < 6\,\mathrm{GeV}/c$ and $12 < p_{\mathrm{T1,trig}} < 16\,\mathrm{GeV}/c$, $6 < p_{\mathrm{T2,trig}} < 8\,\mathrm{GeV}/c$. In both trigger configurations a fluctuation of the background triggers appeared. This one fluctuation affects all $p_{\mathrm{T,assoc}}$ bins of that trigger configuration. But in both plots most of the points pass the Barlow 2σ criterion.
The uncertainty in general can be analyzed by counting the points which pass the different Barlow confidence levels. In Table 8.1 the number of points which pass each Barlow criterion are presented. Each point is listed at the minimum σ cut it passes. A measurement which is within 1σ compatible with unity is obviously compatible within 2σ as well. Consequently this point is not mentioned at the 2σ level. Most points are within the confidence interval of 1 or 2σ. There are two measurements which differ by 4σ. One has been mentioned before and the other one belongs to the trigger configurations $12 < p_{\mathrm{T1,trig}} < 16\,\mathrm{GeV}/c$, $6 < p_{\mathrm{T2,trig}} < 8\,\mathrm{GeV}/c$ with

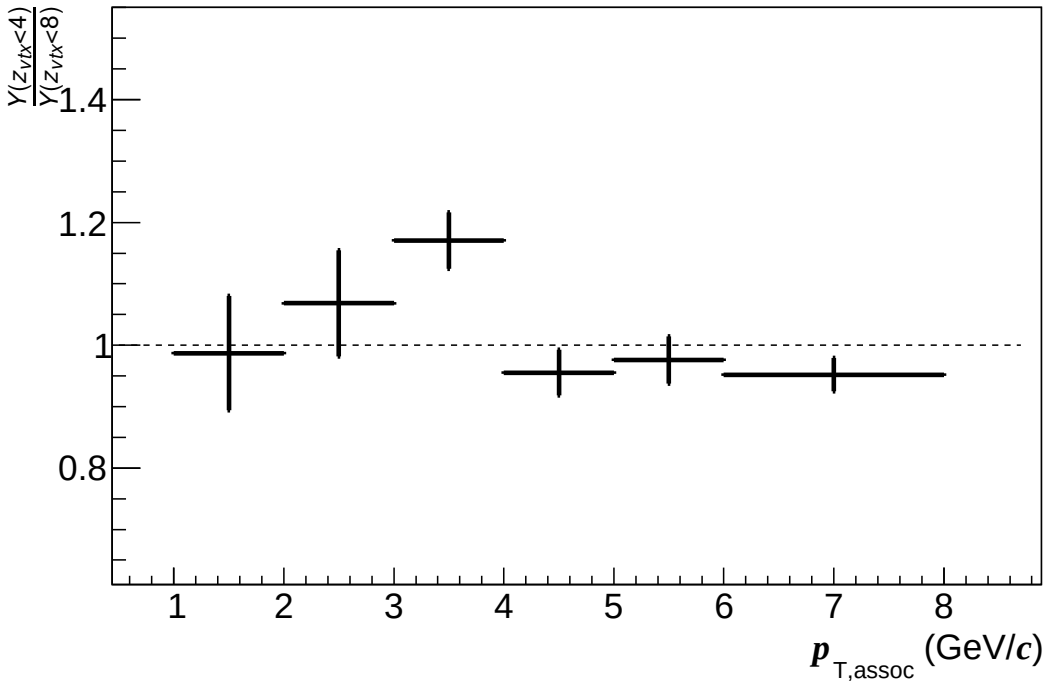

Figure 8.2.: Ratio of the peak yield for $|z_{vtx}| < 4\,\text{cm}$ and $|z_{vtx}| < 8\,\text{cm}$ as function of $p_{\text{T,assoc}}$.

$5 < p_{\text{T,assoc}} < 6\,\text{GeV}/c$. Different flucutuations have been identified to cause the failed Barlow checks. Because all other points fulfill the Barlow criteria, the Barlow check is accepted. This means no systematic uncertainty is assigned due to the z_{vtx} cut.
If for another uncertainty source the Barlow criteria are not passed, a systematic uncertainty has to be assigned. How this uncertainty is estimated will be explained for every failed Barlow check individually in the following sections.

σ	Barlow criterion passed
1	34
2	18
3	4
4	2
5	0

Table 8.1.: The deviation of each measurement in Figure 8.3 from unity is divided by the uncertainty of this measurement. The result is rounded up to the next full integer which represents the Barlow confidence level.

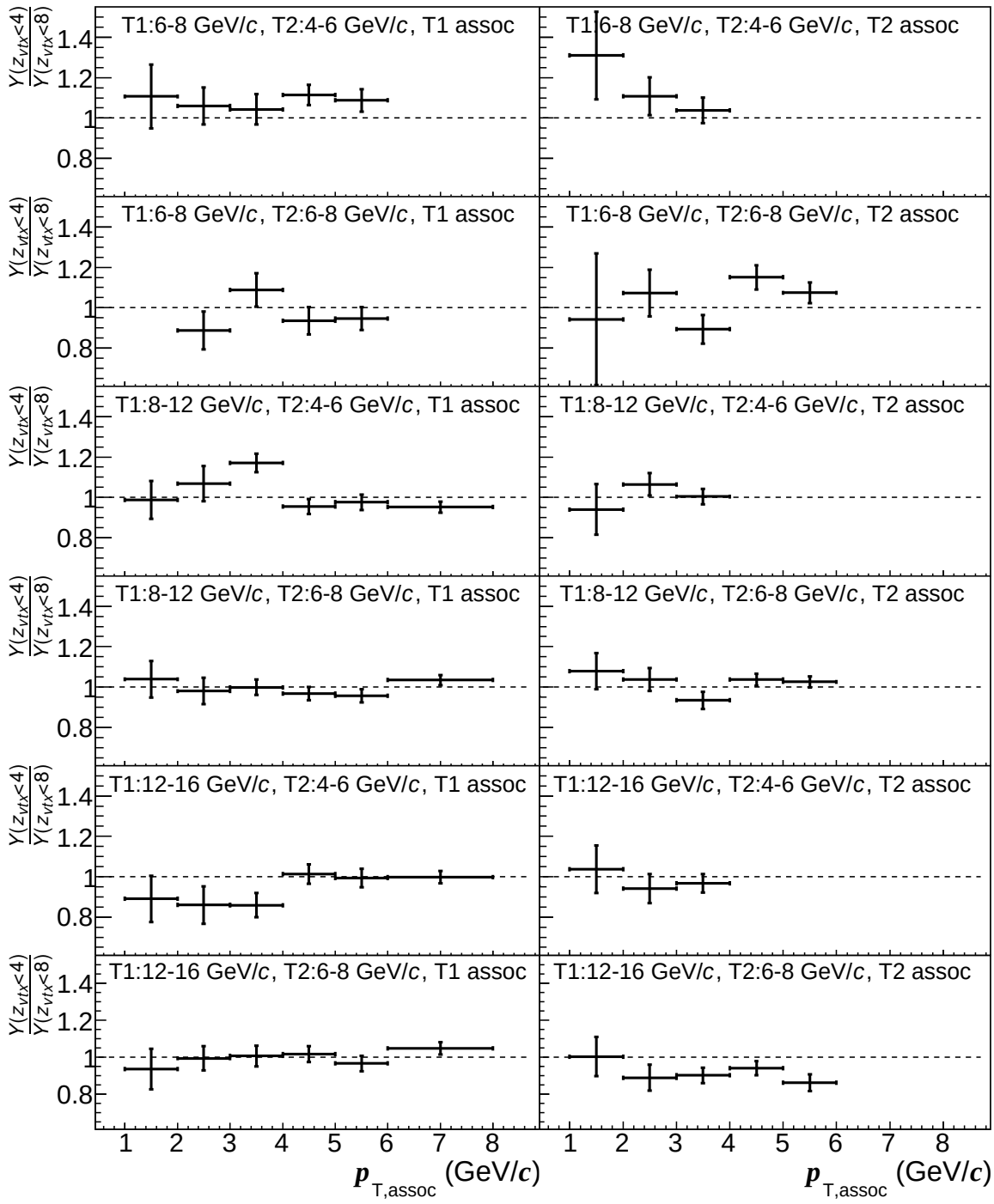

Figure 8.3.: Ratio of the peak yields for two different z-vertex ranges. On the left side the trigger 1 associated yield comparisons and on the right side the trigger 2 associated yield comparisons are shown. Unity is indicated with the dashed line.

$p_{\mathrm{T,assoc}}$ (GeV/c)	0–7.5%	30–50%	I_{CP}	R_{T1T2}
1–2 GeV/c	5.5%	2.5%	3.0%	-
2–3 GeV/c	10.0%	5.0%	5.0%	-
3–8 GeV/c	11.5–14.5%	6.5–7.0%	4.0–7.5%	-

Table 8.2.: Systematic uncertainty in the analysis due to the 2010-2011 track cut uncertainty.

8.2. Sources of Systematic Uncertainties

The Barlow criteria are checked for many possible systematic uncertainties. All possible sources except the reduced z_{vtx} cut are listed in the text below. The results of the Barlow checks are presented at the end of this section in Table 8.3.

Track Selection Instead of hybrid track cuts global track cuts are used to select tracks in the detector. The differences between these track cuts are described in Section 4.5. This track selection analysis has been done for Pb–Pb events but not for pp events because the used pp data format does not support the global track cut analysis. It is assumed that the uncertainties are on the same level as for Pb–Pb events. Because the Barlow criteria are passed for Pb–Pb events this is assumed for pp events as well.
A systematic difference was found within ALICE for the associated particle yield measured in the 2010 and 2011. It is explained as a difference in the understanding of the detector efficiencies in these years [GKM16]. In Table 8.2 the relative differences of the associated particle yield in 1+1 collisions from 2010 and 2011 are presented. Because this is a constant effect in the particle yield of each event, this can be directly used for 2+1 correlations as well. These relative differences are directly used as systematic uncertainties.
The values are determined for the 0–7.5% and for the 30–50% most central events. The difference of the values at the two centralities can be used as uncertainty on the I_{CP}. The R_{T1T2} has no effect because the same relative effect is observed for trigger 2 than it is observed for trigger 1.
In pp events a track selection uncertainty much smaller than the Pb–Pb uncertainty is expected. Thus no systematic uncertainty is assigned to the pp yield. Consequently the I_{AA} has an uncertainty equal to the uncertainty of the Pb–Pb yield which is used for the calculation of the I_{AA}.
This observed systematic effect is treated as systematic uncertainty in this thesis. As a conservative approach the maximum values from Table 8.2 are used.

Bin Position The $\Delta\eta$ bin positions in the peak yield have been changed by half a bin width. In Figure 8.4 both bin positions are compared. Independent of the bin position the peak yield is integrated the same way. In this example the peak yield agrees well with each other. But in the Barlow check many measurements deviate from

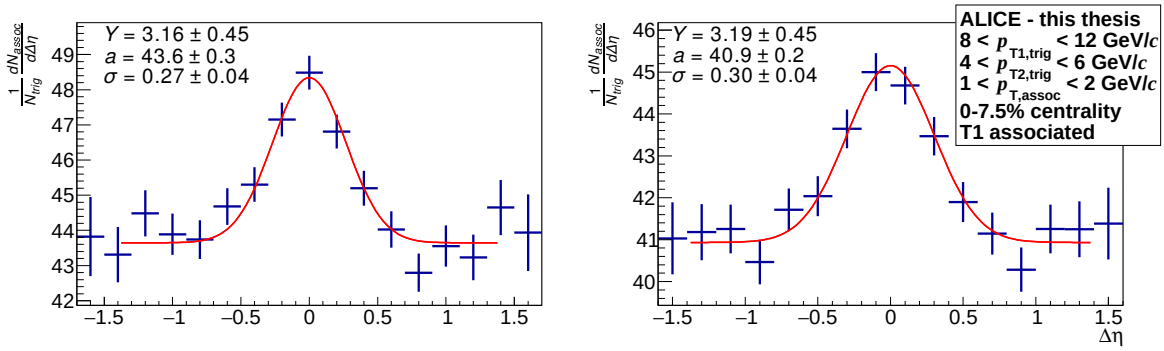

Figure 8.4.: 2+1 peak yield measurement for two different $\Delta\eta$ bin positions. The binning in the right panel is used in the standard analysis.

unity by 4 or 5σ. So this configuration change does not pass the Barlow check and a systematic uncertainty is found. The absolute systematic uncertainty is determined with the method described further below in Section 8.3.
This effect can be avoided by doing the 2+1 peak yield analysis with a $\Delta\eta$ bin width of 0.1 which is half the standard bin width. In the smaller bins the systematic effect is reduced. But the statistical uncertainties increased strongly. So the larger bin width was chosen to reduce the statistical uncertainties.
The full systematic uncertainty analysis, which is presented in this chapter, was repeated for both bin positions shown in Figure 8.4. The bin configuration with bin edges at $\Delta\varphi = 0$ was found to have smaller systematic uncertainties. Consequently this bin configuration is used.

Yield Extraction The yield extraction method is varied in multiple ways. Instead of fitting the $\Delta\eta$ plot, the analysis uses the $\Delta\eta$ gap subtraction and the bin counting method to obtain the peak yield (see Section 6.6). The bin counting method is used for the $\Delta\varphi$ and the $\Delta\eta$ projected distribution.
In Figure 8.5 the peak yield is compared for both yield extraction methods. The example is given for the $\Delta\eta$ projection.
The peak yield from the fit was determined to $Y_{fit} = 3.17 \pm 0.50$ and the peak yield determined with the bin counting method is $Y_{binCounting} = 3.01 \pm 0.63$. Even by taking into account that the statistical uncertainties are correlated, the yield agrees well with each other. The ratio is determined to be $Y_{binCounting}/Y_{fit} = 0.95 \pm 0.12$.
In the Barlow check this comparison for all trigger configurations and associated momenta agrees well. So no systematic uncertainty is assigned due to this yield extraction method.

$\Delta\varphi$ Integration In the integration of the 2+1 peak yield the projection range of $\Delta\varphi$ (see Section 6.6) is varied to analyze the systematic effect of this range. The integration range is increased by 33% from $\pi/6$ to $2\pi/9$. At this distance to the trigger particle the peak yield is very small and the fluctuations dominate. For the increased projection

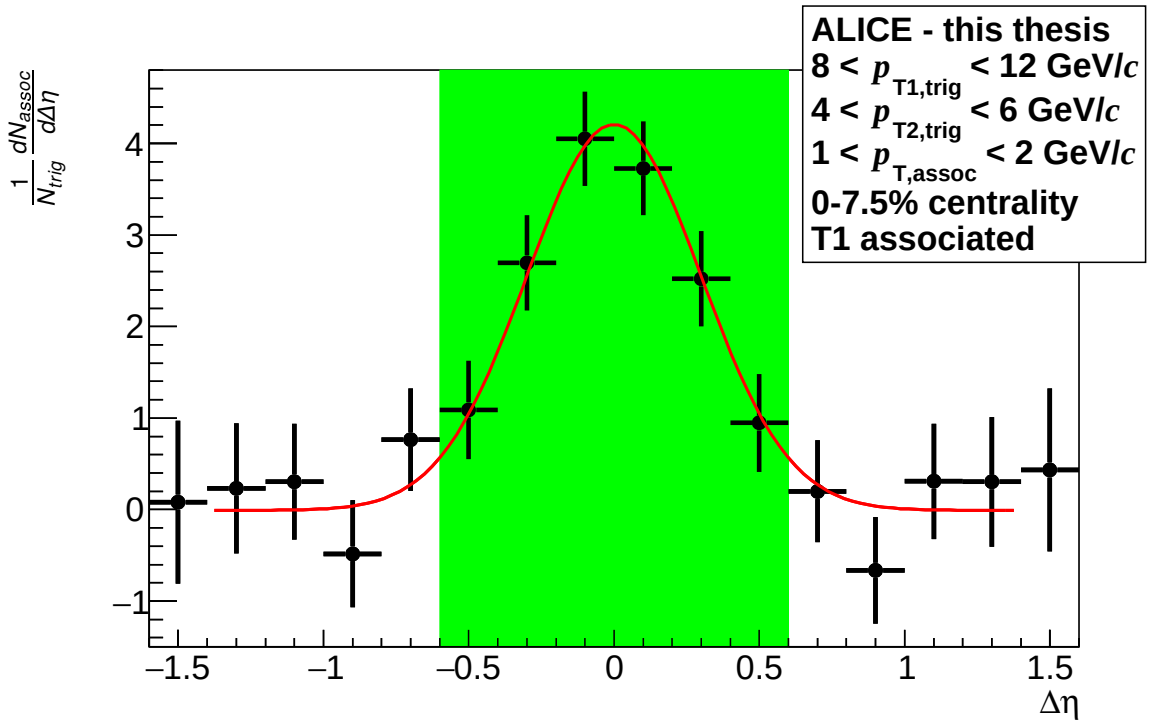

Figure 8.5.: Example yield extracted with the bin counting method. The peak yield is determined once with the fit and once by integrating the yield within $|\Delta\eta| < 0.6$, which is marked with the green box. The background has been subtracted with the $\Delta\eta$ gap method.

range the statistical uncertainty of the peak yield is larger. In Figure 8.6 the points for both projection ranges are shown for a trigger configuration which has a large difference. But even there the fit is very similar. The Barlow criteria showed that no systematic effect is observed.

$\Delta\eta$ Integration In addition to the variation of $\Delta\varphi$, the fit range of $\Delta\eta$ is varied. Instead of using $|\Delta\eta| < 1.4$ (see Section 6.6), the smaller fit range $|\Delta\eta| < 1.0$ is used. The data points are the same, but the peak yield estimation considers a different range for the background estimation. An example with a large effect is shown in Figure 8.7. The Gaussian fits are only marginally different. The main effect is on the baseline which is slightly shifted up. The Barlow check confirms that no systematic effect exists.

Background Triggers Instead of using the number of background triggers from the background same method, the background is obtained from the mixed combinatorics method.
The standard background analysis with the background same method overestimates the number of background triggers slightly due to correlated trigger particles at $\Delta\varphi = \pi/2$ (see Section 6.4.3). Alternatively the background trigger combinations can be

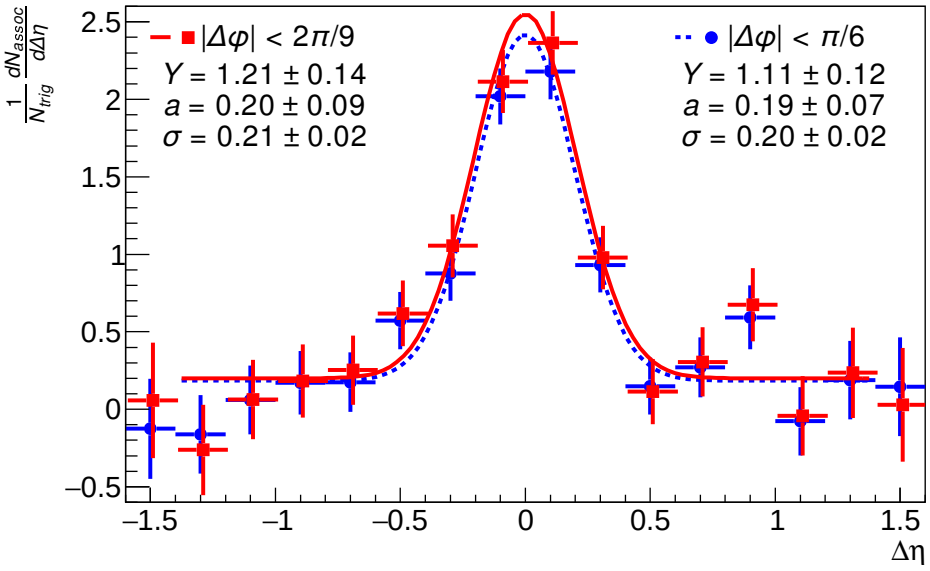

Figure 8.6.: Gaussian fit of the 2+1 peak yield for two different $\Delta\varphi$ projections. The trigger 1 associated yield is measured with the trigger configuration $8 < p_{\mathrm{T1,trig}} < 12\,\mathrm{GeV}/c$ and $4 < p_{\mathrm{T2,trig}} < 6\,\mathrm{GeV}/c$. The associated momentum is $2 < p_{\mathrm{T,assoc}} < 3\,\mathrm{GeV}/c$ and the centrality is 0–7.5%. For a better visibility the points from the larger $\Delta\varphi$ projection (red squares) are slightly displaced from their correct position.

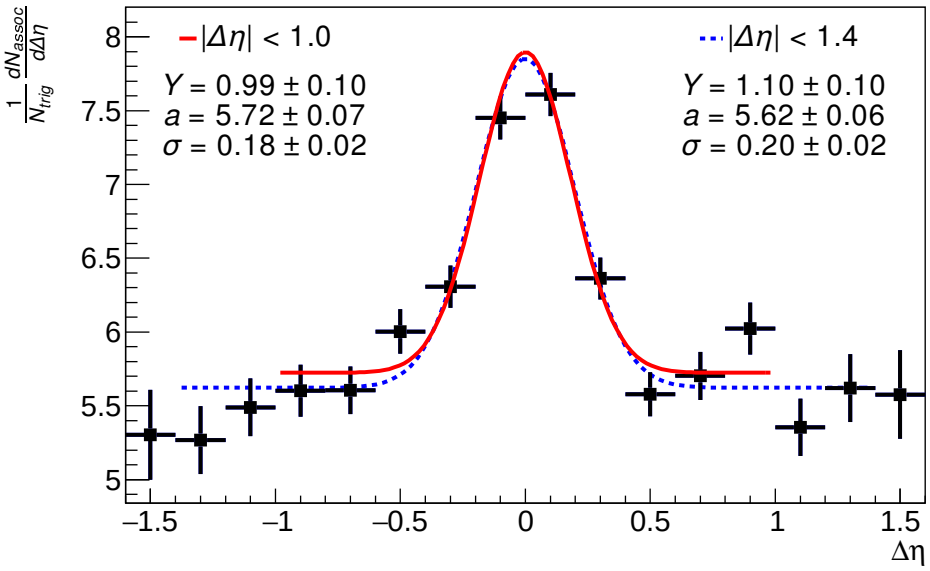

Figure 8.7.: Gaussian fit of the 2+1 peak yield for two different $\Delta\eta$ fits. The trigger 1 associated yield is measured with the trigger configuration $8 < p_{\mathrm{T1,trig}} < 12\,\mathrm{GeV}/c$ and $4 < p_{\mathrm{T2,trig}} < 6\,\mathrm{GeV}/c$. The associated momentum is $2 < p_{\mathrm{T,assoc}} < 3\,\mathrm{GeV}/c$ and the centrality is 0–7.5%.

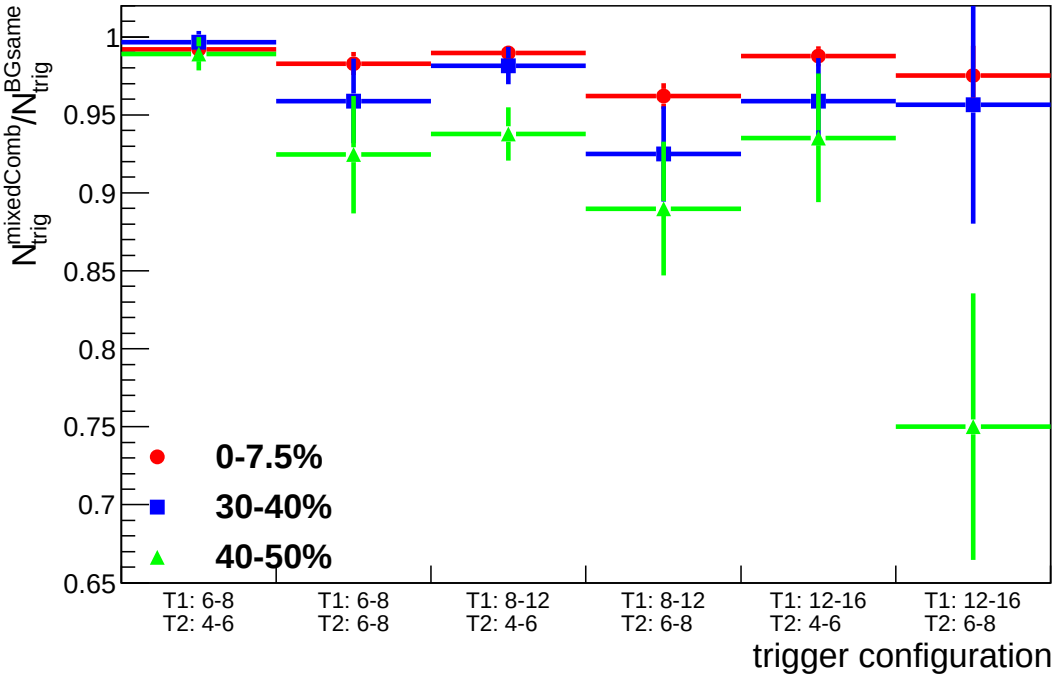

Figure 8.8.: Ratio of the background triggers determined with the background same and mixed combinatorics method.

taken from the mixed combinatorics method which underestimates them due to a missing bias in the events. The correct number is in between these two estimations.
For the uncertainty estimation the 2+1 correlation yield is determined with the mixed combinatorics method as background estimation. The result is compared to the analysis with the background same background subtraction. In Figure 8.8 the ratio between the background triggers determined with the two methods are shown. In the 0–7.5% most central events the ratio is a few percent below unity and in more peripheral events this increases up to 10%. For the highest momentum trigger configuration and the centrality 40–50% the deviation goes up to 25%. But this one trigger configuration has a small background so that there are large uncertainties on this value. Averaged over all trigger configurations and centralities the deviation below unity in the data analysis is roughly 1/3 of the deviation measured in HIJING events (see Figure 6.7) which is in between 5 and 20%.
The number of background triggers deviate more for trigger configurations at higher transverse momenta. But in these trigger configurations the purity is larger which reduces the influence of the background on the final measured 2+1 yield. The Barlow checks have been passed for both Pb–Pb centrality ranges. So no systematic uncertainty is assigned due to the background trigger number.
In the pp yield the Barlow check shows an increased amount of 4 and 5σ deviations for the different background trigger determinations. This is an effect from a larger bias effect in the background same method. The bias in pp events is stronger than in

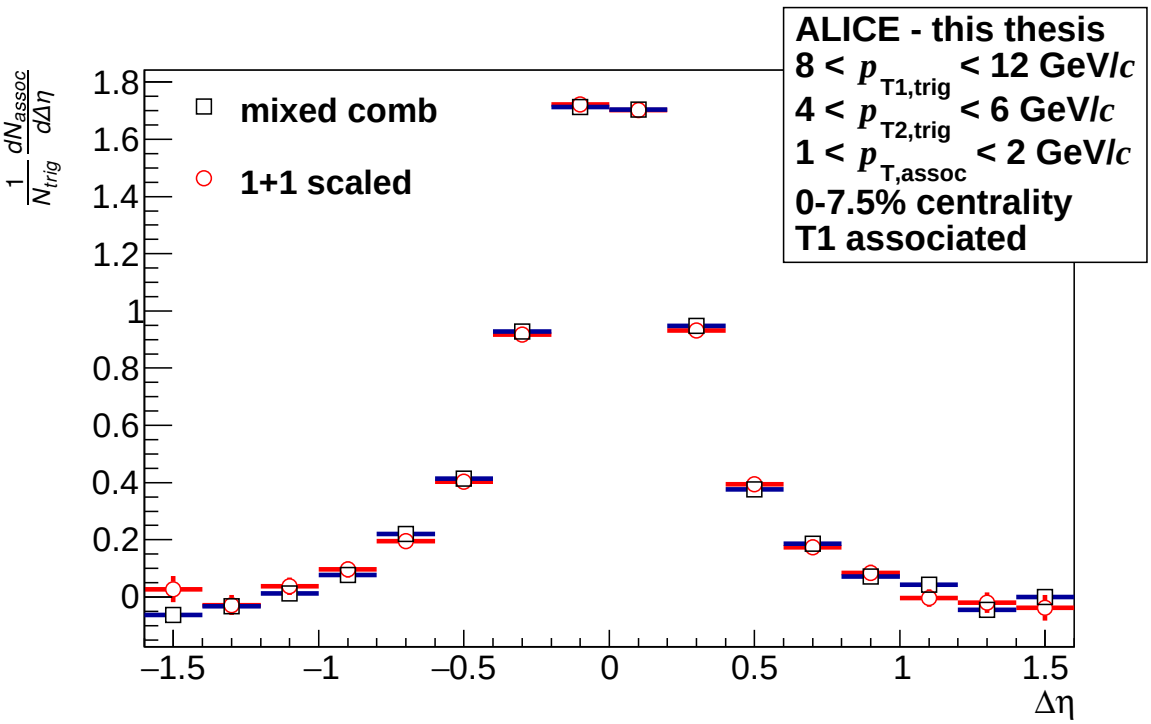

Figure 8.9.: Per trigger associated particle yield from 1+1 correlations and the mixed combinatorics method in 2+1 correlations. From both peaks the baseline has been removed so that they can be compared with each other.

Pb–Pb events at the centrality 40–50%. The analysis presented in Figure 8.8 has been repeated with pp events and the trigger ratio is below 0.2. Due to the strong bias effect the background estimation from the mixed combinatorics method is much worse than the estimation from the background same method. The value obtained in the background same method is the correct one which has to be used in the subtraction and the discrepancy in the Barlow check is explained. Consequently no systematic uncertainty is assigned.

Background Yield Instead of the scaled 1+1 event yield (see Section 6.4.4), the mixed combinatorics event yield (see Section 6.4.1) is used for the background subtraction. Before the subtraction this event yield is scaled with the number of background trigger pairs from the background same method.
In Figure 8.9 the per trigger 1+1 yield is compared with the per trigger mixed combinatorics yield. The baseline of the peaks are subtracted so that they can be compared with each other. Both yields agree with each other very well. The exchanged yield used in the background subtraction passed the Barlow criteria. An important remark about the Barlow checks are the missing points for the trigger configuration $6 < p_{\mathrm{T1,trig}} < 8\,\mathrm{GeV}/c$ and $6\,\mathrm{GeV}/c < p_{\mathrm{T2,trig}} < p_{\mathrm{T1,trig}}$. In this trigger configuration the background yield is taken from the mixed combinatorics analysis anyway (see Section 6.4.4). So no uncertainty can be calculated in this bin and the Barlow check is

uncertainty source	Yield from 0–7.5%					Yield from 30–50%					Yield from pp				
	1σ	2σ	3σ	4σ	5σ	1σ	2σ	3σ	4σ	5σ	1σ	2σ	3σ	4σ	5σ
smaller z_{vtx}	34	18	4	2	0	24	21	11	2	0	31	18	6	1	1
track selection	24	26	5	1	2	28	22	7	1	0	-	-	-	-	-
$\Delta\eta$ bin position	12	11	22	10	3	12	11	19	12	4	27	17	7	5	1
yield extraction	36	16	5	1	0	33	15	8	1	1	38	17	2	0	0
$\Delta\varphi$ integration	38	17	3	0	0	32	15	9	2	0	33	19	4	1	0
$\Delta\eta$ integration	35	16	4	2	1	34	17	6	0	1	40	14	2	1	0
background triggers	24	20	13	1	0	24	33	1	0	0	28	19	3	6	1
background yield	35	10	2	3	0	44	5	1	0	0	-	-	-	-	-

Table 8.3.: Number of associated momentum bins which pass the Barlow criteria. Points which pass a certain σ cut automatically pass all higher σ cuts as well and they are not listed there. For the pp yield some measurements could not be provided. These checks are marked with "-". In these cases no uncertainty is assumed because the Pb–Pb analysis fulfilled the Barlow checks.

based on the other trigger configurations.
In pp events the purity is much higher than in Pb–Pb events. This means the background from randomly combined trigger particles is much lower. The statistical uncertainty of the measured background is larger because less background trigger combinations are measured. In the background same method, some trigger configurations have almost no background trigger combinations. The determined background trigger combinations are of the order of ten trigger combinations. Due to the missing bias effect in the mixed combinatorics method there are even less trigger combinations measured. Because of this low amount of found triggers the mixed combinatorics method does not work for determining the background yield. Due to the high purity, the background subtraction has only a small impact on the final yield. So the uncertainty source from the background yield is neglected.

In Table 8.3 the Barlow check for all analyzed systematic uncertainties sources are shown. The Barlow checks are passed for all uncertainty analyses except for the choice of the $\Delta\eta$ binning. Consequently a systematic uncertainty has to be assigned which is explained in the next section. Additionally for the track selection an uncertainty has been assigned due to a general track uncertainty.

8.3. Systematic Uncertainty from the Bin Positions

The analysis of the systematic uncertainty has shown that only the track selection and the choice of the binning create a systematic uncertainty. The uncertainty due to the track selection have been evaluated in the last Section. In the following the

σ	Yield			I_{CP}	I_{AA}		R_{T1T2}
	0–7.5%	30–50%	pp		0–7.5%	30–50%	
1	12	12	27	26	34	30	22
2	11	11	17	23	19	19	18
3	22	19	7	6	3	6	6
4	10	12	5	3	0	1	1
5	3	4	1	0	1	1	1

Table 8.4.: The number of passed Barlow checks are presented for the two choices of the $\Delta\eta$ binning in the analysis. The comparison is done for the peak yield in pp and Pb–Pb events from the 0–7.5% and 30–50% most central events. Additionally the Barlow checks of the I_{CP}, I_{AA} and the R_{T1T2} are shown.

uncertainty due to the bin position is quantified.
In Figure 8.10 the ratio of the peak yield measured with the two different $\Delta\eta$ bin positions are shown for all trigger configurations and associated momenta. This example is from the 0–7.5% most central events. The associated peak yield measured with one bin around $\Delta\eta = 0$ is systematically smaller than the peak yield from the measurement with a bin edge at $\Delta\eta = 0$. This systematic effect is of the same order as the statistical uncertainty of many points. With the failed Barlow test the systematic effect is discovered.
The Barlow criteria are not checked for the I_{CP}, I_{AA} or R_{T1T2} if both peak yields passed the Barlow checks. If all yields are unchanged, the ratios are not affected as well. But if a systematic effect in the yields was observed, the Barlow criteria have to be checked for the I_{CP}, I_{AA} and R_{T1T2}. In case the systematic effects are identical in the yields, the ratios can be unaffected by changing the binning. In Table 8.4 the results are shown together with the Barlow check of the peak yields. Indeed, the Barlow checks for the I_{CP}, I_{AA} and the R_{T1T2} show that no systematic effect exists.
The systematic uncertainty is quantified by the average of all deviations from unity. For the peak yield from the 0–7.5% central events in Figure 8.10 this results in a systematic uncertainty of 5.9%. The same analysis has been repeated for the peak yield from the 30–50% most central events. The uncertainty is determined to be 5.3%. In the analysis of pp events an uncertainty of 5.8% was determined. These uncertainties are summarized in Table 8.5.

8.4. Summary

The Barlow checks have been performed for the 2+1 correlations analysis to investigate the systematic uncertainty. All possible sources of systematic uncertainties except the track selection and the bin positions have shown no systematic effect. This is summarized in Table 8.6. All observables which passed the Barlow check are marked with "-". For the failed Barlow checks the range of the systematic uncertainty is indicated. The uncertainty due to the track selection is created from the track selection uncertainty

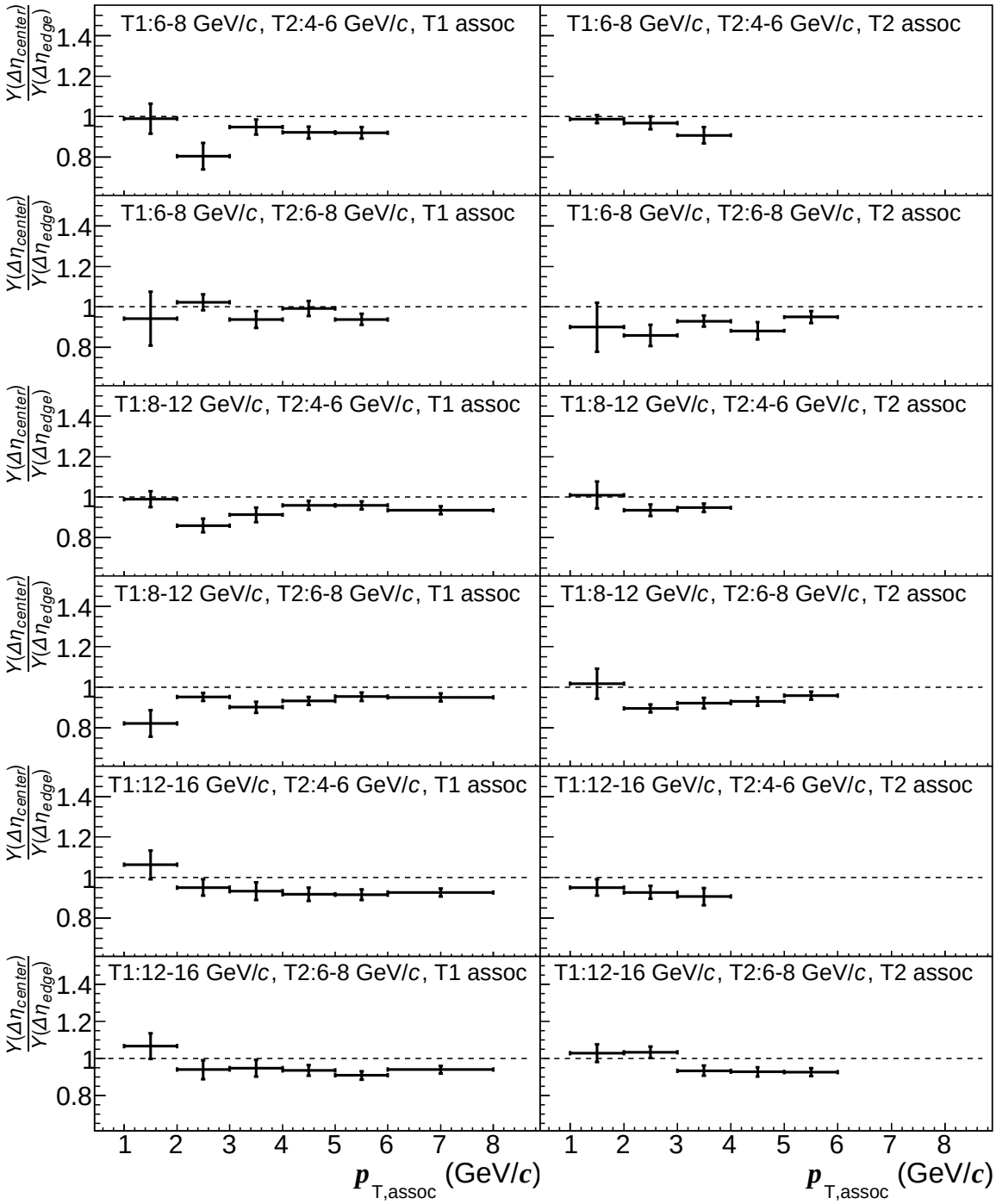

Figure 8.10.: Analysis of the systematic uncertainty for the choice of the $\Delta\eta$ bin positions. The measurement with a bin center at $\Delta\eta = 0$ is divided by the measurement with a bin edge at $\Delta\eta = 0$. Unity is indicated with the dashed line. This example is from the 0–7.5% most central events.

measurement	uncertainty
Pb–Pb(0–7.5%)	5.9%
Pb–Pb(30–50%)	5.3%
pp	5.8%
I_{CP}	-
I_{AA}(0–7.5%)	-
I_{AA}(30–50%)	-
R_{T1T2}	-

Table 8.5.: Assigned uncertainty due to the $\Delta\eta$ bin positions. The observables which passed the Barlow criteria are indicated with "-" instead of a value for the uncertainty.

	Yield	I_{CP}	I_{AA}	R_{T1T2}
smaller z_{vtx}	-	-	-	-
track selection	2.5–14.5%	3.0–7.5%	2.5–14.5%	-
$\Delta\eta$ bin position	5.3– 5.8%	-	-	-
yield extraction	-	-	-	-
wider $\Delta\varphi$ integration	-	-	-	-
smaller $\Delta\eta$ integration	-	-	-	-
background triggers	-	-	-	-
background yield	-	-	-	-

Table 8.6.: The found systematic uncertainty is shown as a range for each source of the uncertainty. If the Barlow checks were passed and no systematic uncertainty is assigned, the source is labeled with "-".

between the 2010 and 2011. This is a general uncertainty which is present in many correlation analysis of ALICE.
The uncertainty due to the bin position is a consequence of the small statistics. If more events would be available the same measurements could be repeated with a finer binning which would reduce the systematic uncertainty.
In the final yield the uncertainty due to the track uncertainty and due to the $\Delta\eta$ bin positions is added in quadrature. The result is presented in Table 8.7.
These are the systematic uncertainties which were determined within the current statistical uncertainties. If further systematic uncertainties exist they are much smaller than the statistical uncertainties.

Observable		$p_{\mathrm{T,assoc}}$		
		1–2 GeV/c	2–3 GeV/c	3–8 GeV/c
Yield	Pb–Pb(0–7.5)%	8.1%	11.6%	15.6%
	Pb–Pb(30–50)%	5.9%	7.3%	8.8%
	pp	5.8%	5.8%	5.8%
I_{CP}		3.0%	5.0%	7.5%
I_{AA}	0–7.5%	5.5%	10.0%	14.5%
	30–50%	2.5%	5.0%	7.0%
R_{T1T2}		-	-	-

Table 8.7.: Total systematic uncertainty. The R_{T1T2} passed all Barlow checks and the absence of a systematic uncertainty is indicated with "-".

9. Two Plus One Particle Correlations in Pb–Pb Collisions

The 2+1 particle correlations are analyzed in Pb–Pb collisions measured with ALICE at the LHC. In Section 9.1 the signal extraction is illustrated with one example trigger configuration. Afterwards in Section 9.2 the measured trigger particles are presented for Pb–Pb and pp collisions. The per trigger associated particle yield is compared for different parameters in Section 9.3. The integration of the yield is demonstrated in Section 9.4. In the same section the integrated per trigger particle yield is compared for multiple trigger configurations, centralities and associated particle momenta.
For a more detailed analysis of these values the I_{CP} and I_{AA} are calculated and presented in the Sections 9.5 and 9.6. Another ratio to analyze the integrated peak yields is the R_{T1T2} which is presented in Section 9.7 for pp and Pb–Pb events.
For a direct comparison with the STAR results from Section 2.8 the I_{AA} is recalculated within the same transverse momentum bins in Section 9.8.

9.1. Signal Extraction

The 2+1 particle correlation method is illustrated in the following. In Figure 9.1a and b the trigger 2 same and mixed event yield for the trigger configuration $6 < p_{\mathrm{T1,trig}} < 8\,\mathrm{GeV}/c$ and $4 < p_{\mathrm{T2,trig}} < 6\,\mathrm{GeV}/c$ with the associated momentum $2 < p_{\mathrm{T,assoc}} < 3\,\mathrm{GeV}/c$ are shown. These yields are determined from the 30–50% most central events. For the mixed event the average yield of all centrality and z_{vtx} bins is shown. In Figure 9.1c the ratio of these two yields is plotted.
The same event yield shows a triangular shape in $\Delta\eta$, which originates from the limited η acceptance. After the mixed event correction the η acceptance effect vanished and the peak can be seen on a flat background. But this is not the peak yield from correlated trigger particles. It contains the background from uncorrelated trigger particles (see Section 6.4). This background is subtracted with the scaled 1+1 yield which is shown in Figure 9.2a. It is subtracted from the same event yield which was shown in Figure 9.1c. The difference between these plots is shown in Figure 9.2b.
The background corrected yield contains a peak structure around $\Delta\varphi = \Delta\eta = 0$ and a ridge at $\Delta\varphi = 0$. The peak contains particles which are from the same jet as trigger 2. The ridge has two contributions. One is created due to particle flow and the other one is a residual background from uncorrected trigger particles (see Section 6.4). This second part cannot be subtracted with the scaled 1+1 events. It will be part of the

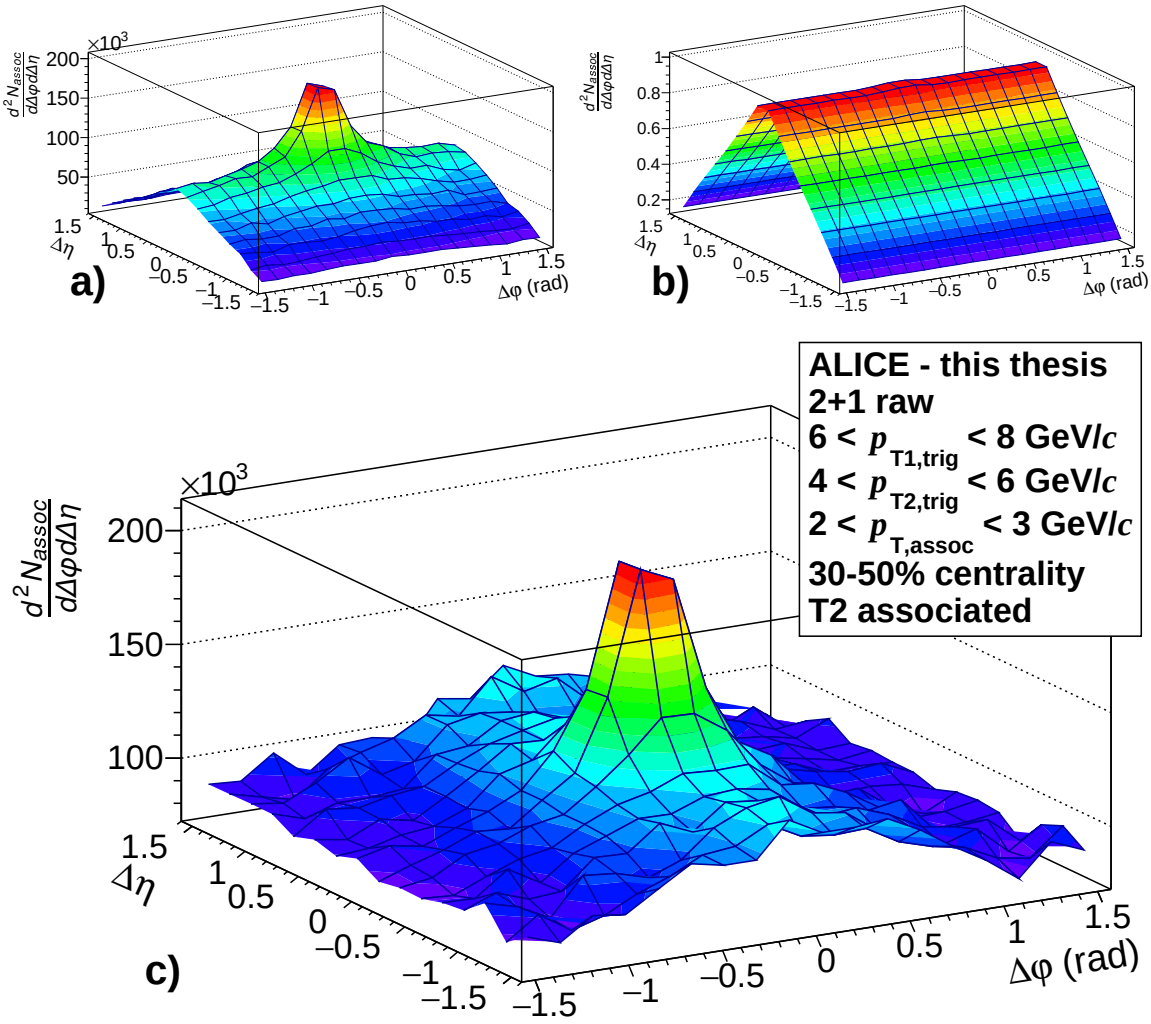

Figure 9.1.: In a) the 2+1 same event yield before the mixed event correction is shown. The corresponding mixed event yield is shown in b). In c) the ratio of these two yields is illustrated.

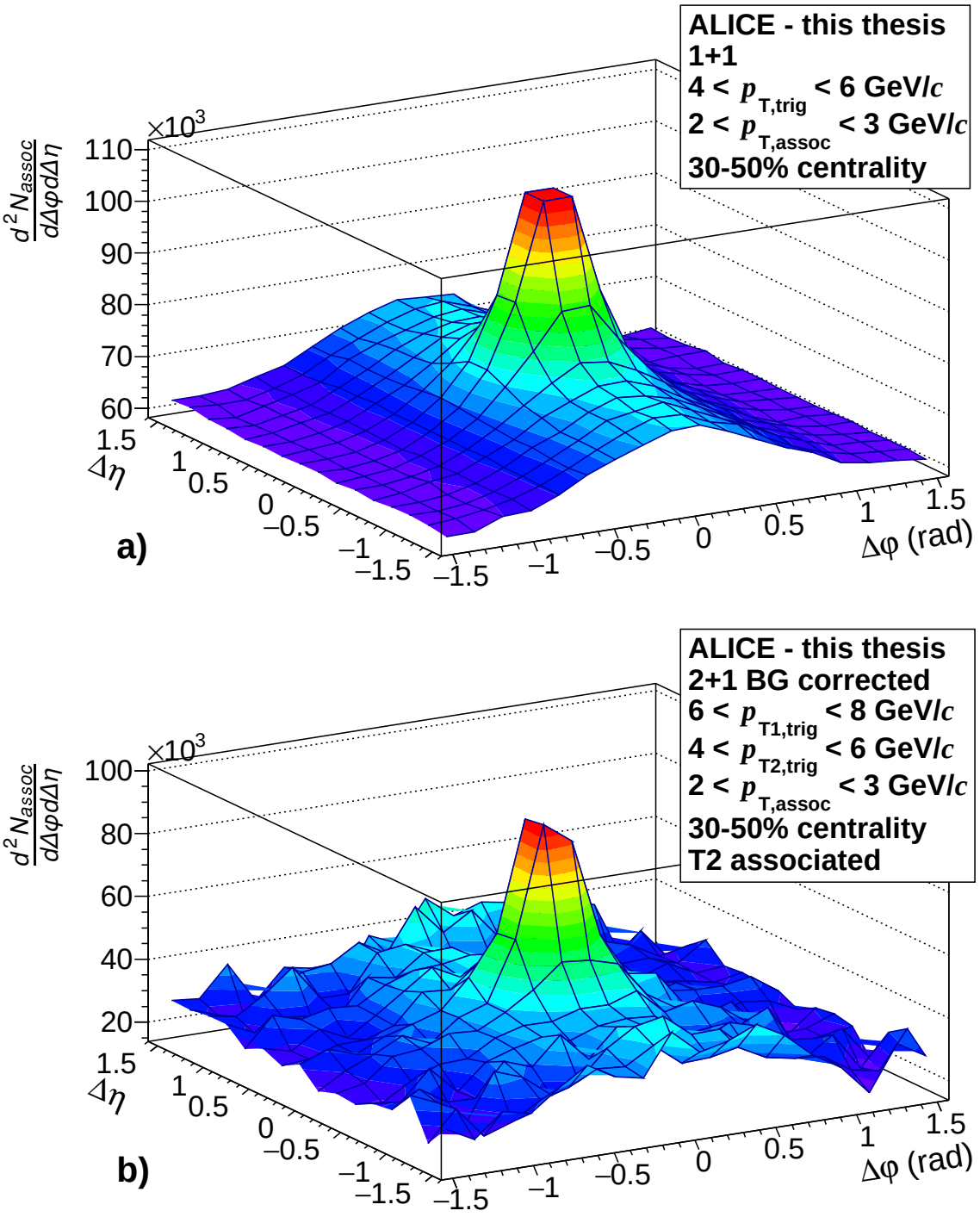

Figure 9.2.: In a) the scaled 1+1 yield is shown. This yield is subtracted from the same event yield in Figure 9.1 c). The resulting background corrected yield is shown in b). The plot contains a peak structure at $\Delta\varphi = \Delta\eta = 0$ and a ridge around $\Delta\varphi = 0$.

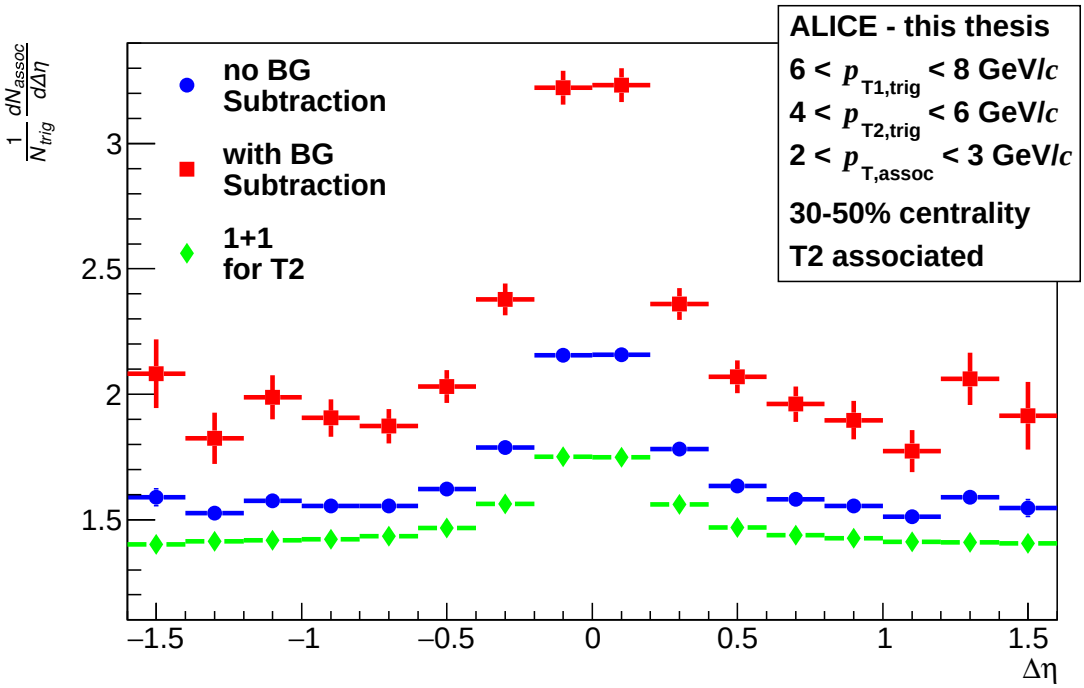

Figure 9.3.: The per trigger associated particle yield of trigger 2 is shown with and without background subtraction. This is compared to the 1+1 yield obtained with $p_{\mathrm{T2,trig}}$ as $p_{\mathrm{T,trig}}$. Due to the low purity in the same event yield, the statistical uncertainty of the background corrected yield is much larger than the uncertainty of the uncorrected yield.

background in the fit of the peak yield.
Due to the high background subtraction the background corrected yield has a much larger statistical uncertainty than the same event yield before the correction. The raw 2+1 yield is measured from $7.5 \cdot 10^4$ trigger combinations which contains $5.4 \cdot 10^4$ background trigger combinations. Consequently in the background subtraction the particle yield from $2.1 \cdot 10^4$ correlated trigger combinations is obtained.
In the next analysis step the peak is projected on the $\Delta\eta$ axis for $|\Delta\varphi| < \pi/6$. This projection is shown in Figure 9.3 for the background corrected yield, the uncorrected yield and the 1+1 yield. All yields are normalized per trigger so that they can be compared to each other. The per trigger same event yield without background correction is in all bins larger than the per event 1+1 yield because the events with trigger combinations contain more correlated particles. Consequently the background corrected per trigger yield is increased. This effect is observed for all trigger configurations.

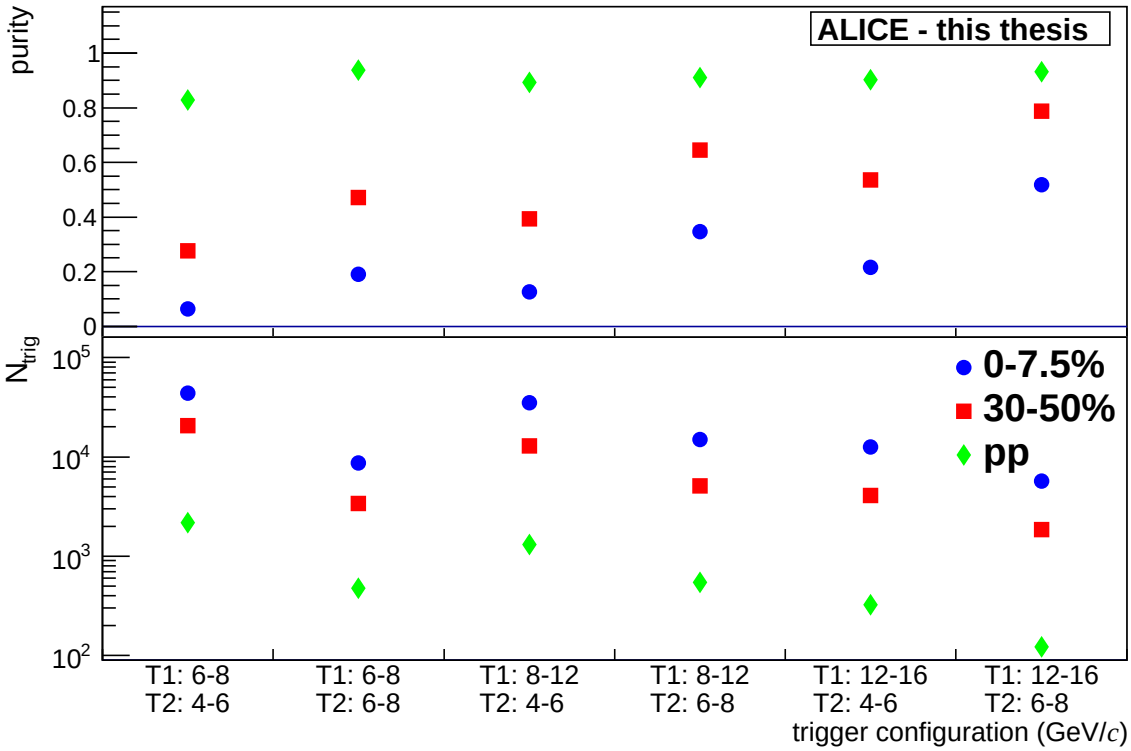

Figure 9.4.: The upper plot shows the purity of the trigger combinations. At a high purity more real trigger combinations are found than random trigger combinations. The number of correlated trigger pairs for pp and Pb–Pb events is shown in the lower plot. The Pb–Pb collisions are divided into central events at 0–7.5% and semi central events at 30–50% centrality. More events have been measured for the more central events.

9.2. Trigger Combinations

The uncertainty of the background corrected yield depends on the measured statistics and on the purity with which the trigger combination is measured. In the example in Figure 9.2 the correlated trigger combinations are 28% of the measured trigger combinations. This number represents the purity of the measurement.
In Figure 9.4 in the lower plot the found trigger combinations N_{trig} are shown for each trigger configuration used in this thesis. They are compared for different collision centralities in Pb–Pb events and for pp. In the upper plot the purity is shown. The lower the purity, the more statistics are needed for that trigger configuration so that the associated yield of the correlated trigger particles can be extracted.
Collisions with a higher multiplicity contain more trigger combinations. This means in more central Pb–Pb collisions with a high average multiplicity more trigger combinations are found than in more peripheral Pb–Pb collisions or pp collisions. At the same time the purity is lower at collisions with higher multiplicities.
The particle multiplicity in the collisions decreases as a function of p_{T}. This explains

the decreasing number of trigger combinations N_{trig} and the increasing purity as a function of the trigger p_{T} for all collision systems.
The lowest statistics in Pb–Pb collisions are measured in the 30–50% most central events for the trigger configuration $12 < p_{\mathrm{T1,trig}} < 16\,\mathrm{GeV}/c$ and $6 < p_{\mathrm{T2,trig}} < 8\,\mathrm{GeV}/c$. In this measurement 1900 trigger combinations have been measured which is sufficient for the signal extraction.
For the pp collisions with the same trigger configuration there is basically no background (purity is almost at 1.0). Due to the small background the associated particle yield can be measured at low $p_{\mathrm{T,assoc}}$, although only 123 trigger combinations have been found. At high $p_{\mathrm{T,assoc}}$ the associated particle yield is within the uncertainty in agreement with zero. The pp data at this trigger configuration is included in the analysis but it fluctuates in some bins too much so that no conclusion can be obtained.
Due to the low amount of correlated trigger configurations the 2+1 measurement can neither be performed in Pb–Pb nor in pp events at higher trigger transverse momenta than $12 < p_{\mathrm{T1,trig}} < 16\,\mathrm{GeV}/c$ or $6 < p_{\mathrm{T2,trig}} < 8\,\mathrm{GeV}/c$. The number of associated particles would be too low to be extracted.
At the lowest trigger transverse momenta $6 < p_{\mathrm{T1,trig}} < 8\,\mathrm{GeV}/c$ and $4 < p_{\mathrm{T2,trig}} < 6\,\mathrm{GeV}/c$ the 2+1 measurement has a low purity. The statistical uncertainty of the measured yield reflects this. For trigger combinations with even smaller trigger p_{T}, a signal cannot be extracted due to low purity.

9.3. Comparison of the per Trigger Yield

The 2+1 per trigger associated particle yield is measured for multiple collision systems (Pb–Pb, pp), $p_{\mathrm{T,assoc}}$, trigger p_{T} and trigger particles. The example in Section 9.1 has been chosen for a good illustration of the 2+1 correlation method. In the following the effects from different configurations are illustrated with the yields projected on $\Delta\eta$ to allow a quantitative comparison.
In Figure 9.5 the per trigger peak yield is compared for different collisions systems. The yields are measured from the 0–7.5% and 30–50% most central Pb–Pb events and from pp events. At more central Pb–Pb events a higher background (= lower purity) is expected. This increases the statistical uncertainty of the measurements compared to pp events and for more peripheral Pb-Pb events despite the larger number of recorded central events.The per trigger peak yield is observed to be larger in more central Pb–Pb events. This effect is analyzed in more detail in Section 9.5.
In Figure 9.6 the per trigger peak yield is compared for different trigger configurations in the 0–7.5% most central Pb-Pb events. At high p_{T} trigger configurations the uncertainty is large due to small statistics. At low trigger p_{T} the uncertainties are increased due to the low purity. The smallest uncertainties are measured for the trigger configuration $8 < p_{\mathrm{T1,trig}} < 12\,\mathrm{GeV}/c$ and $4 < p_{\mathrm{T2,trig}} < 6\,\mathrm{GeV}/c$.
The associated particle yield for different trigger configurations is larger for higher trigger p_{T}. On average trigger particles with higher trigger p_{T} represent jets with higher energies. Due to the higher jet energy a larger particle content at a given $p_{\mathrm{T,assoc}}$ is

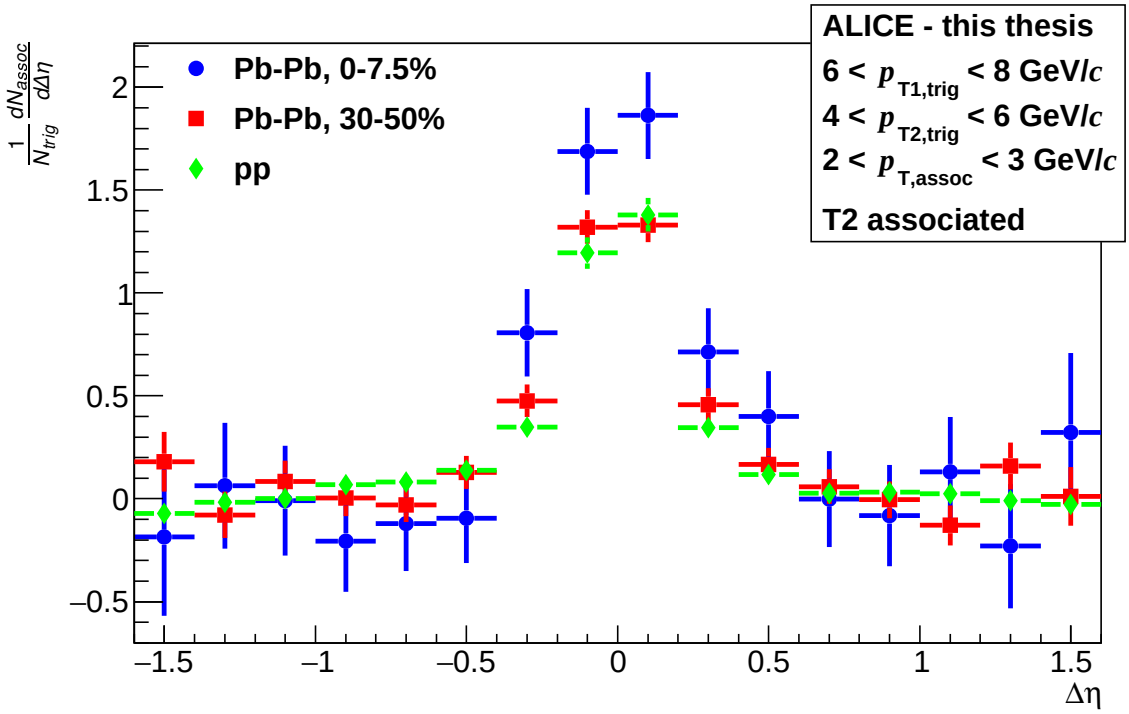

Figure 9.5.: The 2+1 associated peak yield is shown for multiple collision types (Pb–Pb and pp). For Pb–Pb collisions two centralities are used. For illustration purposes from all yields a baseline has been subtracted.

observed.
The associated particle yield for different $p_{\mathrm{T,assoc}}$ is illustrated in Figure 9.7. In this example the yield is measured in the 0–7.5% most central Pb-Pb events with the trigger configuration $8 < p_{\mathrm{T1,trig}} < 12\,\mathrm{GeV}/c$ and $4 < p_{\mathrm{T2,trig}} < 6\,\mathrm{GeV}/c$. By increasing $p_{\mathrm{T,assoc}}$, the associated peak yield drops significantly. At the same time the statistical uncertainty drops because the background from uncorrelated particles is reduced more than the yield from correlated associated particles.
All example yields which have been presented in this chapter so far are obtained from trigger 2 associated particles. The same procedure can be repeated for the trigger 1 associated particles. The associated particle yield from both trigger particles is compared in Figure 9.8 for two centralities. The yield from both trigger particles agrees with each other within the uncertainties. Although it is not significant it should be noted that the associated yield from trigger 2 it slightly larger than the yield from trigger 1. If this is not a fluctuation, this effect can be created by a measurement bias or by a physics effect. It is quantified in Section 9.7.

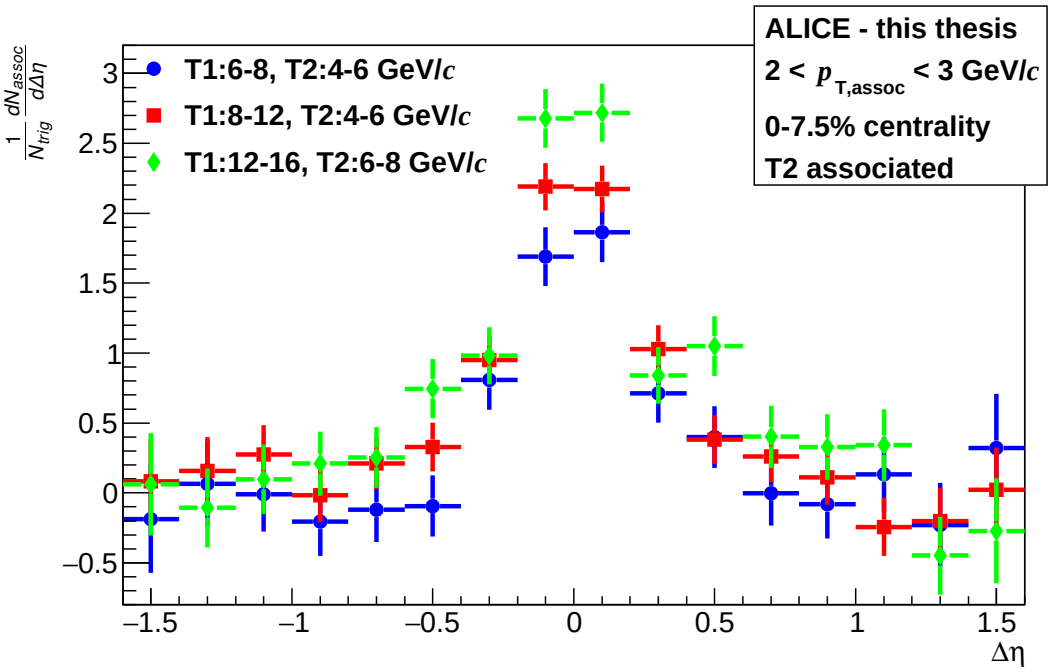

Figure 9.6.: The per trigger associated particle yield is shown for different trigger configurations. For illustration purposes a baseline has been subtracted from each yield.

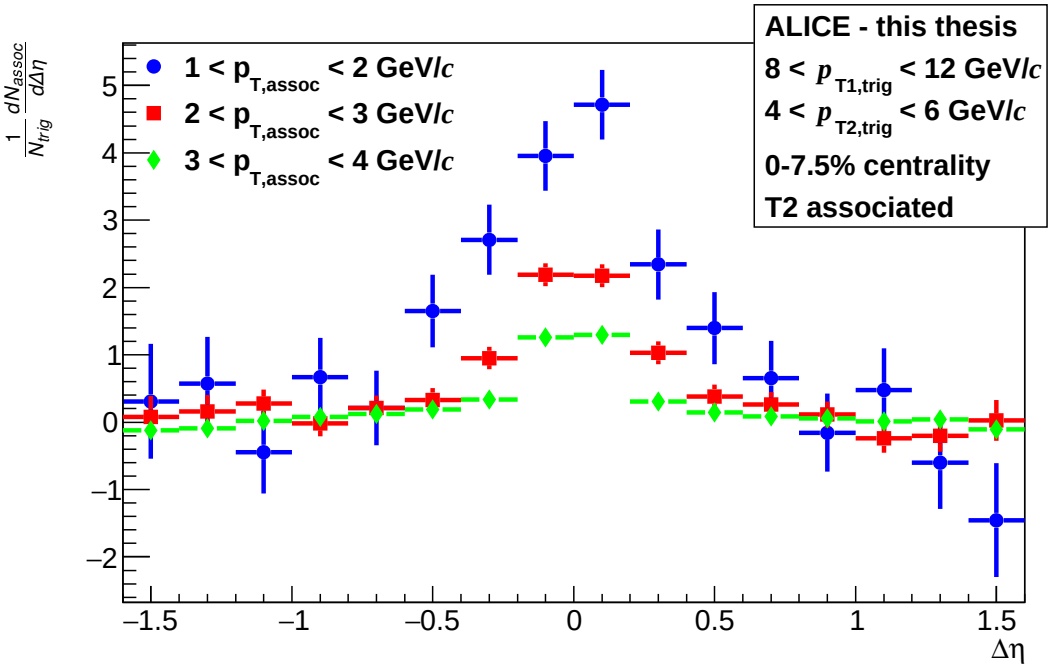

Figure 9.7.: The per trigger associated yield is illustrated for several $p_{\mathrm{T,assoc}}$ ranges. For illustration purposes a baseline has been subtracted from each yield.

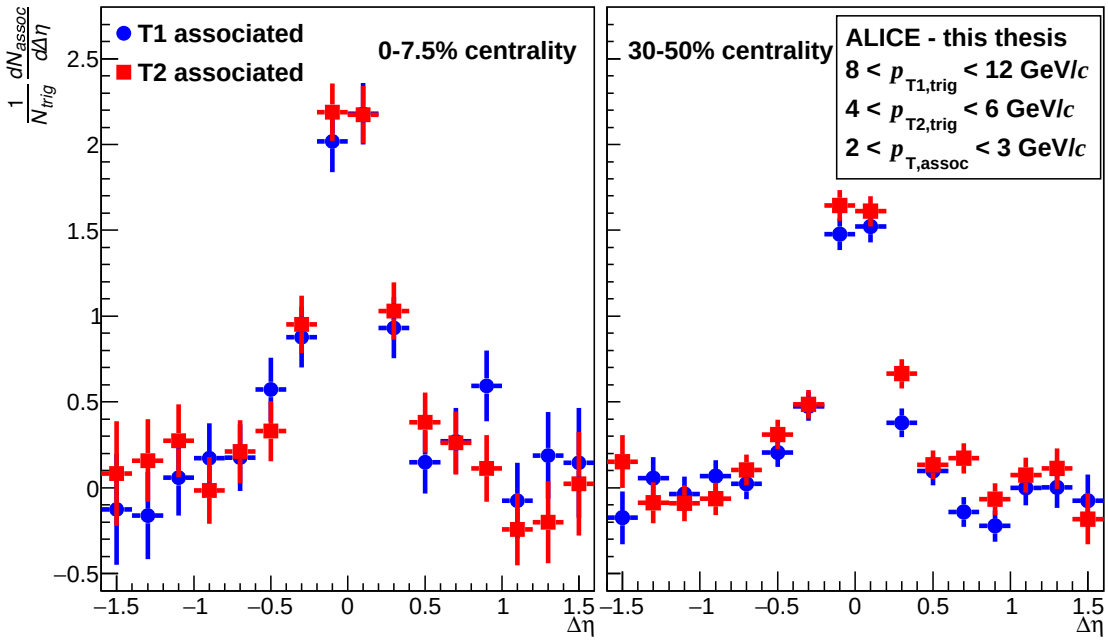

Figure 9.8.: The 2+1 associated peak yield is compared for both trigger particles. In the left panel the yield from the centrality 0–7.5% and in the right panel the yield from the centrality 30–50% is shown. For illustration purposes a baseline has been subtracted from each yield.

9.4. Integration of the Correlated Yield

The associated per trigger yield is integrated with a Gaussian fit (see Section 5.7). The background is estimated with a constant and the integrated 2+1 peak yield Y is calculated from the Gaussian integral. In Figure 9.9 the fit is illustrated.
In Figure 9.10 this yield is shown for all trigger configurations. The associated particles for the first trigger particle are measured up to a maximum transverse momentum of $8\,\mathrm{GeV}/c$. The plot is divided into twelve smaller plots with different trigger configurations. Two plots are always separated with a dashed line. The left side shows the trigger 1 associated particles and the right side the trigger 2 associated particles. Each of these plot pairs represents one trigger configuration. This way all six trigger p_T configurations are shown. Each plot shows the associated particle yield of one trigger particle for several $p_\mathrm{T,assoc}$ from Pb–Pb events at the centralities 0–7.5% and 30–50% and from pp events. The maximum shown $p_\mathrm{T,assoc}$ in each plot varies because the yield is only measured for $p_\mathrm{T,assoc}$ smaller than the correspondent trigger p_T. By definition $p_\mathrm{T2,trig}$ is smaller than $p_\mathrm{T1,trig}$. Consequently the maximum measured $p_\mathrm{T,assoc}$ is larger for the trigger 1 associated particles than for the trigger 2 associated particles.
The systematic uncertainty of the associated particle yield is for most of the measurements within the symbol size. The largest uncertainty of 15.6% in the peak yield of

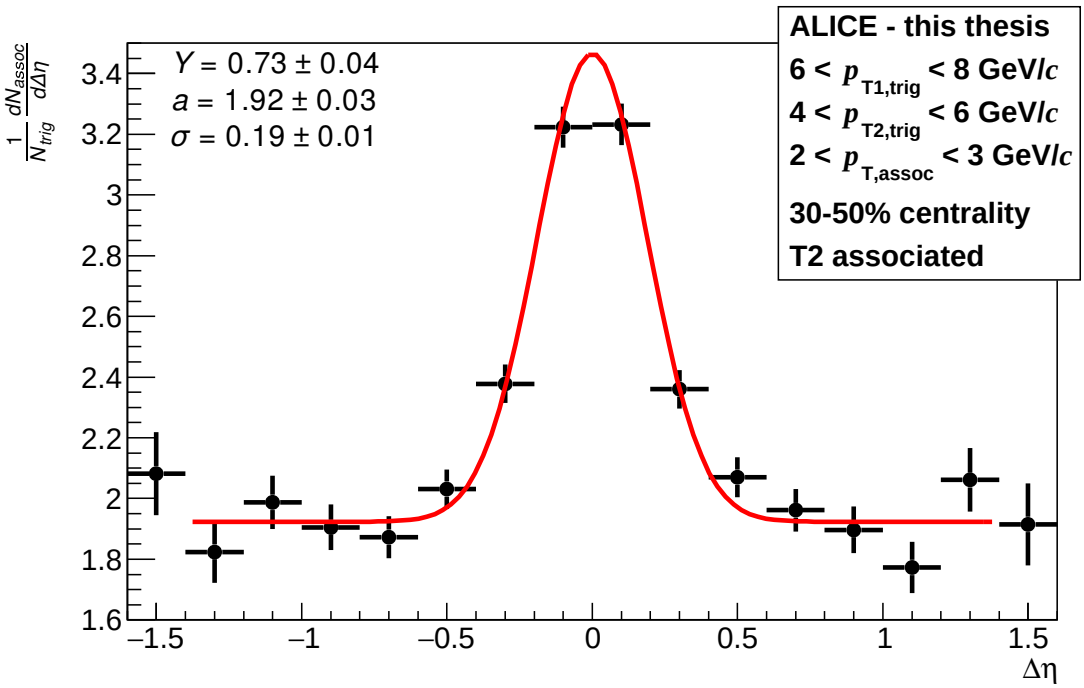

Figure 9.9.: The associated particle yield is fitted with a Gaussian on top of a constant background (see Section 5.7). This is presented for the example of the trigger 2 associated yield from Section 9.1. The peak yield Y is shown together with the other fit parameters on the left.

the 0–7.5% most central events at $3 < p_{\mathrm{T,assoc}} < 8\,\mathrm{GeV}/c$ is of the same order as the symbol size. So the systematic uncertainty is not plotted in Figure 9.10.
For all trigger configurations the associated particles have a similar yield for a given $p_{\mathrm{T,assoc}}$. This means the associated particle yield in correlated trigger particles does not strongly depend on the trigger p_{T}, the centrality or which trigger is used to correlate the particles with. It decreases strongly for all spectra with increasing $p_{\mathrm{T,assoc}}$. At an associated momentum of $1 < p_{\mathrm{T,assoc}} < 2\,\mathrm{GeV}/c$ roughly one to three associated particles are measured in the detector which are correlated with the trigger particle. This decreases to 0.1 to 0.2 particles per trigger in the detector with a transverse momentum of $5 < p_{\mathrm{T,assoc}} < 6\,\mathrm{GeV}/c$.
Although the associated particle yield is similar, there are small effects dependent on the centrality which can be observed for all trigger configurations. The associated yield from the 0–7.5% most central events is larger at small $p_{\mathrm{T,assoc}}$ than the yield from the 30–50% most central events. To better analyze and compare these effects, the I_{CP} is computed as a function of $p_{\mathrm{T,assoc}}$. This is presented in the next section. The same effect can be observed for the comparison with the yield from pp events which is analyzed in more detail with the I_{AA} in Section 9.6.
In Section 9.7 the R_{T1T2} is analyzed. This yield quantifies the difference between the trigger 1 and trigger 2 associated yield. From the plots presented here it can already

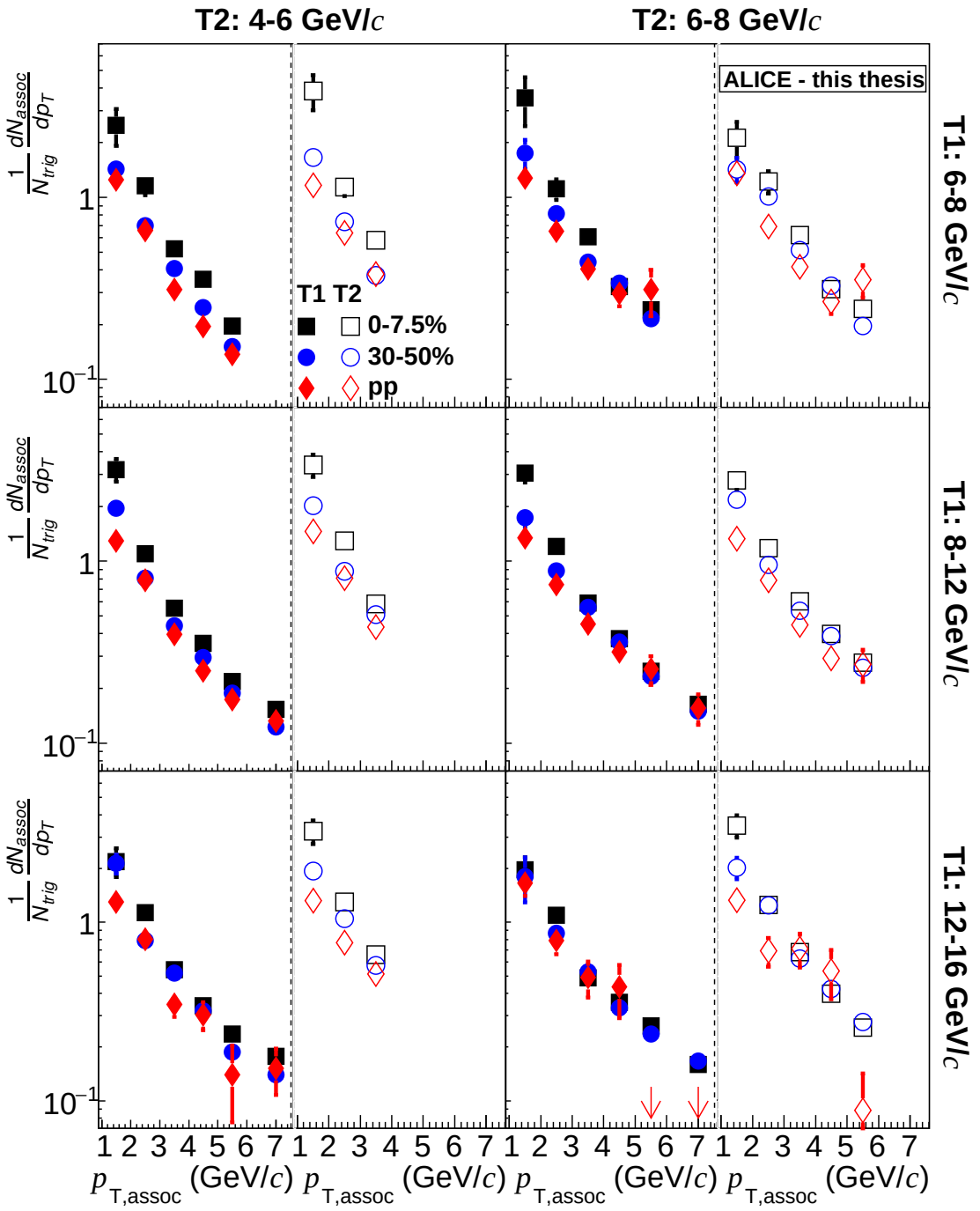

Figure 9.10.: The measured per trigger associated particle yield in Pb–Pb events at the centralities 0–7.5% and 30–50% and in pp events. The $p_{\mathrm{T1,trig}}$ of a plot is indicated on the right, the $p_{\mathrm{T2,trig}}$ at the top of the figure. The red arrows in the bottom right panel indicate that the pp measurement at this $p_{\mathrm{T,assoc}}$ is much smaller than the shown yield. These values are within the uncertainty in agreement with zero. The systematic uncertainty is not plotted because it is smaller or equal the symbol size.

be seen that no major differences exists.
For both trigger particles, the associated yield from high trigger p_{T} in pp collisions is strongly fluctuating.

9.5. Centrality Dependence of the Particle Yield

In Figure 9.11 the I_{CP} (the ratio between the spectra from the 0–7.5% and the 30–50% most central events) is shown for all trigger configurations. The plots are arranged in a similar way as the peak yield before. Each plot contains the I_{CP} for the trigger 1 and the trigger 2 associated particle yield. The systematic uncertainty of the I_{CP} is shown as green box around unity. If no effect from the QGP exists, the I_{CP} is expected to be unity.
For all trigger and associated transverse momenta, the I_{CP} is either above unity or it agrees within the uncertainty with unity. This is a sign for quenching effects from the QGP.
At $6 < p_{\mathrm{T1,trig}} < 8\,\mathrm{GeV}/c$ and $6\,\mathrm{GeV}/c < p_{\mathrm{T2,trig}} < p_{\mathrm{T1,trig}}$ (top right plot) the transverse momentum difference between the trigger particles is very small. This means that this trigger combination selects back-to-back jets which were affected by a similar energy loss. This is especially fulfilled by surface jets[1] which were both not affected by any energy loss. The I_{CP} for this trigger configuration shows that the ratio of the trigger 2 associated yield agrees within the statistical and systematic uncertainties with unity. Although the measured points agree with unity it can be noticed that they are all above unity. This can be seen as a small indication towards a higher associated yield at the 0–7.5% most central events. The trigger 1 associated I_{CP} in the same trigger configuration is slightly larger and above unity for $p_{\mathrm{T,assoc}} < 4\,\mathrm{GeV}/c$. Due to the big uncertainties this is not a strong statement.
At the lowest trigger transverse momenta $6 < p_{\mathrm{T1,trig}} < 8\,\mathrm{GeV}/c$ and $4 < p_{\mathrm{T2,trig}} < 6\,\mathrm{GeV}/c$ the I_{CP} (top left of the Figure) is above unity for both trigger particles. The values agree for the different trigger particles with each other. This means the associated particle yield is much higher in the 0–7.5% compared to the 30–50% most central events. In this plot a small decrease of the I_{CP} as a function of $p_{\mathrm{T,assoc}}$ may be present. Due to the large uncertainties, a constant I_{CP} is possible as well.
The plots in the middle of the figure, which describe the trigger configurations $8 < p_{\mathrm{T1,trig}} < 12\,\mathrm{GeV}/c$, $4 < p_{\mathrm{T2,trig}} < 6\,\mathrm{GeV}/c$ (left side) and $8 < p_{\mathrm{T1,trig}} < 12\,\mathrm{GeV}/c$, $6 < p_{\mathrm{T2,trig}} < 8\,\mathrm{GeV}/c$ (right side), are very similar. The I_{CP} at low $p_{\mathrm{T,assoc}}$ is larger than unity and it decreases towards unity as a function of $p_{\mathrm{T,assoc}}$.
In both plots the trigger 1 and trigger 2 I_{CP} agree with each other within the uncertainties at all $p_{\mathrm{T,assoc}}$. Although a slightly different behavior may be visible which is not significant within the uncertainty. For the higher $p_{\mathrm{T2,trig}}$ bin the enhancement of the trigger 2 I_{CP} over unity at low $p_{\mathrm{T,assoc}}$ is smaller compared to the trigger 2 I_{CP} from the lower $p_{\mathrm{T2,trig}}$ bin. But more statistics would be necessary to analyze this in greater detail.

[1] Surface jets are created at the surface of the QGP fireball.

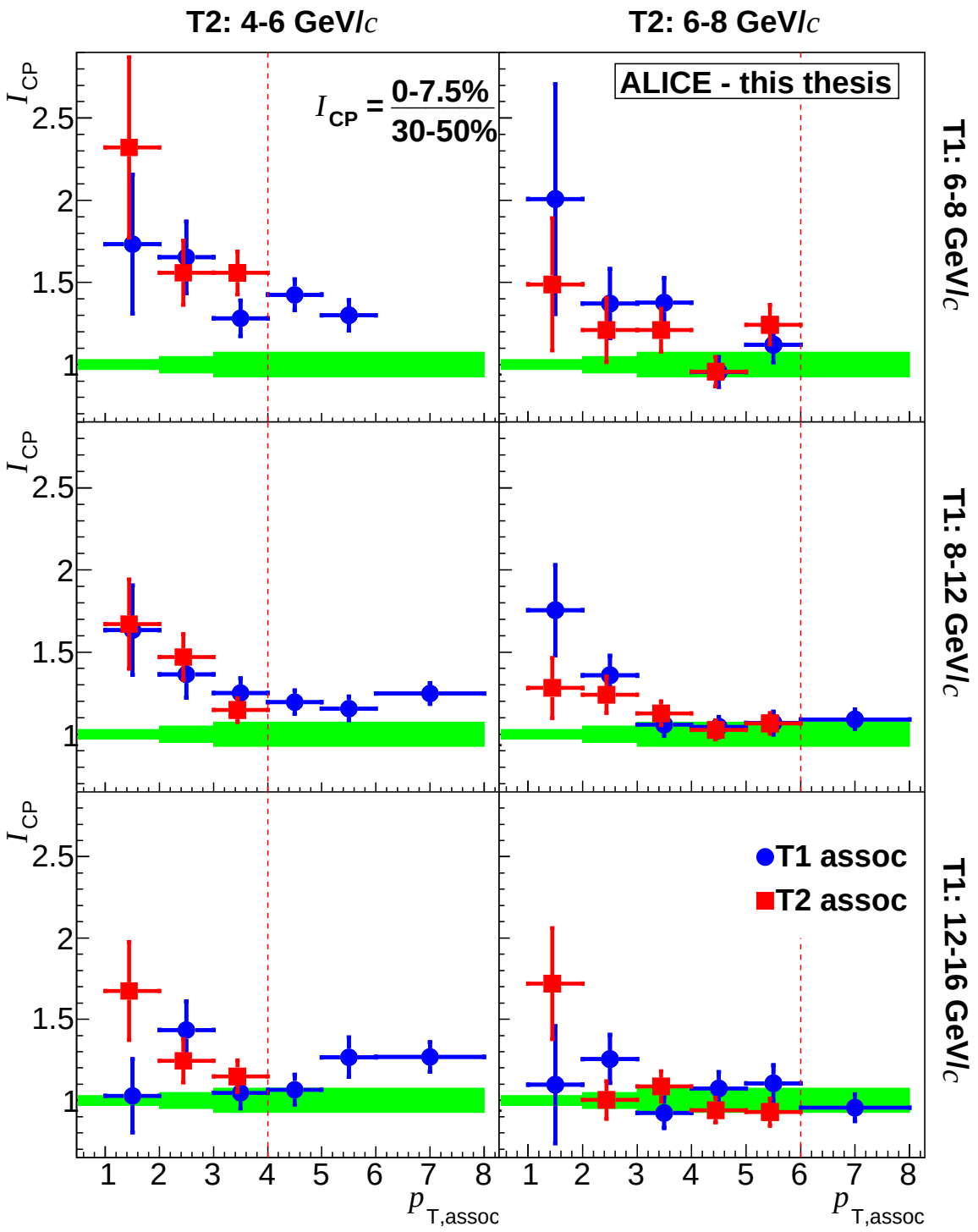

Figure 9.11.: I_{CP} of the per trigger associated yield from Figure 9.10. The red line indicates the minimum $p_{T2,trig}$. At higher p_T only trigger 1 associated particles are measured and thus the I_{CP} can only be calculated for the trigger 1 associated particles. The systematic uncertainty is shown as a green box around unity.

The lower left plot of Figure 9.11 shows the I_{CP} for $12 < p_{\mathrm{T1,trig}} < 16\,\mathrm{GeV}/c$ and $4 < p_{\mathrm{T2,trig}} < 6\,\mathrm{GeV}/c$. The p_{T} difference between these trigger particles is the largest of all trigger combinations which are measured in this thesis. The trigger 2 associated I_{CP} is above unity and decreases towards unity as a function of $p_{\mathrm{T,assoc}}$ like for the trigger configuration with $8 < p_{\mathrm{T1,trig}} < 12\,\mathrm{GeV}/c$ and the same trigger 2 requirement. The trigger 1 associated I_{CP} behaves differently. All points with $p_{\mathrm{T,assoc}} < 5\,\mathrm{GeV}/c$ except the point for $2 < p_{\mathrm{T,assoc}} < 3\,\mathrm{GeV}/c$ agree with unity within the uncertainties. This one point shows a significant deviation. Several interpretations are possible. It could mean that the trigger 1 I_{CP} decreases for very low $p_{\mathrm{T,assoc}}$ for the other trigger configurations as well and this is just not measured because this effect appears below the minimum measured $p_{\mathrm{T,assoc}}$. Alternatively there can be a fluctuation in this measurement. In case of a fluctuation two interpretations are likely. Either the first point has a downward fluctuation which creates the illusion of the reduced I_{CP} and the correct behavior is a monotonous decrease of the I_{CP} as a function of $p_{\mathrm{T,assoc}}$. This would be identical to the behavior of the other trigger configurations with lower trigger p_{T}. Or the second point could be the result of an upward fluctuation and the correct spectrum would be completely in agreement with unity. This would be in a good agreement with the observations at the same trigger 1 and higher trigger 2 transverse momentum.
The highest analyzed trigger transverse momentum configuration $12 < p_{\mathrm{T1,trig}} < 16\,\mathrm{GeV}/c$ and $6 < p_{\mathrm{T2,trig}} < 8\,\mathrm{GeV}/c$ has very small statistics. Within the uncertainties all points for the trigger 1 associated spectrum agree with unity. In case of the trigger 2 associated spectrum all points except the first point at $1 < p_{\mathrm{T,assoc}} < 2\,\mathrm{GeV}/c$ agree with unity. This one point is significantly above unity. Due to the large uncertainties an enhancement of the I_{CP} over unity cannot be excluded at small $p_{\mathrm{T,assoc}}$.
Out of the I_{CP} from all these trigger configurations some common observations can be concluded.

- I_{CP} is never significantly below unity
- I_{CP} decreases as a function of $p_{\mathrm{T,assoc}}$
- the enhancement of the trigger 1 and trigger 2 I_{CP} over unity decreases as a function of $p_{\mathrm{T1,trig}}$
- the enhancement of the trigger 2 I_{CP} over unity decreases as a function of $p_{\mathrm{T2,trig}}$

In the absence of medium effects the same signal is expected in Pb–Pb events from different centralities which would result in $I_{\mathrm{CP}} \approx 1$. This has been shown for HIJING simulations in Section 7.4. Consequently the enhancement of the I_{CP} over unity in the data analysis could be a signal of quenching.
The enhancement can alternatively be explained by a bias on the parton transverse momentum spectrum which is selected by the trigger conditions. For a fixed $p_{\mathrm{T1,trig}}$ and $p_{\mathrm{T2,trig}}$ a larger average parton transverse momentum would be selected at more central Pb–Pb events [ALI12]. Even if the energy loss and the fragmentation are

identical in Pb–Pb and pp events, the I_{CP} would be enhanced due to the bias on the parton transverse momentum. But this bias would still be a result of a medium effect in Pb–Pb collisions.
If the I_{CP} enhancement is created by this bias, the measured di-jets can be created at any position in the fireball. But in the absence of such a bias some details about the position within the fireball can be deduced.
If the measured trigger combinations would originate purely from the surface of the colliding matter with both particles going into the vacuum, only fragmentation effects would be expected. In this case the HIJING analysis showed that the I_{CP} would be at unity (see Section 7.4). Because of the deviation of the I_{CP} from unity, some jet sources at other positions have to exist.
In another scenario one particle from the hard collision can directly fragment into the vacuum while the other one traverses the QGP first. In this case different effects for the I_{CP} would be expected for trigger 1 and trigger 2. The observed trigger 1 and trigger 2 I_{CP} are very similar, so this jet source is not dominating.
The measurements indicate hard collisions inside the QGP. In this configuration both trigger and their associated particles are affected by the QGP. This creates an enhancement of the I_{CP} above unity which is similar for both trigger particles.
The 2+1 trigger 2 I_{CP} cannot directly be compared with the 1+1 away side I_{CP} which was presented in Figure 2.10. Although the trigger 2 is from the away side of trigger 1, this is not describing the same jets as the away side jets in 1+1 correlations. Different jet sources are selected in the 2+1 and 1+1 correlation measurements. Some hard collisions result in one particle having a long path length within the QGP. This results in a good measurement of a trigger 1 and no recoiling jet. In 2+1 correlations the measurement of these interactions might be suppressed, because the recoiling jet transferred so much momentum to other particles within the QGP that the transverse momentum of all measured particles is below the trigger 2 threshold.

9.6. Comparison of the Pb–Pb and pp Peak Yield

The I_{AA} is shown in Figure 9.12 for the Pb–Pb yield from the 0–7.5% most central events and in Figure 9.13 for the Pb–Pb yield from the 30–50% most central events. In general both analysis confirm the observations from the I_{CP}. But in the I_{AA} from the 0–7.5% most central events the enhancement over unity is larger than in the I_{CP}. In the I_{AA} from the 30–50% most central events it is smaller and close to unity indicating stronger medium effects in more central Pb–Pb events. The dependency on $p_{\mathrm{T,assoc}}$ is similar in the I_{AA} compared to the I_{CP}. In the following the I_{AA} from the 0–7.5% most central Pb–Pb events in Figure 9.12 is compared with the I_{CP} which has been analyzed in the previous section.
For the trigger configuration $6 < p_{\mathrm{T1,trig}} < 8\,\mathrm{GeV}/c$ and $4 < p_{\mathrm{T2,trig}} < 6\,\mathrm{GeV}/c$ the trigger 2 associated I_{AA} at $1 < p_{\mathrm{T,assoc}} < 2\,\mathrm{GeV}/c$ is at $I_{\mathrm{AA}} = 3.3 \pm 0.7$. This point is outside of the plot range. The I_{AA} and I_{CP} both show the same behavior as a function of $p_{\mathrm{T,assoc}}$ but the I_{AA} is roughly 10% larger. Within the uncertainties the yields agree

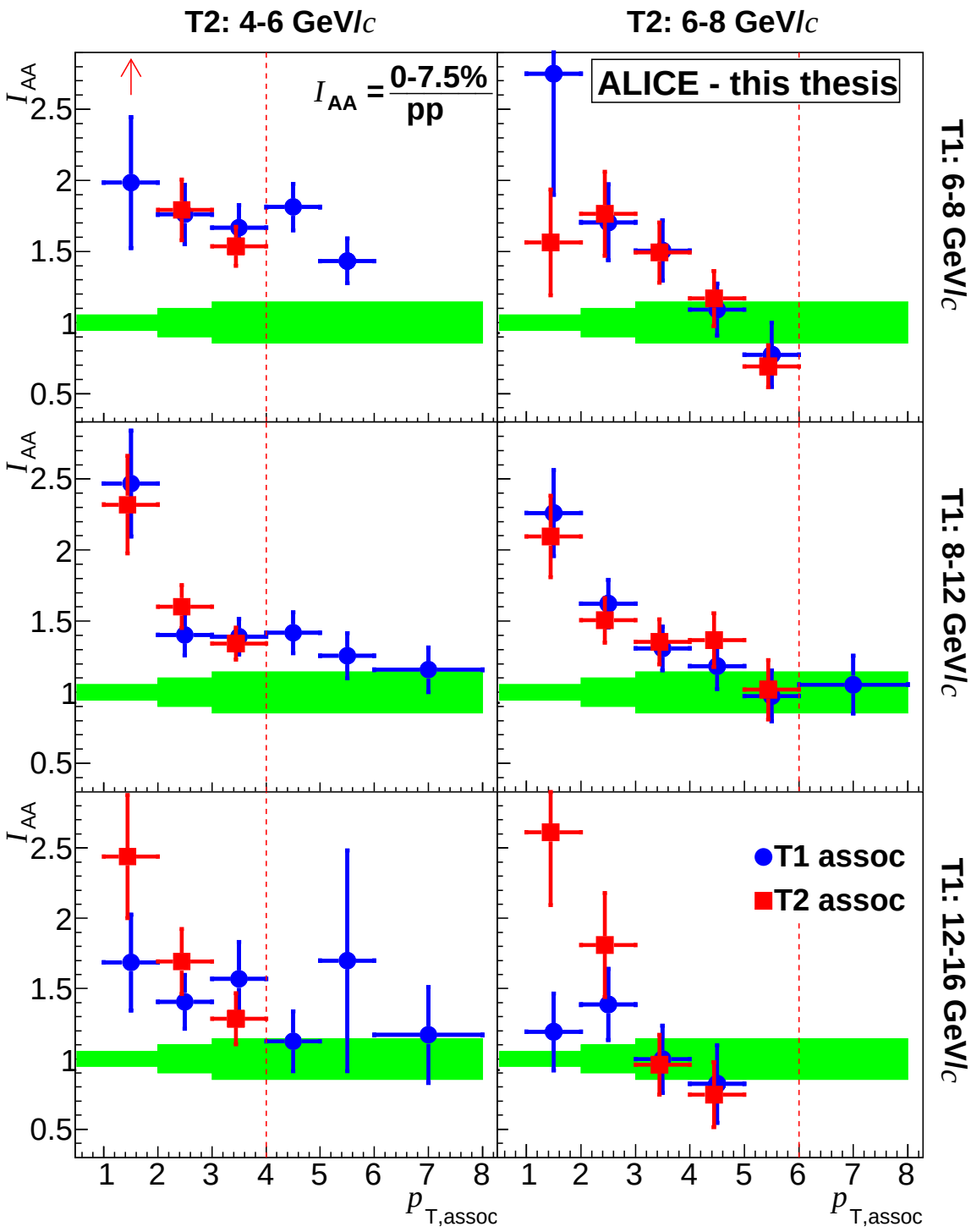

Figure 9.12.: I_{AA} of the per trigger associated yield from the 0–7.5% most central events. The red line indicates the minimum $p_{T2,trig}$. The systematic uncertainty is shown as a green box around unity. In the top left plot the trigger 2 associated yield is above the shown range which is indicated with the red arrow.

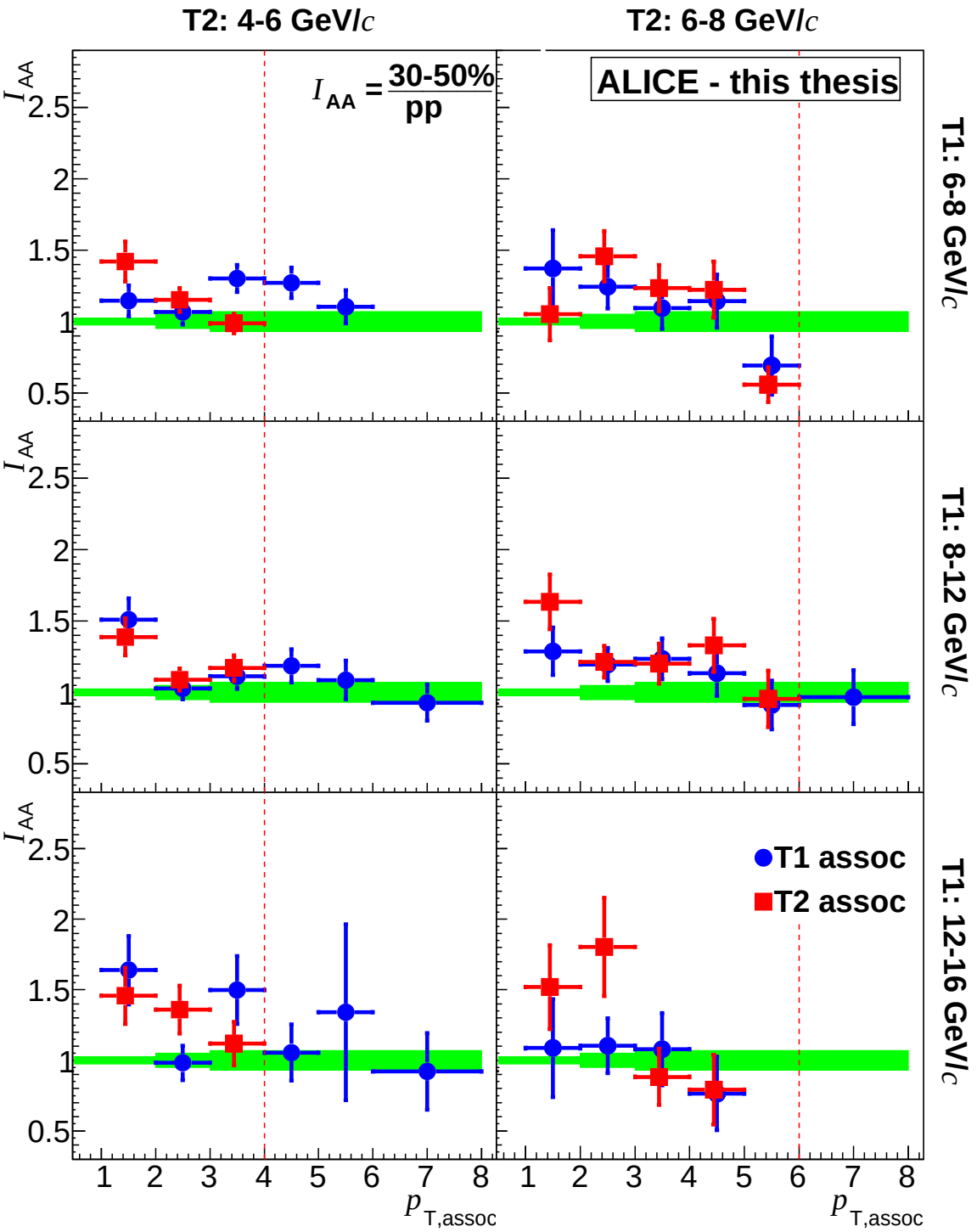

Figure 9.13.: I_{AA} of the per trigger associated yield from the 30–50% most central events. The red line indicates the minimum $p_{T2,trig}$. The systematic uncertainty is shown as a green box around unity.

with each other. In both plots all points are significantly above unity.
In the trigger configuration $6 < p_{\mathrm{T1,trig}} < 8\,\mathrm{GeV}/c$ and $6 < p_{\mathrm{T2,trig}} < p_{\mathrm{T1,trig}}$ the largest changes can be seen. Due to the smaller uncertainties the trigger 2 I_{AA} is significantly above unity for $p_{\mathrm{T,assoc}} < 4\,\mathrm{GeV}/c$. It decreases as a function of $p_{\mathrm{T,assoc}}$ while the I_{CP} has been constant and in agreement with unity. But the I_{CP} is compatible with the I_{AA} as well due to the large uncertainty. The trigger 1 associated I_{AA} decreases like in the I_{CP} over the same $p_{\mathrm{T,assoc}}$ range. Because of the larger enhancement over unity at small $p_{\mathrm{T,assoc}}$ the decrease is stronger in the I_{AA}.
The middle left plot shows the trigger configuration $8 < p_{\mathrm{T1,trig}} < 12\,\mathrm{GeV}/c$ and $4 < p_{\mathrm{T2,trig}} < 6\,\mathrm{GeV}/c$. This plot shows a linear falling behavior as a function of $p_{\mathrm{T,assoc}}$ for both trigger analysis like in the I_{CP} but at a higher amplitude. The trigger 1 associated I_{AA} for $2 < p_{\mathrm{T,assoc}} < 3\,\mathrm{GeV}/c$ deviates from this linear falling behavior.
In the trigger configuration $8 < p_{\mathrm{T1,trig}} < 12\,\mathrm{GeV}/c$ and $6 < p_{\mathrm{T2,trig}} < 8\,\mathrm{GeV}/c$ the I_{AA} of both trigger particles agree very well with each other. The amplitudes are increased compared to the I_{CP}.
The trigger configuration $12 < p_{\mathrm{T1,trig}} < 16\,\mathrm{GeV}/c$ and $4 < p_{\mathrm{T2,trig}} < 6\,\mathrm{GeV}/c$ contains large uncertainties. But for the I_{AA} a decreasing trend as a function of $p_{\mathrm{T,assoc}}$ can be seen. This decrease is stronger for the trigger 2 associated I_{AA} which is observed for the I_{CP} as well. For trigger 1 the I_{CP} contains a signal in agreement with unity, especially at $1 < p_{\mathrm{T,assoc}} < 2\,\mathrm{GeV}/c$. The higher enhancement in the I_{AA} suggests a fluctuation in the I_{CP} and a linearly falling trend as a function of $p_{\mathrm{T,assoc}}$. This was not excluded in the I_{CP}.
The I_{AA} for the trigger configuration $12 < p_{\mathrm{T1,trig}} < 16\,\mathrm{GeV}/c$ and $6 < p_{\mathrm{T2,trig}} < 8\,\mathrm{GeV}/c$ has to be interpreted carefully due to the large uncertainties. Like in the I_{CP} the trigger 1 associated I_{AA} agrees with unity for all $p_{\mathrm{T,assoc}}$. The missing points at $5 < p_{\mathrm{T,assoc}} < 6\,\mathrm{GeV}/c$ and $6 < p_{\mathrm{T,assoc}} < 8\,\mathrm{GeV}/c$ are off scale and with large uncertainties crossing unity. Only very few particles contribute to the pp measurement at this $p_{\mathrm{T,assoc}}$. In the trigger 2 associated I_{AA} a decreasing behavior as a function of $p_{\mathrm{T,assoc}}$ can be seen. There was a hint for such a behavior in the I_{CP} but there only one point was significantly above unity.
Most of the observations in the I_{CP} can be reassured in the I_{AA} from the 0–7.5% most central events.

- I_{AA} is never significantly below unity
- I_{AA} decreases as a function of $p_{\mathrm{T,assoc}}$
- the enhancement of the trigger 1 I_{AA} over unity decreases as a function of $p_{\mathrm{T1,trig}}$

These conclusions support the conclusions which have been drawn from the I_{CP} measurement in the last section. But a decrease of the trigger 2 I_{AA} enhancement as a function of $p_{\mathrm{T2,trig}}$ is not observed as it was observed for the I_{CP}.
The I_{AA} from the 30–50% most central events do not contradict these observations. But this I_{AA} is much closer to unity and compared to the enhancement over unity it has larger uncertainties than the I_{AA} from the 0–7.5% most central events. The

smaller enhancement over unity shows that the QGP effects observed in the I_{CP} and I_{AA} are created by a medium which is larger and longer-lived in more central heavy-ion collisions.

9.7. Trigger Dependence of the Particle Yield

To compare the back-to-back jets, the ratio between the trigger 1 and trigger 2 associated particle yields is calculated for Pb–Pb and pp events. This is the R_{T1T2} and it is presented in Figure 9.14. For all trigger combinations the R_{T1T2} agrees either with unity within the uncertainty or it is very close to it.
All R_{T1T2} from the trigger configuration $8 < p_{\mathrm{T1,trig}} < 12\,\mathrm{GeV}/c$ and $4 < p_{\mathrm{T2,trig}} < 6\,\mathrm{GeV}/c$ are below unity. At the larger trigger 2 transverse momentum $6 < p_{\mathrm{T2,trig}} < 8\,\mathrm{GeV}/c$ of the same $p_{\mathrm{T1,trig}}$ again all points fluctuate around unity and they are not consistently below.
At the lower trigger 1 transverse momentum $6 < p_{\mathrm{T1,trig}} < 8\,\mathrm{GeV}/c$ the statistical uncertainties are larger. Again most R_{T1T2} agree with unity. But the points which deviate most relative to their uncertainties deviate towards lower values.
At the trigger configuration $12 < p_{\mathrm{T1,trig}} < 16\,\mathrm{GeV}/c$ and $4 < p_{\mathrm{T2,trig}} < 6\,\mathrm{GeV}/c$ the R_{T1T2} either agrees with unity within the uncertainties or it is below unity. For all event types at least one point out of three is more than one standard deviation below unity. For the 0–7.5% most central events these are two points and the third one is in agreement with unity but the value is still below unity. This trigger configuration contains the largest energy difference between the triggers of all trigger configurations shown in this thesis.
In the highest transverse momentum trigger configuration $12 < p_{\mathrm{T1,trig}} < 16\,\mathrm{GeV}/c$ and $6 < p_{\mathrm{T2,trig}} < 8\,\mathrm{GeV}/c$ the R_{T1T2} from pp events agrees within the uncertainties with unity but it has too large uncertainties for any further conclusions. The R_{T1T2} from Pb–Pb events at both centralities show a deviation below unity. This deviation is observed for most of the points in both centralities. There might be an increasing trend for the 0–7.5% most central events but within the uncertainties it is difficult to get to a final conclusion.
By looking at all trigger configurations the largest lowering of the R_{T1T2} below unity is observed for the trigger 1 transverse momentum range $12 < p_{\mathrm{T1,trig}} < 16\,\mathrm{GeV}/c$ with both trigger 2 transverse momentum ranges $4 < p_{\mathrm{T2,trig}} < 6\,\mathrm{GeV}/c$ and $6 < p_{\mathrm{T2,trig}} < 8\,\mathrm{GeV}/c$. Another consistent lowering is observed in the trigger configuration $8 < p_{\mathrm{T1,trig}} < 12\,\mathrm{GeV}/c$ and $4 < p_{\mathrm{T2,trig}} < 6\,\mathrm{GeV}/c$. But in this trigger configuration the deviation from unity is not significant within the uncertainties. These three trigger configurations do have the largest p_{T} differences of all trigger configurations analyzed in this thesis. This indicates that the systematic lowering of the R_{T1T2} below unity is dependent on the p_{T} difference between the triggers. The lowering is explained by the trigger bias (see Section 6.7.2). This effect is expected for all collision types and not only for the most central collisions which is exactly what is observed.
The general observations of the R_{T1T2} have a low significance due to large statistical

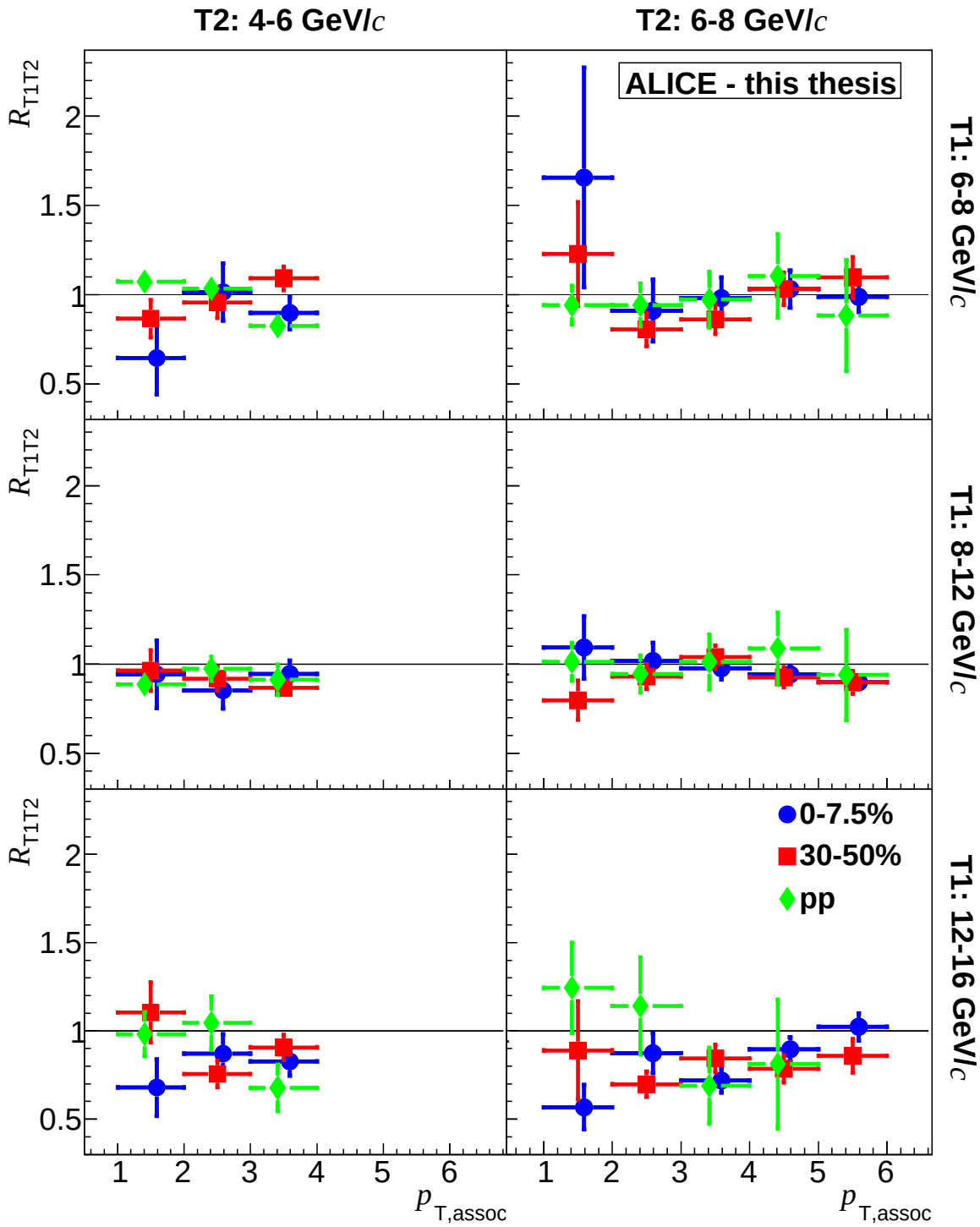

Figure 9.14.: R_{T1T2} is calculated for the 0–7.5% and 30–50% most central Pb–Pb events and for pp events. This measurement does not contain a systematic uncertainty.

uncertainties. They are:

- R_{T1T2} is in agreement with unity or below unity for all measured trigger configurations
- the lowering of R_{T1T2} below unity can be explained by the trigger bias
- at larger $p_{\mathrm{T1,trig}}$ (this is equal to larger transverse momentum differences between the triggers), R_{T1T2} decreases
- no dependency of R_{T1T2} on $p_{\mathrm{T2,trig}}$ or $p_{\mathrm{T,assoc}}$ has been observed

The measured R_{T1T2} below unity means that the associated particle yield from trigger 2 is larger than from trigger 1. The lowering scales with the p_{T} difference between the trigger particles. This is a bias effect which has been observed already in HIJING simulations. Due to the lower $p_{\mathrm{T2,trig}}$ requirement compared to $p_{\mathrm{T1,trig}}$, the jet containing trigger 2 has more energy to create associated particles. No dependence on $p_{\mathrm{T,assoc}}$ has been observed. This indicates that the trigger 1 and trigger 2 associated particles were affected in the same way by the QGP. In case one of the triggers would have been more affected a softening in the associated particle yield would have been expected.

9.8. Comparison of the ALICE and STAR I_{AA}

In Section 2.8 the 2+1 measurements of the STAR experiment were introduced. STAR uses 2+1 correlations for Au–Au and d–Au measurements at a collision energy of $\sqrt{s_{NN}} = 200\,\mathrm{GeV}$. Out of the STAR peak yields the I_{AA} ratio was calculated.
In this Section the ALICE I_{AA} is presented for the trigger configuration which was used by STAR. The analysis of the two experiments differ by the background subtraction methods as discussed in Section 2.8. In this thesis the background is subtracted with the scaled 1+1 events. The remaining background is estimated with a constant at large $\Delta\eta$ in the yield extraction. STAR uses a method similar to the scaled 1+1 events. But the remaining background is subtracted with another 1+1 correlation and a flow estimation from independent STAR measurements.
In Figure 9.15 the ALICE results for the STAR trigger configuration are compared with the results from STAR. For the points up to $4\,\mathrm{GeV}/c$ it can clearly be seen that the ALICE I_{AA} decreases as a function of $p_{\mathrm{T,assoc}}$. The decrease rate is higher for the trigger 1 associated I_{AA} compared to the trigger 2 associated I_{AA}. Unlike the STAR I_{AA}, both ALICE I_{AA} are not in agreement with unity.
The ALICE I_{AA} is for both triggers significantly higher than STAR. Additionally it contains a strong decrease from $1 < p_{\mathrm{T,assoc}} < 2\,\mathrm{GeV}/c$ to $2 < p_{\mathrm{T,assoc}} < 3\,\mathrm{GeV}/c$. In STAR the I_{AA} is constant. For the trigger 2 I_{AA}, a decrease as a function of $p_{\mathrm{T,assoc}}$ is observed in STAR the same way as in ALICE. But in STAR the I_{AA} is smaller and it drops below unity which is not observed for ALICE.
This comparison shows that the jet quenching or effects from a fragmentation bias (see Section 9.5) is much stronger at the LHC than at RHIC.

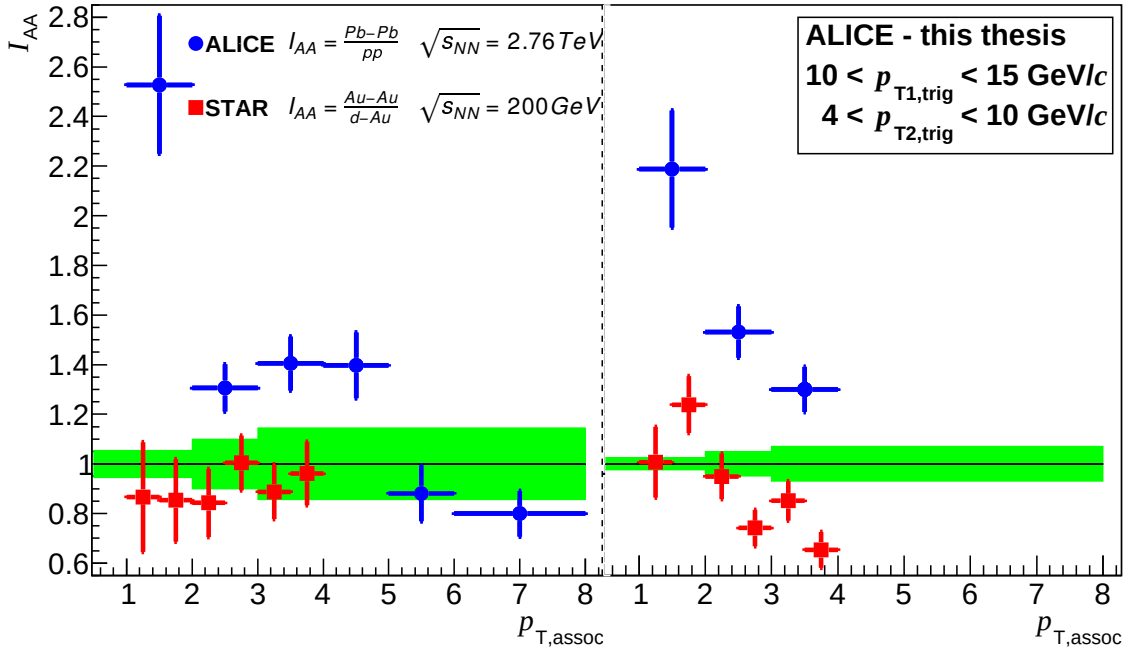

Figure 9.15.: Comparison of the ALICE and STAR I_{AA}. For ALICE the I_{AA} is computed out of Pb–Pb and pp collisions, for STAR out of Au–Au and d–Au collisions. In the left panel the trigger 1 associated and in the right panel the trigger 2 associated I_{AA} are compared. The green boxes show the systematic uncertainties of ALICE. The ALICE trigger configuration is adjusted to the trigger p_{T} bins from STAR.

9.9. Summary

In this chapter the 2+1 correlations in Pb–Pb and pp collisions measured with ALICE have been presented. Six trigger configurations have been chosen for the associated particle yield measurement. A strong decrease of the peak yield as a function of $p_{\mathrm{T,assoc}}$ has been observed.

In the I_{CP} analysis in Section 9.5 the associated peak yield at small $p_{\mathrm{T,assoc}}$ has been found to be enhanced in the 0–7.5% compared to the 30–50% most central Pb–Pb collisions. The same effect was observed by analyzing the I_{AA} in Section 9.6. This is interpreted either as a quenching effect from the QGP or as trigger bias on the parton p_{T}.

Quenching effects cause highly energetic partons to transfer some energy to less energetic partons and to generate new partons due to radiation effects while they traverse the medium. In more central Pb–Pb collisions stronger medium effects are observed as a larger enhancement of the I_{CP} and I_{AA} over unity at small $p_{\mathrm{T,assoc}}$. In this scenario the I_{CP} measurements make it possible to deduce where the measured jets are produced in the fireball. Due to the observed quenching effects for both trigger par-

ticles, they most likely originate from hard collisions within the QGP. This way the associated particles from both triggers are affected by the QGP. If these kind of hard collisions would not contribute to the 2+1 measurements, different signatures would be expected in the measurement for trigger 1 and trigger 2.
If the I_{CP} and I_{AA} are created by the trigger bias, the QGP would have influenced the di-jets in a way so that more jets from high $p_{\mathrm{T,assoc}}$ partons are measured. This scenario makes it impossible to deduce the position of the hard collisions within the fireball.
In Section 9.7 the associated particle yield of the two trigger particles are compared. R_{T1T2} has found a small lowering below unity for most of the trigger configurations. This means the associated particle yield from trigger 2 is larger than from trigger 1. The lowering scales with the p_{T} difference between the trigger particles. This is a bias effect which has been observed already in HIJING simulations. Due to the lower $p_{\mathrm{T2,trig}}$ requirement this jet has more energy to create associated particles.
R_{T1T2} has no dependence on $p_{\mathrm{T,assoc}}$. This indicates that the trigger 1 and trigger 2 associated particles were affected in the same way by the QGP. In case one of the triggers would have been more affected, a softening of the associated particle yield from this trigger would have been expected.
The 2+1 correlations have been measured by STAR at RHIC with Au–Au and d–Au collisions. In Section 9.8 the results from STAR are compared with ALICE. The I_{AA} has been found to be higher in ALICE. These are significantly different medium effects in the LHC ($\sqrt{s_{NN}} = 2.76\,\mathrm{TeV}$) compared to RHIC ($\sqrt{s_{NN}} = 200\,\mathrm{GeV}$).

Summary

This thesis has developed a new 2+1 particle correlation method and applied it for the first time to data from ALICE.
The 2+1 particle correlations use trigger particles which are back-to-back in azimuth as proxies for di-jets. The associated particle yield was analyzed for both trigger particles in multiple centrality classes. This makes it possible to further study quenching effects in the Quark-Gluon Plasma. The measured 2+1 particle yield contains many different yield components which are described in this thesis in detail. Compared to 1+1 correlations the 2+1 correlations contain an additional form of background from uncorrelated trigger particles. A background subtraction technique was developed with the help of a toy event generator and HIJING simulations. It has been applied to the correlation measurement to extract the correlated signal.
The full 2+1 particle correlation measurement was done separately for HIJING and ALICE events. The analysis of MC events from the HIJING generator makes it possible to study the biases of the method and to verify the background subtraction technique. No bias has been found in the measurement of the peak yield for any centrality. Consequently the I_{CP} was found to be at unity which is the expected result in the absence of medium effects. A difference has been found between the associated particle yield of the two trigger particles. The trigger 2 associated particle yield is larger than the trigger 1 associated particle yield, thus R_{T1T2} is biased below unity.
The 2+1 correlations have been measured in ALICE in Pb–Pb and pp collisions at $\sqrt{s_{NN}} = 2.76\,\mathrm{TeV}$. In the I_{CP} a significant enhancement over unity was measured at low associated transverse momenta $p_{\mathrm{T,assoc}}$ for both trigger particles. Considering the I_{CP} is at unity for HIJING events, this indicates that the associated particles of both triggers were affected by stronger medium effects in the 0–7.5% most central Pb–Pb events compared to the 30–50% centrality interval. These observations were confirmed in the comparison between Pb–Pb and pp events in the I_{AA}. The enhancement is either an effect of jet quenching or due to a bias in the parton p_{T} spectrum.
The I_{CP} and I_{AA} measurements showed that the associated particle yield from both trigger particles are affected by the QGP in the same way. This indicates that the partons creating these jets were most likely both affected by the QGP in the same way as well. If the I_{CP} and I_{AA} enhancements are due to quenching effects, this is a constraint on the position within the fireball where the di-jets were created. In this scenario the 2+1 correlations select parton pairs which were created inside the QGP. Both partons of such a parton pair traverse parts of the QGP. There is no preferred selection of azimuthally back-to-back parton combinations for which one parton fragments in the vacuum and the other one traverses the medium before the fragmentation. If many jets from such partons which fragment directly in the vacuum would be included in

the measurement of one trigger particle, the I_{CP} and I_{AA} of the this trigger particle would be expected to be at unity. But some such trigger combinations might be part of the measurement.
R_{T1T2} decreases below unity as a function of the trigger p_{T} difference. At larger trigger p_{T} differences, the lowering below unity is stronger. This is the same trigger bias as in HIJING events. However, it does not mean that the trigger 1 and trigger 2 associated particles were not affected by the medium, it means that the medium effects are identical for both trigger particles.
The ALICE I_{AA} measurements were compared to the measurements from STAR at RHIC. In ALICE a yield difference between Pb–Pb and pp collisions has been found. The associated particle yield for both trigger particles is observed to be larger in Pb–Pb collisions. In STAR no difference between Au–Au and d–Au collisions was observed. This indicates that the QGP created in the LHC ($\sqrt{s_{NN}} = 2.76\,\mathrm{TeV}$) has a significantly different effect on the back-to-back jet production than the QGP created at RHIC ($\sqrt{s_{NN}} = 200\,\mathrm{GeV}$).
In summary the new analysis method of 2+1 correlations has been established within ALICE. It has been successfully used to determine the associated particle yield of di-jets in Pb–Pb and pp collisions. The comparison of these yields shows medium effects in Pb–Pb collisions.

Zusammenfassung

Im Rahmen dieser Arbeit wurde eine neue 2+1 Teilchen-Korrelationsanalyse entwickelt und zum ersten Mal auf Daten von ALICE angewendet.
Die 2+1 Teilchen-Korrelationen verwenden einander azimutal gegenüberstehende Triggerteilchen als Platzhalter für Di-Jets. Die Teilchen-Korrelationen wurden für beide Triggerteilchen bei mehreren Zentralitäten analysiert. Dies erlaubt die Quenching-Effekte im Quark-Gluon-Plasma weiter zu untersuchen. Die gemessenen 2+1 Teilchen-Korrelationen enthalten viele verschiedene Komponenten, die im Detail in dieser Arbeit beschrieben sind. Verglichen mit den 1+1 Korrelationen enthalten die 2+1 Korrelationen eine weitere Untergrundart von unkorrelierten Triggerteilchen. Eine Methode diesen Untergrund zu subtrahieren wurde mit der Hilfe eines Eventgenerators und HIJING Simulationen entwickelt. Diese wurde in der Korrelationsmessung angewendet um das korrelierte Signal zu extrahieren.
Die vollständigen 2+1 Korrelationsmessungen wurden separat ausgeführt für HIJING und ALICE Ereignisse. Die Analyse von MC Ereignissen vom HIJING Generator erlaubt es die Voreingenommenheiten (Bias) der Methode zu analysieren und die Untergrundsubtraktion zu verifizieren. Keine Voreingenommenheiten wurde für die Messung des Korrelationspeaks bei irgendeiner Zentralität gefunden. Infolgedessen ist das I_{CP} bei Eins, was die Erwartungen in Abwesenheit von QGP Effekten bestätigt. Ein Unterschied wude zwischen den Teilchen-Korrelationen von den zwei Triggern gefunden. Die Trigger 2 assoziierten Teilchenkorrelationen sind größer als die Trigger 1 assoziierten Teilchenkorrelationen. Daher ist R_{T1T2} systematisch unter Eins.
2+1 Teilchen-Korrelationen wurden in ALICE in Pb–Pb und pp Kollisionen bei $\sqrt{s_{NN}} = 2.76\,\mathrm{TeV}$ gemessen. Im I_{CP} wurde bei kleinen assoziierten Transversalimpulsen für beide Triggerteilchen eine signifikante Erhöhung über Eins gemessen. Unter Berücksichtigung des I_{CP} bei Eins in HIJING Ereignissen, deutet dies an, dass die assoziierten Teilchen beider Trigger in den 0–7.5% verglichen mit den 30–50% zentralsten Ereignissen von stärkeren QGP Effekten beeinflusst wurden. Diese Beobachtungen wurden im Vergleich von Pb–Pb und pp Ereignissen im I_{AA} bestätigt. Die Erhöhung ist entweder ein Effekt vom Jet quenching oder eine Voreingenommenheit im Parton Transversalimpulsspektrum.
Die I_{CP} und I_{AA} Messungen zeigten, dass die Teilchen-Korrelationen von beiden Triggern auf dieselbe Weise beeinflusst wurden. Dies deutet an, dass vermutlich auch die Partonen, die in diese Jets fragmentierten, beide vom QGP in derselben Art und Weise beeinflusst wurden. Wenn die I_{CP} und I_{AA} Erhöhungen von quenching Effekten verursacht wurden, dann schränkt dies den Ort im Feuerball ein an dem die Di-Jets erzeugt wurden. In diesem Szenario selektieren die 2+1 Korrelationen Partonen Paare, die im QGP erzeugt wurden. Beide Partonen von so einem Partonen Paar durchqueren Teile

des QGPs. Es gibt keine bevorzugte Selektion von azimutal gegenüberliegenden Partonen von denen ein Parton in das Vakuum fragmentiert und das andere die Materie durchquert bevor es fragmentiert. Wenn viele Jets von solchen Partonen, die direkt ins Vakuum fragmentiert sind, in der Messung eines Triggerteilchens enthalten wären, wären die I_{CP} und I_{AA} von diesem Triggerteilchen erwartet bei Eins zu sein. Aber ein paar solcher Triggerkombinationen können Teil der Messung sein.
Das R_{T1T2} ist abgesenkt unter Eins als Funktion der Differenz der Triggertransversalimpulse. Bei größeren Transversalimpulsdifferenzen ist die Absenkung unter Eins stärker. Dies ist die gleiche Voreingenommenheit von den Triggern wie bei HIJING Ereignissen. Aber das bedeutet nicht, dass die trigger 1 und trigger 2 assoziierten Teilchen nicht durch das QGP beeinflusst wurden. Es bedeutet, dass die QGP Effekte gleich sind für beide Korrelationen.
Die ALICE I_{AA} Messungen wurde mit den Messungen von STAR am RHIC verglichen. In ALICE wurde ein Unterschied zwischen den Pb–Pb und pp Korrelationen gefunden. Die Korrelationen von beiden Triggern sind größer in Pb–Pb Kollisionen. In STAR wurde kein Unterschied zwischen Au–Au und d–Au Kollisionen gefunden. Dies deutet an, dass das im LHC ($\sqrt{s_{NN}} = 2.76\,\mathrm{TeV}$) erzeugte QGP signifikant andere Effekte auf die Di-Jet Produktion hat als das am RHIC ($\sqrt{s_{NN}} = 200\,\mathrm{GeV}$) erzeugte QGP.
Zusammengefasst wurde die neue 2+1 Teilchen-Korrelationsmethode etabliert innerhalb von ALICE. Sie wurde erfolgreich verwendet um die Korrelationen von Di-Jets in Pb–Pb und pp Ereignissen zu messen. Der Vergleich dieser Korrelationen zeigt QGP Effekte in Pb–Pb Kollisionen.

A. The LEGO Train System

Most of the analysis work of ALICE is carried out using the LEGO train system on the Grid. The name LEGO stands for 'Lightweight Environment for Grid Operators'. This system is a centralized analysis system which organizes Grid analyses. The system was created at the beginning of 2012 and it developed into the main analysis system of ALICE. In Table A.1 the average number of running analysis jobs run by the trains is compared to the average number of jobs run by the users. The table shows that the absolute and the relative number of LEGO train jobs continuously increased over the years. This shows that the demand for computing resources raised during the last years and more and more analysis is executed with the train system.
In Figure A.1 the number of running jobs submitted by users and the LEGO trains are shown graphically for the years 2013 to 2015. It can be clearly seen that the number of jobs from the LEGO trains increase over the whole period. At the beginning of 2012 the average amount of running jobs submitted by the train system is around 2 000 to 3 000. At the end of 2015 this increased to over 10 000. The average number of running jobs submitted by users stayed on the same level of around 4 000 since 2013. With the overall increasing number of analysis jobs the relative amount of jobs submitted by the train system raises.
During the work on this thesis a considerable amount of work was invested into the LEGO train system. In this chapter a selection of the developments from the past years are shown and the benefits of them are explained.
First the LEGO train system is explained in the Sections A.1 and A.2. This is followed by the description of some developments for the interface in Section A.3. As part of the system improvements statistical tools were developed to monitor the trains and identify possible improvements. In Section A.4 a selection of these tools are shown together with the improvements targeting the bottlenecks which were identified with these tools.

year	LEGO train jobs	user jobs	% of train jobs
2012	2511	7128	26.1
2013	4153	3970	51.1
2014	5570	4428	55.7
2015	9202	3755	71.0

Table A.1.: Average number of running Grid jobs by the train system and by the analysis users.

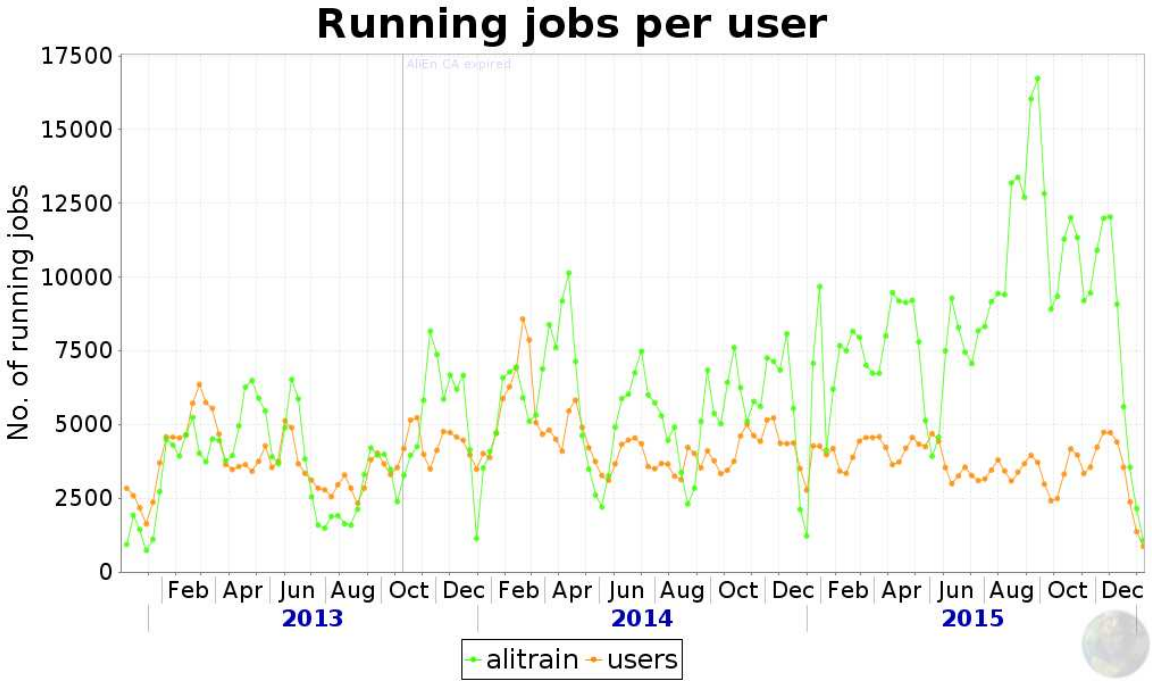

Figure A.1.: The number of analysis jobs running on the grid are shown for the LEGO train system and for all users combined as a function of time. Plot taken from [ALI15c].

A.1. Workflow

The LEGO train system contains many individual trains which are ordered by the Physics Working Group (PWG) and the kind of the analyzed data (MC or data, ESD[1] or AOD[2]). Each train is operated by one or multiple train operators, who are responsible for running the train on a regular basis.
The entry point to the train system is a web page with an overview of all trains. From here every individual train page is linked. This individual train page shows the components of the train. They are the train wagons, the datasets, the handlers and the train runs. The train wagons are defined and activated by the users. Only the activated wagons can run in the trains.
The datasets and train handlers are defined by the operator. The datasets consist of a production identifier and an optional subset of runs from that production. A dataset can be based on measured data or MC simulations. The train handler has to be adjusted to the correct format so that it can read the data from the dataset.
On a regular basis the train operators run the trains. To do so they collect all train wagons which should run over the same dataset and they form a train run out of them. The train operator checks that the train setup is correct and starts the train. When the train finished the users can directly access the result file.

[1]Event Summary Data
[2]Analysis Object Data

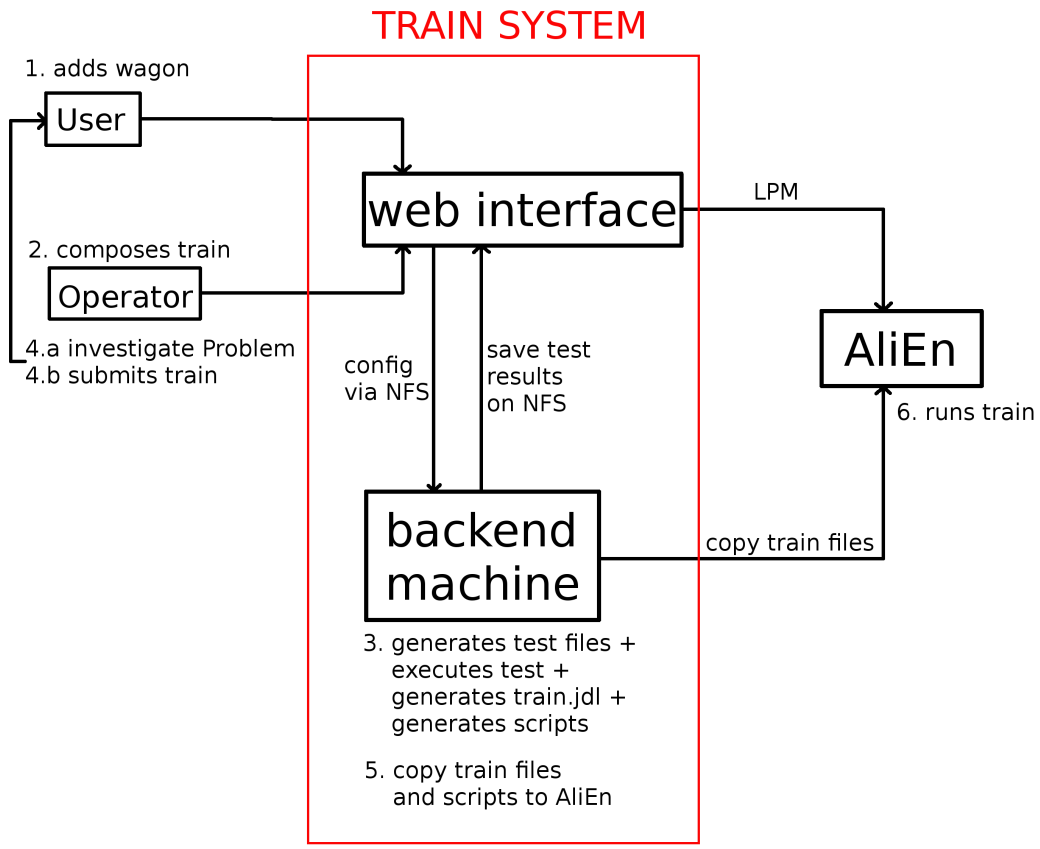

Figure A.2.: Workflow of the train system.

The procedure to form a train and the measures of the system to ensure that the setup is correct is shown in the following section.

A.1.1. Starting a Train Run

The train system is divided into five parts:

- Web interface building upon MonALISA (**Mon**itoring **A**gents using a **L**arge **I**ntegrated **S**ervices **A**rchitecture)
- Backend machine
- AliEn (**ALI**CE **En**vironment)
- AliROOT framework running the user code
- LPM (**L**ightweight **P**roduction **M**anager)

The work flow in the system is shown in Figure A.2. It follows the following steps:

1. **User adds wagon** The user adds a wagon to the train and activates it for a dataset. The user is responsible for ensuring the code is working and checked in into the AliROOT tag.

2. **Train operator composes train** The train operator puts the activated wagons into a train run and starts a test.

3. **Generate test files + execute test** The web interface saves the train configuration in a local directory, which is mounted on the backend machine using the shared network file system (NFS). On the backend machine, the test is executed and the results are stored in the same folder. Thie test first carries out a simple baseline, which only consists of the train environment. Afterwards each train wagon is tested on its own with its dependencies. At the end all wagons are tested together like they would run in the Grid train run. For the test only a small amount of data is used. While the test is executed, the train files for the Grid run are generated. After the test finished, the web interface shows the result.

4a. Problem(s) in the test The train operator has to investigate the problem of the train test, and in case of a problem for a wagon the operator may exclude that wagon or contact the user who owns this wagon. After the problem is fixed or the wagon is excluded the train run needs to be tested again.

4b. Test is fine The operator can start the train run.

5. **Copy JDL and scripts to AliEn** The generated job description files (JDLs) and scripts to execute the jobs and validate the output are copied from the backend machine to AliEn and the train definition is registered in the LPM which will then supervise the submission and execution of the actual analysis and merging jobs.

6. **Train runs** The train runs and the web interface shows the status of the train run.

The storage of the system is ensured by a database to which only the web interface has direct access. The database contains the full information about a train, all the train runs from the past and some statistical information about the sub jobs of the train runs like the running time.
The communication between the LEGO web interface and the backend machine is done via a shared NFS folder on the web server to which both components have write access. The configuration and the status of each train run is saved in files.

A.2. Train Runs

A.2.1. The Web Page

Only members of ALICE can access the LEGO train web page. Here the users and operators define the wagons, datasets and handlers. The web page for an example

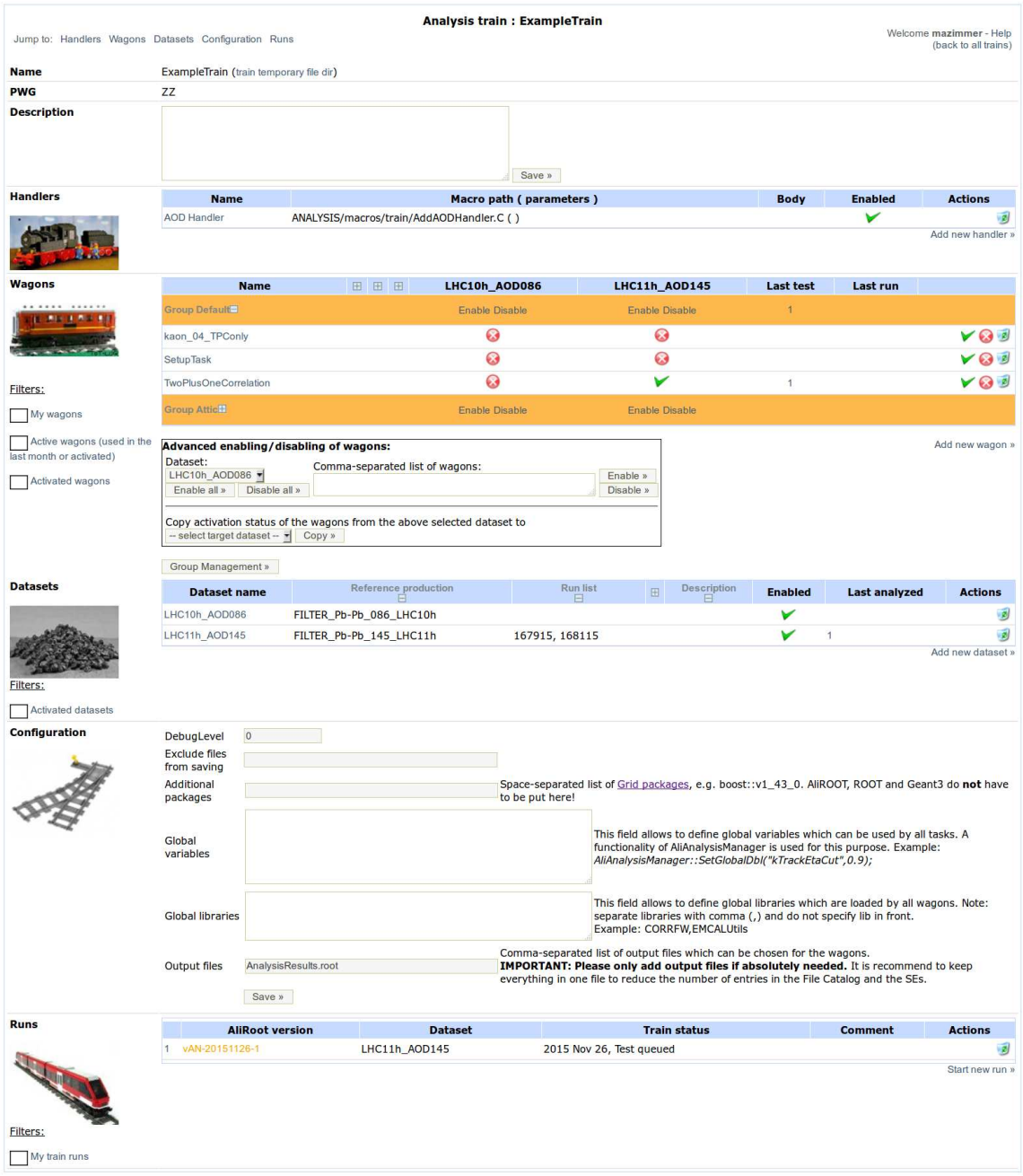

Figure A.3.: Example web page of the train. In this train three wagons and two datasets are defined. At the bottom of the page one train run is shown.

train is shown in Figure A.3. At the top the train name 'ExampleTrain' is shown and below an AOD handler is defined. The handler is used to read the files from the dataset. Dependent on the kind of data (MC or data and AOD or ESD) a different handler has to be used. The activated handler will be used for the new train runs.
In the next area the users can define and activate their wagons. In this example train only the wagon 'TwoPlusOneCorrelation' is activated. Under the wagons different options for the operators are shown to activate some wagons. The next area is the dataset area which contains one dataset called 'LHC11h_AOD145'. Here only operators can define new datasets. The users can have a look at the definition and choose the dataset they want to use.
The handlers and wagons are defined with paths relative to the AliROOT framework. This code framework runs on every computing node of the Grid. It handles the actual running of the user code which is part of the framework itself. The LEGO train web page collects all necessary information to run a train and executes it automatically.
Below the dataset area the operators can configure the train. It is possible to define additional software packages and libraries which are loaded at the beginning of each train run. The operator can define global variables which can be read by all wagons in the train. In this example train these fields are not used. The 'output files' field defines the name of the output file. It is possible to define multiple file names but the smallest possible number of files is preferred. Multiple files need more time and resources in the merging of the train results.
The last area of the train page shows the train runs. The operators can create new runs out of one dataset and several wagons. By clicking on the run number on the left side a new window is opened which shows the status of this train run. This status can be the last test or the results of the finished train. From this window the users can download the results after the train finished.
Many parts of this web page are part of the developments done within this thesis. Some example improvements are explained in Section A.3.

A.2.2. Testing a Train

In Figure A.4 the test of a train is shown. The train test is divided into several smaller tests. A baseline test and a full train test are executed. In between the train wagons are tested individually.
The baseline test does not contain any user code. If this test fails, there is a problem with the configuration of the train or with the general system. The full train test is the closest test to the train run on the Grid. The only difference is a smaller dataset. Consequently this test is the most important to guarantee that the wagons will run on the Grid as well. The other tests are executed to identify a bad wagon in case the train test fails.
For each test several measurements are shown. The first ones are the virtual and resident memory consumption. In this case the virtual memory consumption describes the full memory consumption of the task including any reserved memory on the disk. The resident memory is the used working memory. Both memory consumptions are

Wagon	Status	Memory					Output size	Timing				Merging
		Virtual		Virt. Δ	Resident	RSS Δ		Wall	Wall Δ	CPU	CPU Δ	
Base line stdout | stderr stats | output	OK	Max Avg Slope	470.6 MB 463.5 MB +0.749 KB/evt		310.1 MB 302 MB +0.748 KB/evt		log: 17.73 KB .root: 0 B	6m 19s 54.78ms/evt	6m 19s 54.78ms/evt	5m 40s 49.21ms/evt 89.83%	5m 40s 49.21ms/evt	**No output**
TwoPlusOneCorrelation_centBin @ stdout | stderr stats | output	OK	Max Avg Slope	1000 MB 934.2 MB +9.332 KB/evt	529.6 MB 470.7 MB +8.583 KB/evt	804.1 MB 737.5 MB +9.339 KB/evt	494 MB 435.5 MB +8.591 KB/evt	log: 19.19 KB .root: 20.8 MB	7m 13s 62.63ms/evt	0m 54s 7.85ms/evt	6m 58s 60.48ms/evt 96.57%	1m 18s 11.27ms/evt	OK merge dir
TwoPlusOneCorrelation_vertexBin @ stdout | stderr stats | output	OK	Max Avg Slope	943.1 MB 852.6 MB +18.19 KB/evt	472.5 MB 389.1 MB **+17.44 KB/evt**	744.6 MB 653.7 MB +18.19 KB/evt	434.5 MB 351.7 MB **+17.44 KB/evt**	log: 19.19 KB .root: 24.04 MB	6m 55s 60.07ms/evt	0m 36s 5.29ms/evt	6m 40s 57.89ms/evt 96.37%	1m 8.68ms/evt	OK merge dir
Full train stdout | stderr stats | output	OK	Max Avg Slope	1.408 GB 1.259 GB +30.21 KB/evt	971.1 MB 826.2 MB **+29.46 KB/evt**	1.215 GB 1.066 GB +30.21 KB/evt	933.8 MB 789.1 MB **+29.46 KB/evt**	log: 20.62 KB .root: 44.83 MB	8m 6s 70.33ms/evt	1m 47s 15.56ms/evt	7m 49s 67.81ms/evt 96.41%	2m 8s 18.60ms/evt	OK merge dir
Train file generation generation log | output	OK											

Figure A.4.: Test of a train with 2 wagons. First a baseline is tested without a wagon, then the wagons 'TwoPlusOneCorrelation_centBin' and 'TwoPlusOneCorrelation_vertexBin' are tested. At last the full train is tested containing both wagons. For each line the memory and time consumption is shown. The last row shows the result of the merging test.

shown for the full test and divided per event. If the per event consumption is large, this can indicate a memory leak. Another explanation can be a too small sample size. The next test result is the output size. This shows the size of the output file. In case of too big files they cannot be registered within AliEn anymore.
The validation of the test result is done with a shell script. If the validation is successful, the test result files are duplicated and these copies are merged. This is the merging test. For the test of single wagons, two copies are merged. For the full train test the merging is done with ten copies.
The last part of the train test, is the check if the train files for executing the train on the grid are generated. Only if all these tests are successful, can the train run be started.
For each test (base line, the individual wagons and the full train) a statistics file is generated. In this file the number of events, the resident and virtual memory consumption, the wall- and cpu time and the cpu efficiency are saved using the AliSysInfo functionality. Currently these statistics are gathered in steps of 100 events (Pb–Pb) and 2 000 events (pp).
If a train run is tested for the second time, the folder with the previous test is kept but it is not linked anymore from the web interface. With the correct link it can still be accessed with a web browser. This allows the user to compare the result of different tests. The database is always updated to the information from the last train test.

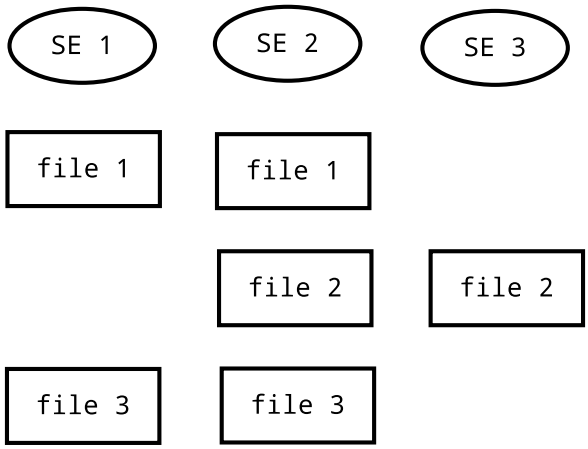

Figure A.5.: The distribution of three files on three SE with two replica each is shown. The files 1 and 3 are in the same basket.

A.2.3. Splitting of the Train Jobs

When the train is submitted each masterjob splits into analysis jobs, which have at maximum a certain number of files. This number is defined in the dataset by the operator. It is possible that there are less input files in a job, because all input files must be from the same basket. A basket is the set of SEs (Storage Elements) which hold a physical copy of a file. This means that two files are in the same basket if their respective SE sets are identical. In Figure A.5 this is illustrated. The files 1 and 3 are both saved on the SE 1 and 2. This means that they are in the same basket. The file 2 is saved on the SE 2 as well but because of the other replica on SE 3 the basket is different.
The job splitting algorithm only puts input files together into one job if they are in the same basket. If there are less files in one basket than would be allowed to run in one job, the files are all executed in one job. In case of more files in a basket than allowed to run in a single job, multiple jobs with files from this basket are created.
After creating the jobs this way, any free computing core close to one of the SEs in the basket can pick up the job. This is called the SE requirement. The requirement exists in order to optimize the network utilization, keeping the data access local to one site and by doing this also increasing the job CPU efficiency.

A.2.4. Merging the Jobs

The merging is divided in two levels. First the merging is executed per masterjob (this means typically per run number). The result of this merging is merged in another separate merging process. This is shown schematically in Figure A.6.
Both merging operations are executed in up to 5 stages. The first one starts when all the analysis jobs have finished. In one merging job at maximum *MaxMergeFiles* files are merged into one file. This number is defined by the operator in the dataset defi-

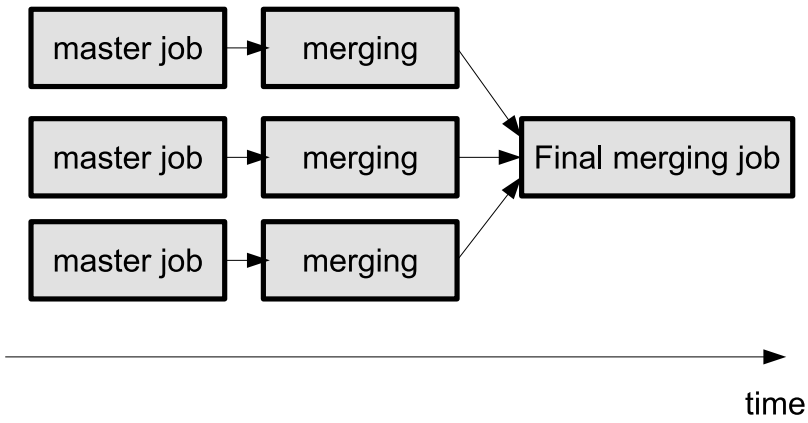

Figure A.6.: Schematic overview over a train run. The master jobs run independent of each other and contain many subjobs. For each master job the subjobs are merged individually. After this merging is finished the result is merged with the result from the other master jobs

nition. Within the merging job the merging is done for 2 files separately. When they finish another file is merged with the previous result and so on. If there is a memory leak in the merging algorithm, errors can appear for a high value of *MaxMergeFiles*. Low numbers increase the time which is necessary to do the merging because more merging stages are necessary. So a moderate value does speed up the merging process and it protects from memory leaks.
In the first merging operation the files have to be on the same SE. When no more merge operations are possible, the final merging is started. Then all files from the different SEs are merged together in one last job. For this one job the SE requirement is dropped and the number of merged files is also not restricted.
The merging of a train run starts automatically as soon as all train jobs are finished. If more than 50% of the sub jobs from one masterjob fail, the merging is not started. In this case it is assumed that the user code has a bug or there is a major issue with the system. In the first case the result would not be important anyway and in the second case the failed jobs may be possible to recover after an administrator intervention. If the jobs are recovered, the merging will start normally as soon as the last analysis job finished. In case that the jobs cannot be fixed, the operators have the option to manually start the merging with all available job results.

A.2.5. Killing and Resubmitting Jobs

Some jobs on the Grid do not finish successfully and end up in an error state. These errors can be caused due to different reasons. The first obvious reason is a bug in the code. Alternatively these errors can be caused by a failure of the computing node. The second type of errors can be recovered in most of the cases by rerunning the job. To recover as many jobs as possible, but to not waste a huge amount of computing power, all analysis jobs which end in an error state are resubmitted once. The merge

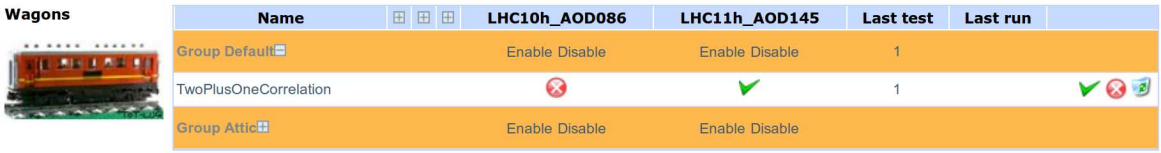

Figure A.7.: Activation of a wagon. The example wagon is activated for the dataset 'LHC11h_AOD145' and it is not activated for 'LHC10h_AOD086'. In the next train run the wagon will be included in the train run with the dataset 'LHC11h_AOD145'.

jobs are resubmitted up to three times, because a lost merging job results in a much higher lost statistics for the user.
The resubmission is done automatically and cannot be done by operators or users. If a job still ends up in an error state after the respective number of resubmissions for its type, it will be left in the error state. The resubmission process is stopped if 50% or more of the train jobs end in an error state because it is assumed that the jobs have a general problem.

A.3. Interface

During the early development stages of the LEGO train system it lacked automated procedures. For the normal train configuration the operators had to do many configurations manually, which often required additional email exchanges with the users. With the first system improvements the necessary informations could be communicated through the system. This way the workload to run a train was significantly reduced. Additionally the handling was simplified so that new users can easier get into the workflow.
A full description of all improvements to the system, which were developed, would exceed the limits of this thesis. Some examples were chosen to illustrate how the interface was improved. In Section A.3.1 the activation process for wagons is described before this improvement was deployed and afterwards. This significantly reduced the necessity to have additional communication between the train operators and users. The introduction of subwagons is described in Section A.3.2.

A.3.1. Activating Wagons

The old wagon design involved the possibility of activating a wagon. Only activated wagons could be included in a train run. With the activation of a wagon the user signaled that this wagon should participate in the next train run. But the dataset for the train run was not defined. Thus the user had to write an email to the operator to clarify the dataset. The operators had to collect the necessary information from several emails and create the train runs accordingly. In the wagon management an error could have easily happened so that a wagon might have run over the wrong

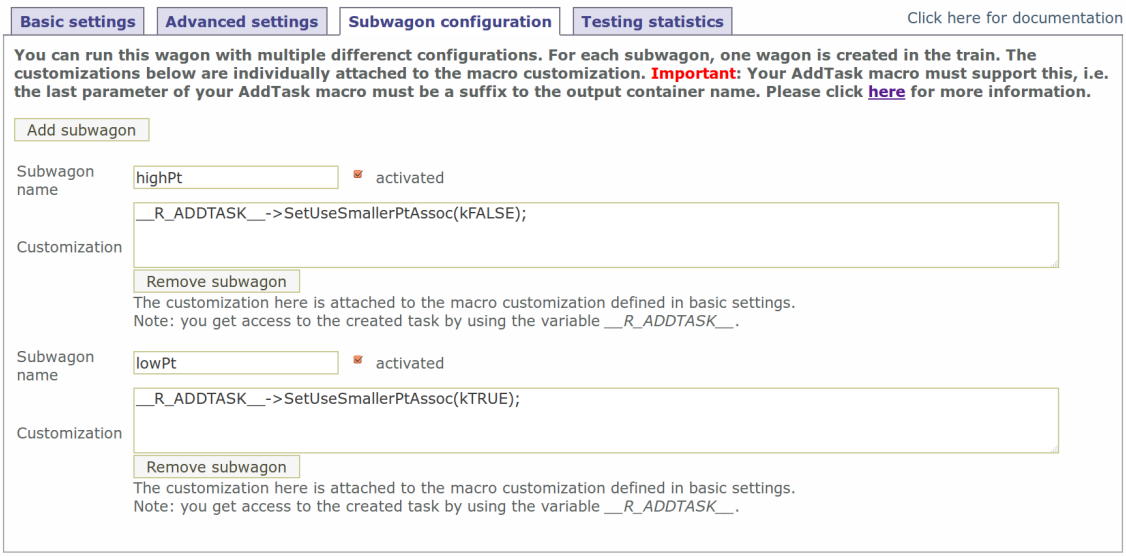

Figure A.8.: Configuration of two subwagons of a train wagon. Both subwagons are activated. This window is part of the wagon definition.

dataset.
This was changed by allowing the users to activate their wagon per dataset. The operators can activate some datasets and the users choose one of them and activate their wagon by clicking on the activation sign of their wagon in the column of the desired dataset. This is shown in Figure A.7 for two datasets. In normal operation the average number of activated datasets is about 10. In this example the wagon is activated for the dataset 'LHC11h_AOD145'. It will be included in the next train run of this dataset. The advantage of this activation system per dataset saves the email communication between the user and the operator. Additionally the wagons are already grouped per dataset for the operator when the train runs are defined.

A.3.2. Subwagons

During the train submission many operators noticed similar wagons. Often the same task should run on the trains in several slightly different configurations. For example for the analysis of the systematic uncertainties with different track cuts or another configuration variable.
To run this in the trains two wagons were required which contain typically around ten lines of configurations but only a few differ between the different wagons. In case another setting was required for the task, this had to be changed at two places (in both wagons). This setup does not only have a higher risk for misconfiguration, it also increases the number of wagons which all need to be activated individually. This makes the train setup more complex.
The development of the subwagon feature allowed the users to run multiple wagon configurations in a train run with one single wagon. Each subwagon contains a cus-

tomization which is applied to the wagon additionally to the normal wagon configuration. In Figure A.8 the subwagons for one example wagon are shown. Each subwagon contains a name, the configuration and a switch if this subwagon is activated. Only the activated subwagons are used in a train run.
Two copies of the same wagon would not be able to run in the same train run because they would write their output into the same output container which would result in a conflict. To avoid this, the users have to adjust their code. The last parameter of the wagon definition macro has to be a string which defines the output container. For an example wagon, which needs the integer parameters par1 and par2, the wagon defining macro is AddWagon(int par1, int par2, char* name). The parameters 'par1' and 'par2' have to be mentioned in the wagon definition. But not the parameter 'name'. Each wagon with subwagons automatically attaches the subwagon name to the parameters of the wagon definition macro.
In the train test and in the train run the subwagons run as if they would be separate wagons.

A.4. System Improvements

At the beginning of the work on this thesis the computing resource consumption was gathered per analysis job on the Grid but not aggregated per train. The operators had little information about the performance of the individual train runs. For the general system it was not clear which effects were mostly slowing down the system.
Part of this thesis work was to create tools to extract statistics about the train runs and understand the bottlenecks of the system. With these tools continuous monitoring of the system was implemented, which helped to identify potential improvements.

A.4.1. Input Files per Train Run

The running time of the train jobs can be adjusted by using more or less input files in a job. This way the resources can be used more efficiently. Because of the basket requirement for the splitting of train jobs (see Section A.2.3), it is not directly clear how many files are really used in each job. For some physics analysis it is important to have a certain minimum amount of files in a job. One example for such an analysis is the mixed event analysis which is explained in Section 5.3.
For all these cases it is important to know the used input file distribution for a train. At the end of each train run this number is gathered from all jobs and displayed in a graph. The train operators and users can access these information. It helps the operators to adjust the number of filer per job for the next train run and it helps the users to judge if there were on average enough files in the jobs to do their analysis in case this is necessary for their analysis.
An example distribution is shown in Figure A.9. The measured plot shows a distribution for a dataset which was chosen to be analyzed with 20 input files per job. The statistics clearly show that only a small amount of jobs actually run with 20 input

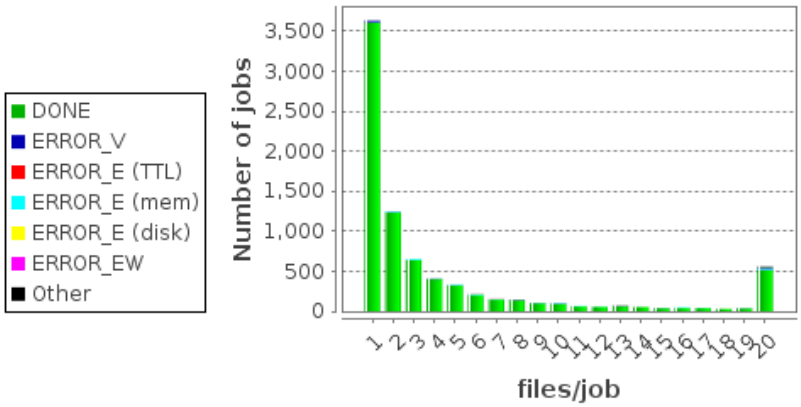

Figure A.9.: Number of input files per job in a standard train run. The train run was designed to run with 20 input files per job. But the statistics clearly show that most of the jobs contain only 1 input file. The different colors indicate different end states of the jobs. Green stands for successful jobs. All other colors stand for different kinds of errors.

files. For this train run a further increase of input files per job would not result in any change because most of the jobs run anyway with one input file. This problem was discovered immediately after the statistics plots were created. The underlying problem causing such distributions is discussed in the following Section. The developed solutions are presented afterwards in the Sections A.4.3 and A.4.4.

A.4.2. Basket Distribution

The presented file distribution in Figure A.9 is representative for many trains. The basket distribution of a dataset is not planned at the creation time of the dataset. It is dependent on free storage space on the SEs and on the place where the data is produced. For measured data the files are distributed on the SEs following a certain protocol from the experiment. The MC files are saved at the closest available location to the place where the files are produced. The MC production can run everywhere in the Grid.
This means that especially for MC produced datasets the files can be in many different baskets. One replica is often on a common SE for many baskets, but the second replica is distributed over all available SEs in the Grid. This means that the baskets are all different and the average number of input files per job is low.
For datasets containing measured data this effect is not that strong. But over time the files of the datasets are moving away from each other. If a replica gets corrupted on one SE and a new copy is created on another SE the basket changed. Sometimes all files from an SE have to be copied somewhere else because of some technical work on the SE. In this process the files may be distributed to many different SEs and thus to many different baskets. This shows that the basket distribution is not a permanent distribution but it is slowly changing.

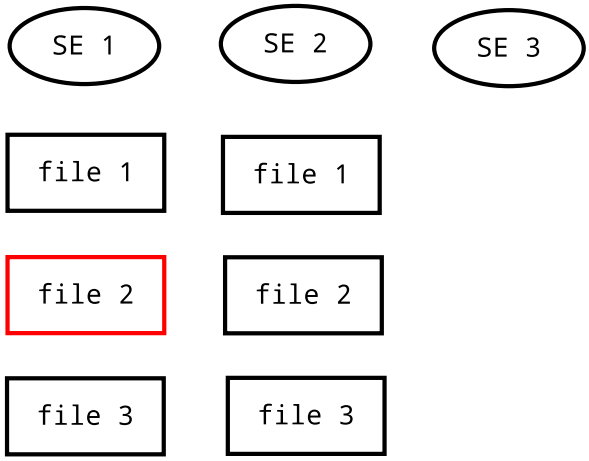

Figure A.10.: The file distribution from Figure A.5 after the clean up. The file 2 was moved from SE 3 to SE 1.

A.4.3. Basket Clean Up

One option to fix the input file distribution is to reorganize the basket distribution. For many baskets one replica is saved already at a common SE. This means by changing the other replica for some baskets, these baskets are adjusted to already existing baskets. During this operation a minimum number of input files is defined which each basket should have after the copy operations are finished.
The method is called basket clean up because at the end less baskets exist and each of them will have enough files to create at least one job with the designed number of input files. If the dataset shown in Figure A.5 would be cleaned up, this would mean that file 2 has to be moved from SE 3 to SE 1. The result is shown in Figure A.10.
The clean up is achieved at the cost of the copy operations, which create network traffic. With an increasing number of input files, which are requested to be in each basket, more copy operations are necessary to create this state. The copy operations are designed so that the network traffic is minimized.
In Figure A.11 the input file distribution for one dataset is shown before and after it was cleaned up. Before the clean up most of the jobs run with one input file. In this distribution it can be seen that the operator tried to run the analysis with 20 input files. But almost no job actually run with 20 input files. After the clean up the same dataset is analyzed and the input file distribution changed towards more files which are used with 10 input files. This number is lower than the number which was used before the clean up, but now many jobs actually use 10 input files. While before the clean up 1 528 jobs were necessary to run the train, afterwards 418 were sufficient.
The designed number of input files per job was reduced from 20 to 10 because with 10 input files the jobs have a reasonable running time. At this running time the computing resources are well used. With more input files the efficient usage of the resources would not further improve. The train would just take longer.

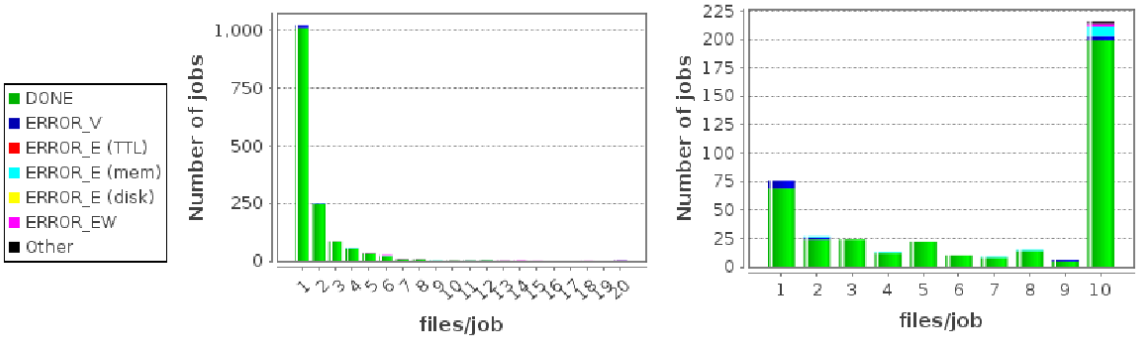

Figure A.11.: Input file distribution of the train jobs before (left panel) and after (right panel) the clean up.

A.4.4. Skip Processing per Run Number

The job splitting so far was executed for each run number separately. Files from the same basket but from different run numbers were running in separate jobs and then they were merged into different intermediate results. This run number requirement can be dropped so that files from all run numbers are considered to be able to run in the same job. This way most of the baskets have enough files to fill the jobs with the requested number of files.
The method is called 'Skip processing per run number' because the results cannot be provided for each run number anymore. Each job contains files from different run numbers. So the intermediate merged results contain results from many run numbers as well. The analysis is only split into multiple masterjobs because the maximum number of sub jobs on the system is reached. With the new splitting method the input file distribution per job is on a similar level as after the basket clean up.
The problem of this method is that some physics analysis cannot mix files from different run numbers. The reason can be that different configuration files have to be loaded for each run number. Or in other cases the runs have to be analyzed independently and then the results have to be scaled to the according cross section.
Because of these reasons it is possible to deactivate the 'Skip processing per run number' feature. In case the users of one of these tasks need many input files per job as well, the clean up method can be used.

A.4.5. Turn Around Time

For the general performance of the system the turn around time of the trains is important. The turn around time of a train is defined as the time interval from the moment when the operator starts the train run on the Grid until the merging is finished. This time interval measures the time the user has to wait for the output. The users prefer this time to be as short as possible to continue their analysis with the train result. For a single train run the turn around time depends on many factors like the analysis

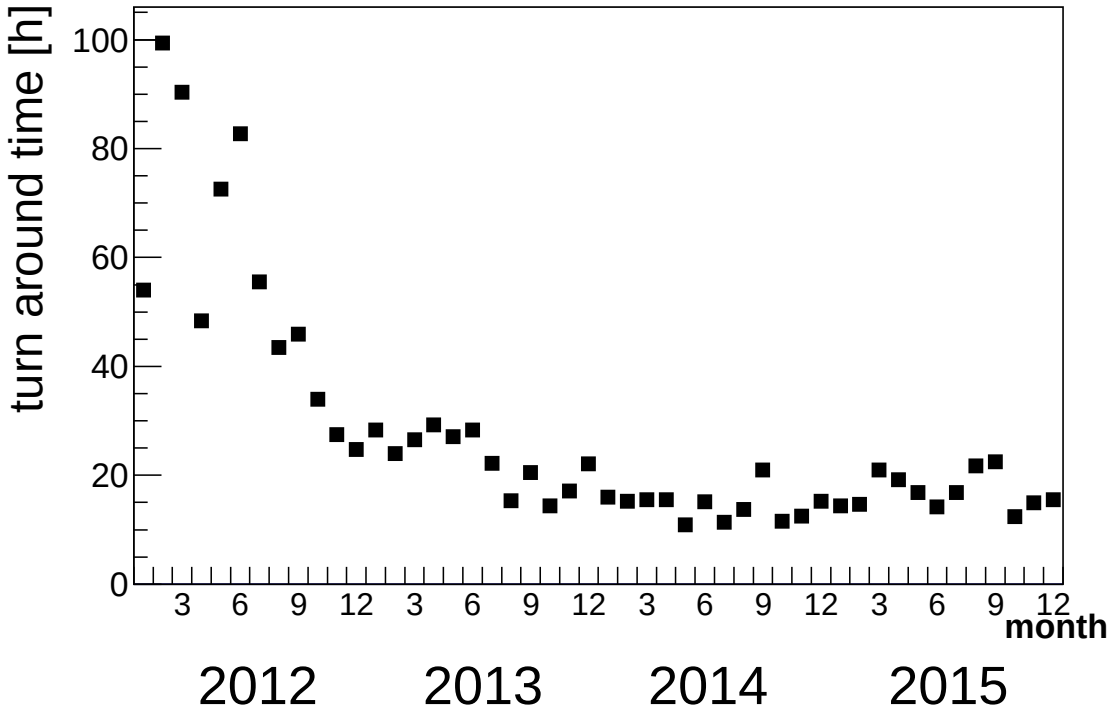

Figure A.12.: Turn around time of all automatically merged trains on the train system from 2012 to 2015.

code, the occupancy of the grid and many other factors. Therefore the monitoring is done for the average turn around time over long time scales and many train runs. This value allows to evaluate the performance of the system.
In Figure A.12 the train statistics from 2012 to 2015 are shown. For the average turn around time only train runs which are automatically merged are considered. If the operator started the merging manually, any time can be in between the finished last job and the moment the operator started the merging.
In the shown time period several improvements were implemented which reduced the average turn around time. The statistics clearly show that the turn around time decreased from 2012 to 2013 by a large factor. During 2013 more improvements were implemented and in July a significant reduction of the turn around time was achieved. This improvement is explained below in Section A.4.6. Further improvements were implemented but a full description would exceed the boundaries of this thesis.
The average turn around time per year is shown in Table A.2. This time is calculated by averaging over all train runs in the year. Because the number of train runs increased over time the average values from the end of the year in Figure A.12 have more influence than the values from the beginning of the year. The table shows the same information as the Figure. The turn around time was reduced every year from 2012 to 2014. From 2014 to 2015 it increased but this increase is much smaller than the reductions before.

year	average turn around time [h]
2012	49.2
2013	22.4
2014	14.5
2015	17.5

Table A.2.: Average turn around time per year. Due to different number of running train runs per month this is not equal to the average of the monthly turn around times from Figure A.12.

A.4.6. Running Time Optimization

For the users the turn around time should be as short as possible so that they can quickly continue with their analysis. To reduce the average turn around time, several improvements were developed.
By analyzing the individual train runs, it was found out that most of the jobs finish quickly while a few jobs run for very long. To speed up these last jobs the SE requirement is dropped when 90% of the jobs finished and 85% of the jobs are successful. At this moment any computing site can pick up a queued job and execute it. The input data of the job is then accessed remotely over the network.
After 98% of the jobs in a train are finished, the remaining running jobs are killed if a sufficient time passed since the 90% of the jobs were finished.
As soon as all jobs are finished, independent if they finished successfully or if they were killed, the merging will start. In Figure A.13 the different stages of a train run dependent on the relative amount of finished jobs is shown.
This improvement was introduced in July 2013. In Figure A.14 a zoom on the 2013 statistics of Figure A.12 is shown. Instead of averaging over all train runs in a month this is done for each week separately. The moment the improvement was implemented is shown with the red bar. The updates reduce the average turn around time significantly. Before the update the turn around time was 26.3 hours, afterwards it improved to 17.1 hours.

A.4.7. Usage of the Train System

Part of the monitoring process was to gather the number of train runs per month and how it evolves with time. In Figure A.15 the number of train runs per month is shown from 2012 to 2015. It can be seen that it was below 100 during 2012. At this time the trains were not running on a daily basis and only some people of ALICE used them. From 2013 on the number of train runs increased continuously over the years. For some months it can be seen that the number fluctuates down but in general it is increasing. The big downward fluctuations are often due to holiday seasons.

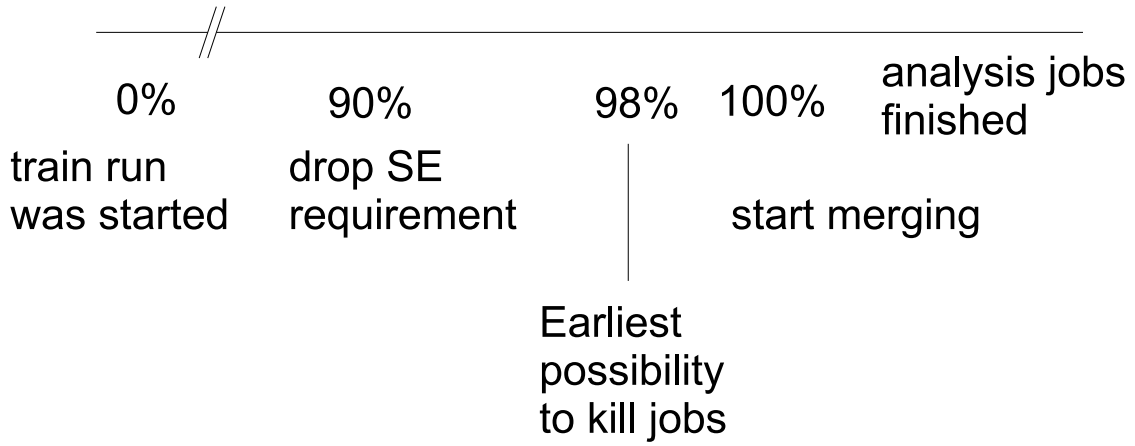

Figure A.13.: Stages of a train run. Shown are the percentages of the finished jobs in a single train run. The different stages are described in the text.

A.5. Summary

The LEGO train system is the centralized Grid submission system of ALICE. As part of this thesis, monitoring tools have been created which helped to identify bottlenecks of the system. Dedicated system improvements have been developed for the interface and for a better usage of the ALICE Grid resources.
The usage of the LEGO trains within ALICE increased during the last years so that it is now the main system which is used for the Grid analysis of the users.

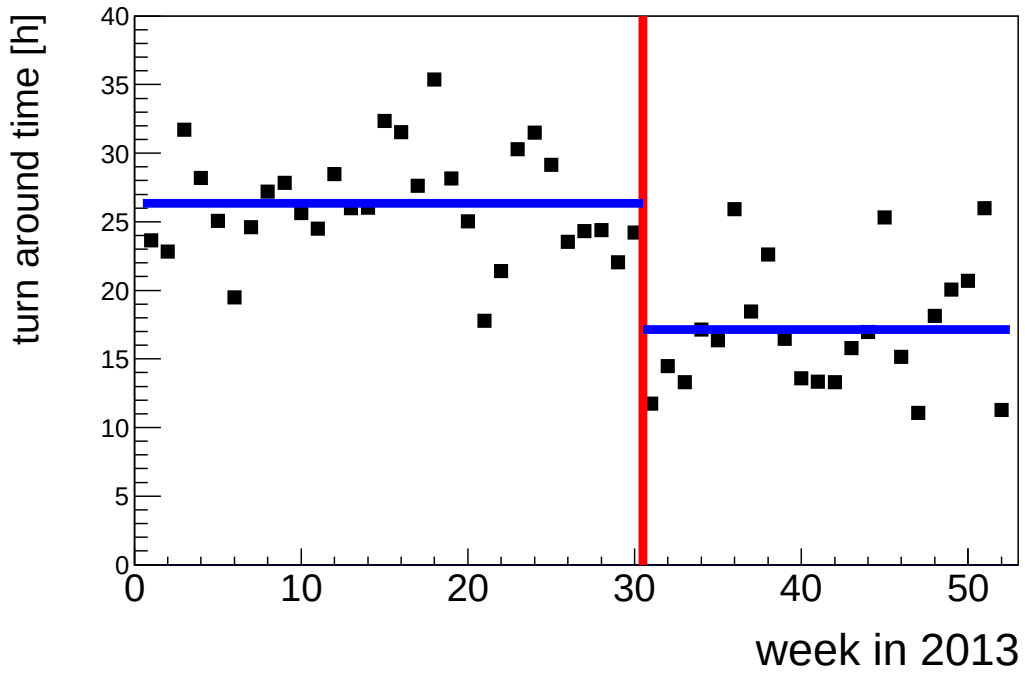

Figure A.14.: The average train turn around time for 2013. This is a zoom into Figure A.12. The same values are shown there averaged over the months, The red bar marks the moment the running time optimizations were deployed on the train system. The blue fits show the average turn around time before (26.3 hours) and after (17.1 hours) the optimizations.

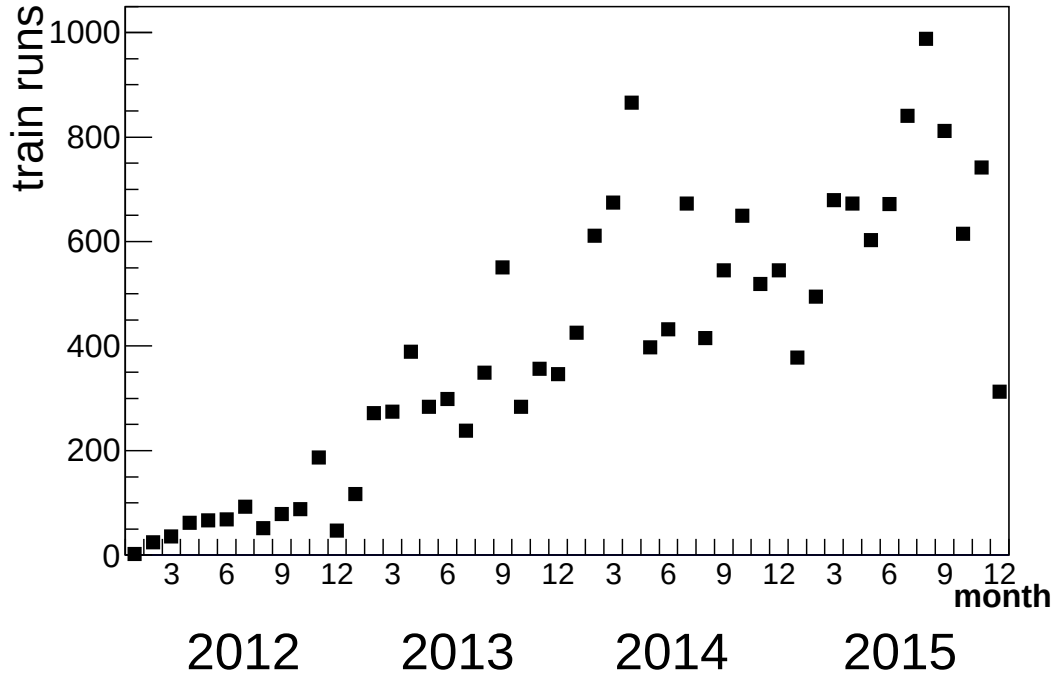

Figure A.15.: Number of train runs per month

B. Acronyms

ALICE	A Large Ion Collider Experiment
ALICE-DCal	ALICE Di-Jet Calorimeter
AliEn	ALICE Environment
AOD	Analysis Object Data
AP	Anchor Point
ATLAS	A Toroidal LHC ApparatuS
BNL	Brookhaven National Laboratory
CERN	European Organization for Nuclear Research (originally: Conseil Européen pour la Recherche Nucléaire)
CMS	Compact Muon Solenoid
DCA	Distance of Closest Approach
EMCal	ElectroMagnetic Calorimeter
ESD	Event Summary Data
FMD	Forward Multiplicity detector
HIJING	Heavy Ion Jet INteraction Generator
HLT	High Level Trigger
HMPID	High-Momentum Particle Identification Detector
IR	Interaction Regions
ITS	Inner Tracking System
JDL	Job Description Language
LEGO	Lightweight Environment for Grid Operations
LEIR	Low Energy Ion Ring

LEP	Large Electron Positron collider
LHC	Large Hadron Collider
LHCb	Large Hadron Collider beauty experiment
LHCf	Large Hadron Collider forward experiment
LINAC	LINear ACcelerator
LPM	Lightweight Production Manager
LS1	Long Shutdown 1
MC	Monte Carlo
MonALISA	MONitoring Agents using a Large Integrated Services Architecture
MRPC	Multi-gap Resistive-Plate Chambers
ndf	Number of Degrees of Freedom
NFS	Network File System
PHOS	PHOton Spectrometer
PS	Proton Synchrotron
pQCD	perturbative QCD
PID	Particle IDentification
PWG	Physics Working Group
QA	Quality Assurance
QCD	Quantum-Chromo-Dynamics
QGP	Quark-Gluon Plasma
RHIC	Relativistic Heavy Ion Collider
RF	Radio Frequency
SDD	Silicon Drift Detector
SE	Storage Element
SM	Standard Model
SPD	Silicon Pixel Detector

SPS	Super Proton Synchrotron
SSD	Silicon Strip Detector
STAR	Solenoidal Tracker At RHIC
SUSY	supersymmetry
TOTEM	TOTal cross section, Elastic scattering and diffraction dissociation Measurement
TOF	Time-Of-Flight
TPC	Time-Projection Chamber
TRD	Transition Radiation Detector
ZDC	Zero-Degree Calorimeter
ZYAM	Zero Yield At Minimum

Bibliography

[AGG13] J. Aichelin, P. B. Gossiaux, and T. Gousset. Collisional and Radiative Energy Loss of Heavy Quarks. *J. Phys. Conf. Ser.*, 455:012046, 2013.

[AK11] Anton Andronic and Christian Klein-Bösing. Lecture notes: Introduction to ultra-relativistic heavy-ion collissions.
Westfälische Wilhelms Universität Münster, 2011.

[ALI04] ALICE Collaboration. ALICE: Physics performance report, volume I. *J. Phys.*, G30:1517–1763, 2004.

[ALI06] ALICE Collaboration. ALICE: Physics performance report, volume II. *J. Phys.*, G32:1295–2040, 2006.

[ALI08] ALICE Collaboration. The ALICE experiment at the CERN LHC. *JINST*, 3:S08002, 2008.

[ALI10] ALICE Collaboration. Elliptic flow of charged particles in Pb-Pb collisions at 2.76 TeV. *Phys. Rev. Lett.*, 105:252302, 2010, arXiv:1011.3914.

[ALI11a] ALICE Collaboration. Higher harmonic anisotropic flow measurements of charged particles in Pb-Pb collisions at $\sqrt{s_{NN}}$=2.76 TeV. *Phys. Rev. Lett.*, 107:032301, 2011, arXiv:1105.3865.

[ALI11b] ALICE. Two-pion Bose-Einstein correlations in central Pb-Pb collisions at $\sqrt{s_{NN}}$ = 2.76 TeV. *Phys. Lett.*, B696:328–337, 2011, arXiv:1012.4035.

[ALI11c] ALICE Collaboration. Centrality dependence of the charged-particle multiplicity density at mid-rapidity in Pb-Pb collisions at $\sqrt{s_{NN}}$ = 2.76 TeV. *Phys. Rev. Lett.*, 106:032301, 2011, arXiv:1012.1657.

[ALI11d] ALICE Collaboration. Suppression of Charged Particle Production at Large Transverse Momentum in Central Pb–Pb Collisions at $\sqrt{s_{NN}}$ = 2.76 TeV. *Phys. Lett.*, B696:30–39, 2011, arXiv:1012.1004.

[ALI12] ALICE Collaboration. Particle-yield modification in jet-like azimuthal di-hadron correlations in Pb-Pb collisions at $\sqrt{s_{NN}}$ = 2.76 TeV. *Phys.Rev.Lett.*, 108:092301, 2012, arXiv:1110.0121.

[ALI13a] ALICE Collaboration. Directed Flow of Charged Particles at Midrapidity Relative to the Spectator Plane in Pb-Pb Collisions at $\sqrt{s_{NN}}$=2.76 TeV. *Phys. Rev. Lett.*, 111(23):232302, 2013, arXiv:1306.4145.

[ALI13b] ALICE Collaboration. Centrality Dependence of Charged Particle Production at Large Transverse Momentum in Pb–Pb Collisions at $\sqrt{s_{\rm NN}} = 2.76$ TeV. *Phys. Lett.*, B720:52–62, 2013, arXiv:1208.2711.

[ALI13c] ALICE Collaboration. Centrality determination of Pb-Pb collisions at $\sqrt{s_{NN}} = 2.76$ TeV with ALICE. *Phys.Rev.*, C88(4):044909, 2013, arXiv:1301.4361.

[ALI14] ALICE Collaboration. Performance of the ALICE Experiment at the CERN LHC. *Int. J. Mod. Phys.*, A29:1430044, 2014, arXiv:1402.4476.

[ALI15a] 2015. ALICE Matters 'ALICE: from LS1 to readiness for Run 2' available at `http://alicematters.web.cern.ch/?q=ALICE_LS1_readiness`.

[ALI15b] 2015. Offline web page at `http://aliceinfo.cern.ch/Offline`.

[ALI15c] 2015. MonALISA Repository for ALICE `http://http://alimonitor.cern.ch`.

[ALI15d] ALICE Collaboration. Centrality dependence of particle production in p-Pb collisions at $\sqrt{s_{\rm NN}}$= 5.02 TeV. *Phys. Rev.*, C91(6):064905, 2015, arXiv:1412.6828.

[ALI15e] ALICE Collaboration. Multiplicity dependence of jet-like two-particle correlation structures in p–Pb collisions at $\sqrt{s_{NN}}$=5.02 TeV. *Phys. Lett.*, B741:38–50, 2015, arXiv:1406.5463.

[Ali15f] M. Zimmermann for the ALICE Collaboration. The ALICE analysis train system. *J. Phys. Conf. Ser.*, 608(1):012019, 2015, arXiv:1502.06381.

[ALI16] ALICE Collaboration. The ALICE Transition Radiation Detector: status and perspectives for Run II. 2016, arXiv:1601.00493.

[ATL08] ATLAS. The ATLAS Experiment at the CERN Large Hadron Collider. *JINST*, 3:S08003, 2008.

[ATL12] ATLAS Collaboration. Observation of a new particle in the search for the Standard Model Higgs boson with the ATLAS detector at the LHC. *Phys.Lett.*, B716:1–29, 2012, arXiv:1207.7214.

[Bag08] S Bagnasco, L Betev, P Buncic, F Carminati, C Cirstoiu, C Grigoras, A Hayrapetyan, A Harutyunyan, A J Peters, and P Saiz. Alien: Alice environment on the grid. *Journal of Physics: Conference Series*, 119(6):062012, 2008.

[Bar02] Roger Barlow. Systematic errors: Facts and fictions. In *Advanced Statistical Techniques in Particle Physics. Proceedings, Conference, Durham, UK, March 18-22, 2002*, pages 134–144, 2002, hep-ex/0207026.

[Bat12] B. Bathen. *Jet Measurements and Reconstruction Biases in Proton-Proton and Pb-Pb Collisions with ALICE at the LHC*. Doktorarbeit, 2012.

[Baz12] A. Bazavov et al. The chiral and deconfinement aspects of the QCD transition. *Phys. Rev.*, D85:054503, 2012, arXiv:1111.1710.

[Ber15] Dario Berzano, 2015. `https://dberzano.github.io/alice/install-aliroot/`.

[Bet09] Siegfried Bethke. The 2009 World Average of alpha(s). *Eur. Phys. J.*, C64:689–703, 2009, arXiv:0908.1135.

[Bha14] Tanmoy Bhattacharya et al. QCD Phase Transition with Chiral Quarks and Physical Quark Masses. *Phys. Rev. Lett.*, 113(8):082001, 2014, arXiv:1402.5175.

[Bor10] Szabolcs Borsanyi, Gergely Endrodi, Zoltan Fodor, Antal Jakovac, Sandor D. Katz, Stefan Krieg, Claudia Ratti, and Kalman K. Szabo. The QCD equation of state with dynamical quarks. *JHEP*, 11:077, 2010, arXiv:1007.2580.

[BS87] Hans-Uno Bengtsson and Torbjorn Sjostrand. The Lund Monte Carlo for Hadronic Processes: Pythia Version 4.8. *Comput. Phys. Commun.*, 46:43, 1987.

[BW09] P. Braun-Munzinger and J. Wambach. ***Colloquium*** : Phase diagram of strongly interacting matter. *Rev. Mod. Phys.*, 81:1031–1050, Jul 2009.

[Cer15] 2015. CERN web page at `http://home.cern/about/engineering/restarting-lhc-why-13-tev`.

[CMS08] CMS. The CMS experiment at the CERN LHC. *JINST*, 3:S08004, 2008.

[CMS11] CMS Collaboration. Observation and studies of jet quenching in PbPb collisions at nucleon-nucleon center-of-mass energy = 2.76 TeV. *Phys. Rev.*, C84:024906, 2011, arXiv:1102.1957.

[CMS12a] CMS Collaboration. Jet momentum dependence of jet quenching in PbPb collisions at $\sqrt{s_{NN}}$ = 2.76 TeV. *Phys. Lett.*, B712:176–197, 2012, arXiv:1202.5022.

[CMS12b] CMS Collaboration. Measurement of isolated photon production in *pp* and PbPb collisions at $\sqrt{s_{NN}}$ = 2.76 TeV. *Phys. Lett.*, B710:256–277, 2012, arXiv:1201.3093.

[CMS12c] CMS Collaboration. Observation of a new boson at a mass of 125 GeV with the CMS experiment at the LHC. *Phys.Lett.*, B716:30–61, 2012, arXiv:1207.7235.

[CMS14] CMS Collaboration. Measurement of momentum flow relative to the dijet system in PbPb and pp collisions at $\sqrt{s_{NN}} = 2.76$ TeV. 2014. `https://cds.cern.ch/record/1703014/files/HIN-14-010-pas.pdf`.

[CMS16] CMS Collaboration. Measurement of transverse momentum relative to dijet systems in PbPb and pp collisions at $\sqrt{s_{\mathrm{NN}}} = 2.76$ TeV. *JHEP*, 01:006, 2016, arXiv:1509.09029.

[CSS12] Matteo Cacciari, Gavin P. Salam, and Gregory Soyez. FastJet User Manual. *Eur. Phys. J.*, C72:1896, 2012, arXiv:1111.6097.

[DK01] Yuri L. Dokshitzer and D. E. Kharzeev. Heavy quark colorimetry of QCD matter. *Phys. Lett.*, B519:199–206, 2001, arXiv:hep-ph/0106202.

[EB64] F. Englert and R. Brout. Broken Symmetry and the Mass of Gauge Vector Mesons. *Phys. Rev. Lett.*, 13:321–323, 1964.

[EB08] Lyndon Evans and Philip Bryant. LHC Machine. *JINST*, 3:S08001, 2008.

[Eur88] European Muon Collaboration. Shadowing in Deep Inelastic Muon Scattering from Nuclear Targets. *Phys. Lett.*, B211:493, 1988.

[GHK64] G. S. Guralnik, C. R. Hagen, and T. W. B. Kibble. Global Conservation Laws and Massless Particles. *Phys. Rev. Lett.*, 13:585–587, 1964.

[GKM16] Jan Fiete Grosse-Oetringhaus, Monika Kofarago, and Andreas Morsch. Jet-like Peak-Shapes in Angular Correlations in PbPb Collisions, 2016. ALICE internal note, `https://aliceinfo.cern.ch/Notes/node/33`.

[GM70] R. J. Glauber and G. Matthiae. High-energy scattering of protons by nuclei. *Nucl. Phys.*, B21:135–157, 1970.

[GO09] Jan Fiete Grosse-Oetringhaus. Measurement of the Charged-Particle Multiplicity in Proton-Proton Collisions with the ALICE Detector. *CERN-THESIS-2009-033*, 2009.

[GW94] Miklos Gyulassy and Xin-Nian Wang. HIJING 1.0: A Monte Carlo program for parton and particle production in high-energy hadronic and nuclear collisions. *Comput. Phys. Commun.*, 83:307, 1994, arXiv:nucl-th/9502021.

[Hig64] Peter W. Higgs. Broken Symmetries and the Masses of Gauge Bosons. *Phys. Rev. Lett.*, 13:508–509, 1964.

[KKP00] Bernd A. Kniehl, G. Kramer, and B. Potter. Fragmentation functions for pions, kaons, and protons at next-to-leading order. *Nucl. Phys.*, B582:514–536, 2000, arXiv:hep-ph/0010289.

[L3 90] L3 Collaboration. The Construction of the L3 Experiment. *Nucl.Instrum.Meth.*, A289:35–102, 1990.

[Lef09] C Lefevre. LHC the guide, 2009. CERN-Brochure-2009-003-Eng at `http://cdsweb.cern.ch/record/1165534?ln=de`.

[LHC08a] LHCf. The LHCf detector at the CERN Large Hadron Collider. *JINST*, 3:S08006, 2008.

[LHC08b] LHCb. The LHCb Detector at the LHC. *JINST*, 3:S08005, 2008.

[LHC15] LHCb Collaboration. Observation of J/Ψp Resonances Consistent with Pentaquark States in $\Lambda_b^0 \to J/\Psi K^-$p Decays. *Phys. Rev. Lett.*, 115:072001, 2015, arXiv:1507.03414.

[Mil07] Michael L. Miller, Klaus Reygers, Stephen J. Sanders, and Peter Steinberg. Glauber modeling in high energy nuclear collisions. *Ann. Rev. Nucl. Part. Sci.*, 57:205–243, 2007, arXiv:nucl-ex/0701025.

[MoE16] MoEDAL Collaboration. Search for magnetic monopoles with the MoEDAL prototype trapping detector in 8 TeV proton-proton collisions at the LHC. 2016, arXiv:1604.06645.

[Par14] Particle Data Group. Review of Particle Physics. *Chin. Phys.*, C38:090001, 2014.

[Per00] D.H. Perkins. Introduction to high energy physics. 4th ed. *Cambridge University Press*, 2000. ISBN 0-521-62196-8.

[RSR11] S. Rossegger, B. Schnizer, and W. Riegler. Analytical solutions for space charge fields in TPC drift volumes. *Nucl.Instrum.Meth.*, A632:52–58, 2011.

[SB87] Torbjorn Sjostrand and Mats Bengtsson. The Lund Monte Carlo for Jet Fragmentation and e+ e- Physics. Jetset Version 6.3: An Update. *Comput. Phys. Commun.*, 43:367, 1987.

[Sne11] Raimond Snellings. Elliptic Flow: A Brief Review. *New J. Phys.*, 13:055008, 2011, arXiv:1102.3010.

[STA11] STAR Collaboration. Studies of di-jet survival and surface emission bias in Au+Au collisions via angular correlations with respect to back-to-back leading hadrons. *Phys. Rev.*, C83:061901, 2011, arXiv:1102.2669.

[STA13] STAR Collaboration. Experimental studies of di-jets in Au + Au collisions using angular correlations with respect to back-to-back leading hadrons. *Phys. Rev.*, C87(4):044903, 2013, arXiv:1212.1653. data taken from `https://drupal.star.bnl.gov/STAR/files/starpublications/191/data.html`, Figure 9.

[TOT08] TOTEM. The TOTEM experiment at the CERN Large Hadron Collider. *JINST*, 3:S08007, 2008.

[WG91] Xin-Nian Wang and Miklos Gyulassy. HIJING: A Monte Carlo model for multiple jet production in p p, p A and A A collisions. *Phys. Rev.*, D44:3501–3516, 1991.

[YHM05] K. Yagi, T. Hatsuda, and Y. Miake. *Quark-Gluon Plasma: From Big Bang to Little Bang*. Cambridge Monographs on Particle Physics, Nuclear Physics and Cosmology. Cambridge University Press, 2005.

[ZG14] Markus Zimmermann and Jan Fiete Grosse-Oetringhaus. The LEGO Train System, 2014. ALICE internal note, `https://aliceinfo.cern.ch/Notes/node/342`.

Acknowledgements

I would like to thank Johannes P. Wessels for giving me the opportunity to do my PhD in his working group and to perform the work at CERN. I thank Jan Fiete Grosse-Oetringhaus for supporting my doctoral student application. The work was sponsored by the Wolfgang Gentner Programme of the Federal Ministry of Education and Research.
A very special thanks goes to Jan Fiete Grosse-Oetringhaus for the supervision of my work. I am grateful for all the long and fruitful discussions and the detailed explanations. He improved this thesis with many good advice.
I enjoyed working in the group of Johannes P. Wessels in Münster and in the group of Andreas Morsch at CERN. I would like to thank all members of these working groups for the nice working atmosphere.
For the enjoyable teamwork on the LEGO train system, I thank Jan Fiete Grosse-Oetringhaus and Costin Grigoras. They taught me a lot about the LEGO trains and how to develop improvements on such a system. Further I thank the whole ALICE Offline group for the support of my work and for the good working atmosphere.
I thank the ALICE collaboration, in particular the physics working group on Correlations, Fluctuations and Bulk (CF). Especially, I thank Michael Weber, Megan Connors, Leonardo Milano, Alice Ohlson, Jürgen Schuhkraft, Andreas Morsch, Raghava Varma and Greeshma Meethaleveedu for the productive discussions on 2+1 correlations.
For many corrections and suggestions during my thesis work, I thank Jan Fiete Grosse-Oetringhaus, Alice Ohlson, Leticia Cunqueiro, Hugo Day and Andreas Morsch.
Many thanks to my family and my friends who emotionally supported me in the last four years. Special thanks to Miryea who always encouraged me. Ein besonderer Dank geht an meine Familie, insbesondere an meinen Eltern Maria und Paul Zimmermann.

Lebenslauf

Name	Markus Zimmermann
Geburtstag	26/08/1988
Geburtsort	Warendorf
Staatsangehörigkeit	deutsch
Eltern	Paul Zimmermann Maria Zimmermann, geb. Gerbert

Schulausbildung

08/1999-06/2007	Gymnasium Collegium Johanneum, Ostbevern
08/1995-06/1999	Ambrosiusschule, Ostbevern

Studium

10/2010-10/2012	Studium der Physik (Master of Science) an der Westfälische Wilhelms-Universität Münster Masterarbeit *Jet Reconstruction and Event-Background Fluctuations in Pb-Pb Collisions*
31.10.2012	Master of Science
10/2007-08/2010	Studium der Physik (Bachelor of Science) an der Westfälische Wilhelms-Universität, Münster Bachelorarbeit *Study of the Response of Different Jet-Algorithms for the ALICE-Experiment*
17.08.2010	Bachelor of Science

Promotionsstudium

12/2012	Beginn der Dissertation am Institut für Kernphysik bei Prof. Dr. Johannes P. Wessels PhD thesis *Multi Particle Correlation Studies in Heavy Ion Collisions at the LHC*

Berufstätigkeit

02/2016-12/2016	Studentische Hilfskraft am Institut für Kernphysik
02/2013-01/2016	Doctoral Student am CERN
09/2010-10/2012	Studentische Hilfskraft am Institut für Kernphysik

Münster, den 21. September 2016